THE EFFECTS OF CAR A-PILLAR AND WINDSHIELD GEOMETRY ON LOCAL FLOW AND NOISE

A thesis submitted in accordance with the regulations for the degree of Doctor of Philosophy

By

Firoz Alam

Department of Mechanical and Manufacturing Engineering

RMIT University

Melbourne, Australia

September 2000

This thesis is dedicated to the loving memory of my maternal grandfather, Sekander Ali Bepari and millions of people who sacrificed their lives for the independence of the People's Republic of Bangladesh.

ABSTRACT

A desirable requirement in the production of modern vehicles world-wide is the provision of a high level of driving comfort. An important aspect of this is the minimisation of aerodynamic noise. As structure-borne, engine, tyre, and power-train noise sources have been reduced in recent years, the aerodynamic noise is significant, especially at driving speeds exceeding 100 km/h. Prior experimental studies have revealed that the flow around a passenger car's A-pillar region is a primary source of aerodynamic noise, since the highest pressure fluctuation occurs here. Also, this region is closest to the driver's ears. Whilst a small part of the noise can come from aerodynamic noise generated by the mirror as the flow is first incident on the A-pillar, this study will only be addressing flow around the A-pillar. It is known that the area and strength of the A-pillar flow separation depend mainly on the local A-pillar and windshield geometry and yaw angle. However, the effects of scaling, local radii and yaw angle on the potential for noise generation are not well understood. Scaling is important so that model-scale results can be translated to the full-scale. Computational Fluid Dynamics methods (CFD) are not sufficiently developed either to predict the surface pressure fluctuations or the resulting acoustic waves with the required degree of accuracy. The objectives of this work were to investigate the scale effects, the influence of the local A-pillar and windshield radii on the flow characteristics, and the influence of yaw angle.

In order to address these objectives, a series of experimental investigations was conducted using five 40% scale generic models with different A-pillar and windshield geometries and using three production vehicles. One model had a sharp-edged vertical windscreen. The other four models had a 60° inclined windscreen, which is a typical slant angle for contemporary production passenger cars, and various degrees of edge rounding including a model with a sharp edge. These models were used to measure the surface mean and fluctuating pressures in the A-pillar region at different speeds and steady yaw angles. Production vehicles were used to evaluate the surface mean and fluctuating pressures close to the A-pillar region, and the 'in-cabin noise' as a function of steady yaw angle and increased rounding of the A-pillar. The production vehicle tests were performed at different speeds and yaw angles in wind-tunnels and on-road. Flow visualisation was used to supplement the pressure data.

The surface mean and fluctuating pressures were converted to non-dimensional pressure coefficients and the frequency content of the fluctuating pressure was investigated via the normalised power spectral density. Generally the surface mean and fluctuating pressure coefficients were found to be independent of Reynolds numbers. However, when yawed, a slight dependency was found to occur on the leeward side. This minor dependency was noted in the separated regions, but was not evident in the re-attached areas. The amplitudes and frequencies of the fluctuating pressures scaled well with velocity head and Strouhal number. Therefore, a scale model can be used for the prediction of the surface hydrodynamic pressures in the A-pillar region of a future vehicle when suitable scaling laws are used.

The magnitudes of fluctuating pressures and the area of flow separation close to the A-pillar region depended largely on the local radii. Most energy from the fluctuating pressures in the A-pillar region was between Strouhal numbers 5 to 12. The maximum hydrodynamic pressure fluctuation was found to be between the separated and re-attached areas rather than at the re-attachment points as has been proposed by other researchers.

Yaw could increase the area and magnitude of the flow separation on the leeward side by an order of magnitude compared to the windward side for the slanted sharp-edged model. However, the model shape with no slant angle (i.e., a vertical windshield) produced an intense but relatively small flow separation on the windward side when yawed. Negligible flow separation was found on the models with corner rounding and increase of yaw angle did not increase the separation substantially, even on the leeward side. However, future work is recommended on an additional model incorporating a smaller corner radius.

For the production vehicles an increased rounding of the A-pillar significantly reduced the magnitude of the external fluctuating pressures, although the 'in-cabin noise' typically reduced by 2-3 dB. The amplitudes and frequencies of the fluctuating pressures scaled well with velocity head and Strouhal number.

Atmospheric turbulence, correlation between the external pressure fluctuations and in-cabin noise, and boundary layer characteristics in the A-pillar region were not included in this work but are thought to be worthy of further investigation.

ACKNOWLEDGMENTS

First of all, I want to express my whole-hearted thanks and gratitude to my senior supervisor, my mentor, Associate Professor Simon Watkins for his guidance, encouragement, advice, constructive criticism and assistance.

I am also indebted to my second supervisor, Mr. Clive Humphris, Manager, Vehicle Refinement & Aerodynamics, Product Development, Ford Motor Company of Australia for advice, feedback, assistance and encouragement.

I would like to acknowledge the assistance of Mr. Christian Peric, Senior Engineer of the Noise and Vibration Research Group, General Motors-Holden, Australia for providing the test car.

I also acknowledge the assistance of the following for their advice and technical assistance: Mr. Ian Overend (Technical Services Manager), Mark Overend, David Goodie, Jeremy Luci, John Haddon, Department of Mechanical and Manufacturing Engineering, RMIT University.

My sincere thanks to all postgraduate students of Automotive Engineering Group, Department of Mechanical and Manufacturing Engineering, RMIT University for their assistance and advice.

I also owe heartfelt thanks to Mr. Peter Dale, Professional Officer and Acoustic Consultant of the Department of Applied Physics, RMIT University for providing microphones and valuable technical advice.

I am also grateful to the Australian Federal Government for financial support through the Australian Postgraduate Award (APA) Scholarships during this period.

Finally, I must express my sincerest appreciation to my wife, Sharmin Alam for her encouragement, inspiration, patience and tolerance during the time it took to complete this work.

DECLARATION OF ORIGINALITY

I, Firoz Alam, hereby declare that this thesis has not been submitted, partly or fully for the award of any other degree or diploma in any university. To the best of my knowledge and belief, this thesis contains no material previously published or written by another person, except where due reference is made in the text.

Firoz Alam

(Signature of Candidate)

September, 2000

TABLE OF CONTENTS

Page No.

LIST OF FIGURES

LIST OF FIGURES CONTAINED IN APPENDICES

LIST OF TABLES

NOMENCLATURE

General

a or c	Speed of Sound
C_p	Surface Mean Pressure Coefficient ($C_p = \frac{p_m - p_s}{\frac{1}{2}\rho V^2}$)
$C_{p^{rms}}$	Surface Fluctuating Pressure Coefficient ($C_{p^{rms}} = \frac{p_{std}}{\frac{1}{2}\rho V^2}$)
f	Frequency in Hertz
Hz	Hertz
Iu	Turbulence Intensity in the Longitudinal Direction ($I_u = \frac{\sqrt{\overline{u'^2}}}{\overline{u}}$)
Iv	Turbulence Intensity in the Lateral Direction
Iw	Turbulence Intensity in the Vertical Direction
M	Mach Number ($\frac{V}{a}$)
L	Characteristic Length or Length Scale of Noise Sources
p	Pressure in Pascal
p_m	Pressure at the Point of Measurement
p_s	Local Static Pressure
p_{std}	Standard Deviation of the Surface Pressure Fluctuation
q	Velocity Head ($q = \frac{\rho V^2}{2}$)
Re	Reynolds Number ($R_e = \frac{V.L}{\nu}$)
S_t	Strouhal Number ($S_t = \frac{f.L}{V}$)
T_{ij}	Lighthill's Turbulence Stress Tensor
u	Longitudinal Component of Resultant Speed
V	Air Speed
Vc	Car Speed

Vw	Atmospheric Wind Speed
Vr	Relative Wind Speed
v	Lateral Component of Resultant Speed
w	Vertical Component of Resultant Speed
ν	Kinematic Viscosity
σ_{ij}	Viscous Stress Tensor
δ_{ij}	Kronecker δ-Function (δ_{ij}=1 if i=j, δ_{ij}=0 if i≠j)
ρ	Air Density (kg/m^3)
φ	Wind Angle Relative to Car Centre Line (in degree)
Ψ	Yaw Angle (in degree)
ω	Angular Velocity of Vortex
∇	Laplacian Operator

Subscripts

rms	Root Mean Square
f	Full-Scale
m	Model-Scale

Abbreviations and Acronyms

A/D	Analogue to Digital
CFD	Computational Fluid Dynamics
DAT	Digital Audio Tape
DDE	Dynamic Data Exchange
ISO	International Standardisation Organisation
OR	On Road
RMIT	Royal Melbourne Institute of Technology
SAE	Society of Automotive Engineers, USA
SAE-A	Society of Automotive Engineers, Australasia
SPL	Sound Pressure Level
WT	Wind-Tunnel
MWT	Monash/RMIT Universities' Aeroacoustic Wind-Tunnel
RWT	RMIT University Aeroacoustic Wind-Tunnel
L	Left Ear of the Aachen Head
R	Right Ear of the Aachen Head
HD	Hard Disk

Abbreviations Used for Idealised Models

C	Circular Model
LE	Large Ellipsoidal Model
R	Rectangular Model
SE	Small Ellipsoidal Model
SER	Slanted Sharp-edged Model
TR	Top Row
BR	Bottom Row
K	km/h
'-'	Negative Yaw Angle (Leeward Side)
'+'	Positive Yaw Angle (Windward Side)

Chapter One

INTRODUCTION

In this chapter an overview of vehicle aerodynamics and aeroacoustics is presented with particular reference to aerodynamically induced noise from the car A-pillar region. Relevant acoustic theory and background literature is also presented and the chapter concludes with the major objectives and layout of the work.

1.1 Vehicle Aerodynamics- An Overview

Road vehicle aerodynamics has become an important part of Automotive Engineering as it encompasses vehicle performance, comfort, safety, stability, cooling and visibility. These all depend on the flow field around and through the vehicle. During the Middle East war in the 1970's, an oil embargo and subsequent world wide fossil fuel crisis compelled vehicle manufacturers to pay more attention to the aerodynamic efficiency of their products. A moving vehicle displaces the surrounding air and creates a resultant resistive force on the vehicle, which is called aerodynamic drag. Typically, the aerodynamic drag of a medium-sized car accounts for 75-80 percent of the total resistance to motion at 100 km/h, the rest being mainly rolling resistance, Hucho (1998). Therefore, reducing aerodynamic drag contributes significantly to the fuel economy of a car. Drag reduction, more efficient engine technology and weight reduction, became the primary design goals for vehicle engineers and designers around the world. Average drag coefficients for typical cars dropped substantially from around 0.5 in the 1960's to typically 0.3 in the late 1980's and mid 1990's.

Whilst improved aerodynamics lowered fuel consumption, the streamlining of car shapes created other issues. Passenger comfort became an essential criterion for marketing. In addition, the forward movement of the car's centre of pressure (a common consequence of streamlining) can lead to a degradation of vehicle stability, particularly in crosswind conditions. Aerodynamics, comfort, pleasing styling and

efficient performance are important marketing aspects for a new vehicle, which often conflict with the necessary requirements for adequate engine cooling and vehicle cross wind stability. Stability problems have been of concern, Cooper (1984), and are still part of ongoing research (eg. Nguyen et al., 1997). Other recent problems with lower drag vehicles, which have surfaced in recent years, are those of contamination, such as the accumulation of rain water and dirt on lights, exterior mirrors and windows, Popat (1991). Comfort is now the dominating and demanding field of research in vehicle dynamics. A spectrum of tasks for vehicle aerodynamics, adapted from Hucho (1998), is shown in Figure 1.1.

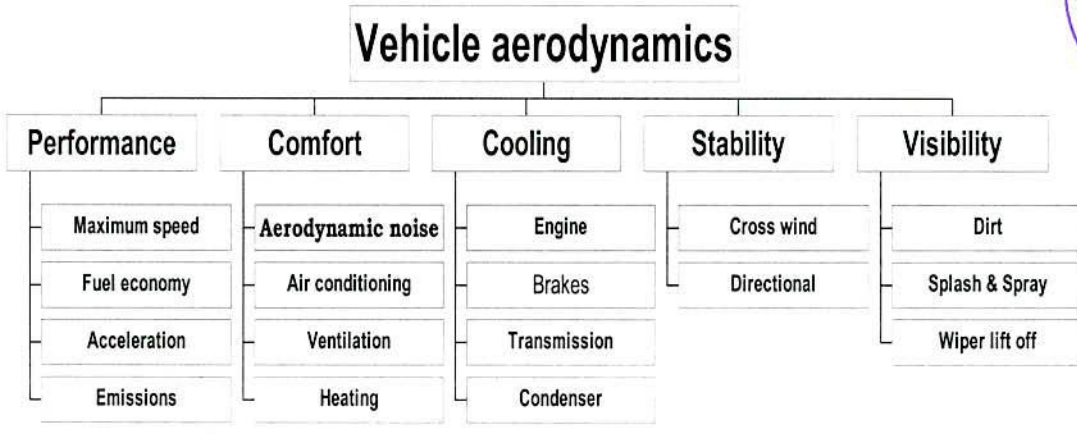

Figure 1.1: The Main Spectrum of Vehicle Aerodynamics (after Hucho, 1998)

The airflow around a vehicle is responsible for its aerodynamic resistance (drag) and aerodynamic directional stability, including response to atmospheric crosswinds. Ideally, the outer flow close to the surface should be optimised to prevent droplets of rainwater from accumulating on windows, outside mirrors and headlights, and also to reduce externally generated wind noise, which will be discussed in the next section.

Along with vehicle dynamics, vehicle aeroacoustics is a new and fast growing research area, which deals with, amongst other subjects, the understanding and reduction of aerodynamically induced noise from road vehicles. The following subsections will elaborate on vehicle aeroacoustics.

1.2 Vehicle Aeroacoustics

Aerodynamic noise reduction work requires a working knowledge of both acoustics and aerodynamics. In the next subsection, background information on acoustics will be presented and the process of aerodynamically generated noise relevant to car geometry will also be discussed.

1.2.1 Acoustics, Noise and Sound: A General Overview

Any pressure variation from the mean atmospheric pressure that can be detected by the human ear and propagates through an elastic medium at some characteristic speed is called sound. Sound is the molecular transfer of motional (kinetic) energy and cannot therefore pass through a vacuum. For sound propagation, the medium must have inertia and elasticity. The amplitude of the pressure fluctuations (disturbance) is determined by the magnitude of fluctuations of the propagation speed (acoustic particle velocity), pressure, medium density, entropy (energy) and square of local sound speed, Goldstein (1976). There are two fundamental mechanisms responsible for sound generation: the vibration of solid bodies resulting in the generation and radiation of sound energy and referred to as structure-borne sound, and the flow-induced noise resulting from pressure fluctuations induced by unsteady flows and turbulence, called aerodynamically induced sound, Norton (1989). Generally, any unwanted sound is called noise. A sound that has only one frequency is known as a pure tone (the number of pressure variations per second is called frequency and is measured in Hertz). In practice, pure tones are seldom encountered and most sounds are made up of different frequencies. Most noise consists of a wide mixture of frequencies known as broad band noise. If the noise has frequencies evenly distributed throughout the audible range, it is known as white noise and it sounds rather like rushing water, Bruel & Kjaer (1984). The normal range of hearing for a healthy young person extends from approximately 20 Hz up to 20,000 Hz. The human ear responds not only in a logarithmic way to fluctuations in sound pressure, but also differentially throughout the audio frequency spectrum; subjectively, high frequencies

generally appear much louder than low frequencies. A logarithmic scale makes the presentation of the data more compact. The human response to sound may be approximated by the two laws of Weber and Fechner. Both are approximate and based on observations of human physiological and psychological reactions to external stimuli. Weber's law states that 'the minimum increase of stimulus which will produce a perceptible increase of sensation is proportional to pre-existent stimulus'. Fechner's law concerns the intensity of the human response to a stimulus and states that the intensity of human sensation changes logarithmically with the energy that causes the sensation, Anderson et al. (1993).

Often the range of hearing is broken into segments called octave bands where the top frequency of each band is twice the bottom frequency of that band, and the top frequency of one band is of course the bottom frequency of the next. For more precise work each octave is divided into three and sounds are often measured in third-octave bands. The loudness or strength of a sound wave is related to the magnitude of the air pressure fluctuations, also known as the acoustic pressure.

The most common measure of sound is sound pressure level (SPL). SPL is usually expressed in terms of the deciBel (dB) scale named after Alexander Graham Bell. It is important to understand that the decibel is fundamentally a ratio of sound pressures. The SPL is defined as the following: $\boldsymbol{SPL(dB)}=10\log(\frac{\boldsymbol{p}^2}{\boldsymbol{p}_{ref}^2})$

where $\boldsymbol{p}$ is the root mean square (rms) acoustic pressure and $\boldsymbol{p}_{ref}$ is the reference pressure $2_x10^{-5}\boldsymbol{N}/\boldsymbol{m}^2$ or 20 μPa (The value of the reference pressure is approximately the value of the rms (root mean square) sound pressure corresponding to a very faint sound that can just be heard by a human in the mid frequency range).

When acoustic measurements are made with a microphone, the microphone senses the pressure signal and converts this (via suitable signal conditioning) to a fluctuating voltage. This signal is often fed to a spectrum analyser, which performs a Fast Fourier Transform (FFT) and produces a graph of the sound pressure level versus frequency.

If time-frequency information is required, a Short-term Fourier Transform or Wavelet analysis is performed using purpose written or commercial software.

Sound measuring instruments are designed to better replicate human perception of sound by the use of electronic weighting curves. There are four ISO recommended weighting curves, namely A, B, C and D, used in scientific measurements worldwide. Strictly speaking, A-weighting is intended for levels below 55 dB (ref. 20 μPa), B-weighting between 55 dB and 85 dB (ref. 20 μPa), and C-weighting above 85 dB (ref. 20 μPa). D-weighting follows a contour of perceived noisiness and was originally intended for aircraft noise measurements. Usually different weighting networks are applied to different levels to match the differences exhibited in the equal loudness contours but for most purposes, the A-weighting is used since B and C-weightings do not correlate well with subjective tests. One reason for this lack of correlation between subjective tests and B and C-weighted measurements is because equal loudness contours were based on experiments which used pure tones while most common sounds are not pure tones but very complex signals made up of many different tones, Bruel & Kjaer (1984).

1.2.2 The Process of Aerodynamic Noise Generation

Vehicle aeroacoustics is concerned with sound generated by aerodynamic forces or motions originating in the airflow around the body of a vehicle rather than by externally applied forces or motions of structures to the fluid. (The sounds generated by vibrating violin strings and loudspeakers are in the latter category). On the other hand, sounds produced by the unsteady aerodynamic forces and turbulent flows per se, or their interactions with a structure, are considered the domain of aeroacoustics. Therefore, aeroacoustics is the study of sound associated with airflow, and is thus a combination of aerodynamics and acoustics. In this work, discussions will be limited to the noise produced by aerodynamic flows and their interaction with the car's external structure. Aerodynamic noise is an inhomogeneous acoustic wave that can result from a number of different mechanisms including separated flow, vortex shedding, free shear layers (including high Mach number jets), attached shear layers,

resonance in cavities etc. Idealised aerodynamic noise sources will be discussed in the next subsection.

1.2.2.1 Monopole, Dipole and Quadrupole Sources of Noise

There are three classifications of noise sources that indicate their relative strengths as a function of their fluctuating velocity and the directivity of the sound radiation. These are Monopole, Dipole and Quadrupole sources. Monopoles are the noise sources due to the time varying volume change or mass injection and their intensity scales are proportional to the fourth power of the fluctuating velocity. The monopole source can come from unsteady volumetric flow addition, such as one experiences from the exhaust pipe of an unmuffled piston engine. This is considered a primary monopole source and sources that are considered to be in this class are dealt with as high priority during the development process so that a well-designed car will have these sources minimised. Such is the case of leaks in the sealings of doors or unsteady addition of volume to the passenger compartment through some leak path, Barlow et al. (1999). The sound intensity of a monopole source is proportional to the 4^{th} power of fluctuating velocity.

Dipole sources are due to the time varying momentum fluxes. Unsteady pressures due to the separated flows and vortex shedding can be idealised as dipole sources. If two simple sources of equal strength are placed close together and arranged to be always of exactly opposite phase, then as one produces a net outflow, the other produces an exactly opposite inflow, Hansen et al. (1996). Thus at some distance from the sources there is no net fluid influx. However, being of opposite sign there is a net thrust exerted on the fluid from the more positive to the more negative source, which periodically fluctuates in orientation. It is the time rate of change of this force on the fluid, which is important for noise production. Such an arrangement becomes a dipole source in the limit if the separation distance between the sources is made infinitely small, i.e., very much less than the radiated wavelength. The sound intensity of a dipole source is proportional to the 6^{th} power of the fluctuating velocity. The noise

from turbulent flow over a small obstruction in an air stream provides a good example of fluid mechanical dipole source of aerodynamic noise.

Quadrupole noise sources are caused by collisions of fluid elements and are typical of the turbulent shear layer of a jet, Barlow et al. (1999). In the extreme, the net shear may reduce to a local stress on the fluid and the time rate of change of shear or stress plays an important role in producing sound. As fluid can be expected to support such forces poorly, quadrupole sources are relatively poor radiators of noise. However, they do play a dominant part in the mixing region when a fluid jet is introduced into a quiescent atmosphere. The sound intensity of a quadrupole source tends to increase with the 8^{th} power of flow velocity. For low Mach number flow ($M < 0.3$), which is the case for road vehicle applications, the monopole is the most efficient noise source followed, in increasing order of effectiveness, by dipoles and quadrupoles.

For flows relevant to vehicles, a boundary layer grows from the stagnation point (where pressure is maximum and velocity is zero) initially as a laminar layer, but if the length scale of the body is sufficient, transition to a turbulent layer occurs. When the flow reaches a sufficiently strong adverse pressure gradient, separation will occur and all the vorticity will be contained within the shed boundary layer, now referred to as a 'separated shear layer'. Such layers are inherently unstable, especially if turbulent, and entrain the flow on both sides. This entrainment has the dual effect of causing a reversed flow after separation and also a reduction of pressure in the separated flow region. Where reattachment to the surface is possible, the boundary layer re-establishes and the separated flow region remains as a re-circulating low-pressure flow. An experimental investigation conducted by Fricke et al. (1968) has revealed that the magnitude of aerodynamic noise in the separated flow varies significantly depending on the patterns of flow. The study further reported that at least three regions behind a fence in the separated flow could produce noise. They were firstly the turbulent shear layer from the tip of the fence similar to the turbulent mixing region of a jet, secondly, the neighbourhood of the reattachment point which generates a different and stronger dipole type noise, and thirdly, the boundary layer noise in the reversed flow behind the fence and beneath the separated region.

Hucho (1998) reported that the process of re-attachment has the ability to produce noise at lower Mach numbers. However, where reattachment does not occur, the unsteady thin shear layer has a tendency to roll up and feeds energy to the recirculating flow. Thus an unsteady thin shear layer produces a strong vortex and under the right circumstances, the vortex can be shed into the wake when the energy level is too high to be fed further. Usually, when vortices build-up on either side of a bluff body, they can self interfere, and the shedding becomes alternate. This is known as "von Karman vortex street" and it has the ability to create an oscillating wake. A symmetrical flow in the separated region exists only (on a bluff body) for small Reynolds numbers. For large Reynolds numbers, the vortex shedding occurs periodically, and the flow in the separated region is generally unsteady. The kinetic energy from the vortex flow dissipates and renders into frictional heat that leads to a significant pressure loss in the separated region.

A free shear layer in a nominally steady mean flow can execute large-amplitude fluctuations when small, mean flow inhomogeneties trigger the growth of Kelvin-Helmholtz instability waves, Howe (1981). The subsequent motion is often quasi-periodic in time. The periodicity is associated with the existence of a source of feedback that initiates a new instability wave in the shear layer. The typical feedback sources are produced by: the pairing of discrete vortices formed in the layer; the impingement of a shear layer on an edge or other obstacle; the proximity of an acoustic resonator, such as a wall cavity and a vibrating solid body close to the flow field. The free shear layer noise is insignificant for low Mach number flow (0.3 or less) but it is dominant in sonic and high sub-sonic flows.

Generally, separated and reattaching flow exists between the point of reattachment of a free shear layer and a point where it becomes an equilibrium turbulent boundary layer again. As with vortex flows, the problem of scaling arises when one tries to build a model of wall pressure fluctuations in reattached flows. The impingement and splitting of the shear layer at reattachment produces high levels of turbulence activity in the reattached flow, and as this energised flow convects downstream it undergoes a relaxation and development process. Thus, the reattached flow is a fundamentally inhomogeneous, non-equilibrium flow. In a Ph.D. dissertation, Farabee (1986)

estimated that the reattached flow might extend up to 100 times the height of the separation bubble. According to Farabee, if the height of a separation bubble is 1 mm in the side glass offset region, the reattached flow can be extended to 100 mm in length. Therefore, even if a very small separation occurs, the reattached flow probably covers a large area. Figure 1.2 extracted from Katz (1995) shows possible flow separation and re-attachment areas in the forefront of a car.

In the next subsection, the specific noise problems in passenger cars will be discussed.

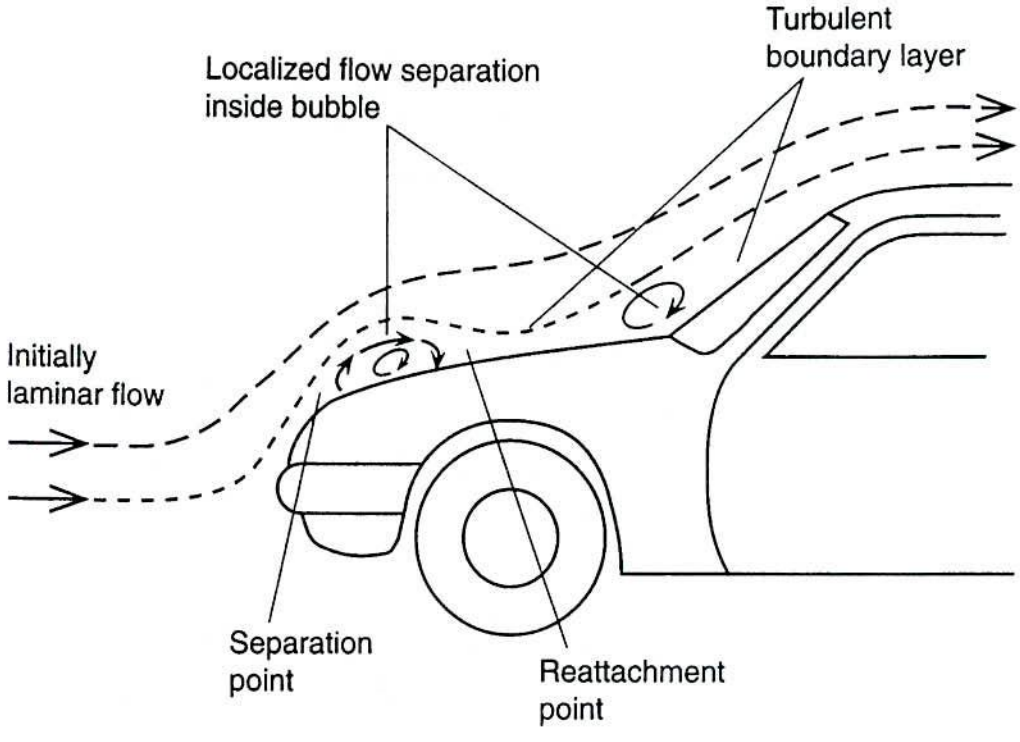

Figure 1.2: Schematic Description of Flow Pattern in the Forefront of a Car (from Katz, 1995)

1.2.2.2 Specific Noise Generation Mechanisms in Passenger Car

As discussed earlier, air in front of a moving vehicle displaces and flows around the automobile causing not only aerodynamic drag but also aerodynamic noise. High aerodynamic noise levels can make it difficult for vehicle occupants to converse or listen to the radio. Apart from this, aerodynamic noise can add to driver fatigue on a long highway trip. Today, high levels of driving comfort in passenger cars are considered an essential requirement in the car market throughout the world. Part of this requirement pertains to the aerodynamic noise. The reduction of structure-borne, engine, tyre and powertrain noise has meant that the significant source of noise at speeds above 100 km/h is the aerodynamic noise.

Aerodynamic noise along with other noises (powertrain, road/tyre interaction and structure-borne noise) heard by the occupants inside the car is called interior noise and this interior noise is of interest for the satisfaction and comfort of the vehicle users. As other sources of noise were reduced, interior noise mainly generated by external flow became an increasing problem for the car manufacturers, designers and engineers. Although there has been much progress in aerodynamic drag reduction, much work needs to be done to reduce aerodynamic noise. A layman might expect that a car with low aerodynamic drag will have low levels of aerodynamic noise. This is not true in practice. No correlation between aerodynamic drag and interior wind noise levels was found in a survey of fifteen production cars, Buchheim et al. (1982). However, this is to be expected since the acoustic power radiated from a jet is typically only $\frac{1}{10^5}$ of aerodynamic power, Hansen et al. (1996). This is because aerodynamic drag is a function of the time-averaged mean pressure distribution acting upon the vehicle surface, where aerodynamic noise depends upon the strength of the highly time-dependent surface pressure fluctuations about the mean value, George et al. (1996). Another explanation given by Hucho (1998) is that the aerodynamic drag depends largely on the exterior airflow over the rear of the car where the flow separates from the vehicle. Conversely, interior wind noise depends greatly on the

details of the exterior airflow around the A-pillar (the corner post between the front side glass and the windshield) and windshield. In addition, small openings around the doors and windows may contribute a great deal to wind noise if left imperfectly sealed, but will have little or no effect on aerodynamic drag.

Aerodynamic noise originates mainly from unsteady pressure fluctuations on the vehicle exterior surfaces. Automobiles are bluff bodies, which means they generally have attached flow over most of the body and large regions of flow separations from a blunt base. However, in the A-pillar region flow separations also occur. Noise sources mostly arise from turbulent flow separations and re-attachments, turbulent boundary layers and natural turbulence inherent in the oncoming airflow. Other typical noise sources are vortex shedding from antennae, roof racks and other protrusions as well as aspiration or leak noise through the door and window seals. It is very important and beneficial to examine the aerodynamic noise sources and paths in the vehicle development process.

Aerodynamic noise propagates through various paths into the inside of the vehicle generating interior noise. One path by which noise can get inside the car is through openings or leaks in the basic structure of the car. The other possible way in which noise can get inside the car is through panels, windows and seals depending upon their particular transmission losses.

Airflow over the automobile causes a difference in time-averaged pressure at different locations on the vehicle surface. The pressure differential between the outside and inside of the car controls the magnitude and direction of leak path. The air pressure is usually lower outside of the car than inside, and the pressure difference causes the air to flow out of small gaps at relatively high velocity generating sound. Leak noise is usually generated by a monopole mechanism. The monopole source comes from unsteady volumetric flow addition, similar to that of an exhaust pipe of an unmuffled piston engine. It is the most efficient source at low Mach numbers, and therefore, applicable to most automotive applications. If a pressure fluctuation on the vehicle's exterior surface causes an unsteady volumetric flow addition to the interior of the vehicle through a leak path, then a strong secondary monopole sound source will

result, George et al. (1995). Since a monopole mechanism is quite efficient in generating sound at low Mach numbers, and since the sound may be tonal in nature and may fluctuate in time, the leak noise is noticeable and annoying. Leak noise is so strong that generally its presence will always dominate other wind noise sources. The most common locations for leaks are the door seals, movable glass seals, and fixed glass seals[1]. Figure 1.3, adapted from George (1989), shows schematically how a leak around a seal can generate monopole, dipole and quadrupole-like noises. Current production cars are generally very well sealed as a result of considerable attention paid by the car companies to this issue. Due to the interaction of external flow with cavities, separation, boundary layer turbulence and atmospheric turbulence, leak noise is usually investigated experimentally, Hucho (1998).

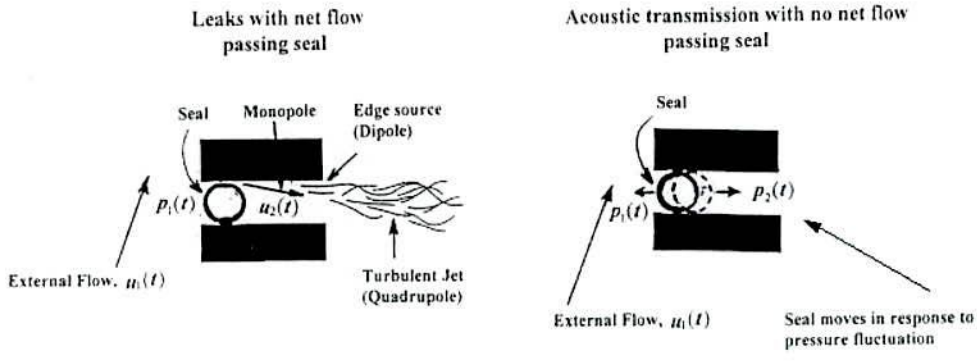

Figure 1.3: A Schematic Representation of Leak Flow (after George, 1989)

The presence of cavities on the vehicle exterior can also generate aerodynamic noise. Aerodynamic noise produced by a cavity is very strong if the cavity is located in the A-pillar area or around the outside rear-view mirror. Common cavity noise sources on a car are the gaps around the doors, exposed gaps on the outside rear-view mirrors, and gaps in the radiator grille area. Although cavity noise can be generated by several different mechanisms, Rockwell et al. (1980), noise is usually caused by the trailing edge wake from the front of the cavity impinging on the rear surface of the cavity. Since the shear layer flow is turbulent, there is no preferred frequency and the resulting cavity noise is broad band in nature. Another mechanism for cavity noise is

[1] Development of good sealing systems is costly; the development for one door can cost USD 400,000 to 750,000, George et al. (1996).

due to feedback and resonance phenomena. For more details on mechanisms of cavity noise refer to George et al. (1989, 1996). A schematic of noise generation mechanisms for flow over the cavity, adapted from George (1989), is shown in Figure 1.4.

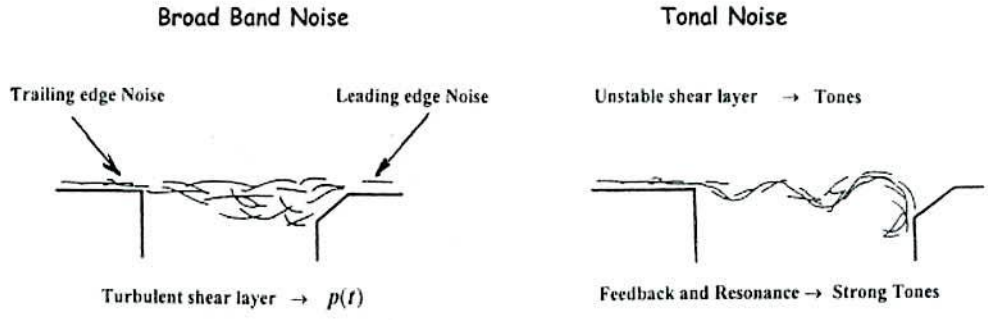

Figure 1.4: Noise Generation Mechanisms for Flow Over Large Open Cavities (After George, 1989)

Another dominant aerodynamic noise is called wind rush noise. It is generated by the fluctuating pressures on the exterior of the vehicle caused by the flow over the surface. A road vehicle is covered by a turbulent boundary layer. Thus, the pressure over much of the vehicle surface fluctuates with time. Even if the vehicle surfaces were perfectly rigid and leak-free, the fluctuating pressure on the surface would generate dipole-type noise that would radiate in all directions. Since the vehicle structure is not perfectly rigid, the fluctuating pressure causes the vehicle windows and body panels to vibrate and radiate noise into the vehicle interior. Separation regions and reattachment points are potential sources of wind rush noise (generally called wind noise). Usually the most serious wind noise problems are associated with the A-pillar area flow and flows due to other adds-on. A schematic of flow pattern over a passenger vehicle is shown in Figure 1.5.

As mentioned in the previous subsection, the Sound Pressure Level (SPL) is proportional to the 4^{th} power of flow velocity for a monopole source, 6^{th} power of flow velocity for a dipole source and 8^{th} power of flow velocity for a quadrupole source. However, the SPL of automobile aerodynamic noise varies between the 4^{th} and 6^{th} power of the flow velocity as automobile aerodynamic noise is typically a

mixture of monopole and dipole sources, George et al. (1996). Therefore, any aerodynamic noise mechanism located in the A-pillar region will be extremely important due to the local velocity being larger than the free stream. Hucho (1998) cites it will be at least 17 dB louder than if the mechanisms were on a comparable surface exposed to the free stream velocity. In addition, the flow in the A-pillar region due to the A-pillar geometry is separated and highly turbulent, hence it produces strong pressure fluctuations and unsteady flows on the side window, on the door and window seals, and on part of the roof. Measurements have shown that the level measured in the separation area behind the A-pillar can be more than 30 dBA higher than that measured in the centre of the roof (an area of attached airflow). Thus, it is also in the interests of the aeroacoustic engineers to avoid airflow separation as far as possible, Hucho (1987). It should be noted that this region is closest to the driver's ears, hence A-pillar noise is the single most important sources of a car occupants' discomfort with regard to wind noise. The following sub-chapter will give an insight on the aerodynamically induced noise generated by the A-pillar.

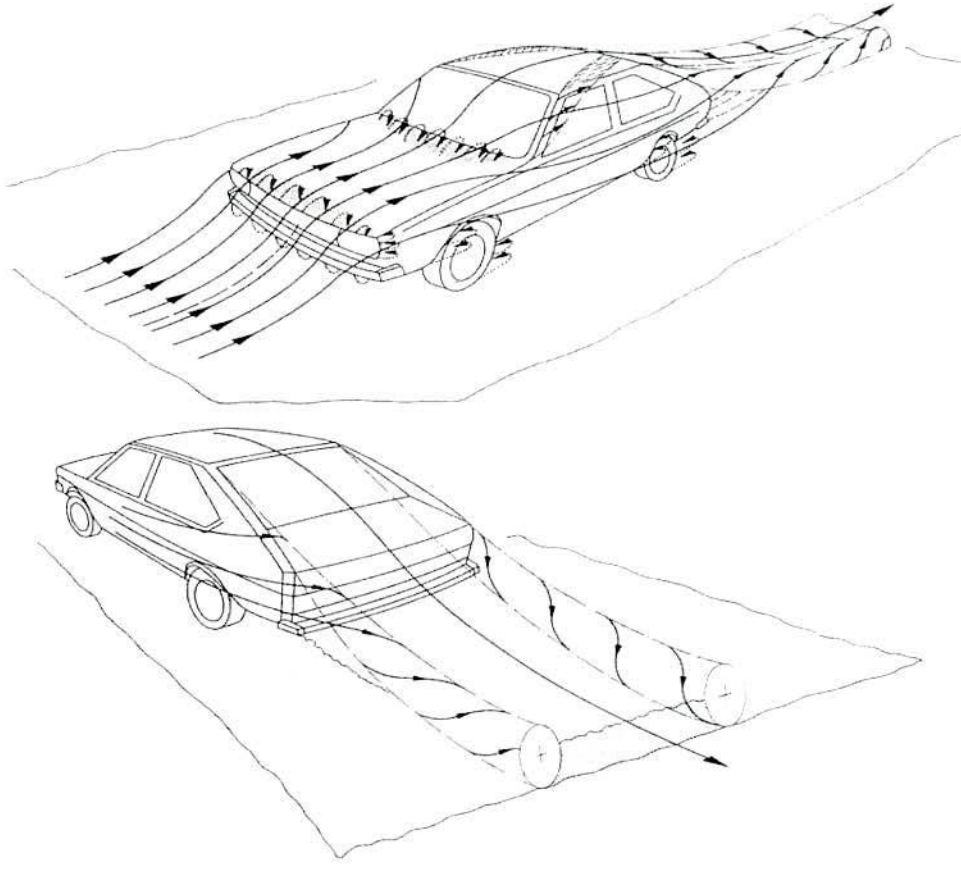

Figure 1.5: A Schematic Flow Pattern Around a Passenger Car, after Hucho (1998)

1.2.2.3 Noise Problems in the A-pillar Region of a Car

A conical vortex with resulting flow separation forms in the A-pillar region and travels downstream and upwards along the window to the roofline, where the flow expands and adds to the interior noise of the car. The conical vortex re-attaches along a diagonal line further back on the side window. Figure 1.6 and Figure 1.7 show schematic representations of the flow field found in this region, including the re-attachment line and the stagnation line where the flow separates on the upstream side.

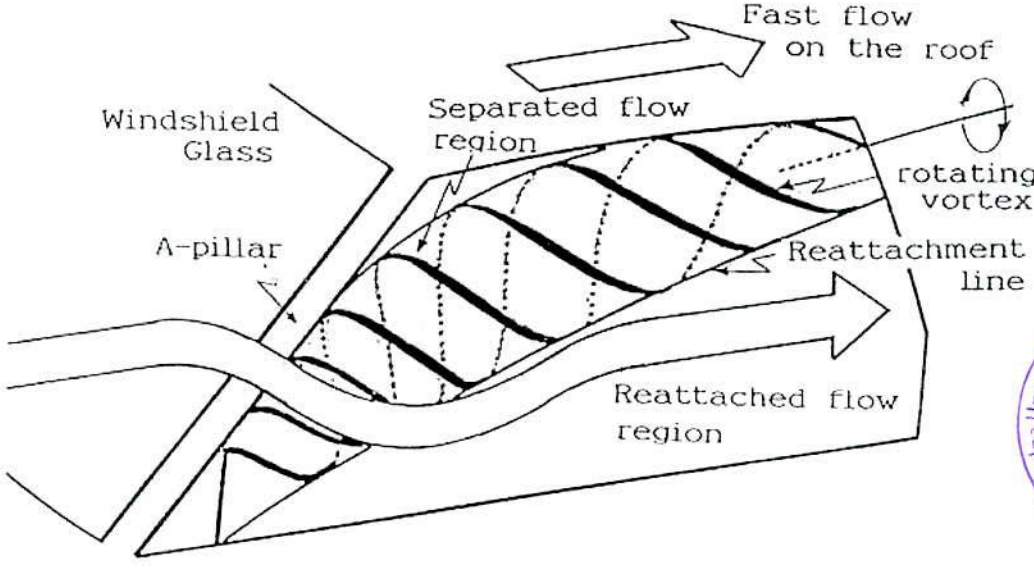

Figure 1.6: Schematic of Flow Field Around the A-pillar (Haruna, 1990)

The noise from the A-pillar region is transmitted through the side windows into the passenger cabin. The air around the exterior of a car travels at high speed with respect to the car surface. Since the car has to push air out of the way and the A-pillar is usually close to the maximum projected frontal area, the flow velocity around the exterior of the side window in the A-pillar region can be more than 50% faster than the car's nominal road speed. The flow is complex and turbulent due to the A-pillar vortex and local turbulence intensities have been found to reach 40% close to the side glass, Watkins et al. (1999), depending upon the yaw angles. Yaw angle is defined as the angle between the vehicle centreline and the mean direction of the wind as seen by the moving vehicle (for more details refer to subsection 1.3.3.3). Noise generated in the A-pillar regions is sometimes so intense that it makes spoken conversation among

the vehicle occupants difficult or impossible, and consequently can be a major cause of customer dissatisfaction, Callister et al. (1996).

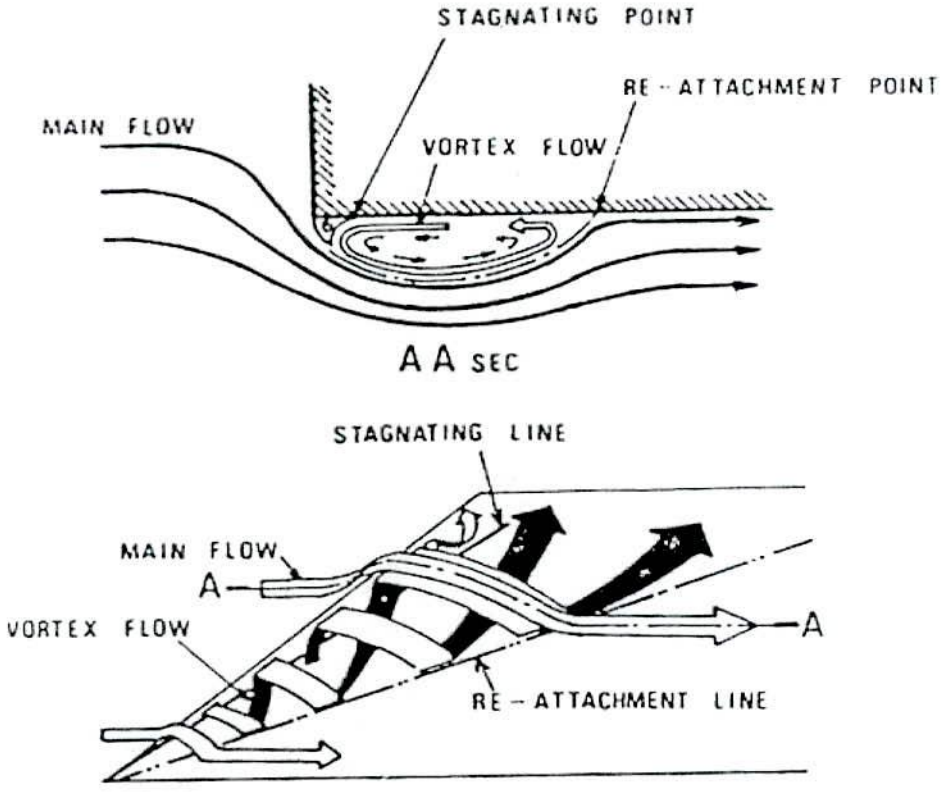

Figure 1.7: Schematic of the A-pillar Conical Vortex (Watanabe, 1978)

Popat (1991) carried out experimental investigation of the A-pillar vortex on small scale idealised sharp-edged road vehicle models. His investigation was aimed at examining the effect of windshield angle on the A-pillar vortex (flow structure) and flow-induced noise. His study was based on static and dynamic pressure measurements in the A-pillar region. Popat also used flow visualisation techniques to supplement the pressure data. The study showed that the A-pillar angles have significant influence on vortical flows. The A-pillar slant angle changed the flow pattern along the side window from a bubble separation at angles below 20° (an A-pillar angle is generally measured from the vertical), to a vortex-bubble (mixed flow) in between 30° to 40° and finally a fully developed conical vortex at angles between 50° to 60°. It may be noted that the angles between 50° to 60° are the approximate A-

pillar slant angles for a typical production car. Popat noted some Reynolds number sensitivities for some of his models depending upon the A-pillar angle. However, Popat's study did not reveal any detail of correlation between the A-pillar flow structure and aerodynamically induced noise. Popat did not consider the effects of yaw angle and turbulence (which both exist on the road) or A-pillar and windscreen curvatures in his study. His study was based on idealised small-scale models tested in a smooth low turbulence flow in a small wind tunnel at relatively low Reynolds numbers.

Bearman et al. (1989) studied the flow around a scale model based on wake surveys. The study found a strong unsteady A-pillar vortex close to the A-pillar, which might cause the pressure fluctuations and generate a strong irritating wind noise. The study attempted to understand how an A-pillar vortex could generate acoustic noise.

Sadakata et al. (1988) investigated the relationships between the airflow fluctuations and aerodynamic noise using an extremely idealised rectangular model at zero yaw angle. The study revealed that the interior noise level in the vehicle depends on the external aerodynamic noise due to the body panels. The modification of body shape can reduce the interior noise. They also found, based on their simplified model experiments, that the aerodynamic noise is generated mainly by the airflow around the A-pillar. Sadakata and his colleagues attempted to establish a relationship analytically between the front body shape, the air fluctuation and the aerodynamic noise and replicate it for a real vehicle as the aerodynamic noise is induced by the velocity or pressure fluctuation of the external airflow. However, further details were not revealed and the flow phenomenon was not well explained.

The relationship between the overall vehicle shape and wind noise of a specific road vehicle was studied by Watanabe et al. (1978). They reported that the sound pressure level is higher at the separation and re-attachment points and drew the conclusion that if the separated flow does not re-attach, less noise will be generated as a result of weakened vortex intensity. Studies by Sadakata and Watanabe did not include the effects of A-pillar angles and curvature, windshield curvature, wind yaw angles and atmospheric turbulence on the aerodynamically induced-noise. In addition, their

studies did not include the effects of the A-pillar radii as well as wind gusts and transients.

Other researchers including Haruna et al. (1990) studied the aerodynamic noise generated around the A-pillar of a production car. The car was tested in a wind-tunnel at one speed (50 km/h) and two yaw angles (0 and 10 degrees, although their report did not mention whether 10° yaw was on the leeward or windward side). They found that the sound pressure level varies with the yaw angle. A cone-shape three dimensional flow pattern with separated and re-attached flow regions existed on the side window near the A-pillar whose vortices rotate in opposite direction. Most of the acoustic energy was found in the frequency range 100-400 Hz. Haruna and his colleagues did not address the effects of real world conditions, such as wind gusts and transients, A-pillar geometry, and A-pillar inclination angle in their research.

Dobrzynski et al. (1994) investigated the effects of car-like bodies with different simplified forefront configurational parameters on the surface pressure characteristics on the side window area for different inflow (yaw) angles. Unsteady surface pressure measurements were conducted in a wind-tunnel at a constant speed for different yaw angles. The study found that the surface pressure around the side window varies with the yaw angles and vehicle's forefront shapes. The maximum spectral energy was found to occur at about 200 Hz. Dobrzynski's investigations did not include the effect of wind gusts and transients, A-pillar and windshield curvatures.

Another study conducted by Nienaltowska (1993) tried to establish coherence between the velocity fluctuation on the side window and the upstream velocity. The study was based on the measurements of local velocity and fluctuating pressure at several points around the A-pillar regions of a full-scale production car and a geometrically similar model car. No apparent significant coherence between the fluctuating pressure and local flow was found due to the wind-tunnel quality (pressure fluctuation signals captured by microphone were severely influenced by background noise and other sources of interference). The study concluded that the flow around the A-pillar region was extremely turbulent and could be the reason for aerodynamically induced noise.

Hamel et al. (1996) studied the fluctuating pressures on the surface of a side glass near the A-pillar as function of A-pillar heights and location of side rear view mirror. A driver's side quarter model of a full-size vehicle in a small wind tunnel was used to measure the surface fluctuating pressure varying the A-pillar height. Tests were performed with and without the rear side view mirror at three different speeds. The study found that the height of the A-pillar has significant effects on the surface fluctuating pressures with and without the side rear view mirror. The presence of the mirror had minimal or no effect on the A-pillar vortex. The driver's side quarter was not yawed. The study did not consider the effects of A-pillar radii and windshield curvatures on the A-pillar flow structures. Details about the shape, size, geometry and position of the side rear view mirror tested were also not revealed.

In conclusion, noise can increase as the side of the vehicle is yawed to the leeward direction (defined here as negative yaw angle) as it has been shown that the leeward vortex is larger than the windward side vortex[2]. However, the effects of scale on noise variation are relatively unknown. No work on the effects of scale has been found in the open literature. The surface pressure fluctuations on the side window generated by the A-pillar vortex are greatly influenced by the strength and size of vortex, location of separation/reattachment positions, and the degree of unsteadiness, but relationships between these factors are not yet known. Furthermore, the effects of the A-pillar curvature incorporated with the windshield curvature on the aerodynamically induced noise is completely absent in the literature. However, it has been shown that the structural joints between the windshield, A-pillar and side window can play a vital role in the elimination or significant reduction of aerodynamic noise generated from the A-pillar region. The strength and size of the separated flow near the A-pillar depends on the A-pillar geometry (A-pillar angle and A-pillar curvature), windshield geometry (longitudinal and lateral curvatures) and A-pillar rain gutter height. The next sub-chapter will review the possible aerodynamic noise evaluation methods.

[2] This was shown by Alam et al. (1999).

1.3 Vehicle Aerodynamic Noise: Methods of Evaluation

Three different approaches can be used to assess the wind noise characteristics and evaluation for road vehicles. They are analytical, computational and experimental methods, the application of which varies significantly depending on the area of interest. A brief description of each of these methods is furnished below.

1.3.1 Analytical Methods

The study of noise generated by flow began with the theory of propeller noise development by Gutin (1948). However, it was not until 1952, when Sir James Lighthill introduced his acoustic analogy to deal with the problem of jet noise, Goldstein (1976). Lighthill first gave a basic theory of aerodynamic sound generation, and its application to the noise radiated from airflow, in two papers (Part I and Part II) in 1952 and 1954 respectively. Lighthill's 1952 paper theorised how the sound radiates from a fluctuating fluid and its estimation. His 1954 paper detailed the origin of noise from turbulent jets. Lighthill considered a fluctuating hydrodynamic flow, covering a limited region, surrounded by a large volume of fluid, which is at rest apart from the infinitesimal amplitude sound waves radiated from the flow. It was postulated that all the non-linearities in the motion of matter act as sources of sound. Therefore, sources of sound in a fluid motion are simply the difference between the exact equations of fluid motion and the acoustical approximation, known as Lighthill's "Acoustic Analogy". Lighthill derived his famous equation reorganising the exact equations of continuity and momentum so that they reduce to the homogeneous acoustic wave equation $\frac{1}{c_0^2}\frac{\partial^2 \rho'}{\partial \tau^2} - \nabla^2 \rho' = 0$ at large distances from the turbulent flow. Where $\rho' = \rho - \rho_0$ is the fluctuating air density (ρ and ρ_0 are the air density and constant reference air density respectively), c_0 is the constant reference speed, τ is the time associated with emission of a sound wave and ∇ is the Laplacian

(divergence) operator. Reorganising the continuity and momentum equation, Lighthill developed his famous equation $\frac{\partial^2 \rho'}{\partial \tau^2} - c_0^2 \nabla^2 \rho' = \frac{\partial^2 T_{ij}}{\partial y_i \partial y_j}$,

where $T_{ij} = \rho V_i V_j + \delta_{ij}[(p - p_0) - c_0^2(\rho - \rho_0)] - \sigma_{ij}$ is Lighthill's turbulence stress tensor. V_i and V_j are velocity components, δ_{ij} is the Kronecker delta function (1 if $i = j$; 0 if $i \neq j$), p and p_0 are local pressure and uniform mean pressure at large distances; and σ_{ij} is the viscous stress tensor. Lighthill's acoustic analogy shows that the equation cannot be solved without the knowledge of Lighthill's stress tensor (T_{ij}). According to Goldstien (1976), the knowledge of T_{ij} is equivalent to solving the complete non-linear equations governing the flow problem, which is virtually impossible for most flows of interest. The logarithmic behaviour of human ears as a detector of sound tends to anticipate the need for highly accurate predictions of acoustic fields. However, it is often possible to obtain fairly good estimates of T_{ij} for certain types of flows and good estimates of the sound field using Lighthill's acoustic analogy.

For a low Mach flow, $(p - p_0)/p_0$ and $(\rho - \rho_0)/\rho_0$ are very small, entropy is constant and viscous shear stress is virtually negligible, so the Lighthill's stress tensor, T_{ij}, is approximately equal to $\rho V_i V_j$ inside the flow and almost equal to zero outside the region. Taking into account that the density fluctuation is negligible, the approximation of Lighthill's stress tensor, $T_{ij} \cong \rho_0 V_i V_j$ is the Reynolds stress of the fluid. Since a very small fraction of the energy in the flow gets radiated as sound, it is reasonable to suppose that the Reynolds stress ($\rho_0 V_i V_j$) can be determined by measurement or estimation of turbulence without the prior knowledge of the sound field. Then the right term of Lighthill's equation can be treated as the source term, Goldstein (1976).

The source term in Lighthill's equation exhibits a quadrupole nature (more details on quadrupole, dipole and monopole sources of noise were given in Sub-chapter 1.2.2.1). The acoustic power output varies to the 8th power of the jet velocity and as a consequence it becomes too small at low velocities for any measurement to have been

found possible at Mach numbers below 0.3. Therefore, Lighthill's acoustic analogy cannot be applied directly to automobile noise evaluation. As most of the automotive noise sources are monopole and dipole in nature, the Lighthill's stress tensor cannot be determined by experiment or estimation of turbulence until the quadrupole nature of the sound sources are established. Goldstein (1976) stated that the Lighthill's stress tensor estimation at an early stage could introduce monopole and dipole sources that can cause significant errors due to their relatively higher acoustic efficiency. The other drawback of Lighthill's theory is that it ignores back-reaction, where the sound generated by the flow is reflected in some manner and influences the flow, i.e., a feedback mechanism. According to Lighthill, this will only occur where there is a resonator (such as a vibrating solid body) close to the flow field.

From a fundamental mathematical viewpoint, the ideas of Lighthill were subsequently extended by Curle (1955), Powell (1960), Ffowcs-Williams (1970), as described by Goldstein (1976), Blake (1986) and Jenvey (1989). Their works have covered many aspects of aerodynamic sound. Powell (1960) described a theory of vortex sound, the action that causes the formation of vortices resulting in aerodynamic sound. Aerodynamic sound is generated by the movement of vortices or the movement of vorticity in an unsteady flow. Powell considered in his work that the wavelength of vortex sound is much larger than the dimension of any body immersed in the flow. He also assumed that the turbulence is isotropic and homogeneous (usually it is not). The flow is considered incompressible at low Mach numbers and consequently, fluid density variation can be ignored. Powell confirmed Lighthill's findings that the sound intensity is proportional to the 8^{th} power of fluid velocity (for quadrupole sources of noise) and large vorticity creates most of the sounds. In conclusion, Powell formulated that upon knowing the movement of vorticity sound power can be determined without the determination of complex fluid velocity and pressure fields.

Howe (1975 and 1993) extended Lighthill's theory to cover noise generation from turbulent and separated flows at different flow and boundary conditions. He extended Lighthill's stress tensor further to include the effects of refraction and scattering that significantly modify the acoustic field. Howe attempted to rearrange the Lighthill's equation to deal with the unsteady mean flow near the surface edges, bluff bodies or

contractions of ducts as in the wind-tunnel. He came to a conclusion that the turbulence generates unsteady forces that radiate noise and the edge of the surface provides a strong source of sound radiation. For the case of turbulence in duct flow, the intensity of acoustic radiation was stated to be proportional to the 6^{th} power of turbulent fluctuating velocity whereas sound intensity was stated to be the 8^{th} power of turbulent fluctuating velocity in open space, agreeing with Lighthill's 1952 theory. Howe further added that the sound is generated due to effective interaction between the turbulent Reynolds stress and the rate of strain field of the body shape.

Howe (1993) reported that acoustic radiation does occur if a definite interaction takes place between the vorticity of turbulence and some structural members of the body (such as an edge, sharp corner, step, etc.). The characteristic length of the structural member must be smaller than the acoustic wavelength in order to guarantee interaction effects.

After reviewing these fundamental works open to the public domain, it appears that none of these works can be applied directly to evaluate the road vehicle aerodynamic noise where it comprises mainly monopole and dipole type sources of noise. It is especially difficult to evaluate the noise generated from the A-pillar regions, an area of very complex airflow.

1.3.2 Computational Methods

Computational fluid dynamics (CFD) has made considerable progress recently in the evaluation of aerodynamic forces and moments, and other aeronautical applications, especially in aircraft and spacecraft design, as many of these problems are time independent. However, aeroacoustic problems are time varying (time dependent) and therefore time averaged CFD methods cannot be applied directly to evaluate aerodynamic noise generated by bluff bodies like road vehicles. Nevertheless, some CFD methods were applied to evaluate the aerodynamic noise for simpler cases to validate experimental results. Ogawa (1999), Kumarasamy (1999), Tam (1995) and Zhu (1993, 1994) reported some of the recent developments of CFD applications in aerodynamic noise evaluation.

Ogawa and Kamioka (1999) conducted a review of aerodynamic noise prediction using CFD methods. According to them, theoretically, aerodynamic noise can directly be calculated by solving unsteady Navier-Stokes equations. However, such a direct method is not realistic as it needs a large number of volume elements to compute the flow properties. The authors tested several CFD schemes (Large Eddy Simulation and Kawamura-Kuwahara methods) and compared them with experimental data. The comparison revealed that the difference was 5 to 10 dB in the low frequency range and it increased up to 20 dB in the high frequency range. Ogawa and Kamioka concluded their review by saying that at present, due to the difficulties with respect to computing time and memory, it is not possible to predict pressure fluctuations induced by unsteady motions of vortices at a practical use level.

Kumarasamy et al. (1999) conducted a computational and experimental study of noise generated by a forward step fence placed on a plane wall (a fence was used to represent an A-pillar rain gutter in isolation) using a two-step procedure. The first step of the two step procedure includes Direct Numerical Simulation (DNS), Large Eddy Simulation (LES) or Reynolds Averaged Navier-Stokes (RANS) equation solution, depending upon the accuracy and the Reynolds number. The second step includes Lighthill's acoustic analogy (LAA), Lighthill-Curle equation (LC), Ffowcs-Williams and Hawkins equation (FWH), Kirchhoff's equation and a perturbation method. The

authors used Lighthill-Curle equations in their CFD. As mentioned earlier, a forward step was placed on a wall and tested to study the so called "cause-and-effect" with some fundamental assumptions. The study revealed that computational values showed poor agreement with experimental results. In a real situation, the disparity between results might have been greater where the rain gutter faces different oncoming airflow over a curved surface.

Tam (1995) raised some of the issues and methods in computational aeroacoustics. In his paper, Tam explained the difficulties of using CFD methods in evaluation of aerodynamic noise. He drew a conclusion that until a reliable CFD method is found, it will be merely a research subject but not an engineering tool.

Zhu et al. (1994) studied numerically three-dimensional flow separation around a sharp-edged front Pillar of a simplified model. They conducted a time dependent Navier-Stokes simulation to understand the mechanism of wind noise generation due to the vortical flow motion. The surface fluctuating pressures were examined in terms of wind noise, based on a simplified Lighthill-Curle's equation. However, Zhu and his colleagues did not reveal anything from their findings except that a relationship existed between the vortical motion associated with the flow separation and surface pressure fluctuations on the front side window. No further information on validation of their numerically calculated results with experimental findings was available from their studies.

Unlike aircraft, road vehicles are bluff bodies and hence have separated flow regions, and they also possess more complex geometry. The airflow characteristics of aircraft and road vehicles also differ due to the ground boundary proximity. The typical eatures of the flow around a road vehicle are three dimensional, closed or open gions of separated flow. The smaller closed regions of separated flow occur at body endages such as headlights, mirrors, door handles, windshield wipers, l/windshield junctions, etc. Larger, three-dimensional regions of separations are nt on the A-pillar, at the rear end, at the body underside, and in the wheel wells. ure of the environment in which a road vehicle operates is the ambient turbulent at is almost always present. Generally, this is not the case for commercial

aircraft since they fly above the (turbulent) atmospheric boundary layer. Road vehicles can also travel at relatively high yaw angles. The resulting yawed flow is asymmetrically deformed and contains increased separated flow on the leeward side of the vehicle, adding to the complexity of the flow field. Temporal changes in ambient conditions superimpose a time history on the phenomena in addition to the inherent unsteadiness of separated flows. Therefore, it is difficult to apply any theoretical model to simulate through computational methods as the nature, characteristics and objectives of aeroacoustics problems are distinctly different from those commonly encountered in aerodynamics. Only a very few limited and simple cases can be modelled with the computational aeroacoustics method.

To date, although some simplified numerical solutions do exist for specific problems relating to wind noise, there is not yet a single agreed method to deal with the problem of road vehicle wind noise, covering all aspects of wind noise problems described earlier. For now the wind-tunnel remains as the most important tool to evaluate and improve the aeroacoustic field around an automobile, Barlow et al. (1999).

1.3.3 Experimental Methods

Experimental work on aerodynamically-induced vehicle noise consists of wind-tunnel tests and on-road tests, either full-size or reduced scale. These will be discussed in the next subsection.

1.3.3.1 Wind-Tunnel Simulation

The wind-tunnel provides a simulation that approximates the flow over the prototype vehicle in its on-road environment. The accuracy of the simulation depends on the extent to which the environment of the prototype is replicated in the wind-tunnel, on the accuracy of the geometry of the model, and whether the vehicle scale and wind speed are matched to road conditions by Reynolds number similarity (see sub-section 1.3.3.1.1).

In wind-tunnel testing, tyre, engine and other mechanical noises are usually absent and the speed and direction of the flow can be held constant. Furthermore, the vehicle can be yawed to simulate primary (time-averaged and invariant with height) effects of atmospheric winds. Hence, the measurements made in a wind-tunnel are generally very repeatable.

Generally, three different types of wind-tunnel test sections are commonly used for automotive testing: the 3/4 open jet test section, closed-wall test section, and the slotted-wall test section. Regardless of wind-tunnel type the single most important consideration is that the level of background noise must be low enough to provide an acceptable signal-to-noise-ratio. Details and various configurations of aeroacoustic wind-tunnels (where aerodynamic drag measurement, cooling performance evaluation and wind noise measurement can sometime also be performed) are described by Lindener et al. (1994). There are no set standards to define a limit on background noise but experience has shown that a signal-to-noise-ratio of about 10 dB within a frequency range of approximately 60 Hz to 8,000 Hz is necessary for car interior noise measurement, Kunstner et al. (1995).

The 3/4 open jet wind-tunnel is used for the majority of vehicle acoustic testing (the remaining 1/4 represents the reflecting plane of the road surface), as it provides the opportunity to do out-of-flow measurements in the acoustic far field if the walls and ceiling of the tunnel are sufficiently acoustically non-reflective, thus representing a free field. However, it is difficult to compare different tunnels on the basis of their out-of-flow noise characteristics, due to variations of jet size, plenum chamber characteristics and measurement positions outside the jet. All these parameters will influence the resultant noise levels measured. With the open jet test section, the boundaries of the open jet will affect the quality of unsteadiness due to vortex flow. The shear layer will also distort, scatter, and refract the transmitted sound, which results in spectral broadening, amplitude fluctuations, and phase fluctuations of the original acoustic signal. Therefore, correction procedures may be necessary, George et al. (1996). With a closed-wall test section, exterior measurements are difficult to perform because the microphone must be placed in the flow, and a nose cone must be used to minimise the self-generated noise from the protection grid of the microphone.

Additionally, due to limited space inside the test section and lack of acoustic treatment on the walls, it is often not possible to attain acoustic far-field conditions, George et al. (1996).

In principle, the slotted-wall test section permits acoustic out-of-flow measurements in the surrounding plenum chamber. However, it is likely that due to the solid parts of the test section boundary, sound will be shaded off. In addition, some sound intensification may occur due to reverberation in the test section, and some sound may be generated due to flow across or through the slots, George et al. (1996).

The vast majority of vehicle wind-tunnels around the world are of smooth flow type, the turbulence intensity is approximately 0.1 percent and lower. The main reason for that is to reduce the tunnel self noise and get airflow noise as close to the level of a pure jet as possible, Weidemann et al. (1993). A low turbulence wind-tunnel allows diagnostic wind noise testing and comparison of different vehicles and detail design features, without the masking effects of other noise sources such as extra turbulence.

The number of aeroacoustic wind-tunnels and the role they play in vehicle development is increasing since measuring wind noise in a quiet wind-tunnel is usually much better than making measurements on-road. The German-Dutch Wind-Tunnel (DNW) in the Netherlands, the BMW Technik and the IVK Wind-Tunnels in Germany, the Lockheed Low Speed Wind-Tunnel in the USA, the Mazda Aeroacoustic, the Honda Aeroacoustic and the Nissan Aeroacoustic Wind-Tunnels in Japan have been built to cater the needs of wind noise measurement. More details on some of these wind-tunnels can be found in the review paper by Mercker et al. (1996). Apart from these noted wind-tunnels, several more 'state-of-the-art' aeroacoustic wind-tunnels have already been built or are under construction by Ford, GM and Chrysler in the USA and by others in Asia-Pacific regions.

1.3.3.1.1 Tests with Reduced-Scale Models

During new vehicle development, several versions of reduced-scale models are frequently generated in the design studios in conjunction with the aerodynamicists. These models go through baseline tests and modifications in the wind-tunnel. Reduced model-scale testing has several advantages. Models are fast to build and modify during the development process. Models are easy to transport, thus increasing flexibility with regard to wind-tunnel selection. The risks associated with reduced scale can be avoided if the scale is increased. The extrapolation of results obtained with these miniature models to the full-scale car has some risk for two main reasons: the lack of geometric similarity compared to the full-scale car (often the models are simplified), and the lack of kinematic similarity, which means the Reynolds numbers are too low.

For steady-state forces and moments evaluation, both geometric similarity and kinematic similarity should be maintained, i.e., $Re_{\mathrm{mod}} = Re_{full}$ (where Re_{mod} and Re_{full} are the Reynolds numbers of the reduced-scale and full-scale vehicles respectively) or $\frac{U_{\mathrm{mod}} \cdot l_{\mathrm{mod}}}{\nu_{\mathrm{mod}}} = \frac{U_{full} \cdot l_{full}}{\nu_{full}}$ if exact replication of steady-state flow field characteristics is required. Where, U_{mod}, l_{mod} and ν_{mod} are the velocity, characteristic length of the reduced scale model and the kinematic viscosity of the fluid used for reduced scale model, and U_{full}, l_{full} and ν_{full} are the velocity, characteristic length of the full-scale vehicle and the kinematic viscosity of the fluid used for the full-scale vehicle. If a model test is conducted in a fluid of the same kinematic viscosity in which the full-scale vehicle operates, the requirement for kinematic similarity is satisfied when the products of velocity and length in the two cases are equal. Generally it is difficult to satisfy the above mentioned requirement for reduced scale of less than 30 percent due to limitations of tunnel top speed and compressibility effects. For this reason in the USA and Europe, a larger scale from 30 to 50 percent scale of the original is considered during the design and development program. Usually the Reynolds number scaling is compromised by having a lower model scale Reynolds numbers than the on-road situation.

A lower Reynolds number test result can still be compared with actual full-scale performance. It is now generally accepted that if the flow is attached in the lower Reynolds number case, then it is likely to be attached in the higher Reynolds number case, thus the effects of Reynolds number on force and moment coefficients will be fairly small. However, if flow separations are evident under lower Reynolds number tests it is quite possible that the flow will be attached at higher Reynolds numbers. This effect is due to the possibility of laminar boundary layer separation occurring at lower Reynolds numbers, which is not the case for higher Reynolds numbers. In order to evaluate the Reynolds number effects, model vehicles are often tested over a range of Reynolds numbers. This is in order to see if there is a change in the force and moment coefficient data with Reynolds numbers, indicating a critical Reynolds number has been found. Data are sometimes extrapolated to the full-scale Reynolds numbers to minimise the chances of errors due to incorrect Reynolds numbers. Further details on Reynolds number effects can be found in papers by Cooper (1984 and 1992).

In vehicle aeroacoustics, there is no established similarity rule for measurement of noise as there is for force and moment measurements, Barlow et al. (1999). The effect of scale is relatively unknown. The noise generation mechanism in lower Reynolds numbers sometimes may not be the same as in higher Reynolds numbers. However, non-dimensional parameters such as Strouhal number ($S_t = \frac{f.L}{V}$), where f, L and V are the frequency, characteristic length of the noise source and the fluid velocity respectively, and the fluctuating pressure coefficient ($C_{p\,rms} = \frac{p_{std}}{\frac{1}{2}\rho V^2}$), where p_{std} and $\frac{1}{2}\rho V^2$ are the standard deviation of the fluctuating pressure and velocity head (q) of the fluid respectively, are frequently used to estimate the frequency and magnitude of fluctuating pressures.

1.3.3.2 Comparison with On-Road Testing

A wind-tunnel partially simulates the conditions on a road; it does not reproduce them exactly. However, by analysing on-road driving, the on-road conditions can at least be identified in principle, Hucho (1998). Examples of the lack of correct simulation include the effects of tunnel boundaries, a lack of the correct (moving) ground simulation and non-rotation of wheels. On the road, the flow speed and direction usually vary due to the presence of atmospheric winds. Unlike time-averaged forces and moments that vary approximately with velocity squared, wind noise generally varies with wind speed to the sixth power. Thus a wind noise test on-road at 100 km/h can add 2.5 dB to interior wind noise levels for a 10-km/h gust, Hucho (1998). In addition to that, engine noise and tyre noise are present during on-road tests and make it difficult to determine which components of the noise are due to the wind environment alone. Therefore, it is very hard to make good and repeatable measurements on-road. Flow unsteadiness including turbulence in the atmospheric wind has additional effects that are not captured in the wind-tunnel, where the free stream flow is quite steady and free of large-scale turbulence.

On road the wind velocity varies with time and space, Watkins et al. (1999). If there is any appreciable atmospheric wind, then the wind gusts are heard as a change in the noise experienced by the car occupants. Therefore, on-road tests are useful to determine the real wind noise performance of a car. However, for a better understanding of the factors affecting the noise and a complete aerodynamic noise assessment, both wind-tunnel and on-road testing are used.

1.3.3.3 Effects of Atmospheric Winds

The atmospheric wind varies in direction and speed continuously, as characterised by spectral analysis on long term wind records. Additionally, atmospheric wind is inherently turbulent. The longitudinal turbulence intensity, which largely depends on wind speed and road side obstructions, is typically 3 to 5%, Watkins et al. (1995). In an open and unobstructed environment, the length scale of this turbulence ranges from 2 to 17 meters (average length scale is approximately 7 meters), Saunders and Mansour (2000). They also reported that the presence of upstream vehicles can reduce the length scales to 0.5 to 1.5 meters (average length scale is approximately 1.2 m) and the upstream vehicles can increase the turbulence intensity from 5 to 20%. Although an effect of atmospheric turbulence on a passenger car is to modulate the aerodynamic noise, see Watkins et al. (2001). The study of this is beyond the scope of this work. A vector diagram of velocity components for a moving vehicle in an atmospheric crosswind, adapted from Watkins et al. (1992, 1995), is shown in Figure 1.8. It shows that the largest yaw angle that can be generated occurs when the relative wind velocity (Vr) and the atmospheric wind velocity (Vw) are perpendicular, as shown by the dotted lines.

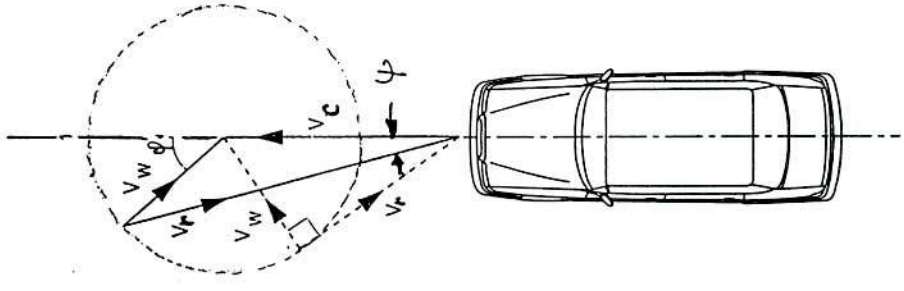

Figure 1.8: Mean Velocity Diagram for a Moving Vehicle (after Watkins, 1992)

In any wind-tunnel test while measuring aerodynamic noise, it is usual to simulate the atmospheric crosswind on A-pillar designs, which provide good performance at zero yaw angle. However, this can be degraded severely when a crosswind is encountered on the road. This simulation is accomplished by yawing the vehicle to the mean flow direction to allow for the mean effects of yaw angles and by changing the tunnel speed to allow for the mean effects of different air speeds.

In wind-tunnels, the flow is usually smooth and statistically stationary and by yawing the vehicle into the wind, the mean effects of steady state crosswinds can be determined. Figure 1.9, Cooper (1985), shows the probability of a given yaw angle with the vehicle direction based on the mean airflow. It is very unlikely that a vehicle travelling at speeds higher than 100 km/h will face crosswinds with more than ±10° yaw angle (Figure 1.9).

It may be noted that the plot in Figure 1.9 is based on the averaged mean atmospheric wind in North America (the effects of gusts and transients were not included in this plot and yaw angle was expressed via β), however, this will be considered in this work.

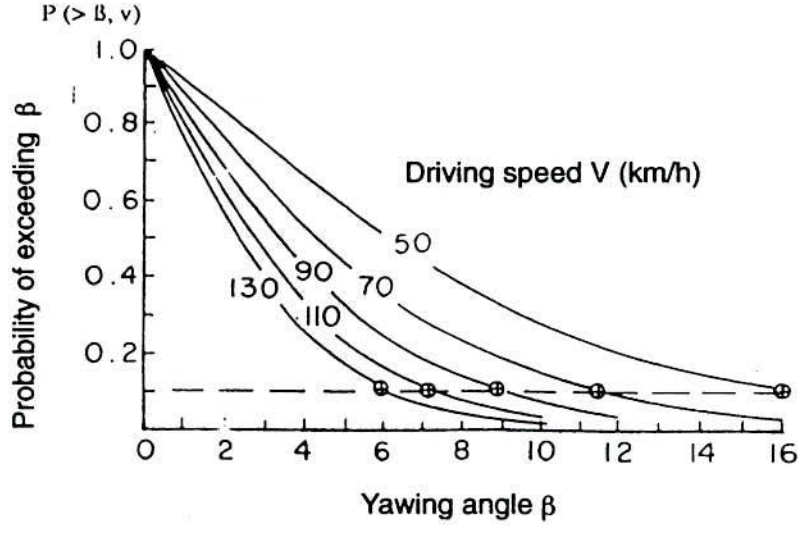

Figure 1.9: Plot of Probability of Exceeding Yaw Angles with Vehicle Speeds, Cooper (1985)

1.4 Conclusions from Prior Work

The studies reviewed here show that the noise problem in passenger cars is important. Currently, most vehicle development work is being carried out experimentally, as few aerodynamic noise problems can be solved analytically or computationally with sufficient accuracy, due to strong unsteadiness of motions created by separated, separated and re-attached, and attached flows.

The A-pillar region is the dominant source for unwanted cabin noise. In the public domain, no systematic and detailed studies about the effects of shape on noise or surface pressure fluctuations are available, apart from work on sharp-edged bodies by Popat (1991). The effects of yaw angle are not well understood nor are the effects of A-pillar radii for typical vehicle geometry.

Modern cars have increasingly curved A-pillars and this trend is likely to continue. If some of the changes to vehicle materials eventuate, the A-pillar region may become more curved. The amount of compound curvature available to stylists is limited by laminated (toughened) glass but the use of new plastics can overcome some of these limitations.

The effects of Reynolds numbers on the A-pillar flow characteristics are unclear. No comprehensive comparison of wind-tunnel test data with real world situations has been reported in literature in the public domain.

Reducing the noise at source is desirable rather than adding sound transmission loss or sealing materials. Adding additional materials means increase of cost, mass and compromise on passive safety issues (e. g., the driver will not be able to hear the audio sirens of emergency vehicles). The non-linearity of human hearing means that as noise levels decrease the human ear will still be sensitive to noise, especially fluctuating noise.

1.5 Objectives and Scope of this Work

From an examination of the prior work done in this area, one may conclude that there are significant gaps in understanding of flow separations in the car A-pillar region. Therefore, the research questions to be answered by this research project are as follows:

- What are the effects of curvature in the windshield and A-pillar location on the downstream time-averaged and fluctuating surface pressures?
- How do these pressures change with steady yaw angles?
- What are the effects of scales (e.g., Reynolds number) on the surface mean and fluctuating pressures?
- How does the 'in-cabin noise' of a production vehicle compare when the testing environment is on-road, in a wind-tunnel or in an idealised physical model?

The relation between the exterior pressure fluctuations and the interior noise level heard by the vehicle occupants is a complex one. It depends upon the magnitude, phase, frequency and wave number of the pressure fluctuations themselves, the materials and structural properties of the vehicle skin, and the acoustic properties of the vehicle cabin. In this work, the focus will primarily be upon the magnitude of the exterior pressure fluctuations in smooth flow generated by various A-pillar geometries in the absence of external rear view mirrors. Some data on the frequency will also be given. The other elements of the problem are not addressed directly. Flow visualisation is used to qualitatively supplement the quantitative pressure data. Experimental work was to be conducted in two major wind-tunnel facilities available to the RMIT University. On-road tests were also to be conducted.

1.6 Thesis Layout

The structure of this thesis is as follows:

Chapter 1 (current Chapter) outlines the background, reviews the relevant literature and describes the aims and scope of this work.

Chapter 2 describes the test facilities, test vehicles (idealised and production vehicles), test equipment, instrumentation and data processing.

Chapter 3 presents results from the idealised scale models. This Chapter also describes the effects of Reynolds number and yaw angle on the surface mean and fluctuating pressures. Also, the frequency-based analysis of the surface fluctuating pressures for the scale models is described in this Chapter.

Chapter 4 outlines results from the surface mean and fluctuating pressure and interior noise measurements for production vehicles in on-road and wind-tunnel tests. Pressure spectra and normalised power spectra are also presented in this Chapter.

Chapter 5 presents general discussion of results for idealised and production vehicles. A comparison of results from scale models with results from production vehicles is made. The industrial implications of the results from this work are also described in this Chapter.

Chapter 6 contains the major conclusions from this work.

Chapter 7 describes recommendations for further work.

Appendices (A to M) are attached at the end of the references and bibliography and contain additional material in support of this work.

Chapter Two

Facilities, Equipment and Data Processing

A brief summary of wind-tunnel facilities, instrumentation, and data acquisition and processing will be discussed in the next subsections. Details of calibration and error assessments can be found in Appendices A, B, C, D, F, and K.

2.1 Facilities and Vehicles

Two major wind-tunnel facilities are available to the RMIT University for vehicle aerodynamic and aeroacoustics research. The RMIT Aeroacoustic Industrial Wind-Tunnel is used mainly for reduced scale testing and the Monash/RMIT Universities' Aeroacoustic Wind-Tunnel is used for full-size vehicle tests. These two tunnels were used for this research. A brief outline of RMIT University Aeroacoustic Wind-Tunnel and Monash/RMIT Universities' Aeroacoustic Wind-Tunnel is given in the next subsections.

2.1.1 RMIT University Aeroacoustic Wind-Tunnel

The RMIT Industrial Aeroacoustic Wind-Tunnel is a closed test section, closed return circuit wind-tunnel and is located at the Department of Mechanical and Manufacturing Engineering. The maximum speed of the tunnel is 145 km/h. The rectangular test section dimension is 2 x 3 x 9 (metres) with a turntable to yaw suitably sized models. Acoustically treated turning vanes and a remotely mounted fan drive motor minimise the background noise and temperature rise inside the test section. The free stream turbulence intensity is approximately 1.8%, which makes the tunnel suitable for various aerodynamic and aeroacoustic experiments. A plan view of the tunnel is shown in Figure 2.1. The tunnel was calibrated before conducting the experiments. The results of the calibration tests are given in Appendix A.

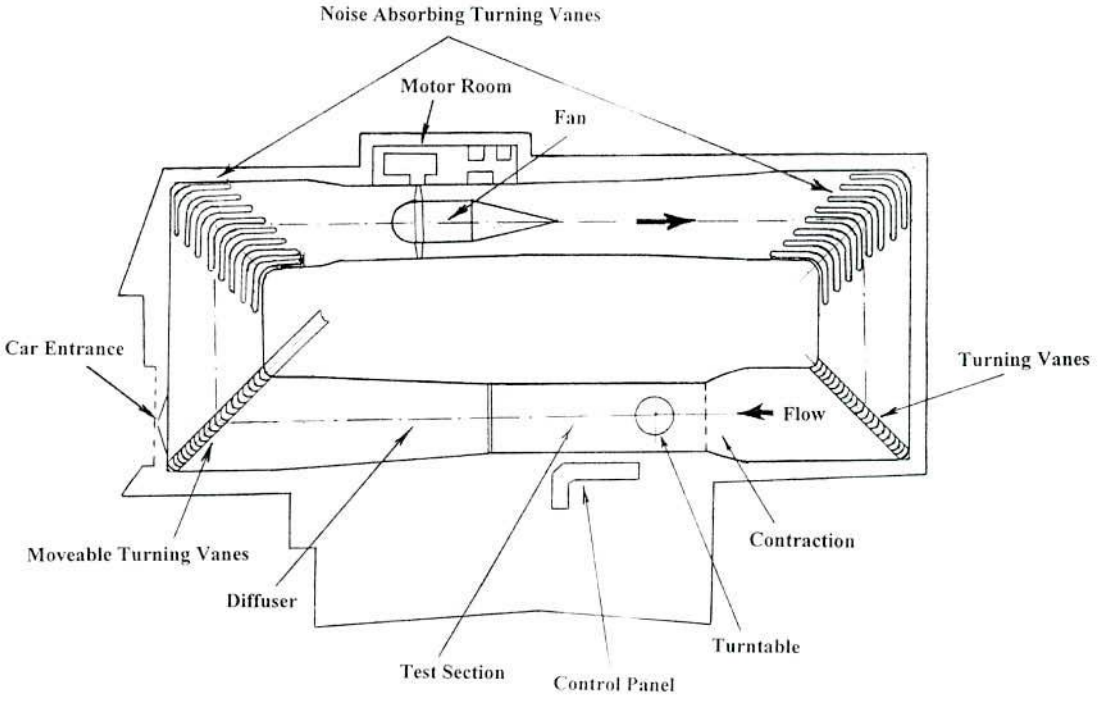

Figure 2.1: A Schematic of RMIT University Aeroacoustic Wind-Tunnel

2.1.2 Monash/RMIT Universities' Aeroacoustic Wind-Tunnel

The Monash/RMIT Universities' Aeroacoustic Wind-Tunnel is run jointly by Monash University and RMIT University. It is a closed circuit 3/4 open jet wind-tunnel with a maximum speed of approximately 180 km/h. The exit nozzle size is 10.55 metres square and the test section has very low levels of background noise. The background noise level in the tunnel is typically greater than 10 dB(A) below a modern passenger car's interior noise, Watkins et al. (1997). The test section has a turntable and is large enough to accommodate a full-size car. The tunnel has a turbulence level of approximately 2.5%. It is driven by two independently controlled fans of 5-m diameter. The layout of the wind-tunnel is shown in Figure 2.2. The Tunnel was calibrated and the calibration details are given in Appendix A.

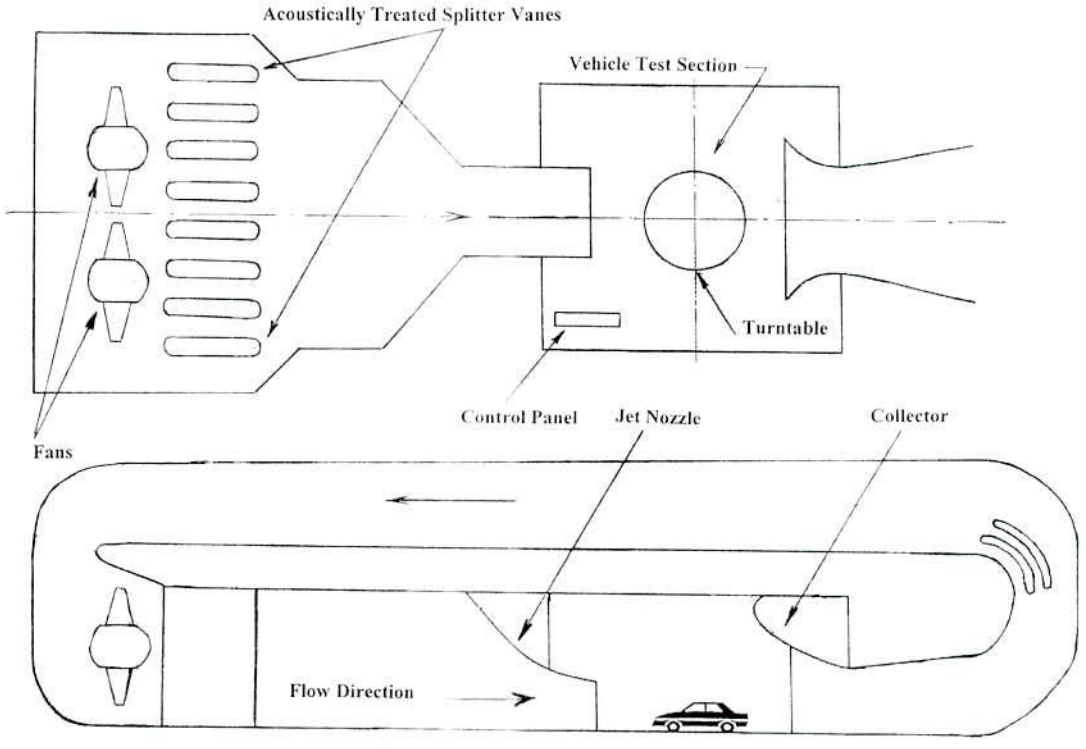

Figure 2.2: A Schematic of Monash/RMIT Universities' Aeroacoustic Wind-Tunnel

2.1.3 Test Vehicles

Three full-size production vehicles were used for this study. One was an EB model Falcon produced by the Ford Motor Company of Australia, and the other two cars were a VR Commodore and a VT Calais, both manufactured by General Motors-Holden, Australia (GMH). The Falcon and Calais are both four-door family sedans (Figure 2.3, Figure 2.5 and Figure 2.6) and the Commodore was a five-door station wagon (Figure 2.4). These vehicles are similar to many large family-size cars mass produced around the world including North America, Europe and Asia pacific regions.

Aside from full-size vehicles, a series of experimental investigations were conducted on several reduced-scale vehicles (models). A general description of these models has been furnished in Chapter Three.

Figure 2.3: A Typical Ford Falcon EB Family Size Passenger Vehicle

Figure 2.4: General Motors-Holden VR Commodore Station Wagon shown in Monash/RMIT Universities' Wind-Tunnel

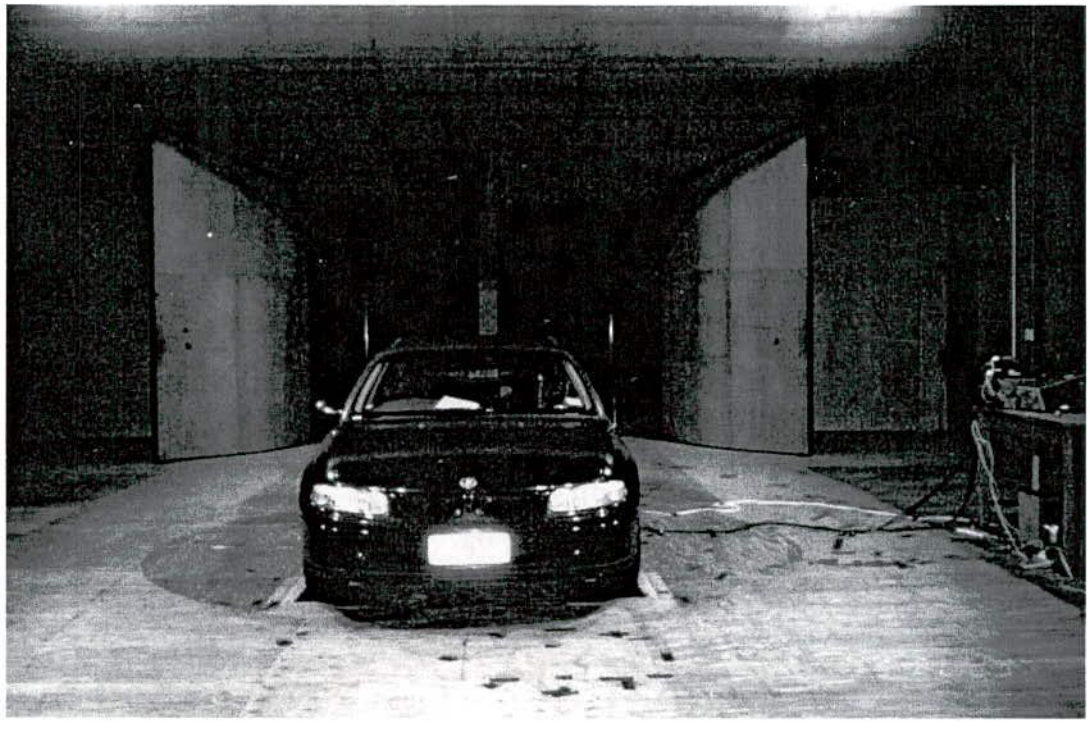

Figure 2.5: General Motors-Holden VT Calais in Monash/RMIT Universities' Wind-Tunnel

Figure 2.6: Side View of General Motors-Holden VT Calais (on the Road)

2.2 Equipment, Instrumentation and Data Processing

The following equipment has been used in this study to measure the time-averaged and time-varying flow properties and in-cabin noise.

2.2.1 Measurements of Flow Properties Away from the Surface with a Cobra Pressure Probe

The most widely used velocity probes for fluctuating flows are hot-wire anemometers. A hot-wire anemometer consists of fine wire supported by two larger-diameter prongs; an electrical current heats the wire to a temperature well above the flow temperature and the time-averaged and time-varying velocities can be deduced via the electrical system involved. These fine wires are extremely fragile and very sensitive to flow temperature, humidity and dirt. Therefore, it is very difficult to use a hot wire probe in on-road tests or under less than ideal conditions.

To avoid these difficulties, a high frequency four-hole Cobra Probe developed by Hooper et al. (1991, 1997) was used to measure the three orthogonal mean and turbulent velocity components at a point in the flow field as well as local static pressure. The probe can be used in relatively harsh environments such as those encountered during road tests. A schematic of the probe is shown in Figure 2.7.

The probe can take up to 20 blocks of data for each calculation. Typically, each block of data has 4096 samples and is obtained in 0.8 second depending on the sampling frequency. The principle of operation is discussed in Appendix B. Details about the calibration have been given by Hooper et al. (1997). A suitable calibration rig for calibrating the steady-state pressure transducers and the dynamic response has been utilised. Again, details can be found in Appendix B. The Cobra Probe cannot be used to measure the turbulent velocity and static pressure without being linked to a

dedicated computer through an appropriate analog to digital (A/D) conversion board, as the calculation scheme used is numerically intensive.

The Cobra Probe used in the wind-tunnel and on the road was connected to a Personal Computer via an A/D board and probe control unit. Dedicated software was used to get the real-time velocity components u, v and w from the pressure files. Local yaw and pitch angles, Reynolds stresses and frequency spectra can be calculated. The probe has a relatively flat frequency response to 1500 Hz. The probe was traversed via a computer control interface on the data acquisition Personal Computer. Figure M.1 in Appendix M shows how the probe was mounted on the floor of RMIT University Aeroacoustic Wind-Tunnel.

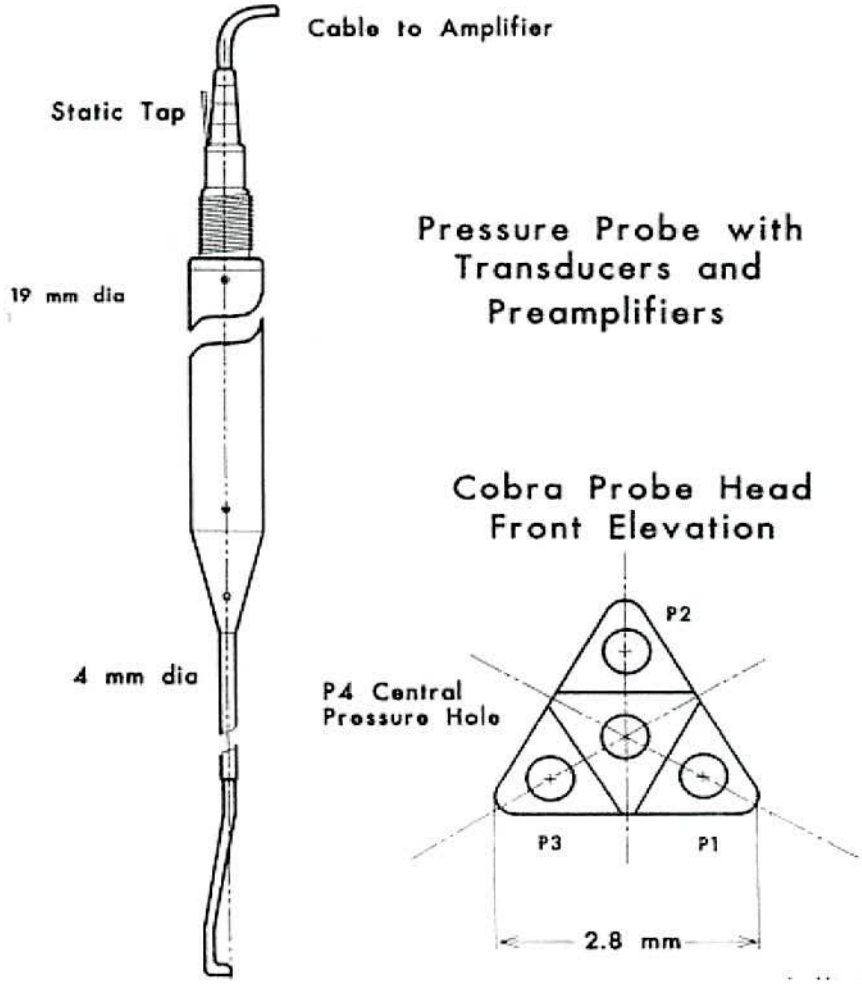

Figure 2.7: A Schematic of a Multi-Hole Pressure Probe, after Hooper (1997,1991)

2.2.2 Measurements of Mean Surface Pressure with a Scanivalve System

The distribution of time-averaged (mean) surface pressures on the vehicle body is generally measured by drilling a small hole in the surface and connecting this point to a manometer or electrical pressure transducer. A short metallic hypodermic tube (50 mm in length) was mounted flush through the drilled hole and the metal tube was connected to a pressure sensor via flexible plastic tubing. In order to obtain a comprehensive pressure distribution, 32 pressure holes on the reduced-scale vehicles and 16 pressure holes on the production vehicle were drilled normal to the window surface in two rows for each top section of the model and the production vehicle. The bottom row was approximately 1/3 distance away from the baseline of the window and the top row was 2/3 the distance of the window base. Each row carried 16 holes for the scale models and 8 holes for the production vehicle. The space between any two adjacent holes was 32 mm for the scale models and 80 mm for the production vehicle (to duplicate scale geometry). Before drilling the holes, flow visualisation was carried out to determine flow in the area of interest (i.e., the region that is influenced by the A-pillar vortex). Details about the flow visualisation will be discussed in subsection 2.3.

A multi-channel Scanivalve pressure measurement unit with a Honeywell (type 160 PC) pressure transducer was used to scan the surface mean pressure. The pressures on the vehicle surface were picked up by the individual pressure holes and were fed to the sensor of the pressure scanner through plastic tubes. A solenoid and channel decoder controlled the Scanivalve. A data acquisition board housed in an IBM Personal Computer with a multi-function A/D board monitored the output from the channel decoder. The pressures from the surface of the model are automatically stepped through by the Scanivalve and passed through the reference port to the Honeywell pressure transducer.

Genie Avantech, a data acquisition software program was used to record the data. The Scanivalve pressure measurement unit can be driven automatically or manually

from a computer interface switcher. The accuracy of the measured pressure typically was ±0.5 Pascal. The scanner was used for time-averaged pressure measurements in the wind-tunnels and on-road. The time-averaged surface pressure measurements set up is shown in Figure 2.8. A data acquisition block diagram and calibration details are given in Appendix C. The output file was then directly fed into a DDE (Dynamic Data Exchange) compliant spreadsheet program in Microsoft Excel.

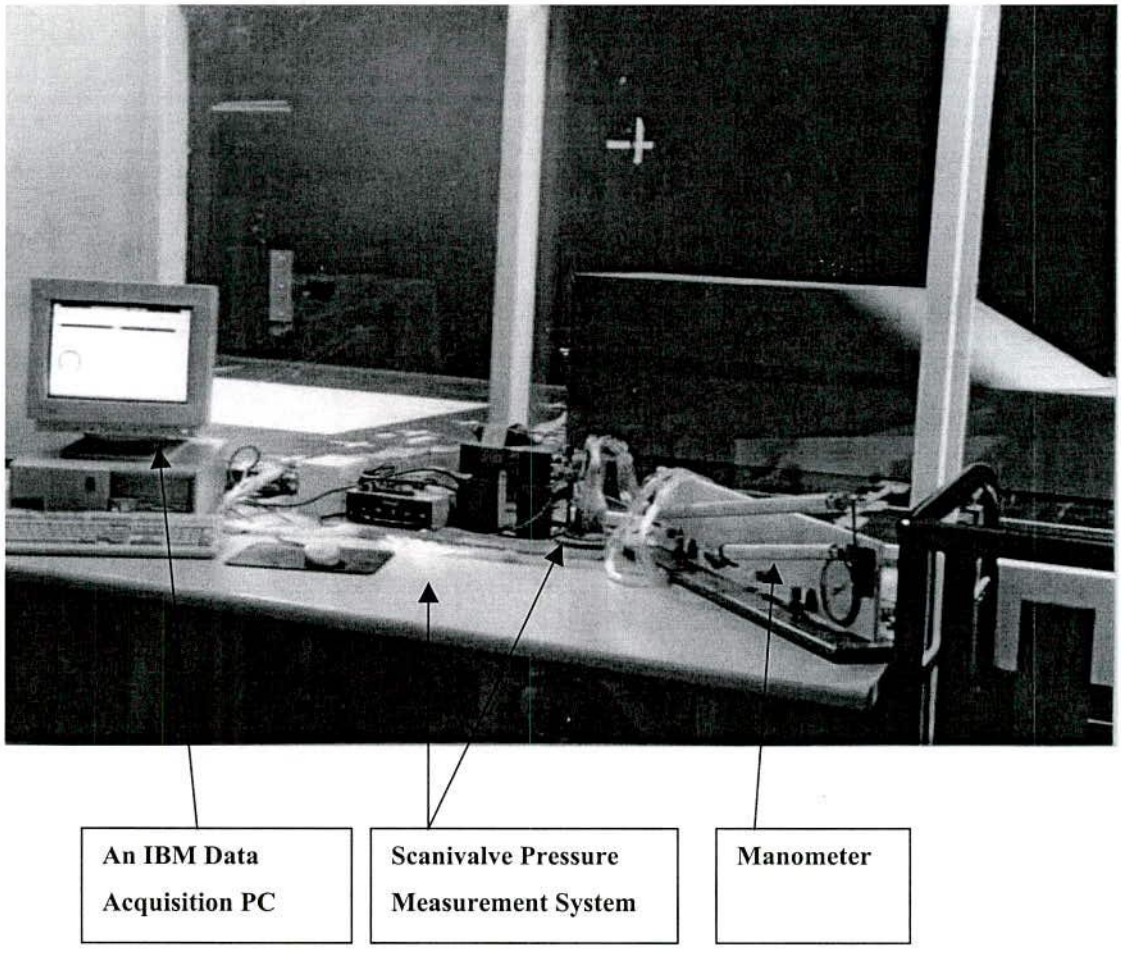

Figure 2.8: Apparatus for Surface Mean Pressure Measurements in RMIT Aeroacoustic Wind-Tunnel

The time-averaged pressure distributions were converted to the non-dimensional pressure coefficients (Cp) using the following relation: $C_p=\frac{p_m-p_\infty}{\frac{1}{2}\rho V_\infty^2}$. Here p_m is the surface pressure at the point of measurement (in this study, the time-averaged surface

pressure on the side window near the A-pillar), p_∞ is the free stream static pressure and V_∞ is the free stream velocity (tunnel air speed). This relationship can be re-arranged in terms of velocity (ignoring the turbulent losses): $C_p=1-\frac{V_m^2}{V_\infty^2}$, where V_m is the local surface velocity (in the absence of viscous effects, which approximates the velocity just outside of the boundary layer). The pressure coefficient is an important parameter in fluid mechanics as it identifies the nature of flow. At the stagnation point, where velocity is zero, $C_p=1$, as $V_m=0$. In an undisturbed flow, far from the vehicle, $p_m=p_\infty$ or $V_m=V_\infty$ thus $C_p=0$. If the local velocity (V_m) is larger than the free stream velocity (V_∞) then the C_p becomes negative. It should be noted that this relationship breaks down in the wake of a bluff body when turbulent losses can be significant.

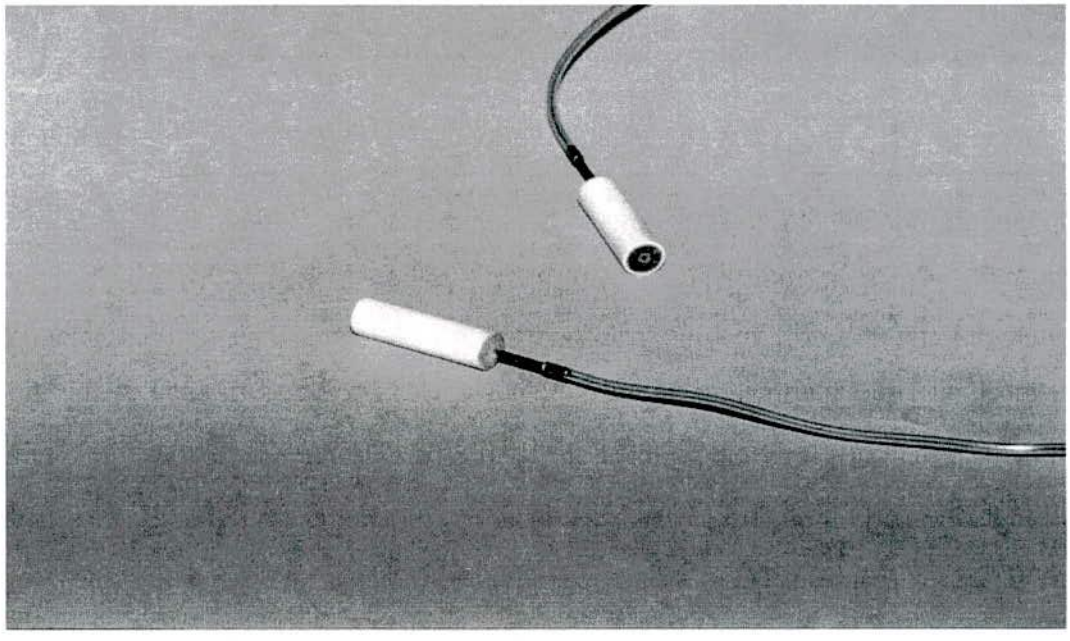

Figure 2.9: Adaptors with Metallic Hypodermic and Flexible Tubes

As the Scanivalve system did not have a sufficiently high frequency response to measure the fluctuating surface pressure, ¼ inch (6.35 mm) diameter microphones were used at the same locations as for the surface mean pressure measurements. Thus, for the surface mean pressure measurement, a series of special cylindrical adaptors holding 1.8-mm external diameter metallic hypodermic tubes were made (Figure 2.9).

All hypodermic tubes were connected to the multi-channel Scanivalve pressure measurement system as described earlier with flexible PVC tube. Prior to data acquisition, all systems were calibrated and properly checked. The calibration details are furnished in Appendix C.

Data were stored in the computer's hard disk for further processing. A schematic diagram of surface mean pressure data acquisition is shown in Appendix C. The Scanivalve controller was operated automatically to switch to the next pressure tapping. Transducer drifting was checked and was found negligible and data were sampled for a sufficiently long time to get a stable average value.

2.2.3 Measurements of Time-Varying Surface Pressures Using Microphones

In order to simultaneously measure the fluctuating surface pressure at several locations, an electret microphone based system was constructed. However, despite considerable effort being expended on this system, satisfactory performance was not attained. This was due to limitation of the dynamic range and significant variation in dynamic calibration. A two channel ¼ inch condenser microphone (G.R.A.S. Type 40BF) with a physical size and frequency response similar to a B&K ¼ inch microphone was instead used in this work. During wind noise testing, it is important to select the right microphone with appropriate frequency range and required dynamic response. The linear pressure response of a microphone breaks down at high frequencies when the acoustic wavelength approaches the microphone diameter. Smaller microphones allow measurements up to higher frequencies, but are much less sensitive than those with large diameters. As for automotive wind noise testing, the audio frequency range of approximately 20 Hz to 8000 Hz is of primary interest. For this work G.R.A.S. ¼ inch microphones were selected that had a dynamic range from 25 dB to 168 dB (overall sound pressure level), which meets the requirements for amplitude response for most vehicle aerodynamically induced noise measurements. Details about the calibration and frequency response can be found in Appendix D. However, in the literature, some reports on amplitude attenuation at high frequency

(over 1000 Hz) due to a microphone diaphragm size were published (for more details, refer to Callister, 1996). The effect of the diaphragm size on amplitude attenuation was ignored in this study, as the noise generated by the A-pillar flow separations is mainly dominant in lower frequencies. The noise generated by the A-pillar flow separations is in between 100 Hz to 800 Hz, Hucho (1987).

Microphones were flush mounted on the surface at the same location where surface mean pressure taps were. Microphones were embedded within the circular adaptors and mounted flush with the surface. They were connected to a 16 channel Digital Audio Tape recorder (SONY PC 216A) through the preamplifiers and power modules (G.R.A.S. type 12AA for polarisation voltage). All microphones were calibrated before and after the measurements via a Pistonphone calibrator. Signals from the microphones were continuously checked with an oscilloscope during the recording. A 10-second sample (out of a 30-second record) obtained at 48,000 Hz was analysed to calculate the non-dimensional fluctuating pressure coefficients (Cp rms) and spectral characteristics. Details on signal processing methods and algorithms are given in Appendix E. The fluctuating pressure measurement set up is shown in Figure 2.10.

The background noise was measured in the empty test section of the RMIT University Aeroacoustic Wind-Tunnel at different speeds (60 to 140 km/h in increments of 20 km/h). The difference between the background flow noise (without the test vehicle in the tunnel) and the lowest level of total aerodynamically induced noise (with test vehicle in the tunnel) was found to be greater than 10 dB. The presence of test vehicles in the wind tunnel may change the load on the fan and this may increase the background noise level. However, it is believed that this noise level increase is negligible. Therefore, no corrections were made. Electrical noise was measured by isolating the microphones from the physical (pressure fluctuation) inputs and found to be negligible.

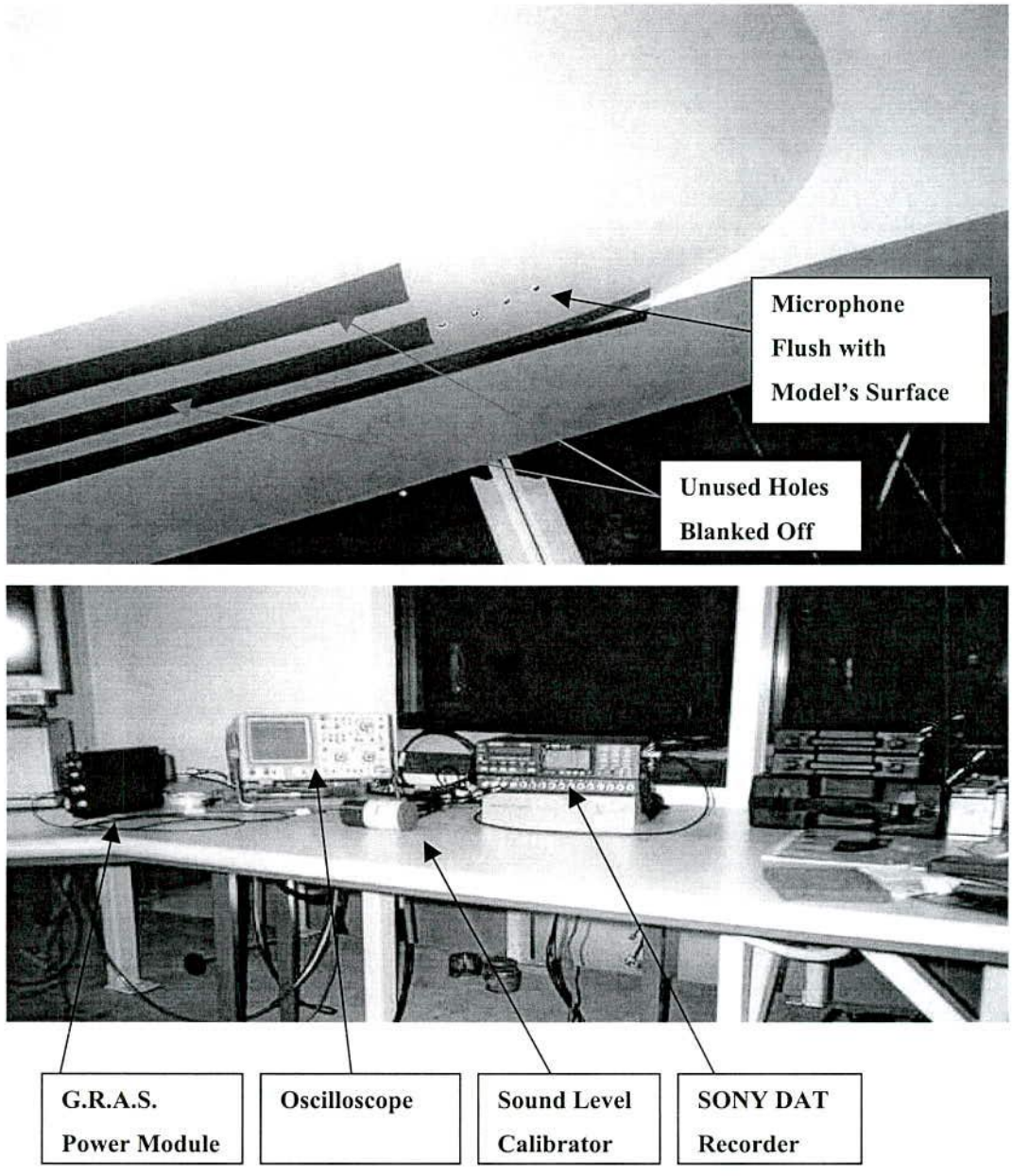

Figure 2.10: Fluctuating Pressure Measurements Set-Up in RMIT Aeroacoustic Wind-Tunnel.

2.2.4 Measurement of 'In-Cabin Noise' Using an Artificial Head System

To assess the effect of A-pillar modifications on production vehicles, the in-cabin sound pressure level was measured using an Artificial Head Measurement System, HMM II, known hereafter as the Aachen Head. The Aachen Head is a binaural measurement system that can reproduce the spatial capabilities of the human auditory system. The Artificial Head Measurement System offers benefits of binaural hearing as compared to a single pressure sensitive microphone for measurement of sound properties. Details of Artificial Head System settings, working principles and calibration are discussed in Appendix F.

2.3 Flow Visualisation

Qualitative information about the flow on a vehicle body can be obtained by flow visualisation. Flow visualisation is primarily used as a diagnostic tool to improve a vehicle's design by visualising the flow field. It is an important and effective tool in detecting the areas of flow separation, re-attachment and circulation. It also helps to explain some of the results obtained from the different tests. The great advantage of flow visualisation is that it can visualise flow structure, whereas velocity probes yield information at only a single point.

Flow visualisation with wool tufts (short strings of yarn taped/glued at one end to a surface) was carried out to see the surface flow pattern. In the case of steady and attached flow, the wool tufts generally remain steady and inclined in the direction of the flow. The wool tufts fluctuate rapidly if the flow is locally separated.

In this study, wool tufts were used to see the flow pattern on the window side and windshield near the A-pillar for all scale models and production vehicles. The flow visualisation was used as quantitative guide to the type of flow generated and also to compare with the surface mean and fluctuating pressure distributions. Flow visualisation was performed at 40, 60, 80, 100 and 120 km/h. Full-size and reduced-

scale vehicles were yawed at ±15° in increments of 5°. Flow structures were documented with video and still cameras.

Chapter Three

Surface Pressure Measurements on a Group of Idealised Road Vehicles

Model-scale tests were undertaken to investigate the influence of A-pillar geometry and yaw angles on the surface mean and fluctuating pressures in order to understand the potential for in-cabin noise generation. These tests and results are described in this chapter. Whilst the underbody flow may have an effect on the A-pillar vortex, preliminary tests, undertaken whilst the models were being manufactured, assessed the influence of Reynolds numbers on the flow close to the A-pillar on a real vehicle in the Monash/RMIT Universities' Aeroacoustic Wind-Tunnel. Additionally, in order to understand whether underbody flow had any significant influence on the A-pillar flow characteristics, a model-scale test was performed on a 30% scale, highly detailed production vehicle. For both preliminary tests it was not possible to pressure tap the production vehicle and scale model, hence the mean and transient parameters close to the A-pillar were measured using the four-hole Cobra pressure probe. The probe description was given in Chapter Two and also in Appendix B.

The details of these preliminary tests can be found in Appendix M and in the paper by Alam et al. (1998). Major conclusions from these tests are as follows:

a) The underbody flow has no significant effect on the flow (local velocity and turbulence) along a vertical plane in the A-pillar regions on the side window. Therefore, floor-mounted models without the underbody flow can be used for the investigation of flow properties on the side window close to the A-pillar.

b) The Reynolds number dependency of normalised velocity was negligible at higher speeds, however, a minor dependency was noted at lower speeds, especially between 40 to 60 km/h (for more details, refer to Alam et al. 1998).

3.1 The Simplified Models

In order to study the effects of A-pillar and windshield geometry on the local flow, five simplified models with different A-pillar and windshield geometry were made by the author. These were approximately 40% scale. The scale model was a compromise between the blockage ratio (the 40% scale model had a blockage ratio of 5.3% in the 3 m x 2 m test section) and Reynolds number. These models were kept as simple as possible without the added complication of wheels, wheel arches, engine compartment flow, side mirrors and fore-body details. In addition, models had no ground clearance and were parallel sided in plan view. The variables were the A-pillar/windshield curvature, Reynolds number (varied by tunnel speed), yaw angle and windshield inclination angle.

The external dimensions of the models are shown in Figure 3.1 and also in Appendix J. Windshield slant angles for four models were fixed at 60° to the vertical. The remaining model had no windshield inclination angle (i.e., it was vertical). It may be noted that most of the production vehicles have variable A-pillar slant angles in relation to A-pillar height and it was also found that the average slant angle for a modern car is close to 60° [3].

Each of the five models consists of three sections: a common base section to represent the main body of a road vehicle, interchangeable top sections to represent the A-pillar and windshield region, and a nose for the base section. Popat (1991) reported that the curvature of the A-pillar and windshield was a critical factor as it could play a vital role in the flow pattern near the A-pillar on the side window. For this reason, five top sections were made each with a different A-pillar and windshield curvature: a semi-circular shape, a small semi-ellipsoidal shape, a large semi-ellipsoidal shape, a slanted sharp-edged shape with a 60° flat windshield inclination angle, and a sharp-edged rectangular shape with a 0° flat windshield slant angle, as shown in Figure 3.1.

---

[3] A survey, conducted by the author, had shown that the average A-pillar inclination angle for modern passenger cars is close to 60°.

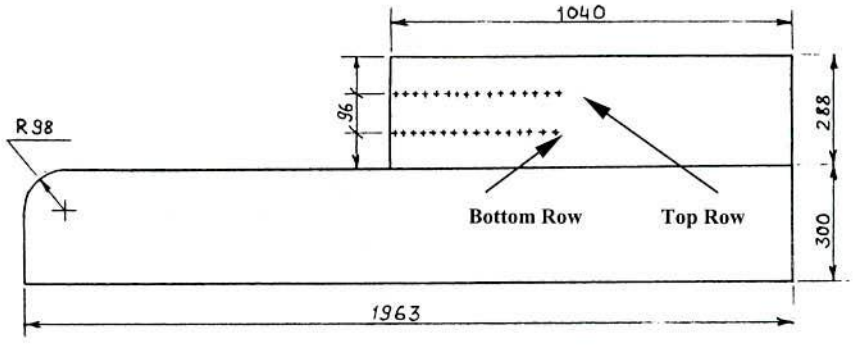

a). Side View of the Rectangular Model (R)

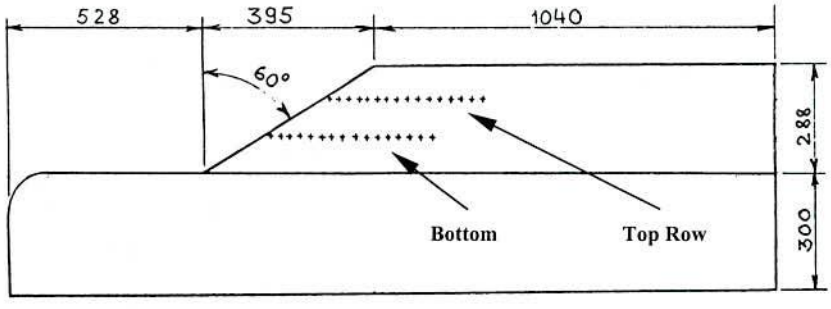

b). Side View of the Slanted Sharp-edged Model (SER)

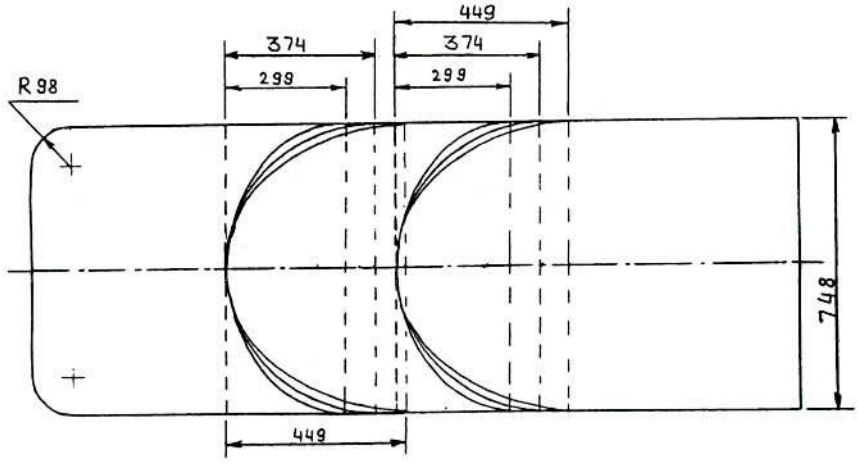

c). Top View of all Five Models

[Rectangular Model (R), Slanted Sharp-edged Model (SER), Small Ellipsoidal Model (SE), Circular Model (C), and Large Ellipsoidal Model (LE)]

Figure 3.1: External Dimension of Simplified Models (in millimetre)

The length of ½ major axis (a) of the ellipsoidal models was the half width (374 mm) of the model, and the length of ½ minor axis (b) of the small ellipsoidal shape was 20% less (299 mm) than the length of ½ major axis (a). The radius of the circular shape was the ½ width (length of ½ major axis = a = 374 mm) of the model. The length of ½ minor axis (b) of the large ellipsoidal shape was 20% larger (449 mm) than the length of ½ major axis (a) of the small ellipsoidal shape. For more details, refer to Figure 3.1 and Appendix J. The nose section for the base was designed to keep the flow attached in order to avoid bluff body flow separation. Both lateral and longitudinal curvatures of the nose were similar to the fore-body of a production vehicle. It may be noted that generous radii and a sharp edge in the A-pillar region of scale-models were considered to ensure the two cases of attached and separated flows.

(NB. One of the reasons for the study of the sharp-edged rectangular model and the slanted sharp-edged model was to compare and extend the results with the published data, especially with the findings of Popat (1991). In his Ph.D. research, Popat conducted surface mean and fluctuating pressure measurements on the side window of a 20% scale model at different A-pillar (windshield) slant angles (0° to 60° in increments of 10°). The model was mounted on a wind-tunnel sidewall and it was tested at three different speeds (93, 126 and 158 km/h) all at zero yaw angle. The influence of A-pillar and windshield curvature on the A-pillar flow structure was not considered.)

All five scale models were tested at 60, 80, 100, 120 and 140 km/h speeds under ±15° yaw angles in increments of 5° in the RMIT University Aeroacoustic Wind-Tunnel. Surface mean and fluctuating pressures were measured at similar positions for all models. Typical positions of surface mean and fluctuating pressure measurements are shown in Figure 3.1 and Figure 3.2. Flow visualisation was also carried out at the same speeds (except 140 km/h) and yaw angles used for the surface mean and fluctuating pressure measurements. Data acquisition, procedure and instrumentation have been discussed in Chapter Two.

Due to strong pressure fluctuations in the A-pillar region on the side window of the sharp-edged model and the rectangular model, the fluctuating pressure was only measured at three speeds (60, 80 and 100 km/h) in order to avoid the microphones

over-ranging. However, the fluctuating pressure for other three models have been measured at all speeds.

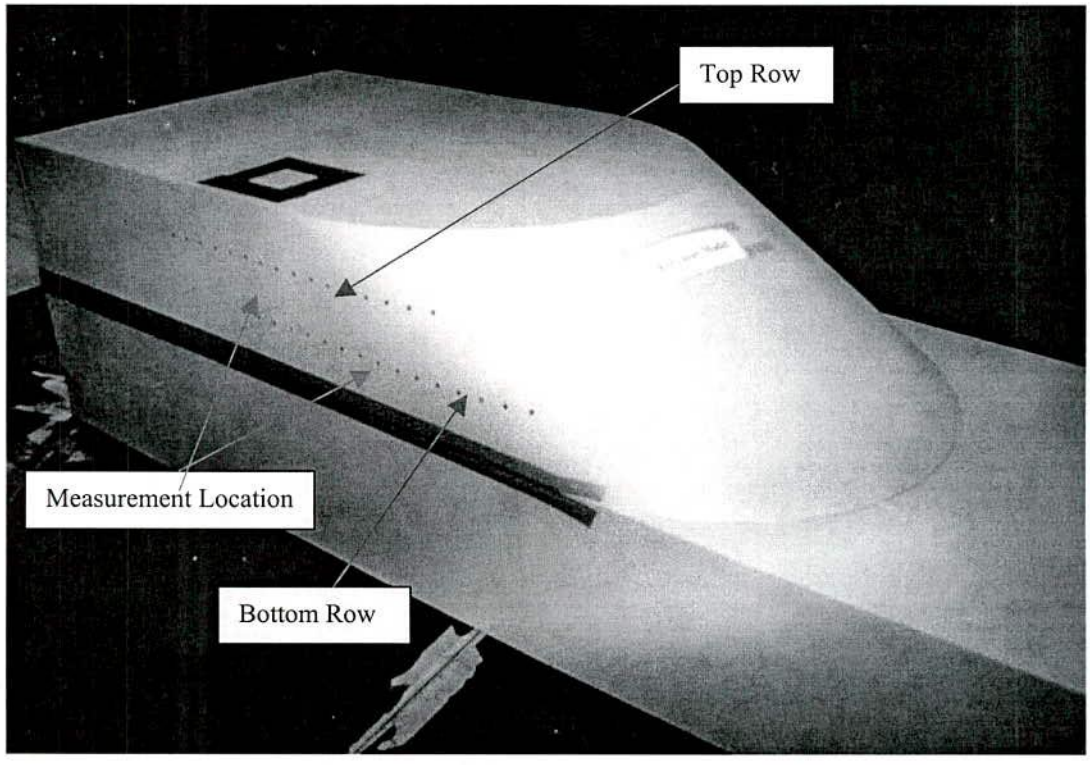

Figure 3.2: A Simplified Model Showing the Location of Pressure Measurements

A general overview about the separated, separated and re-attached, and attached flows was given in Chapter One. However, a graphical interpretation of the flow over a backward-facing step, which has a resemblance to the A-pillar flow separation is useful, hence such a flow pattern behind a step is shown in Figure 3.4. As the airflow cannot negotiate a right angle bend, the flow will separate at the sharp edge corner "S" and produce a clock-wise rotating vortex or bubble. A separation streamline that divides the recirculating flow from the main stream flow re-attaches at a point "R" (refer to Figure 3.4). The separation streamline (thin shear layer) is unstable if turbulent, and tends to entrain the flow on both sides. This entrainment has the dual effect of causing a reverse flow immediately in the separated flow region and a reduction of pressure in the separated region.

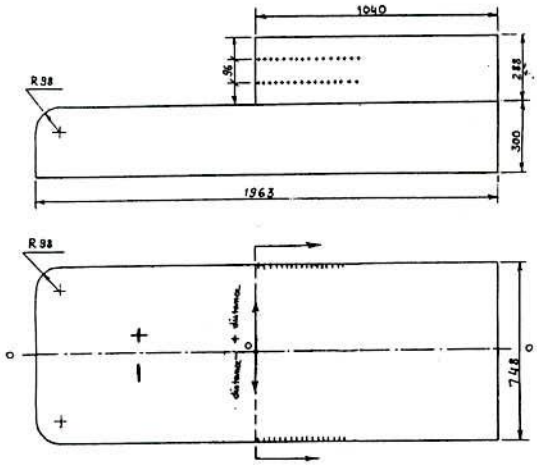

a). **Rectangular Model (R),** Distance from Centre-line 384

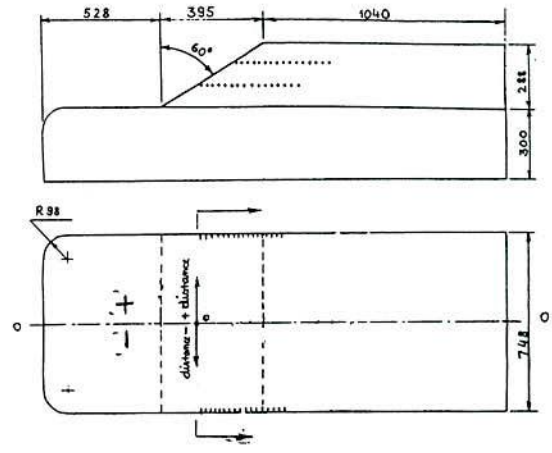

b). **Slanted Sharp-edged Model (SER),** Distance from Centre-line 384 mm

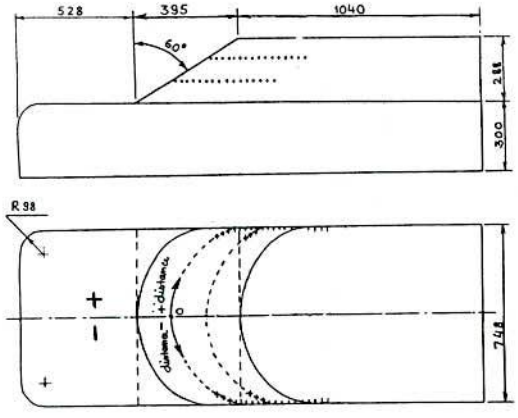

c). **Small Ellipsoidal Model** (SE), Distance from Centre-line 470 mm

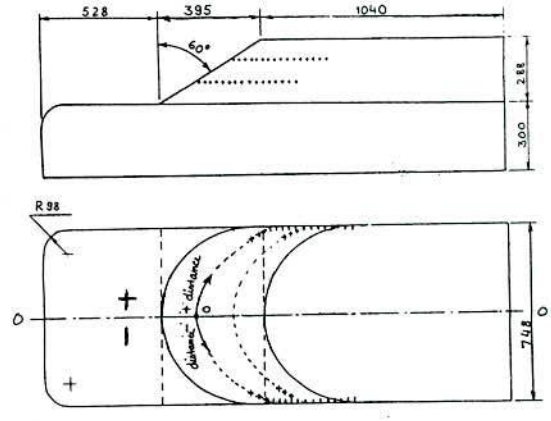

d). **Circular Model (C),** Distance from Centre-line 490 mm

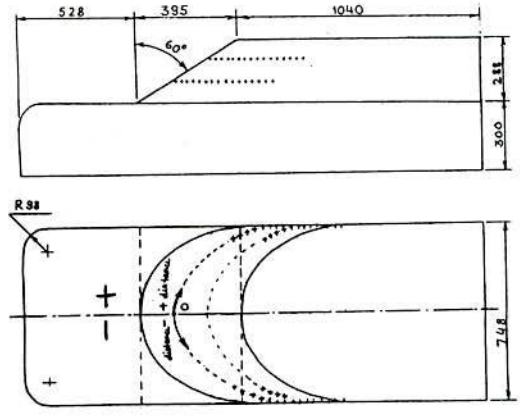

e). **Large Ellipsoidal Model (LE),** Distance from Centre-line 530 mm

Figure 3.3: A Schematic of Data Presentation in Relation to Model's Centre Line.

Hucho (1998) reported that the length of re-attachment (l) from the separated point from a backward-facing step is approximately 3 to 5 step heights (h) depending on the thickness of the boundary layer over the step ahead of the separation point. The flow over a step may have secondary separation and re-attachment depending upon the shape of the body creating the flow. The peak negative pressure coefficient is usually noted close to the separation point, however the pressure coefficient is close to zero at the re-attachment point (see Figure 3.4).

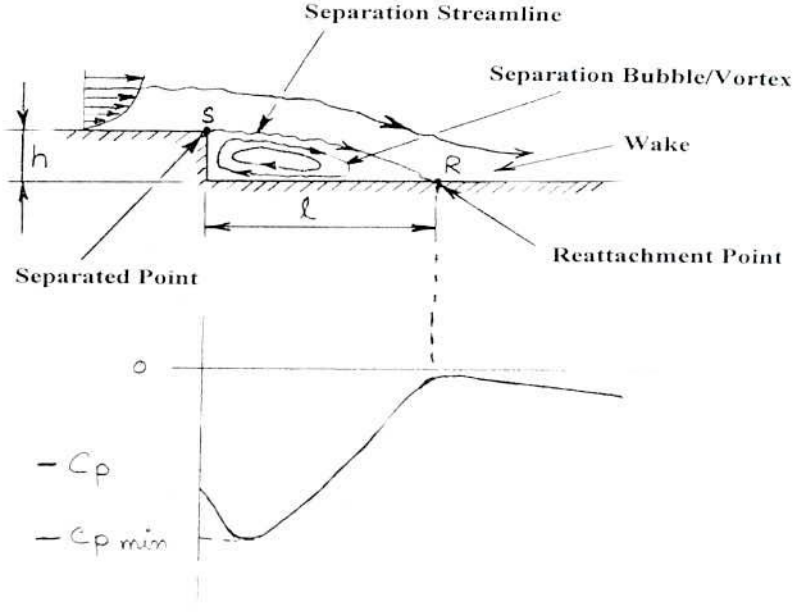

Figure 3.4: Flow Field on a Backward-Facing Step, Adapted from Hucho (1998)

The surface mean pressure coefficients were calculated from the surface pressure data and the fluctuating pressure signals from the microphones were processed to generate root mean squared (rms) pressure coefficients. In this discussion, surface mean and fluctuating pressure coefficients at the bottom row and the top row location are presented. The effects of Reynolds numbers obtained by varying the tunnel speed on the surface mean and fluctuating pressures will be described in the next subsections.

3.2 Rectangular Model

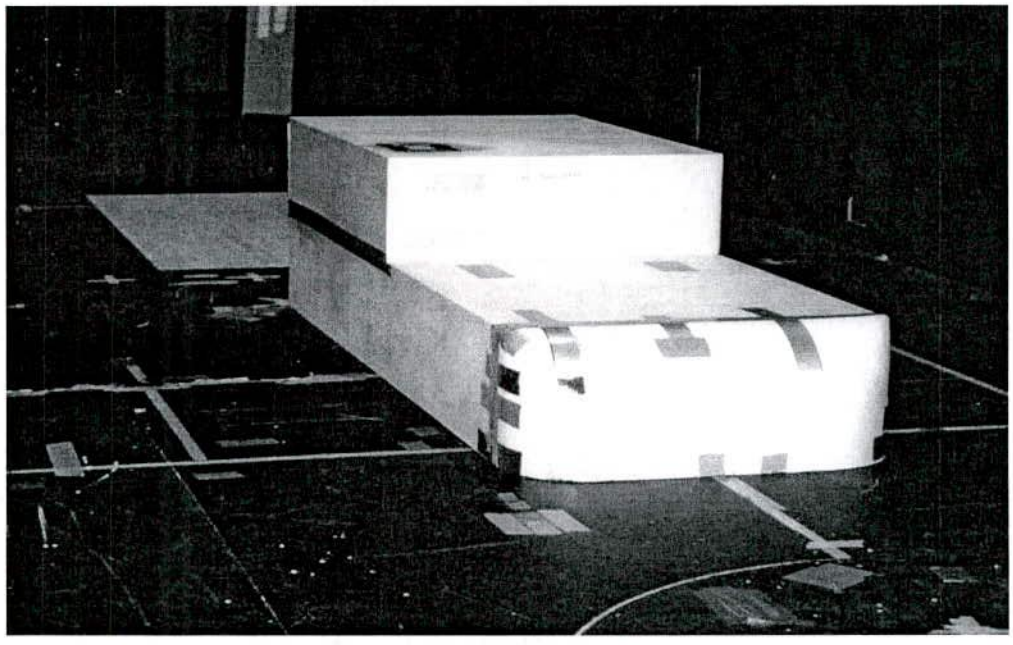

Figure 3.5: Rectangular Model in the Test Section of RMIT Aeroacoustic Wind-Tunnel

3.2.1 Reynolds Number Effects

The coefficients are plotted against the distance from the line of symmetry (at the front) of the models (for details of how the graphical results relate to the model geometry, refer to Figure 3.3). For compactness, when non-zero yaw angle data are presented, data from the upstream and downstream sides are plotted on the same figure. Errors in the surface pressure measurements are considered in Appendix K. The typical error for the surface mean and fluctuating pressure coefficients is approximately 1%.

3.2.1.1 Surface Mean Pressure

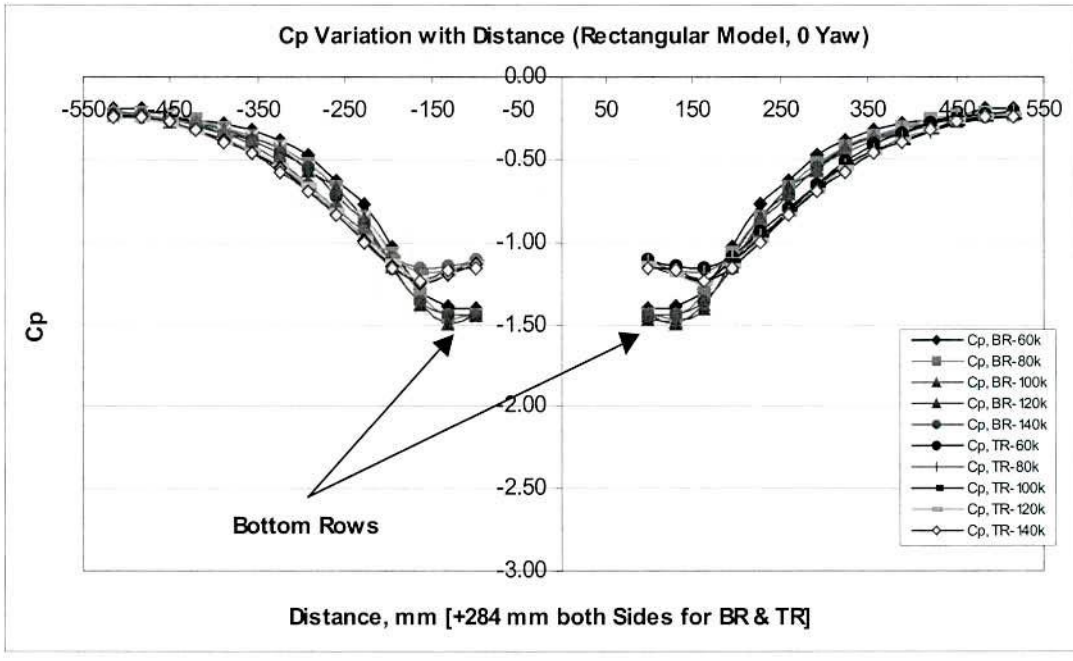

Figure 3.6: Surface Mean Pressure Coefficient Variations, Yaw = 0°

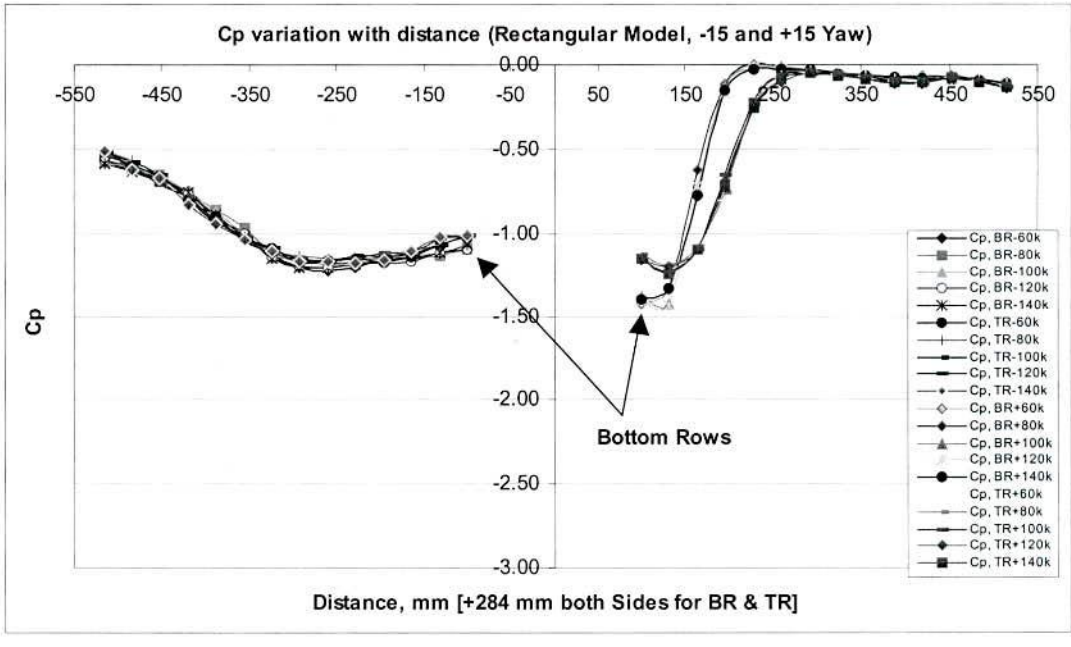

Figure 3.7: Surface Mean Pressure Coefficient Variations, Yaw = -15° and +15°

NB: The abbreviation of 'TR', 'BR' and 'K' used in various plots including Figure 3.7 are Top Row, Bottom Row and Km/h respectively.

The influence of Reynolds numbers and yaw angles on the surface mean pressure is shown in Figure 3.6 and Figure 3.7. Figure 3.6 shows the mirror image of surface mean pressure distribution to the left and right hand sides of the model. Figure 3.7 demonstrates the mean pressure distribution along the leeward side window (-15° yaw angle) and windward side window (+15° yaw angle). All three plots show that the surface mean pressure coefficients are virtually independent of the Reynolds number. However, a very small variation of Cp has been observed in the plot at zero yaw angles. This small variation could be due to the errors of uncertainty, see Appendix K.

3.2.1.2 Surface Fluctuating Pressure

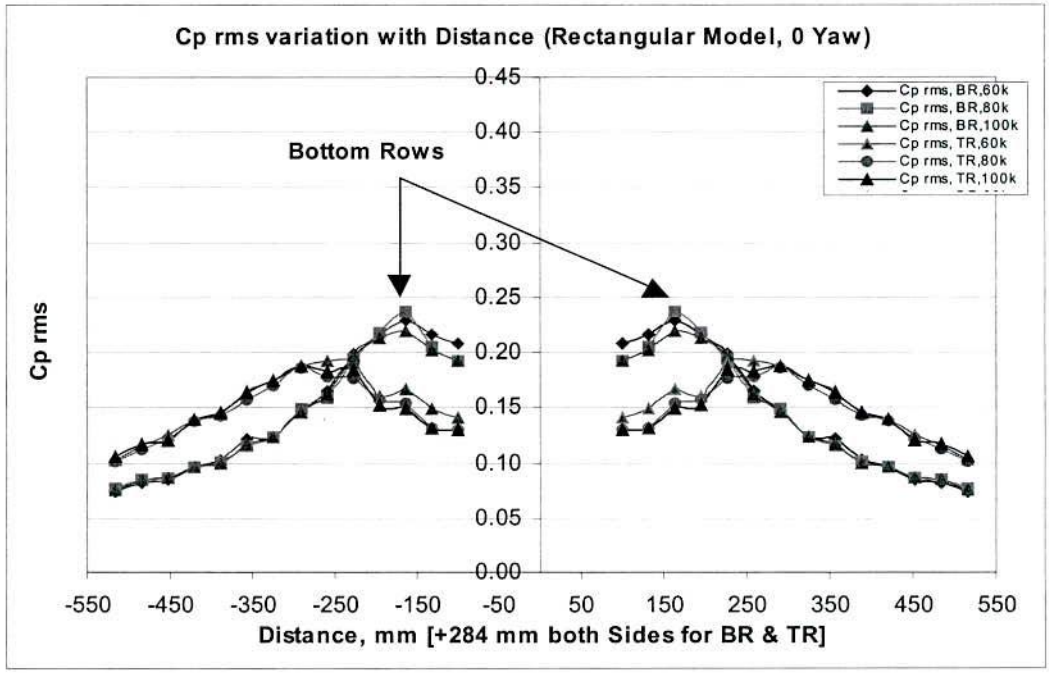

Figure 3.8: Fluctuating Cp rms Variations with Distance, Yaw = 0° (R)

The root mean squared pressure coefficients are shown in Figure 3.8 and Figure 3.9 in three different yaw angles (0°, -15° and +15°). The Reynolds number has no notable effect on the root mean squared pressure coefficients for the rectangular model. However, a very small fluctuation is noted in the middle of the A-pillar vortex for the zero and negative yaw angles between 60 km/h and higher speeds.

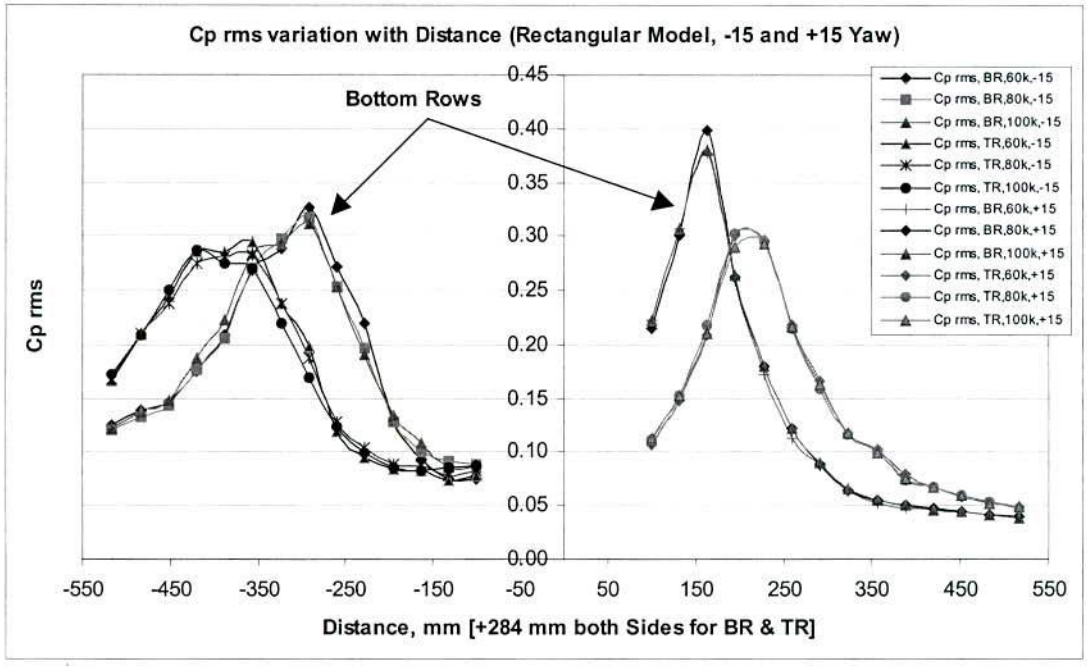

Figure 3.9: Fluctuating Cp rms Variations with Distance, Yaw = -15° and +15° (R)

3.2.2 Effects of Yaw Angles on Surface Pressures

As discussed earlier, all models were tested at ±15° yaw angles in increments of 5°. The results for the maximum negative, positive and zero yaw angles are discussed here. Results for other intermediate yaw angles are shown in Appendix H and Appendix G.

3.2.2.1 Surface Mean Pressure

The variations of time-averaged surface mean pressure coefficients with the distance along the side window have already been shown in Figure 3.6 and Figure 3.7. These figures also demonstrate how the A-pillar flow separation varies with the yaw angle. Figure 3.6 indicates that the pressure in the bottom row recovers faster than the pressure in the top row. Figure 3.6 shows that the intensity of fluctuation in the bottom row is higher than the intensity in the top row. At -15° yaw angle, the maximum magnitude of the A-pillar vortex moves downstream from the A-pillar leading edge and at the positive yaw angle (+15°), the A-pillar vortex peak shifts

towards the leading edge of the A-pillar. The re-attachment zone moves towards the leading edge. The area of separated zones at positive yaw angles reduces significantly compared to negative yaw angles. Flow visualisation (Figure 3.10, Figure 3.11 and Figure 3.12) supports these observations. In Figures 3.11 and 3.12, there appears to be a separation from the hood edge. It is believed that this separation has minimal effect on the A-pillar vortex as the intensity of the A-pillar vortex is much stronger compared to the hood edge separation. However, the sharp-edge hood separation can be the contributor to 'In-Cabin Noise' by generating low frequency hydrodynamic pressures.

The maximum and minimum magnitudes of the surface mean pressure coefficient at zero yaw angle were -1.5 and -0.2 respectively. The values from Popat (1991) were -1.6 and -0.2 respectively. The minor difference between the values found in this study and those of Popat are thought to be due to tunnel blockage effects. Blockage corrections have not been applied in this study as the blockage ratio was approximately 6%. For more details about the blockage ratio, refer to Appendix K.

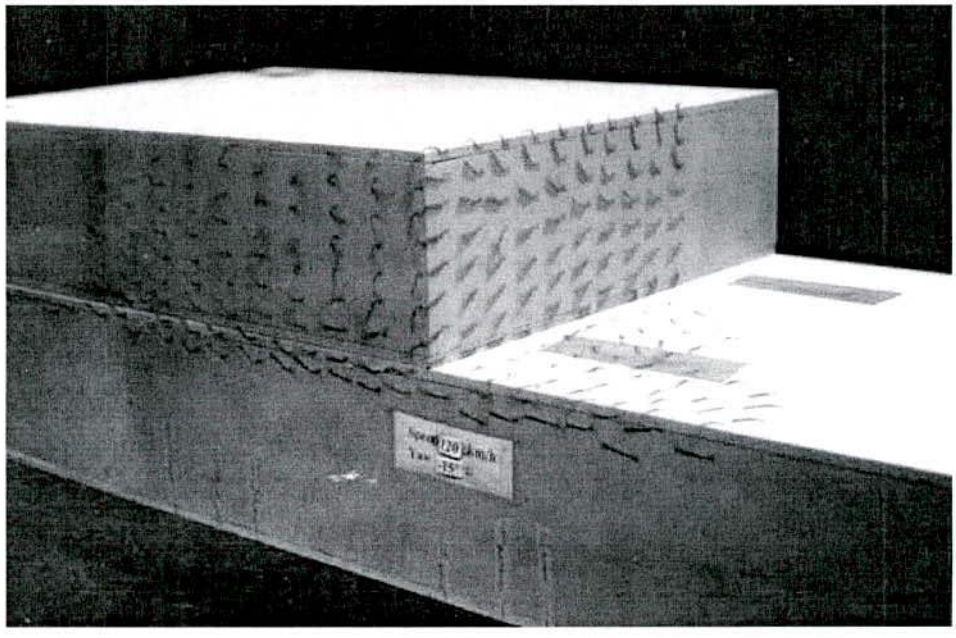

Figure 3.10: Side View of Wind-Tunnel Flow Visualisation, 120 km/h, Yaw = -15° (R)

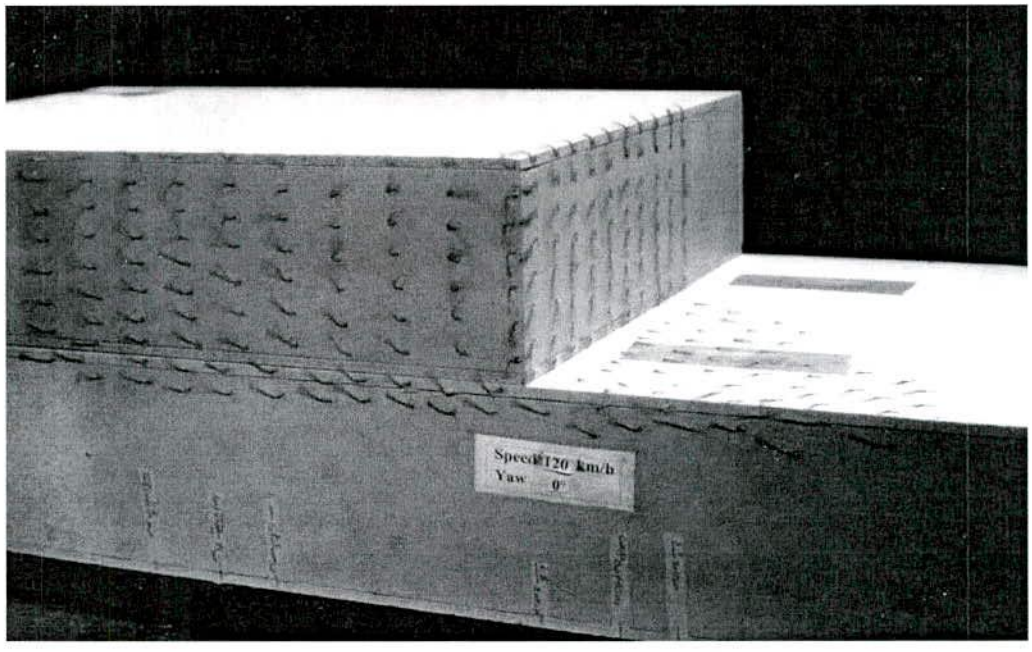

Figure 3.11: Side View of Wind-Tunnel Flow Visualisation, 120 km/h, Yaw = 0°

(R)

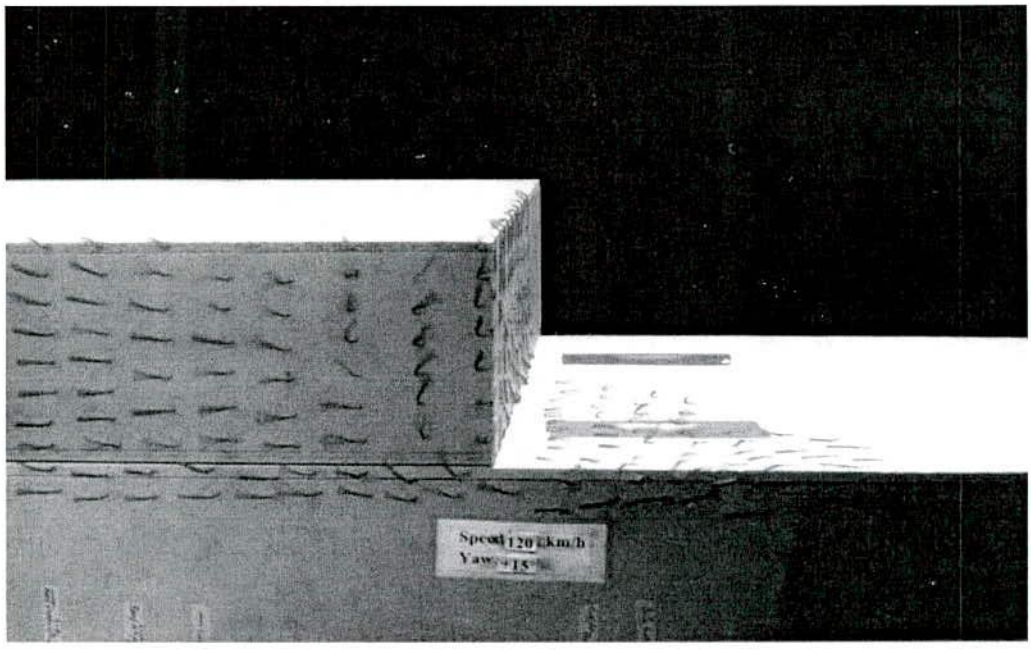

Figure 3.12: Side View of Wind-Tunnel Flow Visualisation, 120 km/h, Yaw = +15°

(R)

3.2.2.2 Fluctuating Pressure

The magnitude of fluctuating pressure coefficients significantly varies with the yaw angles (Figure 3.8 and Figure 3.9). The peak value of Cp rms at the positive yaw angle (+15°) is higher than the peak values of Cp rms in zero and negative yaw angles. For the negative yaw angle (-15°), the area of fluctuating pressure becomes larger than for zero and positive yaw angles and the maximum magnitude of the A-pillar vortex moves away from the A-pillar leading edge. With a positive yaw angle, the conical vortex moves closer to the A-pillar leading edge and the separated area becomes smaller (Figure 3.8 and Figure 3.9). Although the vortex shrinks, the magnitude of the fluctuating pressure coefficients still remains greater than the magnitudes of fluctuating pressures for zero and negative yaw angles. The flow visualisation (Figure 3.10, Figure 3.11 and Figure 3.12) shows how the A-pillar vortex changes with yaw angles. The computed maximum and minimum root mean squared Cps were 0.23 and 0.08 which are the same as those measured by Popat (1991).

3.2.3 Spectral Analysis

Power Spectral Density (PSD) was used to document the energy characteristics of signals in the frequency domain. The procedure for PSD calculation is shown in Appendix E. In this study, the fluctuating pressure data from the position where the maximum fluctuating pressure occurred, (measured at zero and ±15° yaw angles) was used for PSD analysis and plotted against frequency and Strouhal number. The vertical axis (pressure squared) of the power spectrum was normalised by dividing by the velocity head (q). The Strouhal number is defined as, $S_t = \frac{fL}{U}$, where L is a characteristic length scale of the source and U is the reference velocity and f is the frequency. The characteristic length scale (L) is frequently the boundary layer displacement thickness, however in separated flow fields, especially in the A-pillar region, the boundary layer displacement thickness (L) is no longer relevant. Instead, a

characteristic disturbance scale needs to be selected. In automotive noise evaluation where separation on the outside of the car does exist, the mean separation length is an appropriate length scale. Alternatively, an arbitrary constant length scale could be used for data normalisation, George (1989). It is sometimes difficult to determine the appropriate length scale and in those cases L=1 meter is generally accepted. In this study, the spectral density was normalised using L=1 meter.

The PSDs of maximum fluctuating pressure at the locations on the model surface for the negative, zero and positive yaw angles (-15°, 0° and +15°) are shown in Figure 3.13 and Figure 3.14. The normalised PSD plot at zero yaw angle is shown in Figure 3.15.

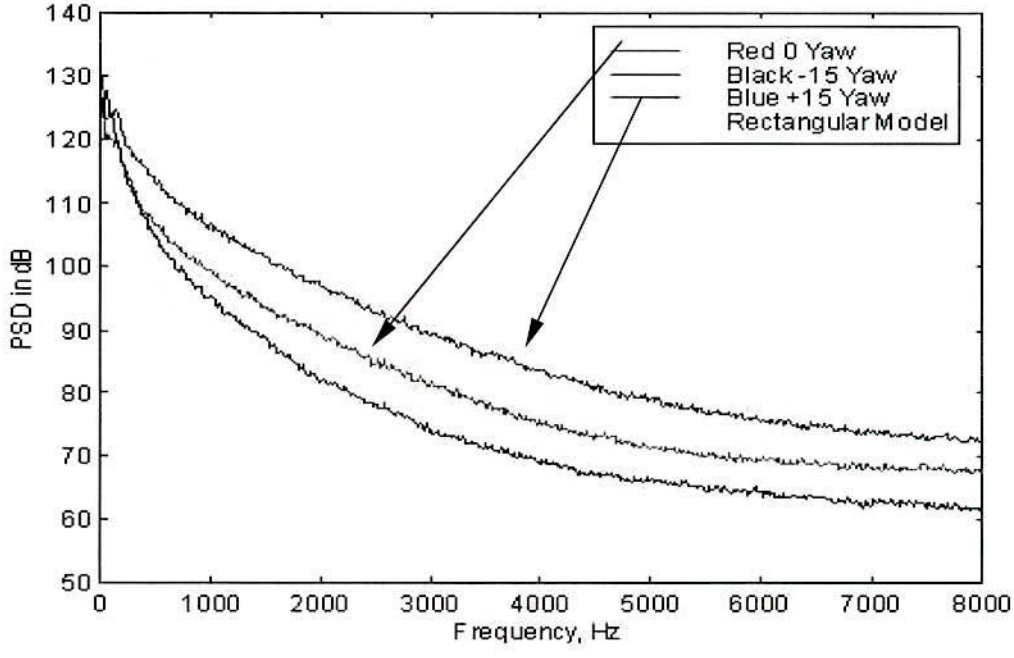

Figure 3.13: Power Spectra Plot of Peak Cp rms, Yaw = 0°, -15°and +15° (R)

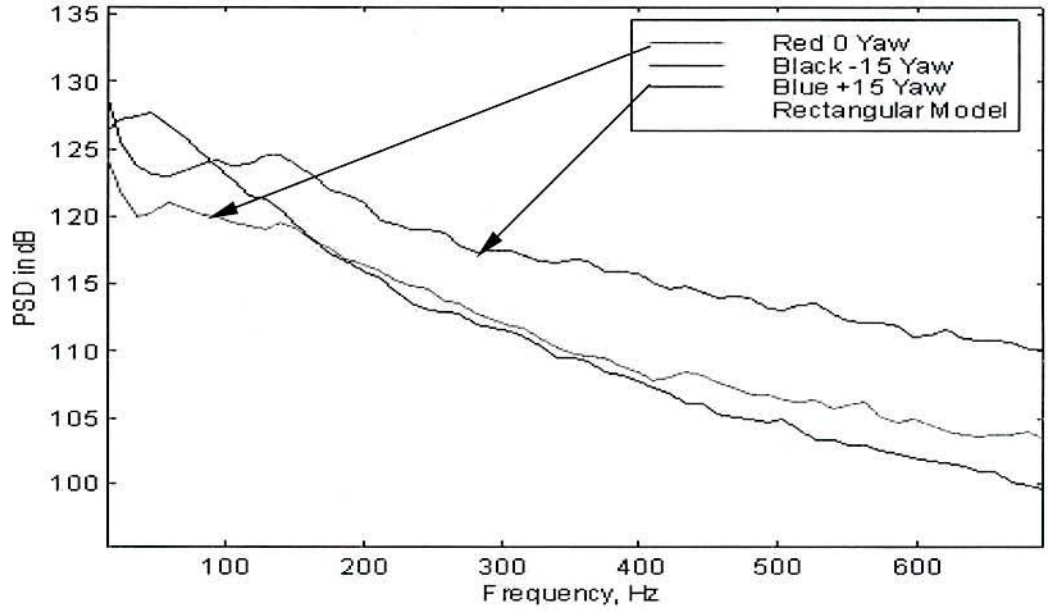

Figure 3.14: Magnified Power Spectra Plot of Peak Cp rms (Figure 3.13)

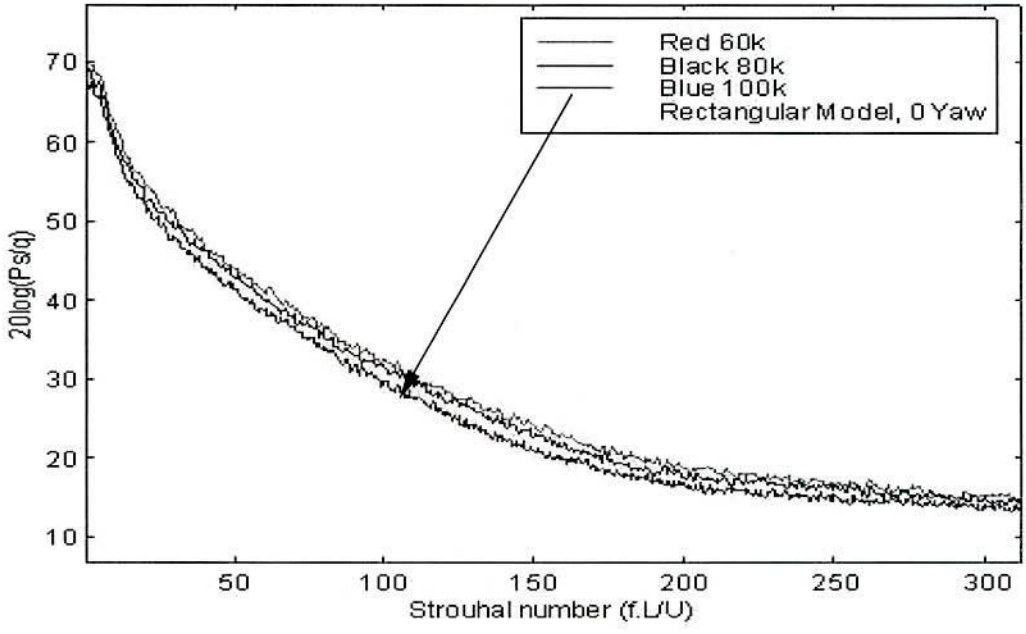

Figure 3.15: Normalised Power Spectra of Fluctuating Pressures, Yaw = 0° (R)

NB: Ps and q shown (in vertical axis), and L (in horizontal axis) in Figure 3.15 are the fluctuating pressure energy, velocity head (dynamic pressure) and the characteristic length-scale of noise sources.

At a positive yaw angle, the energy content is higher at frequencies above 100 Hz. The fluctuating pressure contains less energy in the negative yaw angle than the positive and zero yaw angles, however it shows the highest energy below 100 Hz.

The normalised power spectra plot (Figure 3.15) shows that all three spectra (60, 80 and 100 km/h speeds) are approximately the same.

3.3 Slanted Sharp-Edged Model

A general overview of a slanted sharp-edged model is shown in Figure 3.16.

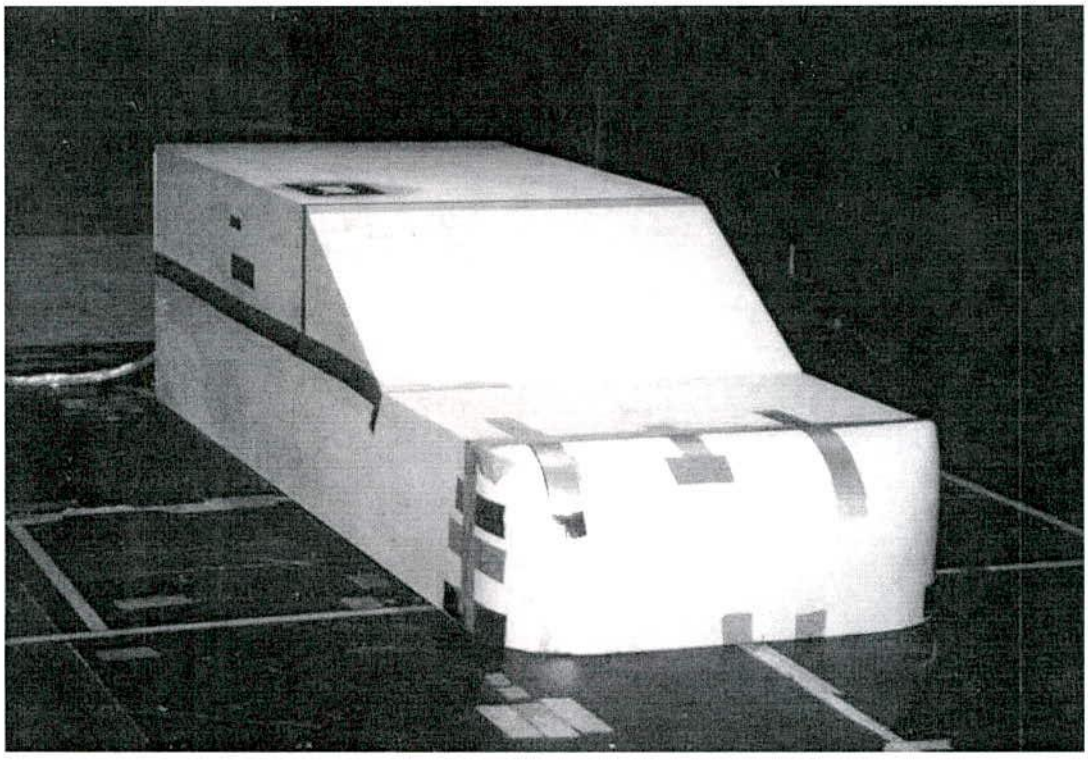

Figure 3.16: The Slanted Sharp-Edged Model in the Test Section of the RMIT Aeroacoustic Wind-Tunnel

3.3.1 Reynolds Number Effects

3.3.1.1 Surface Mean Pressure

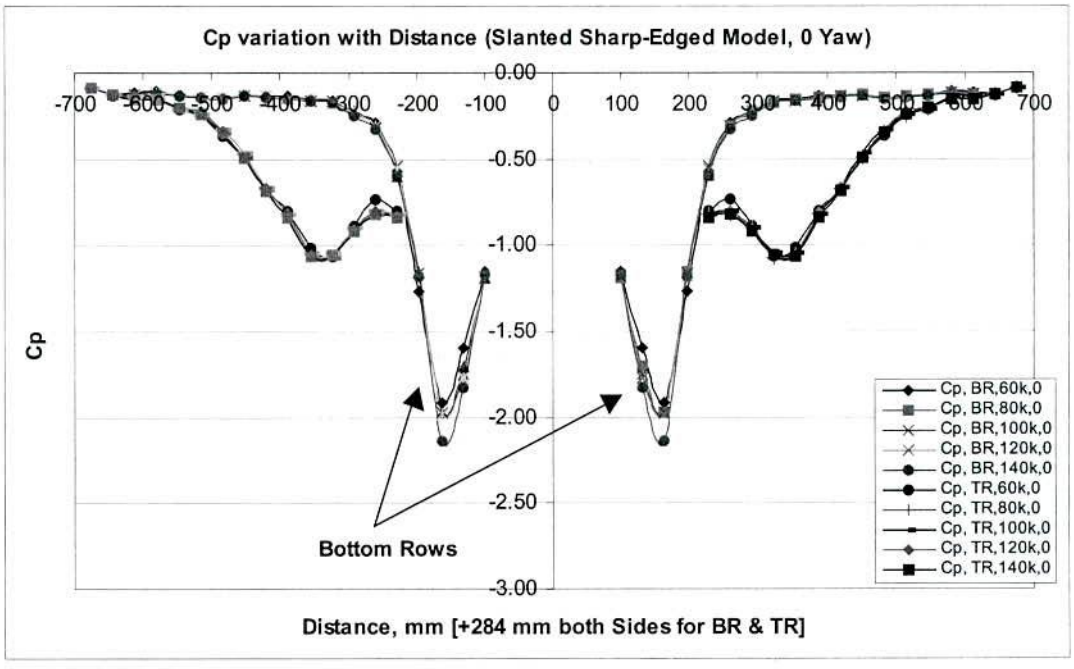

Figure 3.17: Surface Mean Pressure Cp Variations with Distance, Yaw = 0° (SER)

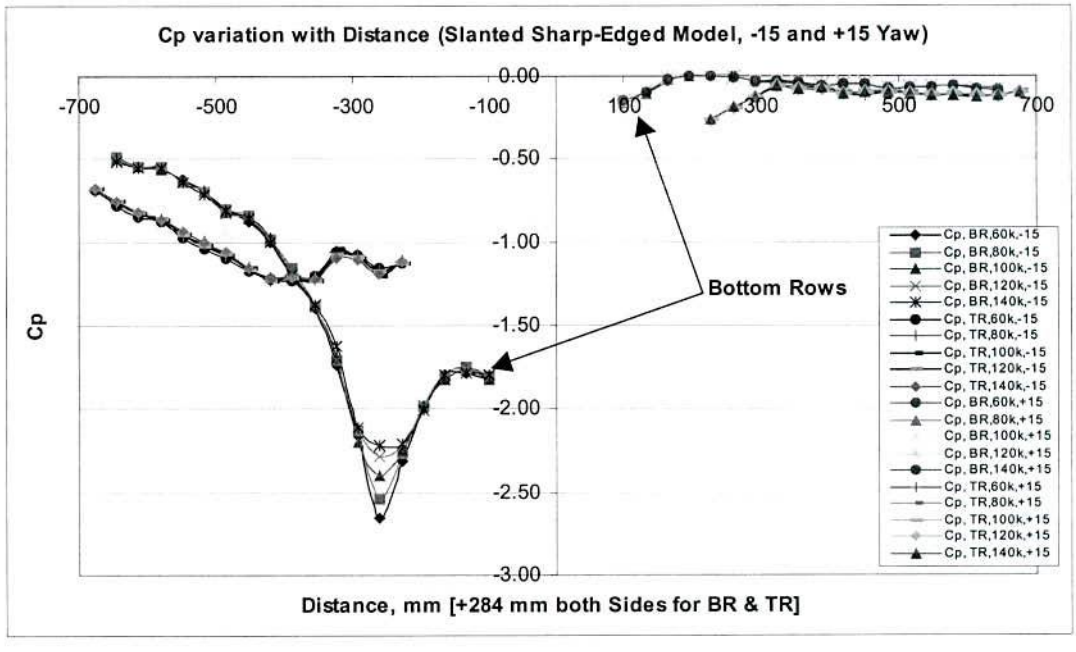

Figure: 3.18: Surface Mean Pressure Cp Variations with Distance, Yaw = -15° and +15° (SER)

The surface mean pressure coefficients are virtually Reynolds number independent except at the location of lowest mean pressure at negative and zero yaw angles (Figure 3.17 and Figure 3.18). The reason for the Cp dependency on the Reynolds number in the location of the lowest mean pressure is not clear. The minimum and maximum surface mean pressure coefficients measured at zero yaw angles were -2.0 and -0.1 respectively. The minimum and maximum values at zero yaw angles computed by Popat (1991) were -2.3 and -0.16 accordingly.

3.3.1.2 Surface Fluctuating Pressure

Reynolds numbers have no effect on the fluctuating pressure at zero yaw angles as shown in Figure 3.19. Small variations are evident with Reynolds numbers in negative and positive yaw angles between 60 km/h and higher speeds (-15° and +15°) in Figure 3.20. The maximum and minimum values of Cp rms found at zero yaw angles in this study were 0.28 and 0.03 compared to 0.21 and 0.06 found by Popat (1991).

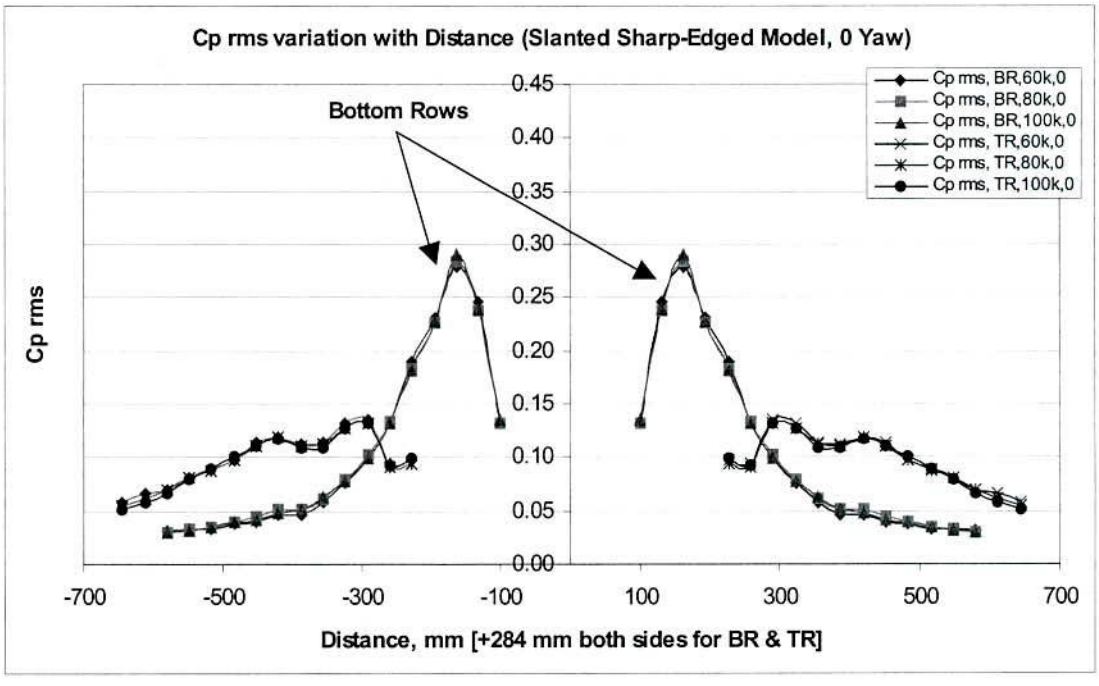

Figure 3.19: Fluctuating Cp rms Variations with Distance, Yaw = 0° (SER)

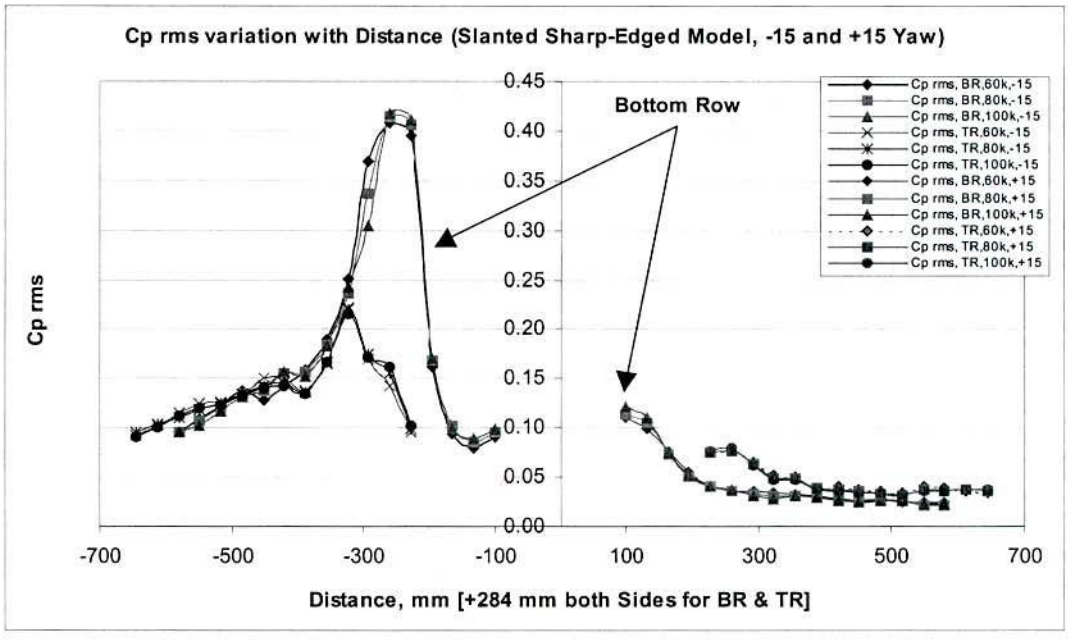

Figure 3.20: Fluctuating Cp rms Variations with Distance, Yaw = -15° and +15° (SER)

3.3.2 Effects of Yaw Angles on Surface Pressures

3.3.2.1 Surface Mean Pressure

The mean surface pressure coefficient strongly varies with the yaw angles (Figure 3.17 and Figure 3.18). The maximum magnitude of the negative pressure moves downstream from the A-pillar leading edge as the negative yaw angle increases. At the positive yaw angles, the peak magnitude moves towards to the leading edge and the A-pillar vortex almost disappears. The maximum magnitude of the pressure is greater at negative yaw angles compared to the maximum magnitude of the pressure in the rectangular model. However, at a positive yaw angle, the maximum magnitude of pressure is smaller compared to the maximum magnitude of pressure in the rectangular model. The photographs of the flow visualisation (Figure 3.21, Figure 3.22 and Figure 3.23) indicate the A-pillar vortex stagnation and re-attachment lines along the A-pillar edge, however the A-pillar vortex stagnation and re-attachment lines were not clearly visible in the rectangular model.

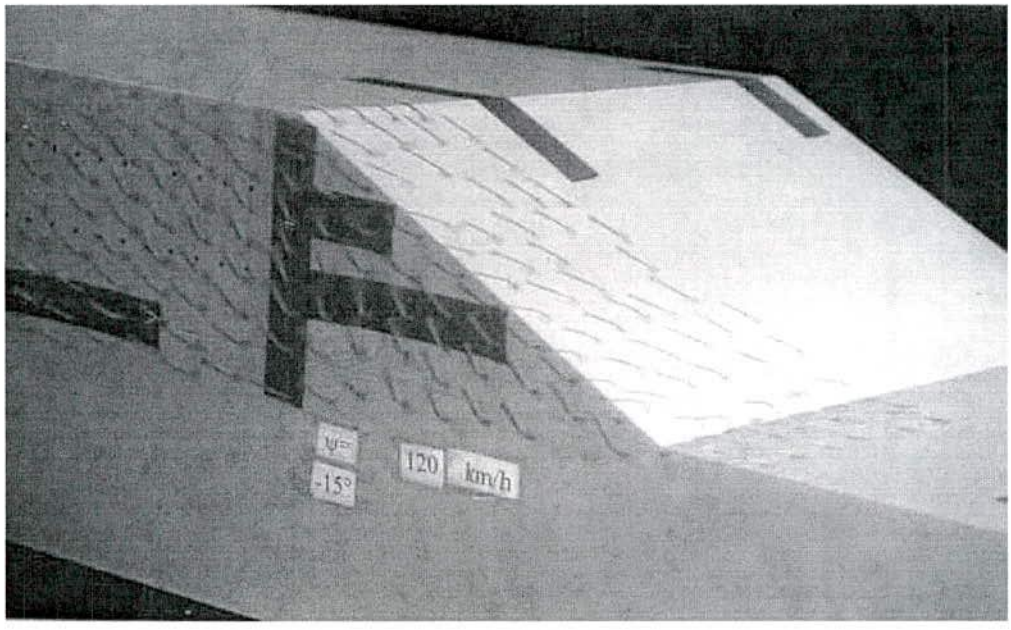

Figure 3.21: Side View of Wind-Tunnel Flow Visualisation, 120 km/h, Yaw = -15° (SER)

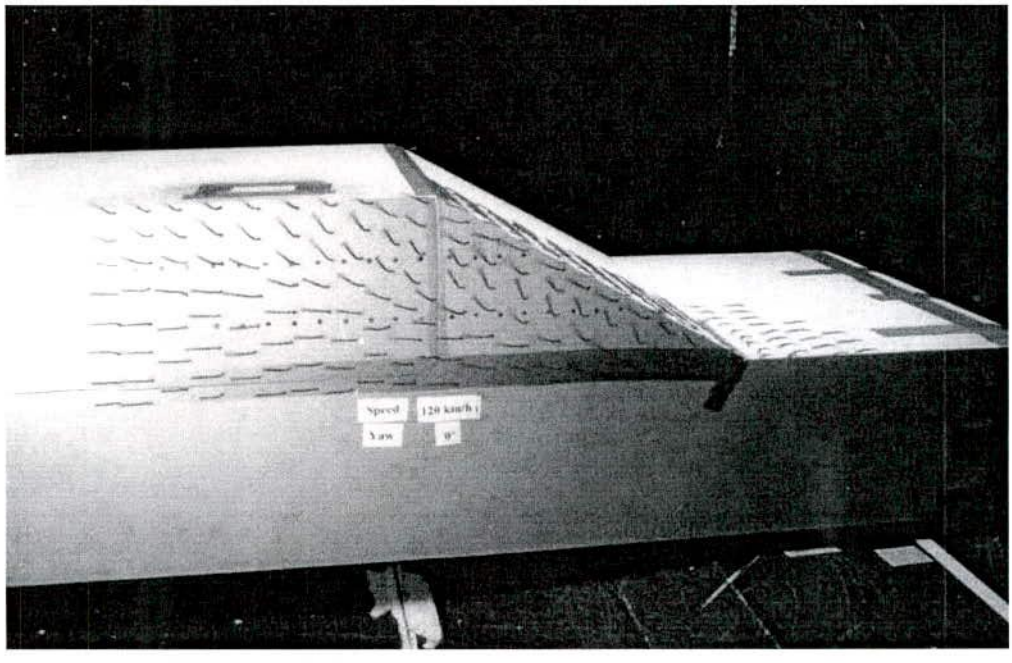

Figure 3.22: Side View of Wind-Tunnel Flow Visualisation, 120 km/h, Yaw = 0° (SER)

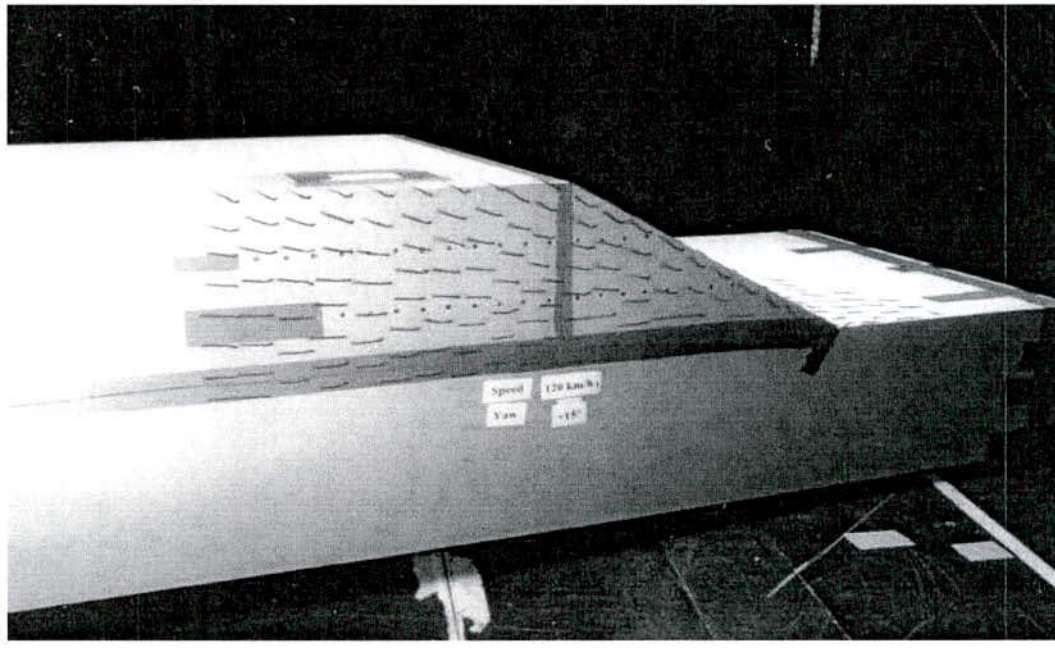

Figure 3.23: Side View of Wind-Tunnel Flow Visualisation, 120 km/h, Yaw = +15° (SER)

3.3.2.2 Surface Fluctuating Pressure

The Cp rms plots (Figure 3.19 and Figure 3.20) show how the magnitude and size of the fluctuating pressure region changes with the yaw angles. The magnitude becomes larger in the negative yaw angle and the peak of fluctuating pressure shifts away from the A-pillar leading edge. The fluctuating pressure is stronger close to the bottom row than the top row by a factor of approximately two. The maximum Cp rms at -15° yaw angle was 0.41. At positive yaw angle (+15°), the magnitude of fluctuating pressure reduces significantly (Figure 3.20). The value of maximum Cp rms at +15° yaw angle was 0.11. The flow visualisation photographs (Figure 3.21, Figure 3.22 and Figure 3.23) demonstrate how the separated zone reduces at the positive yaw angles and increases under the negative yaw angles.

3.3.3 Spectral Analysis

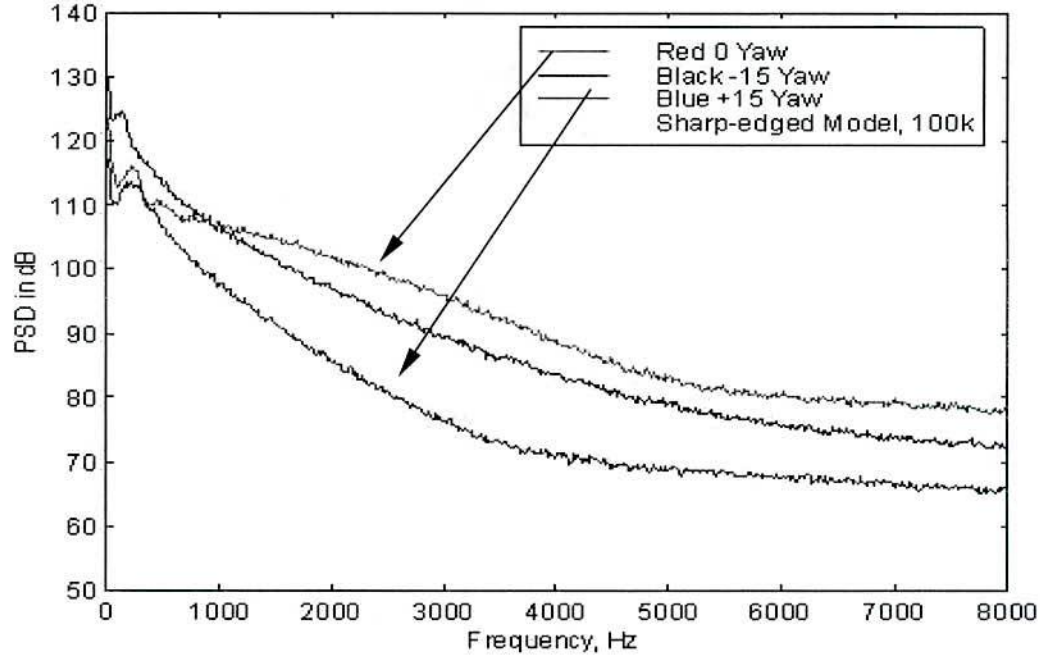

Figure 3.24: Power Spectra Plot of Peak Cp rms, Yaw = 0°, -15° and +15° (SER)

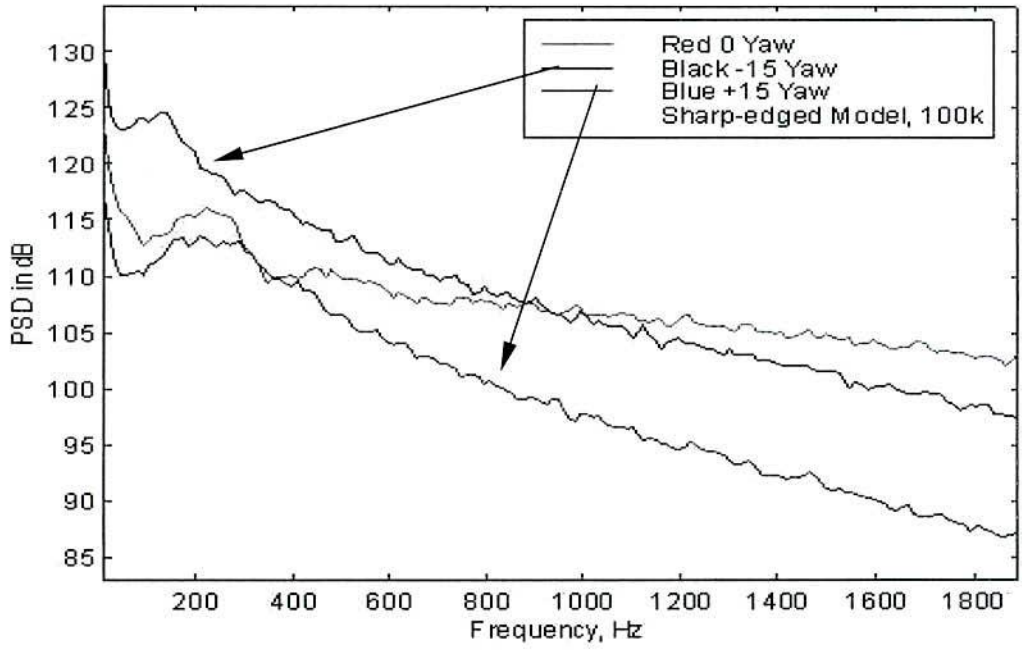

Figure 3.25: Magnified Power Spectra Plot of Peak Cp rms (Figure 3.24)

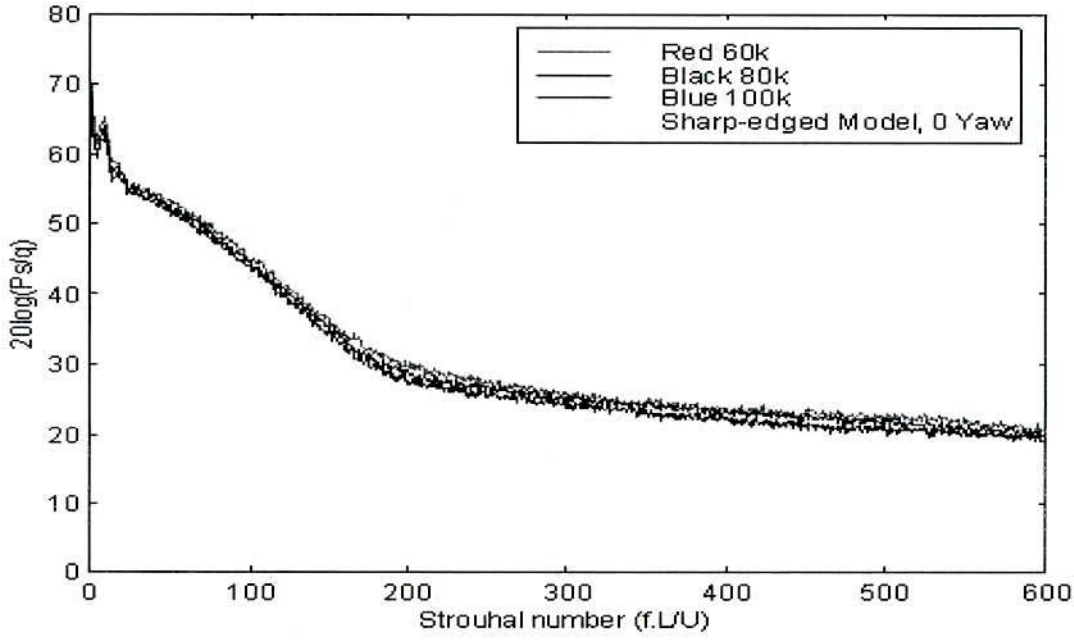

Figure 3.26: Normalised Spectra Plot of Peak Cp rms, Yaw = 0° (SER)

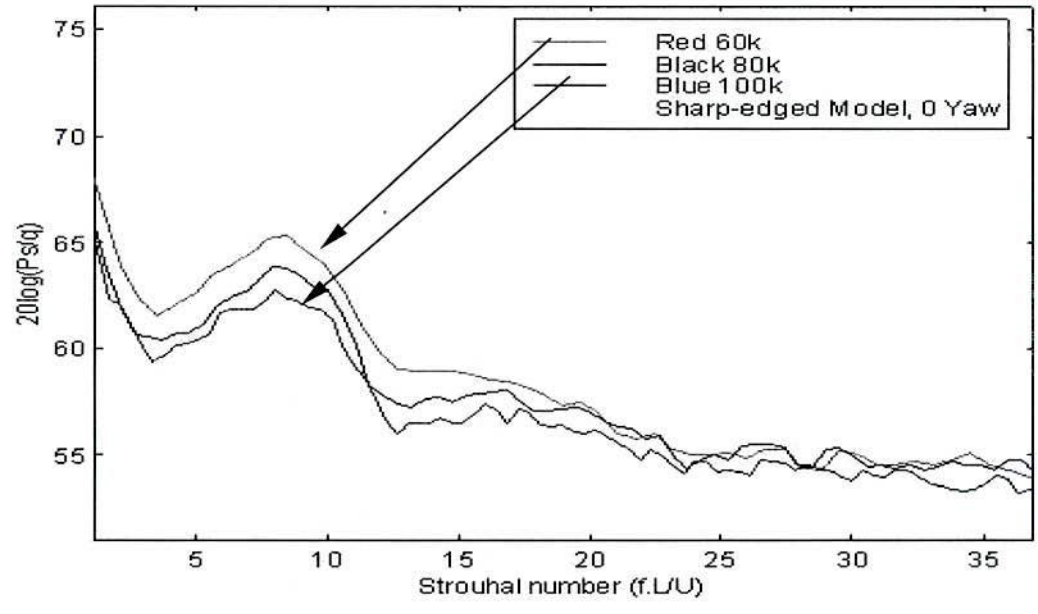

Figure 3.27: Magnified Power Spectra Plot of Peak Cp rms (Figure 3.26)

The PSD plot of the highest fluctuating pressure at negative, zero and positive yaw angles are shown in Figure 3.24 and in a magnified plot in Figure 3.25. The peak fluctuating pressure energy at zero and positive yaw angles lies in between 100 Hz

and 400 Hz. The centre of peaks in both cases is close to the frequency at 220 Hz. The spectral energy in the negative yaw angles dominates significantly in the lower frequencies up to 950 Hz. The peak is close to 150 Hz for the negative yaw angles. Figure 3.24 and Figure 3.25 show that the pressure spectra in negative yaw angles (-15°) possess the highest energy compared to the spectra in zero and positive yaw angles.

The corresponding normalised power spectral densities are shown in Figure 3.26 and in a magnified plot in Figure 3.27. All three spectra collapse onto one curve. However, a significant peak is noted at St = 9 where some variations in spectra are also evident (Figure 3.27).

3.4 Small Ellipsoidal Model

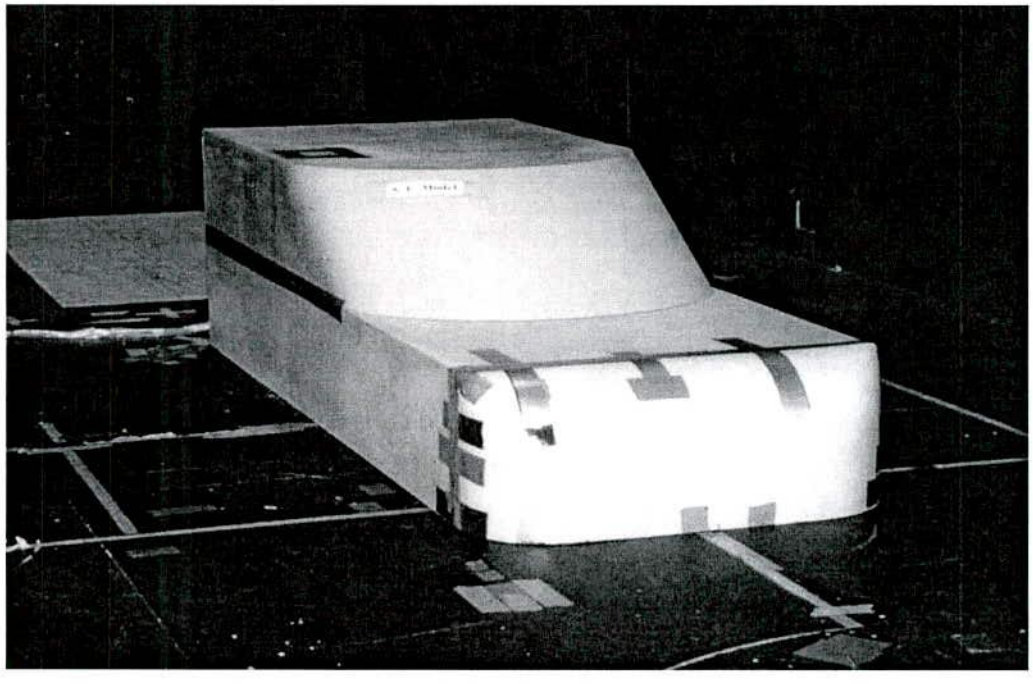

Figure 3.28: Small Ellipsoidal Model in the Test Section of RMIT Aeroacoustic Wind-Tunnel

3.4.1 Reynolds Number Effects

3.4.1.1 Surface Mean Pressure

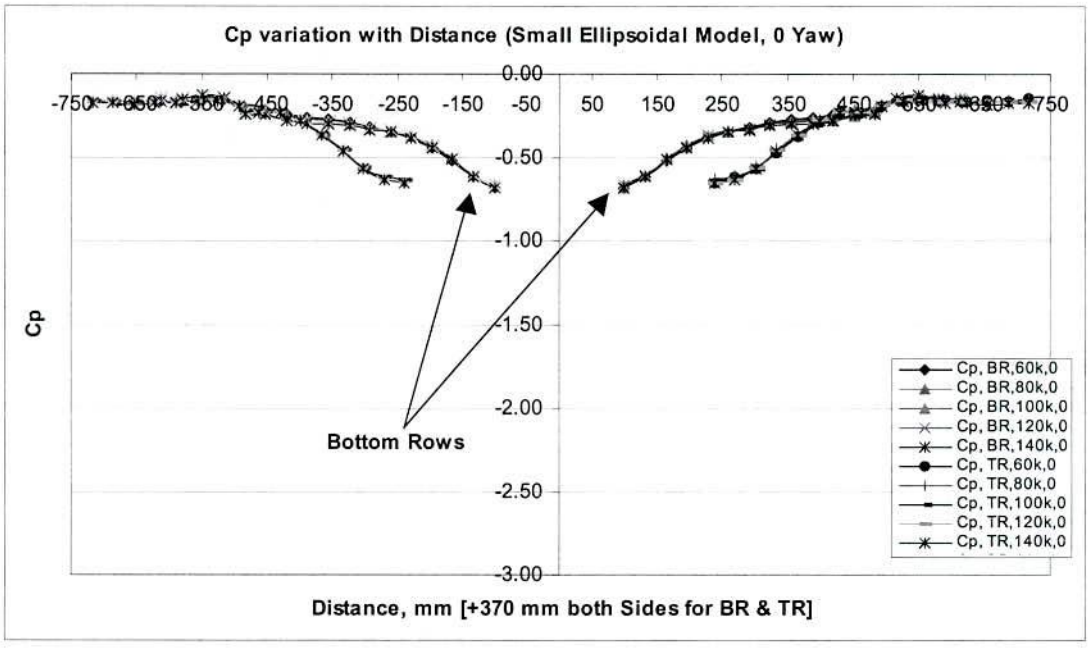

Figure 3.29: Surface Mean Cp Variations with Distance, Yaw = 0° (SE)

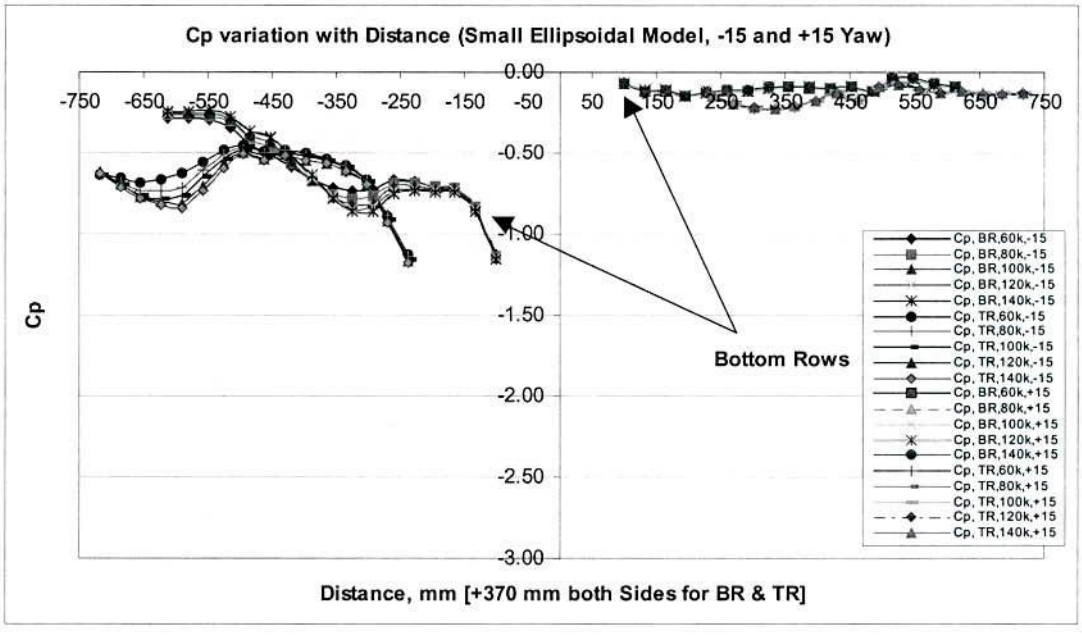

Figure 3.30: Surface Mean Cp Variations with Distance, Yaw = -15° and +15° (SE)

The surface mean pressure coefficient plots against distance are shown in Figure 3.29 and Figure 3.30. The Reynolds number has no significant effect on the surface mean pressure coefficients at zero and positive yaw angles (0° and +15°). However, Figure 3.30 shows that the mean Cp is dependent on the Reynolds number at negative yaw angles (-15°). Additionally, Figure 3.30 demonstrates that the surface mean pressure coefficients in both rows are Reynolds number dependent. The changes are noticeable between 60 and 100 km/h or higher.

3.4.1.2 Surface Fluctuating Pressure

The root mean squared fluctuating pressure coefficients are shown in Figure 3.31 and Figure 3.32. The rms Cp plots show that the fluctuating pressure coefficient does not vary much with the Reynolds number at zero and positive yaw angles. However, variations of Cp rms at negative yaw angles are evident (Figure 3.32).

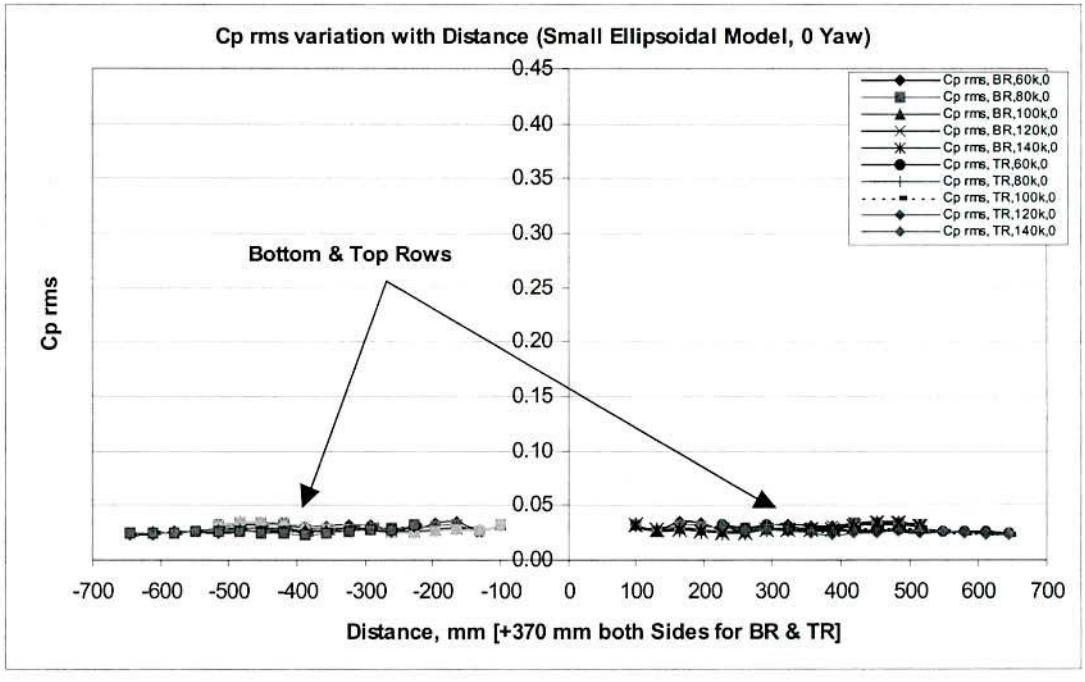

Figure 3.31: Fluctuating Cp rms Variations with Distance, Yaw = 0° (SE)

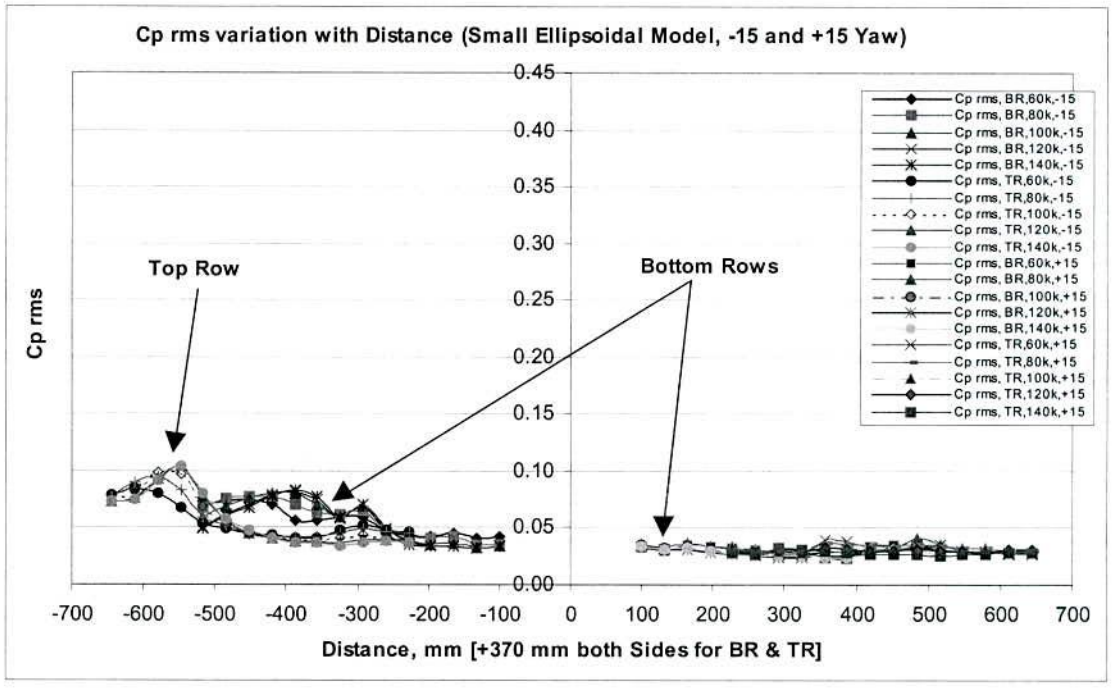

Figure 3.32: Fluctuating Cp rms Variations with Distance, Yaw = -15° and +15° (SE)

3.4.2 Effects of Yaw Angles on Surface Pressures

3.4.2.1 Surface Mean Pressure

The magnitude and size of surface mean pressure varies significantly with the yaw angles (Figure 3.29 and Figure 3.30). A complex flow pattern is evident at -15° yaw angles (Figure 3.30). The flow visualisation photograph (Figure 3.33) and Figure 3.30 show that the flow pattern is complex at the negative yaw angles. The presence of a small separated zone is also evident. At positive yaw angles (+15°), the flow separation virtually disappears and flow remains to be attached (Figure 3.30). The flow visualisation (Figure 3.33, Figure 3.34 and Figure 3.35) indicates no apparent flow separation at negative, zero and positive yaw angles.

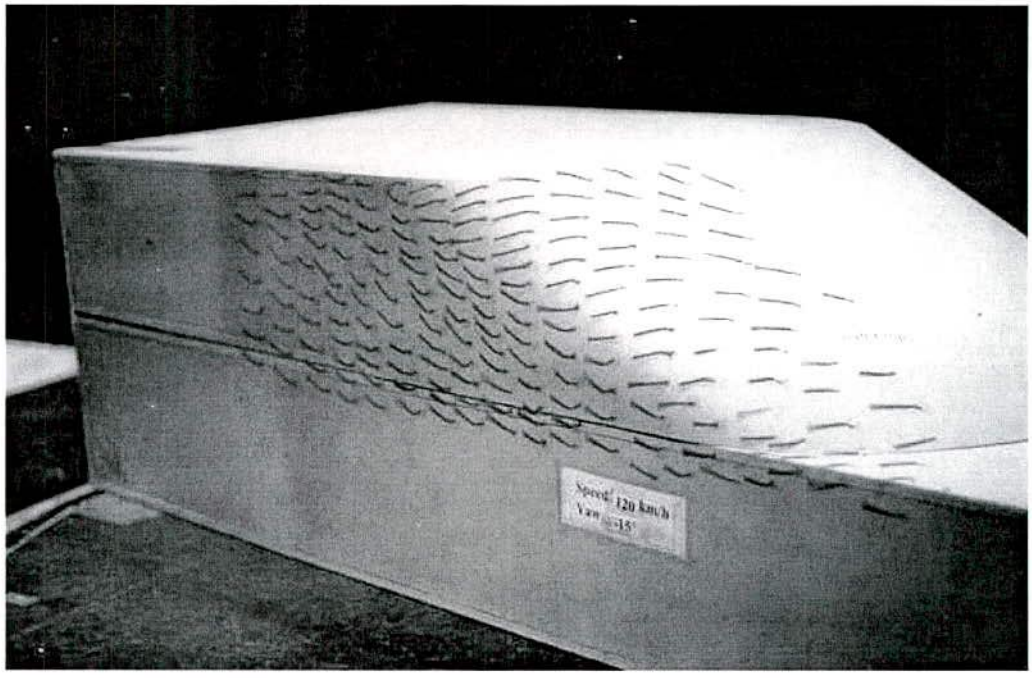

Figure 3.33: Side View of Wind-Tunnel Flow Visualisation, Speed = 120 km/h, Yaw = -15° (SE)

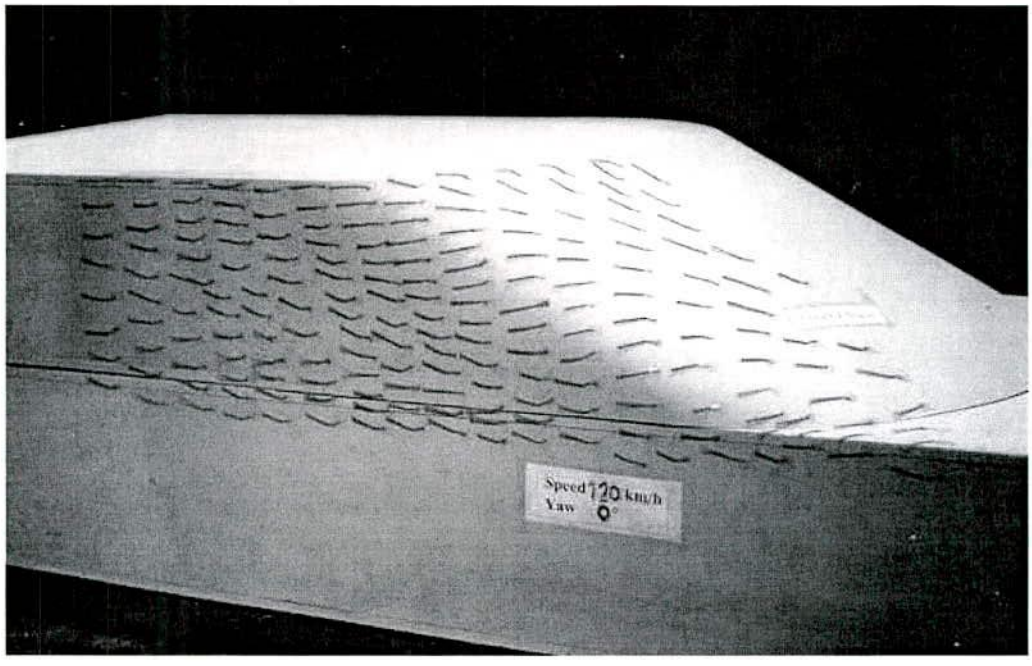

Figure 3.34: Side View of Wind-Tunnel Flow Visualisation, Speed = 120 km/h, Yaw = 0° (SE)

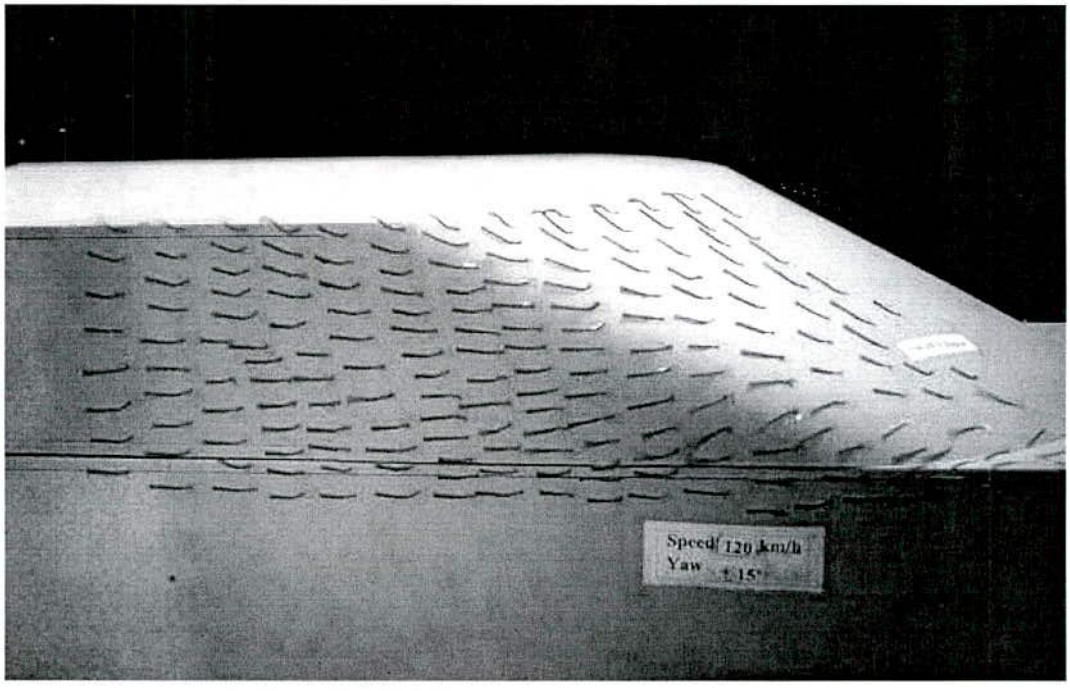

Figure 3.35: Side View of Wind-Tunnel Flow Visualisation, Speed = 120 km/h, Yaw = +15° (SE)

3.4.2.2 Surface Fluctuating Pressure

The magnitudes of the fluctuating pressure coefficients do not significantly vary at zero and positive yaw angles (Figure 3.31 and Figure 3.32). However, some variations are noted in the negative (-15°) yaw angles (Figure 3.32). A complex flow pattern is again evident at negative yaw angles, however it is not evident at zero and positive yaw angles. The flow visualisation photographs (Figure 3.34 and Figure 3.35) show no separation at positive and zero yaw angles. The flow visualisation does not show a clear picture of separations at negative yaw angles (Figure 3.33).

3.4.3 Spectral Analysis

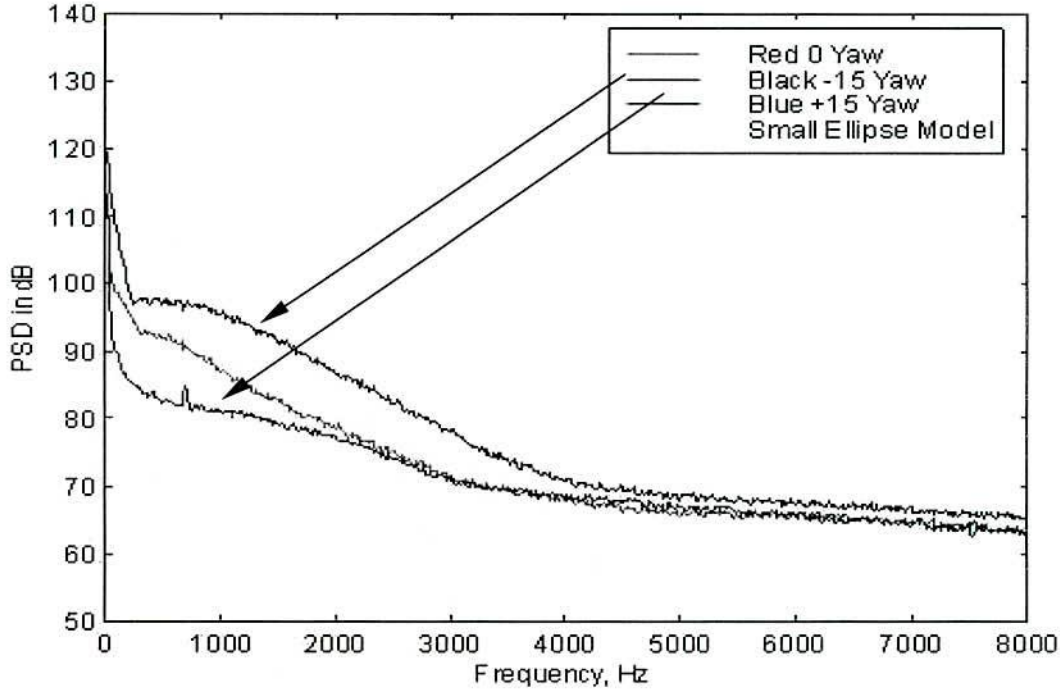

Figure 3.36: Power Spectra Plot of Peak Cp rms, Speed = 100 km/h, Yaw = 0°, -15° and +15° (SE)

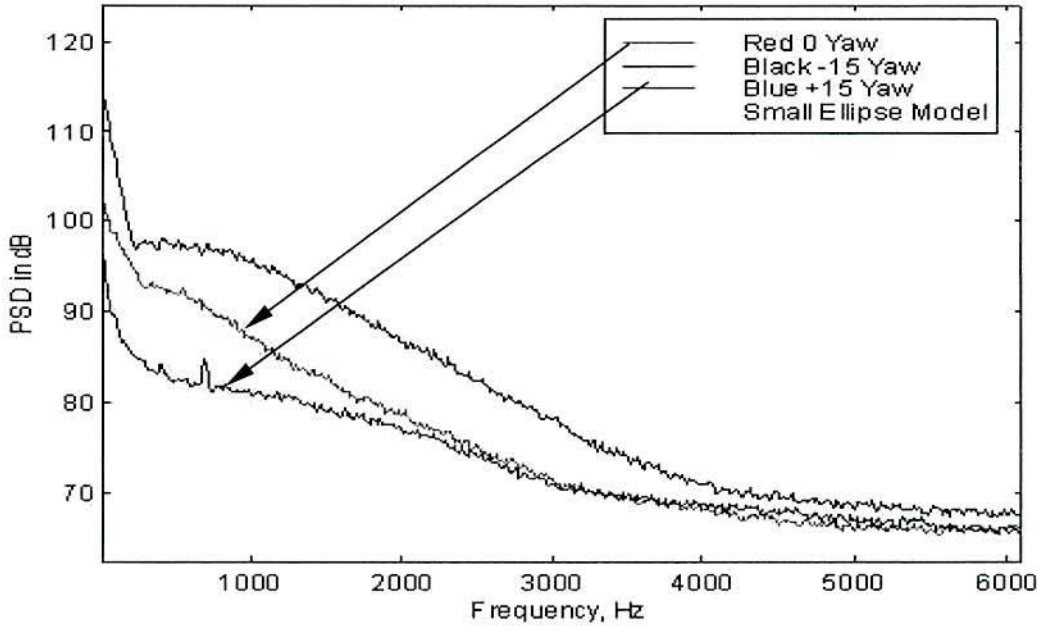

Figure 3.37: Magnified Power Spectra Plot of Peak Cp rms (Figure 3.36)

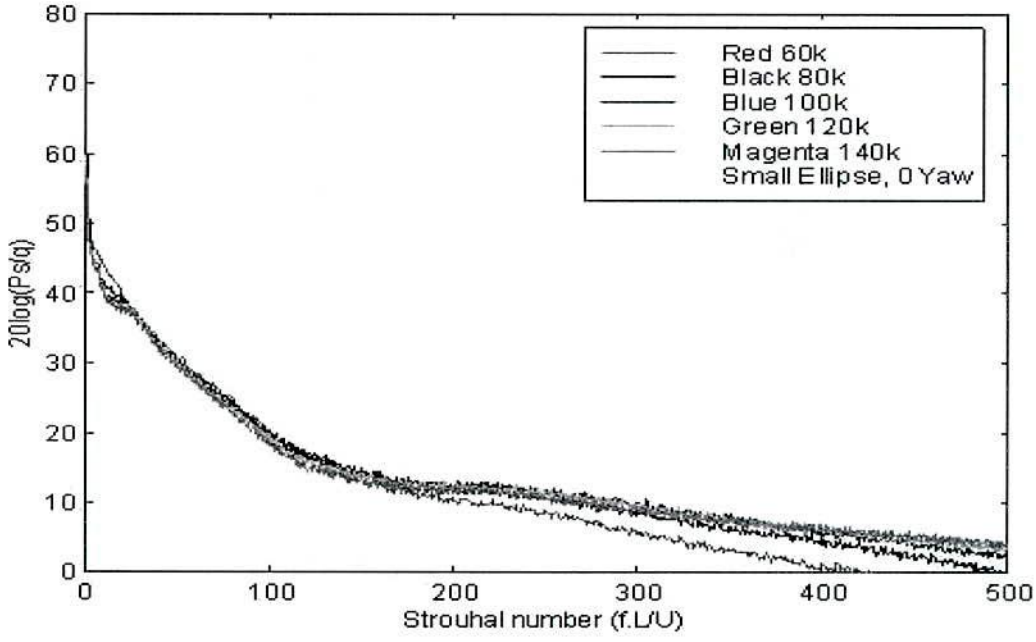

Figure 3.38: Normalised Spectra Plot of Peak Cp rms, Yaw = 0° (SE)

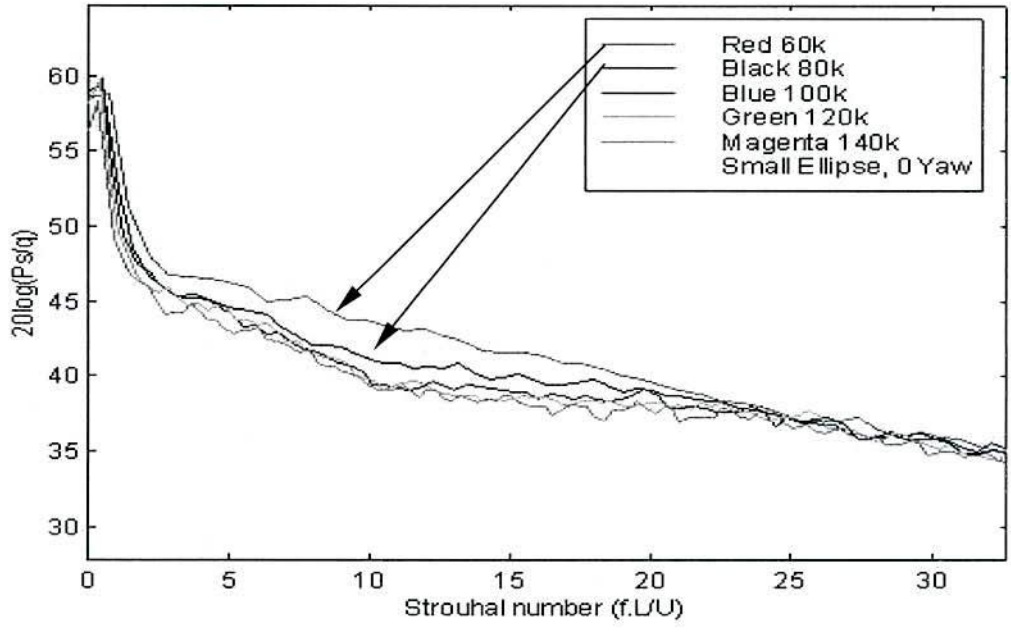

Figure 3.39: Magnified Power Spectra Plot of Peak Cp rms (Figure 3.38)

The spectrum of the fluctuating pressure for negative 15° yaw angles possesses the highest energy when compared to zero and positive yaw angles. At zero yaw angles, fluctuating pressure spectra possess higher energy than the spectra at positive yaw

angles in the frequency range below 3000 Hz. At positive yaw angles, a peak is noted in around 700 Hz (Figure 3.37). The reason for this peak is not clear. The effects of yaw angles on the spectral energy contents are significant and these are especially evident in the frequency range less than 1000 Hz (Figure 3.36 and Figure 3.37).

The normalised power spectra of peak fluctuating pressures at zero yaw angles are shown in Figure 3.38 and Figure 3.39. The spectra of all five speeds (60, 80, 100, 120 and 140 km/h) show a single curve between St = 24 and St = 180. However, a significant variation is noted between the lower and higher Reynolds numbers (especially between 60 km/h and 140 km/h) in areas where the Strouhal number is greater than 180 and less than 24. Figure 3.39 shows a slight variation with Reynolds numbers in the magnified zone with a Strouhal number less than 24.

3.5 Circular Model

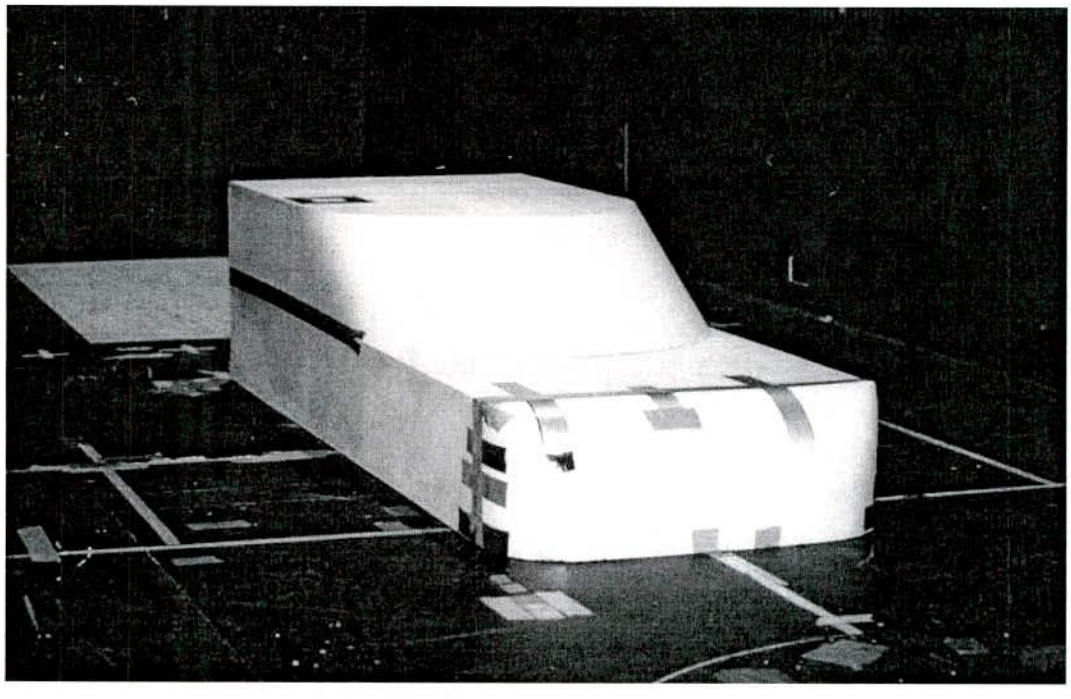

Figure 3.40: A Circular Model in the Test Section of RMIT Aeroacoustic Wind-Tunnel

3.5.1 Reynolds Number Effects

3.5.1.1 Surface Mean Pressure

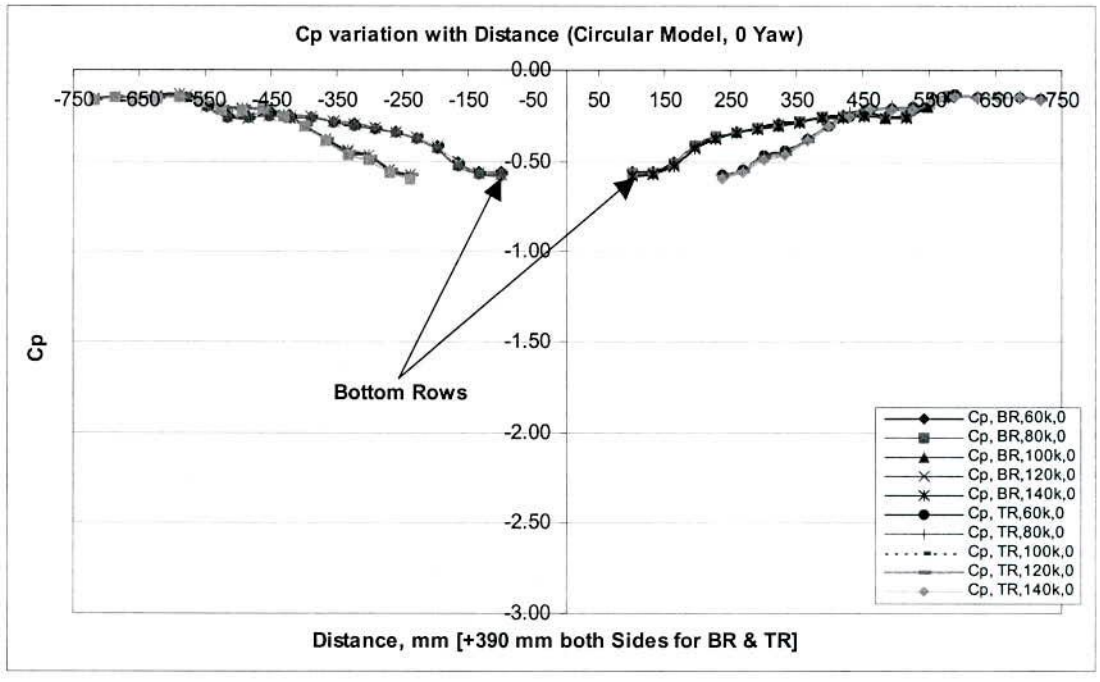

Figure 3.41: Surface Mean Cp Variations with Distance, Yaw = 0° (C)

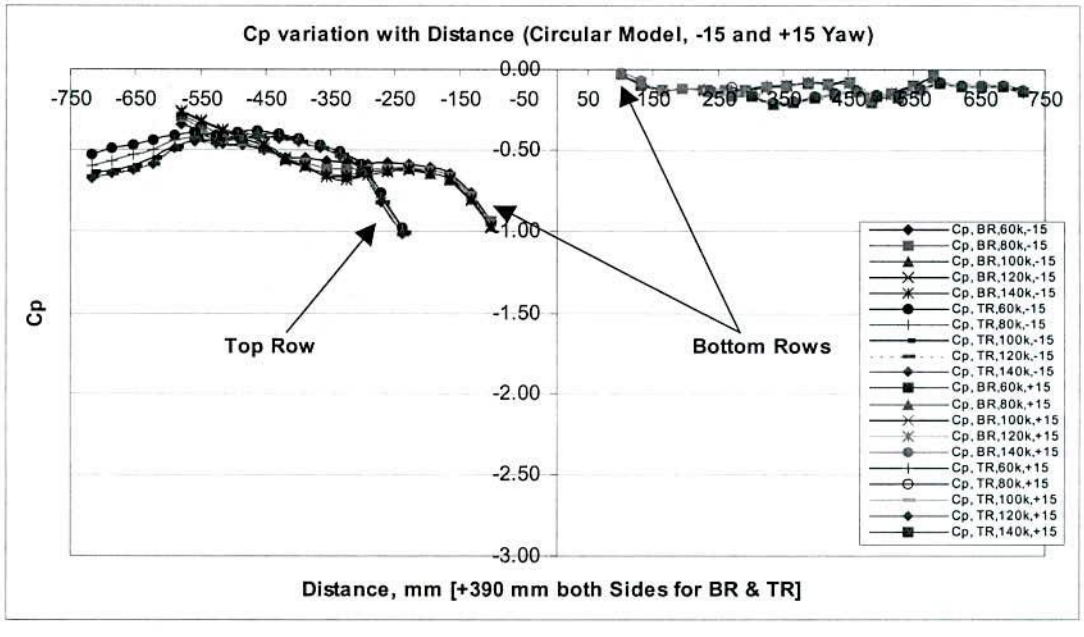

Figure 3.42: Surface Mean Cp Variations with Distance, Yaw = -15° and +15° (C)

Figure 3.41 and Figure 3.42 present the plots of mean Cp against distance. Figure 3.41 shows that the surface mean pressure coefficients for the circular model remain unchanged with the Reynolds number at zero yaw angle. However, a variation of surface mean pressure coefficients with Reynolds numbers is evident in the negative yaw angles for both top and bottom rows (Figure 3.42). The surface mean pressure coefficient remains reasonably independent of Reynolds numbers at positive yaw angles (Figure 3.42). The general trend for the surface mean pressure coefficients is similar to the small ellipsoidal model.

3.5.1.2 Surface Fluctuating Pressure

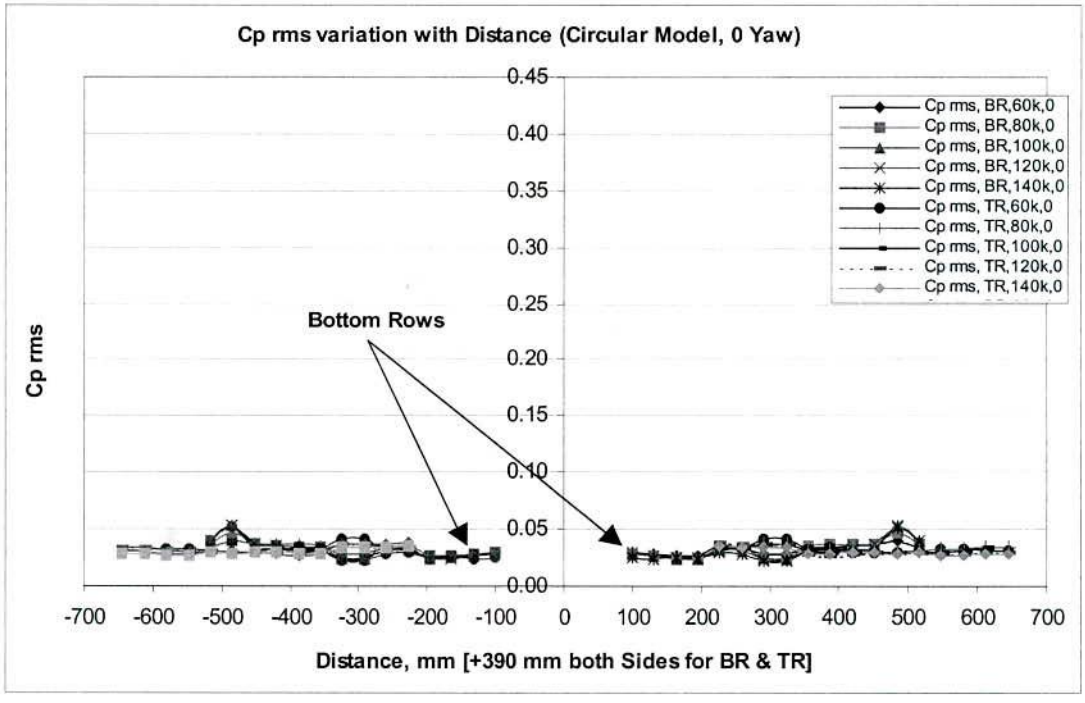

Figure 3.43: Fluctuating Cp rms Variations with Distance, Yaw = 0° (C)

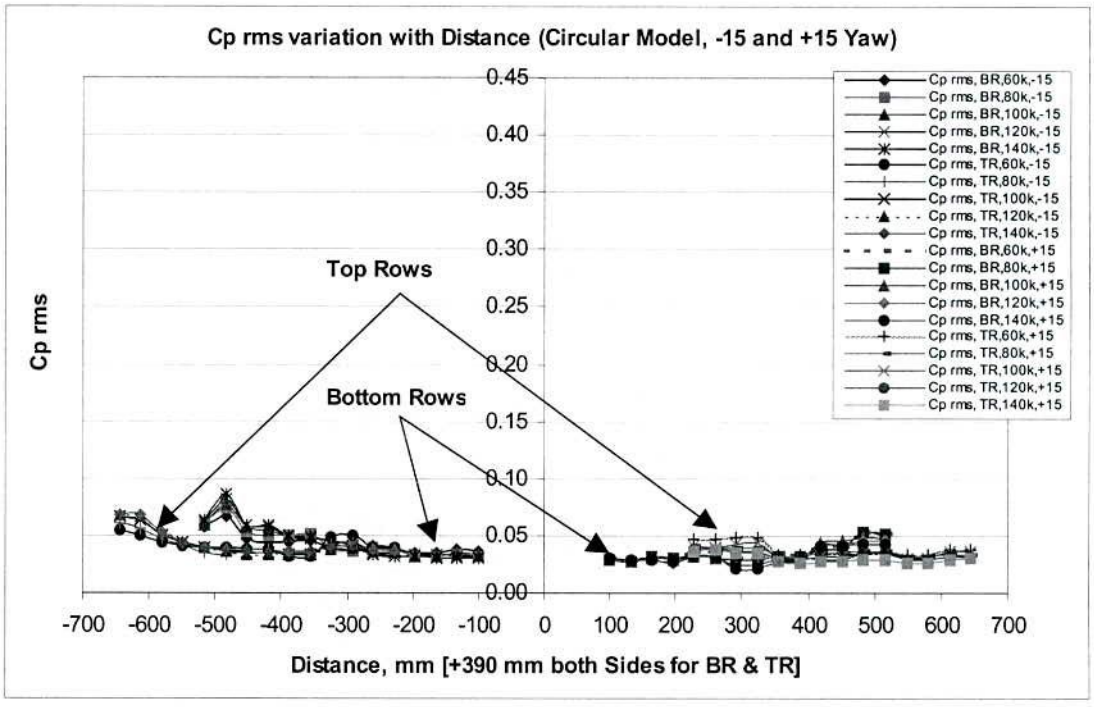

Figure 3.44: Fluctuating Cp rms Variations with Distance, Yaw = -15° and +15° (C)

The fluctuating pressure coefficient plots (Figure 3.43 and Figure 3.44) show some variations of Cp rms with Reynolds numbers at all yaw angles. However, the magnitude of variation is smaller at zero yaw angle (Figure 3.43). The dependency of Cp on Reynolds numbers is mostly evident between the higher and lower Reynolds numbers (60 km/h and 100 km/h and higher) at all yaw angles. These minor Reynolds numbers' sensitivities are evident for both top and bottom rows. A peak is noted at negative yaw angles for the bottom row, which is believed to be due to microphone's incorrect positioning (not completely flush with the model surface).

3.5.2 Effects of Yaw Angles on Surface Pressures

3.5.2.1 Surface Mean Pressure

The yaw angle has a notable effect on the magnitude of surface mean pressure coefficients (Figure 3.41 and Figure 3.42). At large negative yaw angles (-15°), a relatively less complex flow pattern is evident compared to the small ellipsoidal model (Figure 3.42). However, at zero and positive yaw angles (0° and +15°) the flow remains attached and the magnitude of the surface mean pressure is smaller compared to the small ellipsoidal model (Figure 3.41 and Figure 3.42).

The flow visualisation (Figure 3.46 and Figure 3.47) shows that the flow is attached along the side window and no separation is evident for the positive and zero yaw angles. However, the general flow pattern from the flow visualisation photographs (Figure 3.45) for the negative yaw angles shows a minor variation compared to the positive and zero yaw angles. The maximum negative magnitudes of pressure coefficients for this model were found to be 1.0, 0.59 and 0.21 at negative, zero and positive yaw angles (-15°, 0° and +15°) respectively.

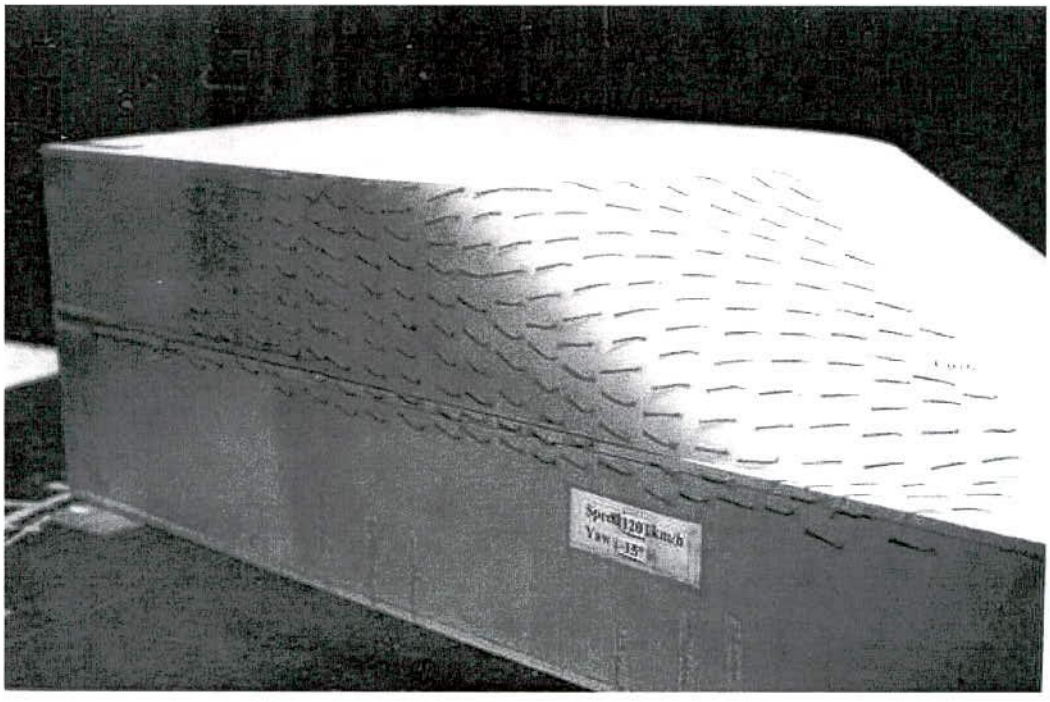

Figure 3.45: Side View of Wind-Tunnel Flow Visualisation, 120 km/h, Yaw = -15°

(C)

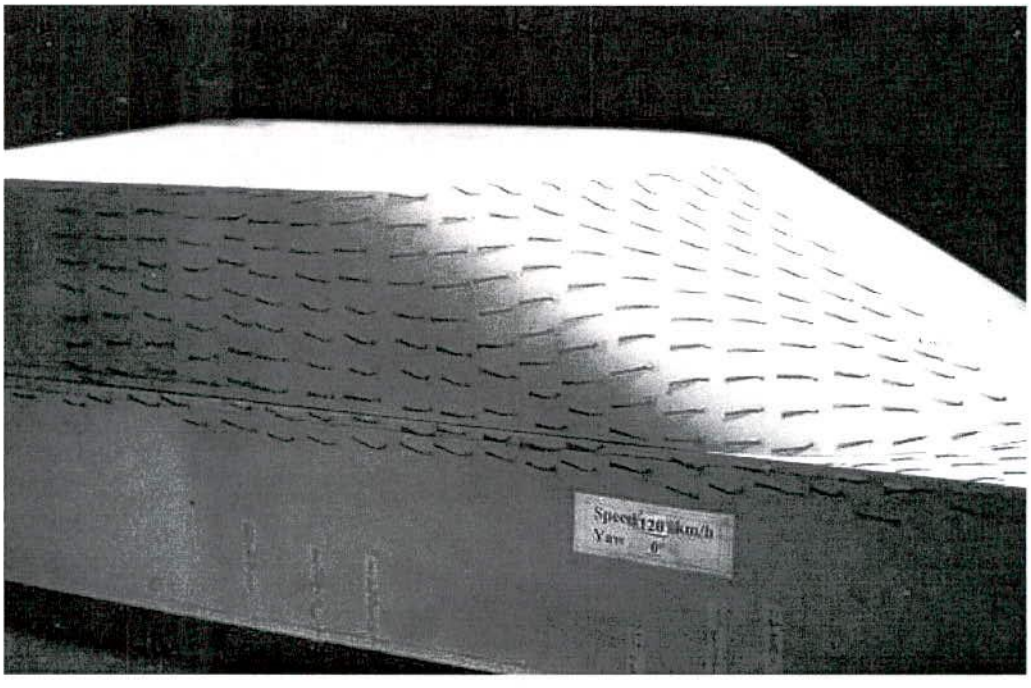

Figure 3.46: Side View of Wind-Tunnel Flow Visualisation, 120 km/h, Yaw = 0°

(C)

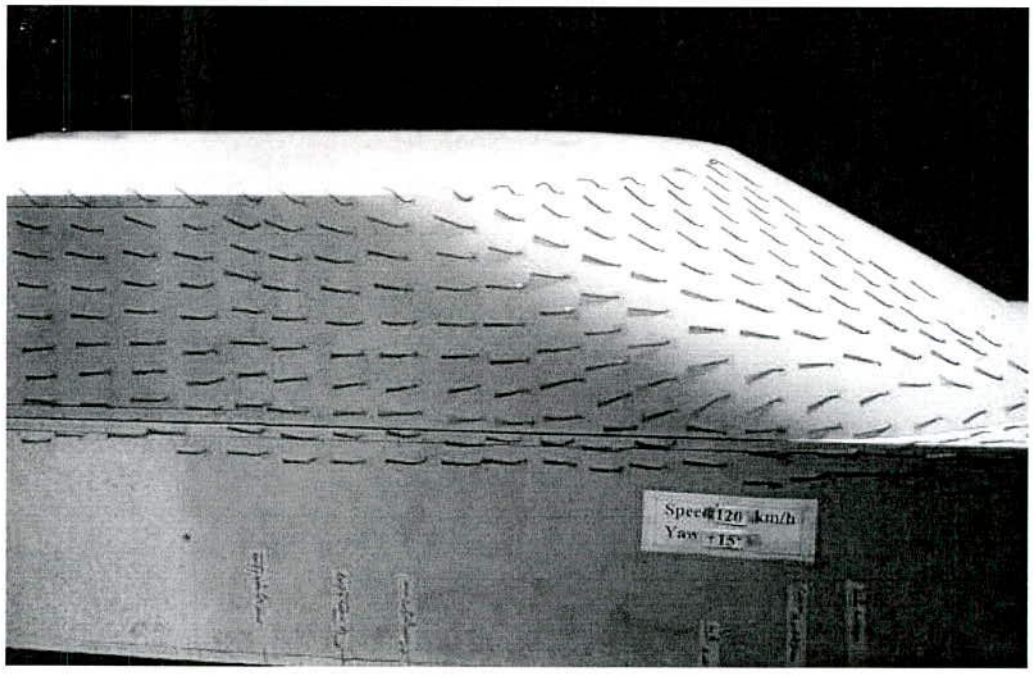

Figure 3.47: Side View of Wind-Tunnel Flow Visualisation, 120 km/h, Yaw = +15° (C)

3.5.2.2 Surface Fluctuating Pressure

The yaw angle has a minor effect on the variation of the fluctuating pressure coefficients in the positive (+15°) and zero yaw angles (Figure 3.43 and Figure 3.44). Compared to the positive and zero yaw angles, a small variation of fluctuating pressure coefficients is evident in the negative (-15°) yaw angles (Figure 3.44). The maximum magnitudes of the fluctuating pressure coefficients computed for the circular model were 0.08, 0.05 and 0.04 at negative, zero and positive yaw angles respectively.

3.5.3 Spectral Analysis

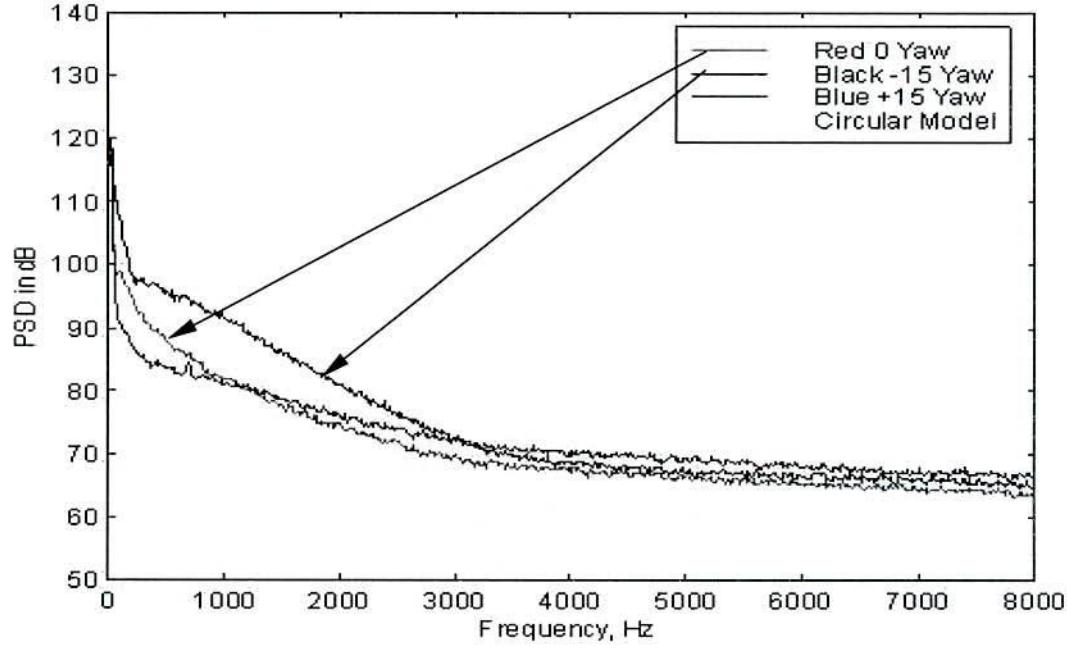

Figure 3.48: Power Spectra Plot of Peak Cp rms, Speed = 100 km/h, Yaw = 0°, -15° and +15° (C)

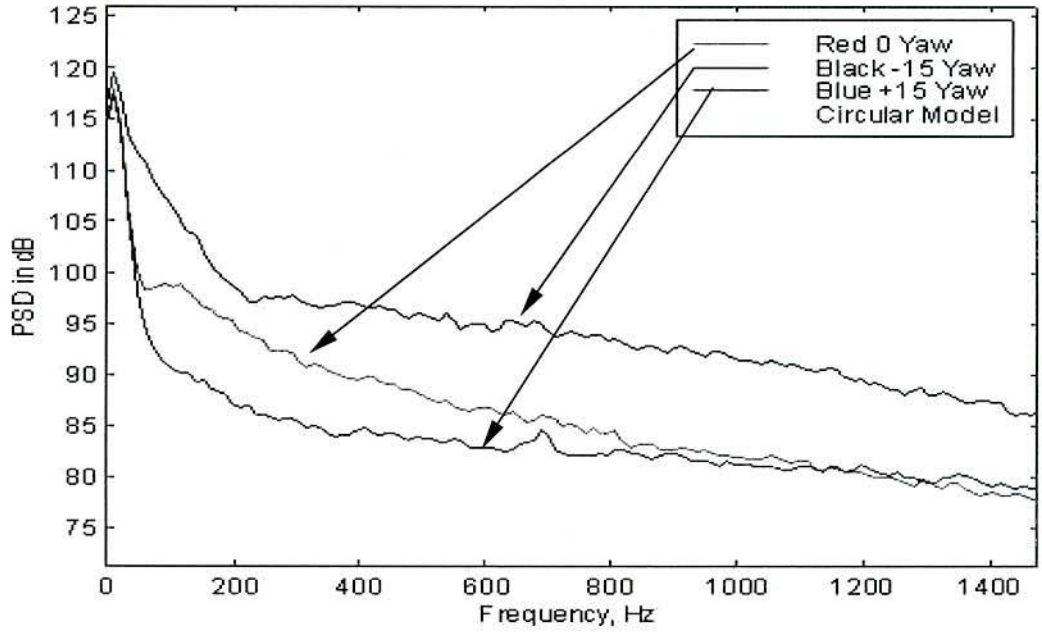

Figure 3.49: Magnified Power Spectra Plot of Peak Cp rms (Figure 3.48)

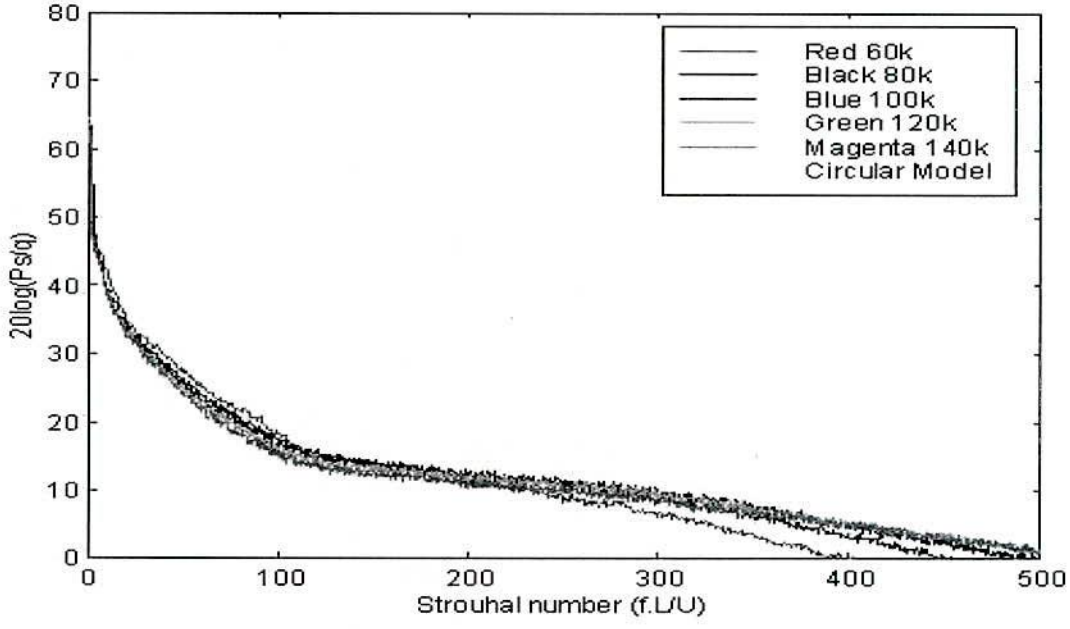

Figure 3.50: Normalised Spectra Plot of Peak Cp rms, Yaw = 0° (C)

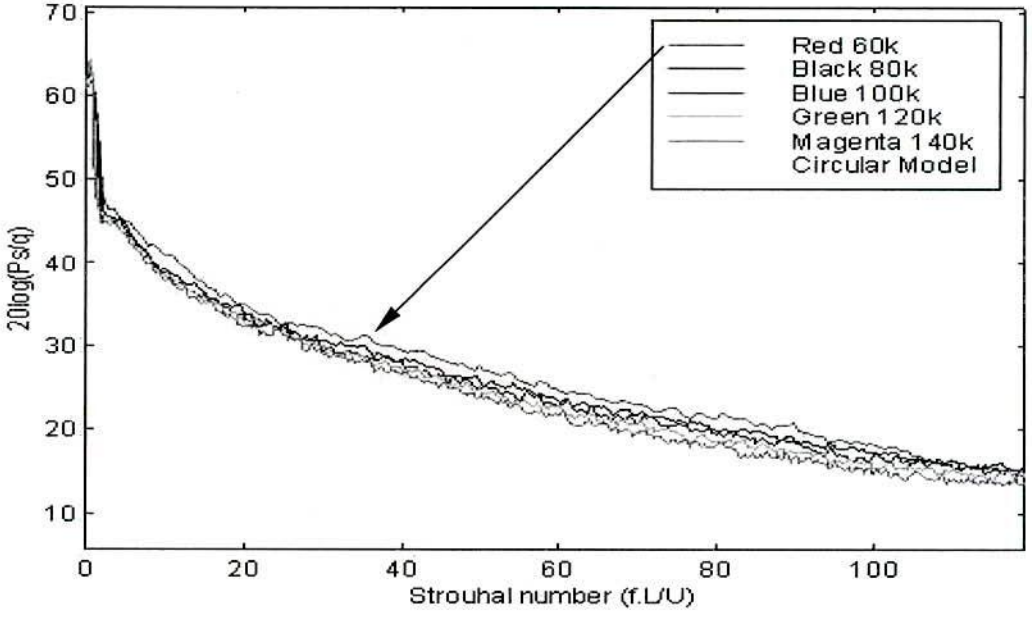

Figure 3.51: Magnified Normalised Spectra Plot of Peak Cp rms, Yaw = 0° (Figure 3.50)

Figure 3.48 and Figure 3.49 show that the fluctuating pressure in the negative yaw angles (-15°) is significant compared to zero and positive yaw angles. At positive yaw angles, a small peak is noted close to 700 Hz (Figure 3.49). Most spectral energy remains for all yaw angles below 200 Hz.

The normalised power spectra of highest fluctuating pressures have almost collapsed onto a single curve up to the Strouhal number 250 (Figure 3.50 and Figure 3.51). The magnified plot (Figure 3.51) shows only slight variations between the lower Reynolds number (60 km/h) and higher Reynolds numbers (100, 120and 140 km/h at a Strouhal number less than 100 (Figure 3.51).

3.6 Large Ellipsoidal Model

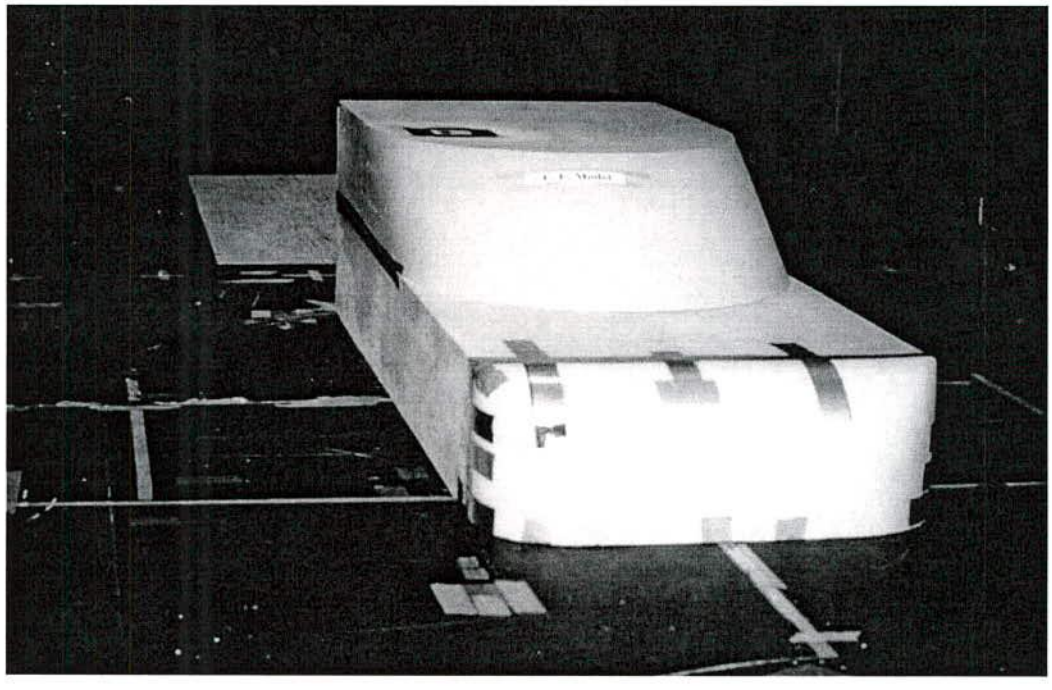

Figure 3.52: A Large Ellipsoidal Model in the Test Section of RMIT Aeroacoustic Wind-Tunnel

3.6.1 Reynolds Number Effects

3.6.1.1 Surface Mean Pressure

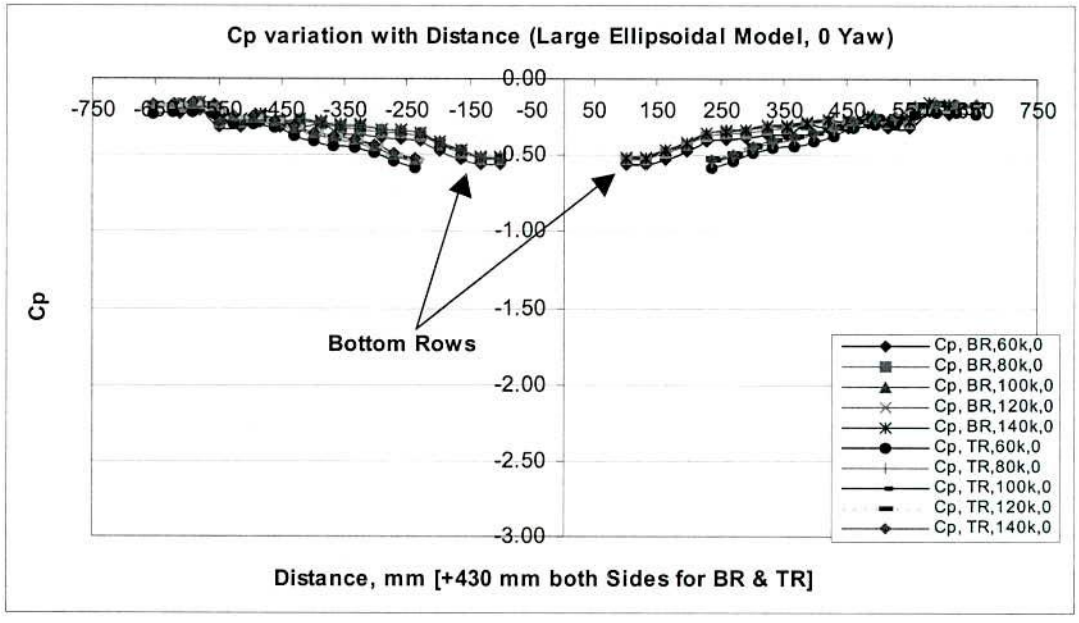

Figure 3.53: Surface Mean Cp Variations with Distance, Yaw = 0° (LE)

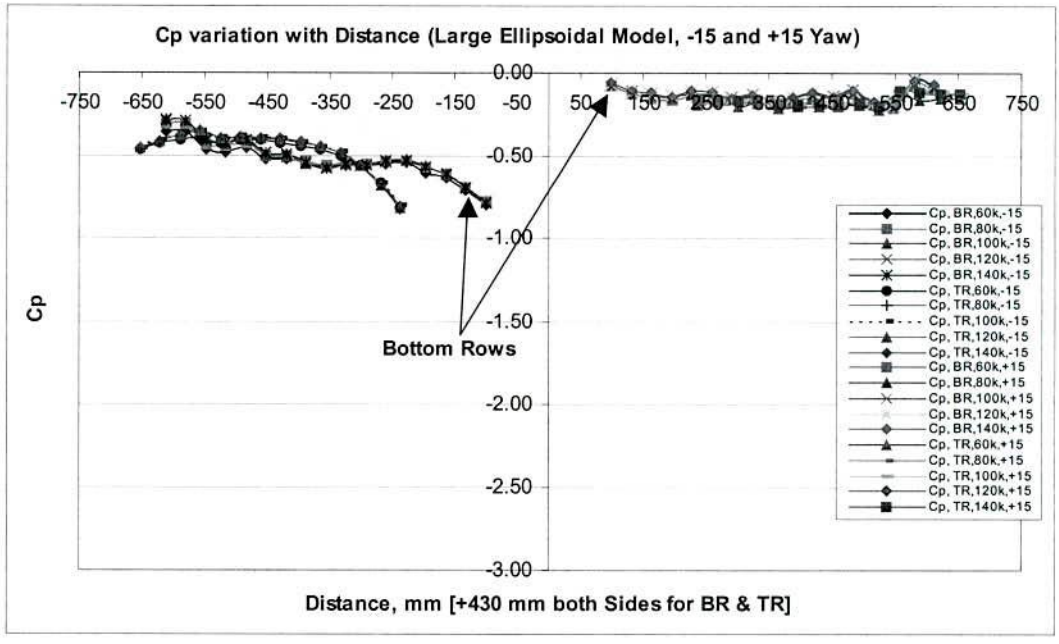

Figure 3.54: Surface Mean Cp Variations with Distance, Yaw = -15° and +15° (LE)

The surface mean pressure coefficient distributions in the negative, zero and positive yaw angles (-15°, 0 and + 15°) are shown in Figure 3.53 and Figure 3.54. The mean Cp shows only slight dependence on the Reynolds number at zero yaw angles. The Reynolds number variations with mean Cp are not evident at negative and positive yaw angles except for some very minor variations.

3.6.1.2 Surface Fluctuating Pressure

Figure 3.55 and Figure 3.56 are the plots of fluctuating pressure coefficients against distance for the large ellipsoidal model. The Cp rms plots show that the fluctuating pressure coefficients are only slightly dependent on the Reynolds number in the negative and zero yaw angles and almost no variation is evident in the positive yaw angles (Figure 3.55 and Figure 3.56). These variations are dominant between the lower (60 km/h) and higher Reynolds number (80 km/h and higher).

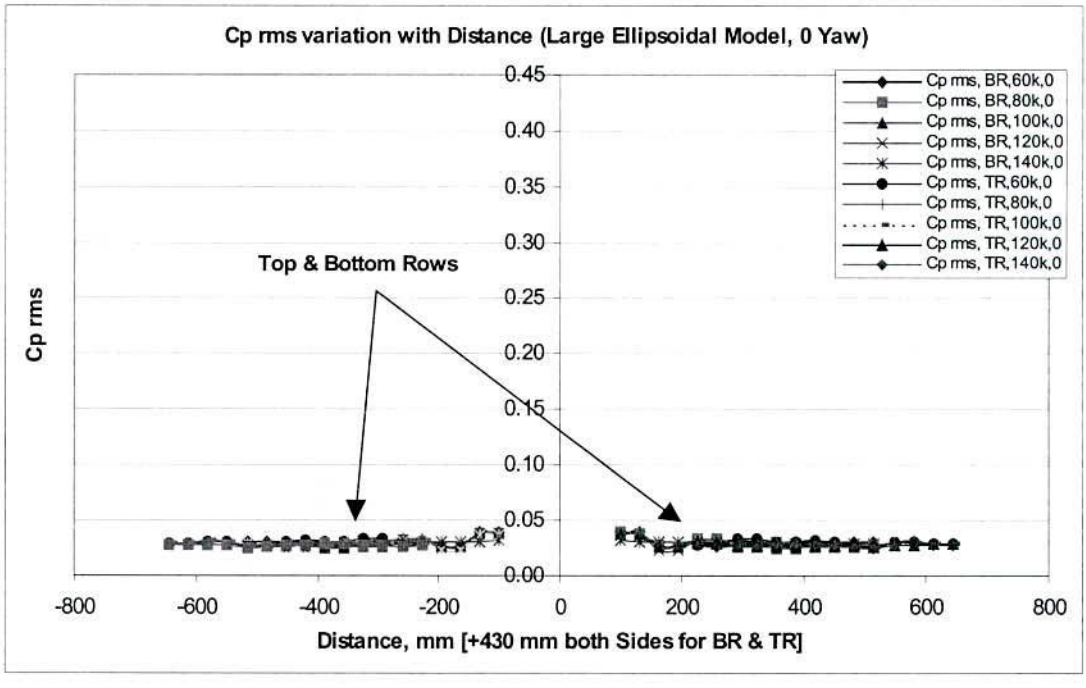

Figure 3.55: Fluctuating Cp rms Variations with Distance, Yaw = 0° (LE)

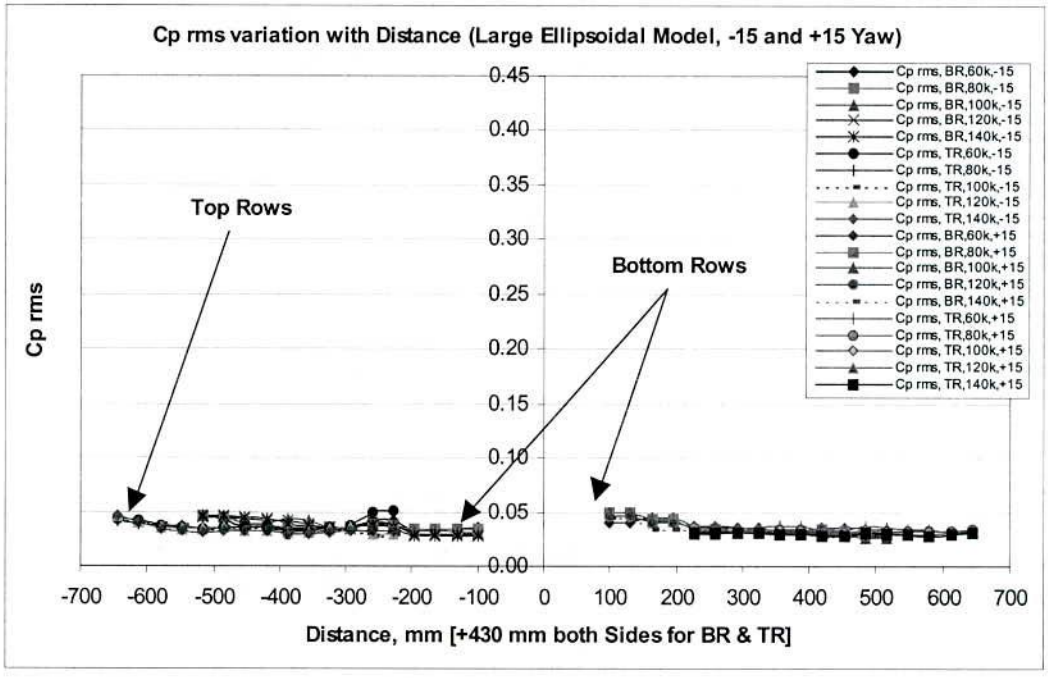

Figure 3.56: Fluctuating Cp rms Variations with Distance, Yaw = -15° and +15° (LE)

3.6.2 Effects of Yaw Angles on Surface Pressures

3.6.2.1 Surface Mean Pressure

The shape and size of the surface pressure coefficient plots are similar to the plots for the circular model. The maximum negative magnitude of mean pressure coefficients measured for the large ellipsoidal model were 0.82, 0.53 and 0.20 in negative, zero and positive yaw angles (-15°, 0° and +15°) respectively. The photographs of flow visualisation (Figure 3.57, Figure 3.58 and Figure 3.59) show that the flow is attached in all yaw angles.

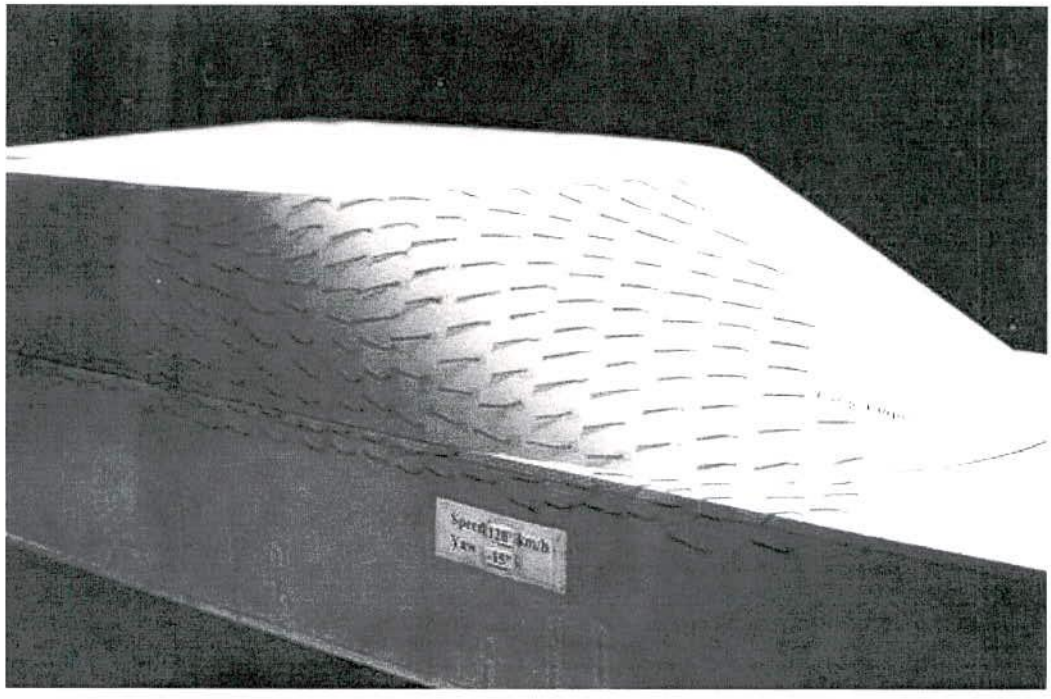

Figure 3.57: Side View of Wind-Tunnel Flow Visualisation, 120 km/h, Yaw = -15° (LE)

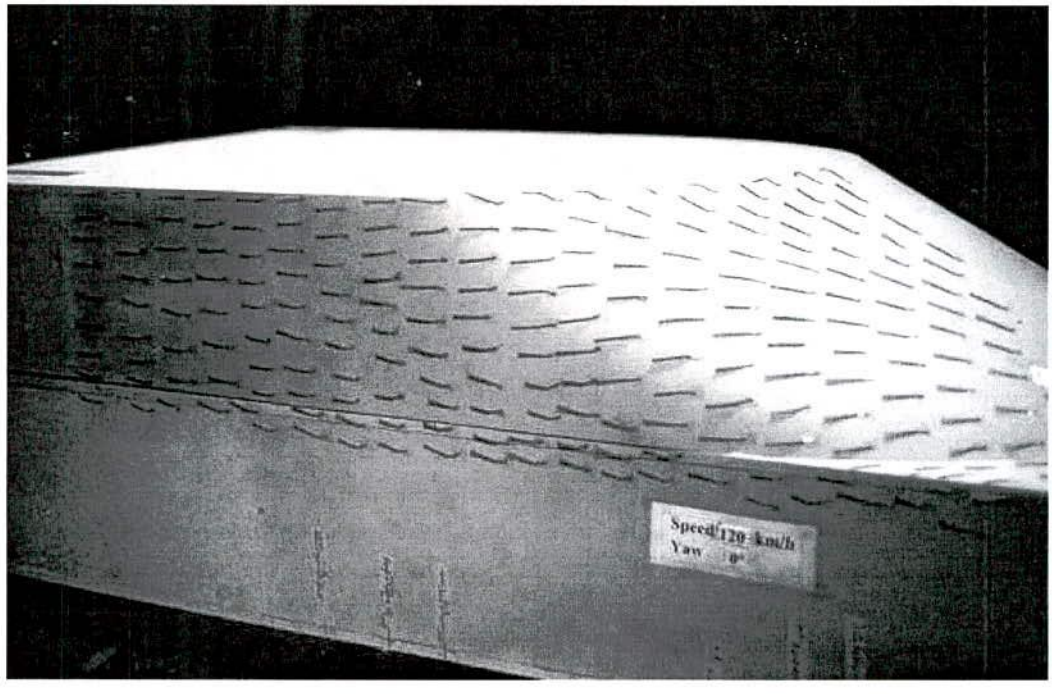

Figure 3.58: Side View of Wind-Tunnel Flow Visualisation, 120 km/h, Yaw = 0° (LE)

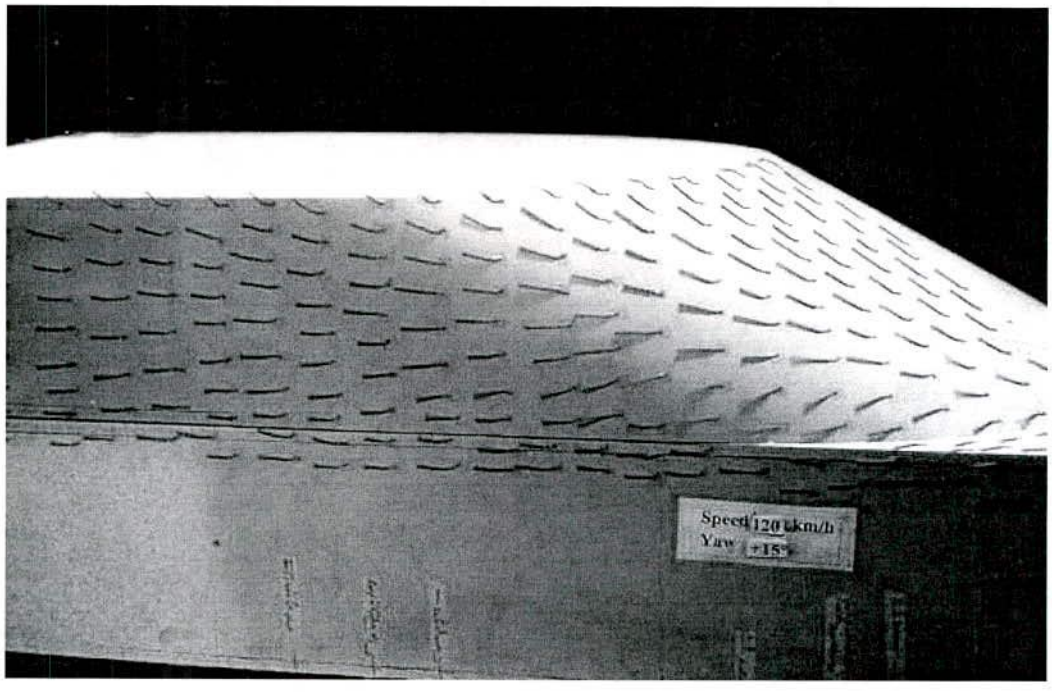

Figure 3.59: Side View of Wind-Tunnel Flow Visualisation, 120 km/h, Yaw = +15° (LE)

3.6.2.2 Fluctuating Pressure

No significant variation of the fluctuating pressure coefficient with yaw angles, particularly between the positive (+15°) and zero yaw angles, is noted. However, the magnitudes of the fluctuating pressure coefficients are slightly higher in the negative yaw angles (Figure 3.56). The maximum magnitudes of the fluctuating pressure coefficients calculated for this model are similar (0.046, 0.040 and 0.045) in negative, zero and positive yaw angles (-15°, 0° and +15°) respectively.

3.6.3 Spectral Analysis

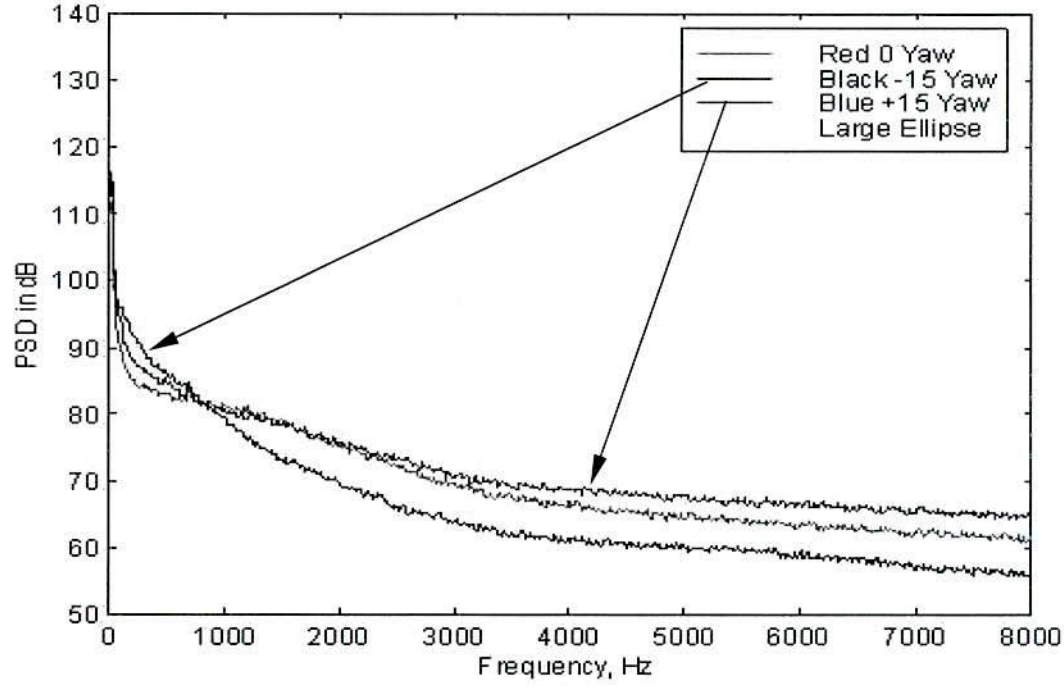

Figure 3.60: Power Spectra Plot of Peak Cp rms, Speed = 100 km/h, Yaw = 0°, -15° and +15° (LE)

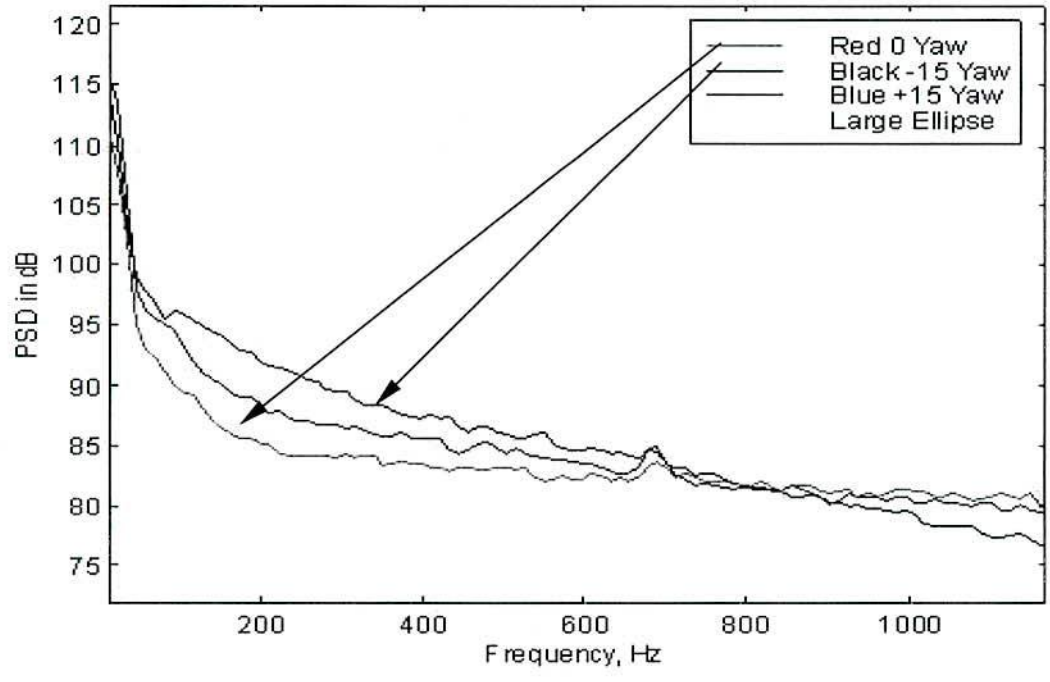

Figure 3.61: Magnified Power Spectra Plot of Peak Cp rms (Figure 3.60)

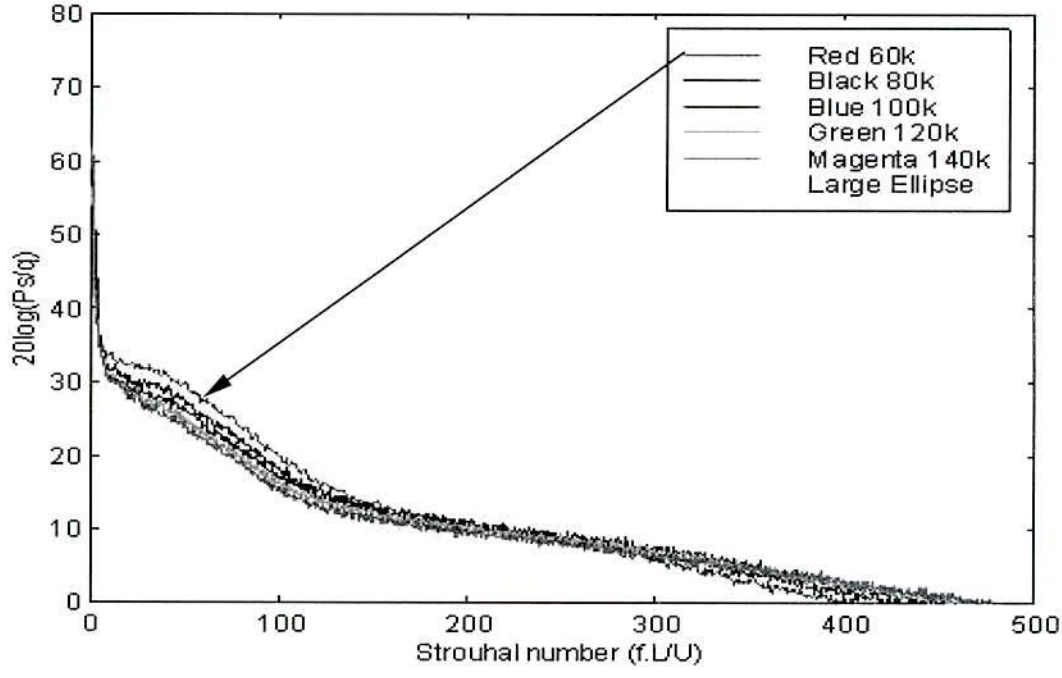

Figure 3.62: Normalised Spectra Plot of Peak Cp rms, Yaw = 0° (LE)

The magnitude of fluctuating pressure energy varies with yaw angles (Figure 3.60 and Figure 3.61). The spectral energy at all yaw angles is mainly concentrated in frequencies between 100 and 800 Hz. However, maximum energy is evident in frequencies close to 100 Hz. The spectrum of the fluctuating pressure at negative yaw angles (15°) possesses higher spectral energy compared to the pressure spectra in zero and positive yaw angles (0° and +15°) in frequencies below 800 Hz. At zero and positive yaw angles, a peak is noted close to 700 Hz (Figure 3.61). The reason for this peak was not clear and it is interesting to note that this peak was evident for the case of the circular model at +15° yaw angle. The effects of yaw angles on the spectral energy contents are significant and these are especially evident in the frequencies below 800 Hz.

The normalised power spectra for all five speeds are shown in Figure 3.62. The spectra for all Reynolds numbers collapse onto a single curve between St = 170 and St = 300. However, a significant variation is noted between the lower and higher Reynolds numbers (especially between 60, 80 km/h and 140 km/h) in areas where the Strouhal number is greater than 300 and less than 170 (Figure 3.62).

3.7 Effects of Geometry (Generic Shape)

The surface pressure fluctuations generated by the A-pillar vortex are greatly influenced by the size and strength of the vortex and the fluctuations are shown to be influenced by yaw angle and the A-pillar geometry. The relatively small influence of Reynolds numbers on the mean and fluctuating pressures has already been discussed. Therefore, in these subsections the effects of shape (geometry) on the surface fluctuating pressures for the bottom row are presented. The reason for selecting the bottom row is that the maximum fluctuating pressure was measured in the bottom row for all models. The plots of fluctuating pressure are presented here for one Reynolds number corresponding to a tunnel speed of 100 km/h.

3.7.1 Effects of Shape on Fluctuating Pressures

(Bottom Row, 100 km/h)

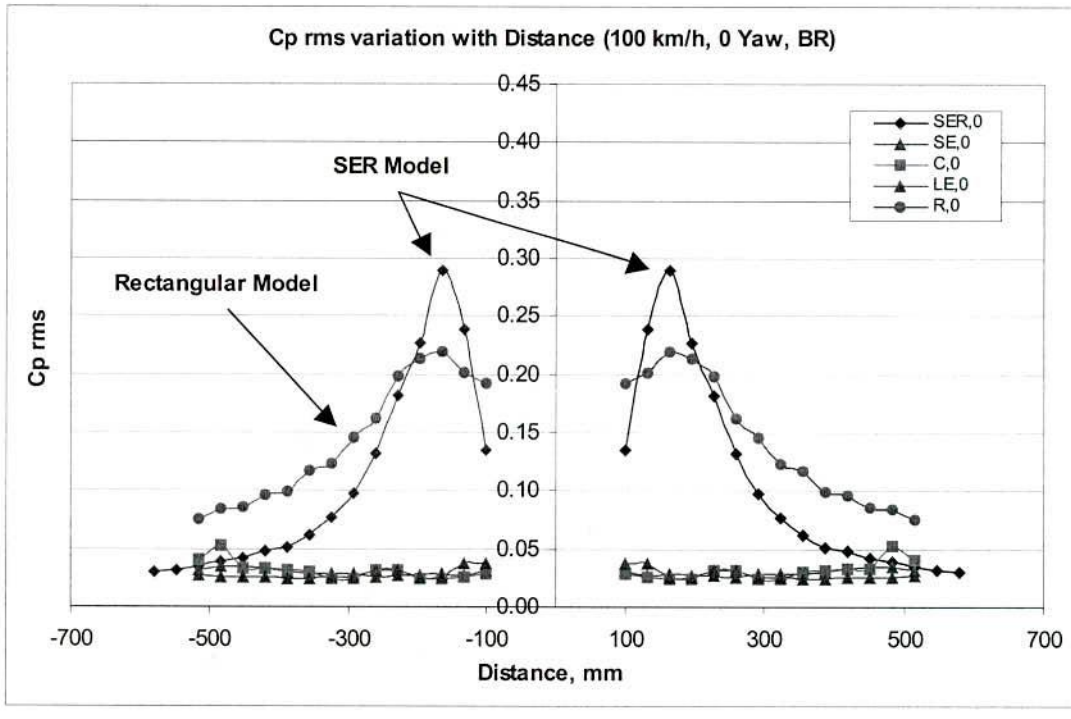

Figure 3.63: Fluctuating Cp rms Variations with Distance, Yaw = 0° (All Models)

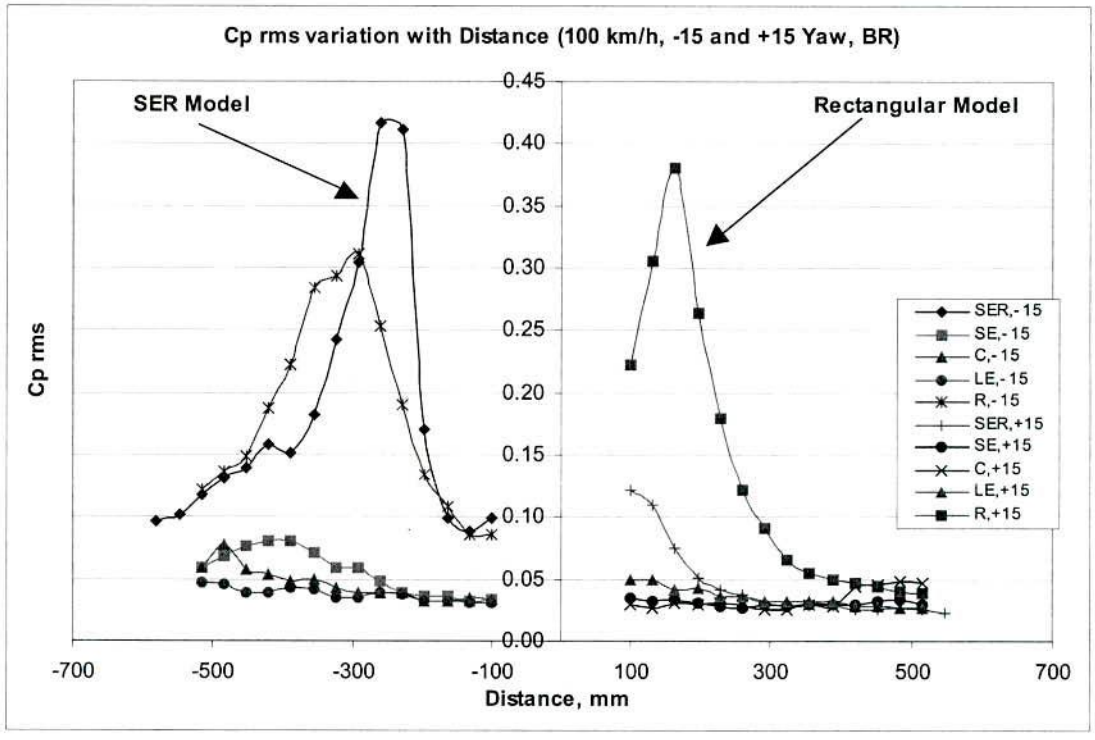

Figure 3.64: Fluctuating Cp rms Variations with Distance, Yaw = -15° and +15° (All Models)

The fluctuating pressure coefficients for zero yaw angles are presented in Figure 3.63 and the negative and positive yaw angle (-15° and +15°) data are shown in Figure 3.64.

For zero yaw angles the slanted sharp-edged model has the highest Cp rms (0.28) and the rectangular model has the second highest value of Cp rms (0.22). Compared to slanted sharp-edged and rectangular models, the small ellipsoidal, circular and large ellipsoidal models have relatively low peak values of Cp rms. However, the value of the Cp rms of the large ellipsoidal model is greater initially than the Cp rms values of small ellipsoidal and circular models and then decreases along the side window. No significant difference between the Cp rms values of the circular and small ellipsoidal models is evident at zero yaw angles in Figure 3.63. The rectangular model has the largest area of separated zone compared to the slanted sharp-edged model at zero yaw angles. However, the highest magnitude of fluctuating pressures was found for the slanted sharp-edged model at zero yaw angles.

Figure 3.64 shows that the magnitude of the fluctuating pressure varies significantly with yaw angles (-15° and +15°). In negative yaw angles, the slanted sharp-edged model has the largest Cp rms value compared to the rectangular model, however in positive yaw angles the rectangular model has the highest value of Cp rms (approximately 3 times).

In the negative yaw angle (-15°) the largest value of Cp rms of the large ellipsoidal model is almost 9 times smaller compared to the largest value of Cp rms of the slanted sharp-edged model. Similarly, the largest values of the circular model and small ellipsoidal model are 5.4 and 4.3 times smaller compared to the largest Cp rms of the slanted sharp-edged model.

At positive yaw angles (+15°), the maximum magnitude of Cp rms was 0.38 for the rectangular model compared 0.12 for the slanted sharp-edged model. The fluctuating pressure coefficient of the large ellipsoidal model is initially larger compared to the Cp rms of the small ellipsoidal and circular models. The reason for this behaviour is not known.

3.7.2 Effects of A-pillar and Windshield Curvatures on Fluctuating Pressures

Since separation is dependent upon the severity of the adverse pressure gradient, and the gradient is a function of the local radius, it is useful to consider the fluctuating pressure as a function of the sharp radius that the flow encounters. For the 60° slanted models this has been calculated using the equations of the ellipse and is the limiting corner radius (in the horizontal plane). The maximum root mean squared fluctuating pressure coefficients of the slanted sharp-edged model (local radius = 0), small ellipsoidal model (local radius = 250 mm), circular model (local radius = 374 mm) and large ellipsoidal model (local radius = 500 mm) are plotted against the radius in Figure 3.65. Figure 3.65 shows how the peak Cp rms varies with radius in zero, negative

(-15°) and positive (+15°) yaw angles. The Cp rms plot (Figure 3.65) is for one Reynolds number (based on a 100-km/h tunnel speed).

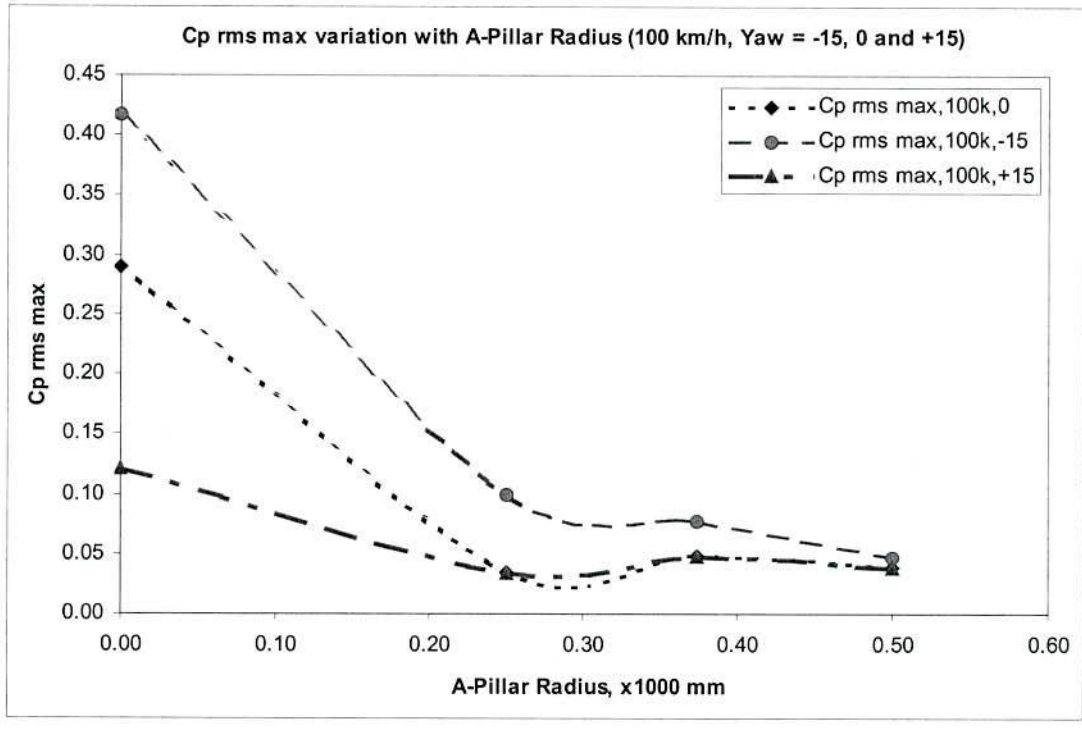

Figure 3.65: Fluctuating Cp rms (max) Variation with Local A-pillar Radii, Yaw = -15°, 0° and +15°

The fluctuating pressure greatly depends on the A-pillar and windshield's curvature and slant angles. Figure 3.65 shows that with the increase of local A-pillar curvature, the time varying fluctuating pressure reduces considerably. The larger A-pillar radius (more than 300-mm) has minimal effect on the fluctuating pressures in positive and zero yaw angles. Nevertheless, in the case of negative yaw angles, the larger radius (more than 300-mm) still reduces the magnitude of fluctuating pressures (Figure 3.65). It may be noted that it is known that most of the aerodynamically induced noise generated in the A-pillar regions comes from the leeward side.

3.8 Effects of Step on Flow Structure

Although one of the objectives of this research was to study the effect of radii on generic shapes, it is interesting to consider the effects of more realistic A-pillar geometries that include areas of separation from surface discontinuity, which exist on current production vehicles. Hence a limited study was undertaken with a forced separation point. While most North American and European vehicle manufacturers have eliminated rain gutters, many Japanese and Australasian vehicles still continue to feature rain-gutters and backward-facing step in the transition from the A-pillar to the side window. To simulate such devices, a rectangular step with a dimension of 230 mm-length, 25 mm-width and 15 mm-height was placed on the A-pillar region to measure the fluctuating pressures behind a step on the relatively smooth curved surfaces of the small and large ellipsoidal models (Figure 3.66 and Figure 3.67). The location of the step was 20 mm ahead of the first measuring microphone. The fluctuating pressure was measured at two positions behind the step at 60, 80, 100 and 120 km/h speeds under zero yaw angles for the large ellipsoidal model and 60 and 80 km/h at zero yaw angles for the small ellipsoidal model. The computed surface fluctuating pressure coefficients with and without the step are shown in Table 3.1 and Table 3.2.

Large Ellipsoidal Model With and Without a Step in the A-Pillar Region, Zero Yaw				
	Pos 1, Standard	Pos 1, Behind Step	Pos 2, Standard	Pos 2, Behind Step
Speed, km/h	Cp rms, std	Cp rms, mod	Cp rms, std	Cp rms, mod
60	0.0394	0.0776	0.0390	0.0350
80	0.0387	0.0857	0.0381	0.0355
100	0.0380	0.0939	0.0374	0.0369
120	0.0362	0.1012	0.0359	0.0386

Table 3.1: Cp rms and SPL behind a Step on the A-pillar Region of the LE Model

Small Ellipsoidal Model With and Without a Step in the A-Pillar Region, Zero Yaw				
	Pos 1, Standard	Pos 1, Behind Step	Pos 2, Standard	Pos 2, Behind Step
Speed, km/h	Cp rms, std	Cp rms, mod	Cp rms, std	Cp rms, mod
60	0.0313	0.1704	0.0301	0.0937
80	0.0273	0.1692	0.0263	0.0918

Table 3.2: Cp rms and SPL behind a Step on the A-pillar Region of the SE Model

The fluctuating pressure behind the step at position 1 is very high as a strong flow separation occurs behind the step. However, the fluctuating pressure reduces

significantly at position 2 as the separated flow re-attaches. For the large ellipsoidal model, the separated flow re-attaches behind the fence earlier compared to the small ellipsoidal model.

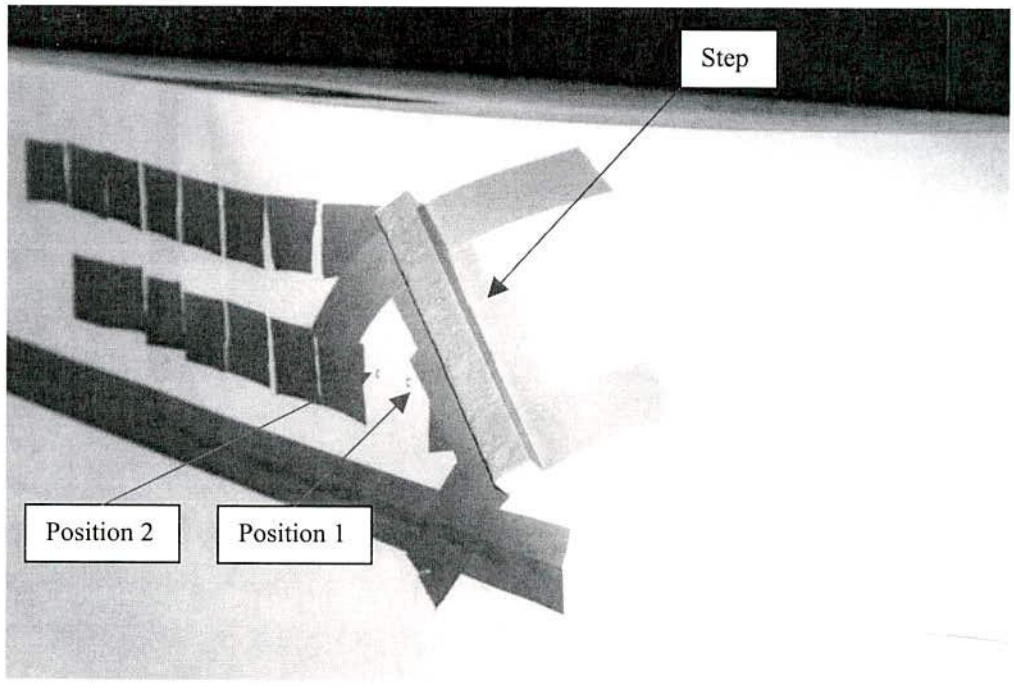

Figure 3.66: Step placed in the A-pillar Region, Oblique View, LE, Yaw = 0°

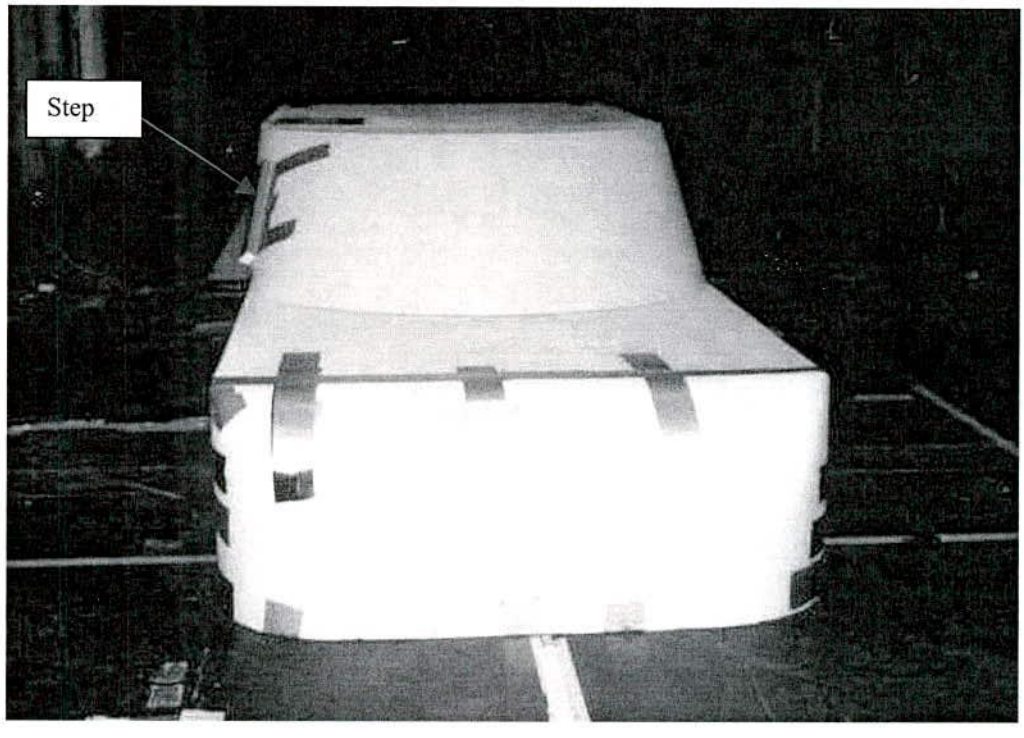

Figure 3.67: Step placed in the A-pillar Region, Frontal View, SE, Yaw = 0°

Chapter Four

Tests on Production Vehicles

With a view to assessing the effects of increased rounding of the A-pillar of a production vehicle on the 'in-cabin noise' and surface flow, two current production vehicles were tested in the wind-tunnel and on the road. These two vehicles were a VR Commodore station wagon and a VT Calais sedan (vehicle descriptions were given in Chapter Two). Additionally, the test aimed to further the understanding of the variation in time and space of the surface pressure fluctuation on the side window in the A-pillar region and the relationship between the surface pressure fluctuation and the in-cabin noise.

The initial test was conducted in Monash/RMIT Universities Aeroacoustic Wind-Tunnel and on the road to measure the cabin noise using the VR Commodore station wagon, which was fitted with a removable fibre-glass modified A-pillar cover that provided a smooth radius over the A-pillar (Figure 4.1). The instrumented Artificial Head Measurement System (general description and calibration of which have been described in Chapter Two and also in Appendix F) was used to measure the in-cabin noise. The Head was secured in the left front seat.

Problems found drilling a production toughened glass side window did not permit measurement of surface mean and fluctuating pressures on a production window. However, this was overcome by using a four-millimetre thick perspex side window mounted so that the curvature approximated the production window. The perspex could be easily drilled for mounting the pressure taps and microphones. The surface mean and fluctuating pressures were measured at 16 locations (2 rows of 8). The horizontal spacing was 80 mm and the position of these two rows from the window belt line was 1/3 and 2/3 the glass height (for details, refer to Figure 4.2 and Figure 4.11).

Data were recorded on digital tape by a SONY DAT recorder (PC160A). The sampling frequency was 24000 Hz (for the VR Commodore testing) and 48000 Hz (for the VT Calais testing) per channel and the duration was 30 seconds. The variation in sampling frequency was due to the number of channels used, 8 for the VR Commodore test allowing a sampling rate of 24000 Hz maximum, and 4 channels for the VT Calais, which permitted sampling at 48000 Hz).

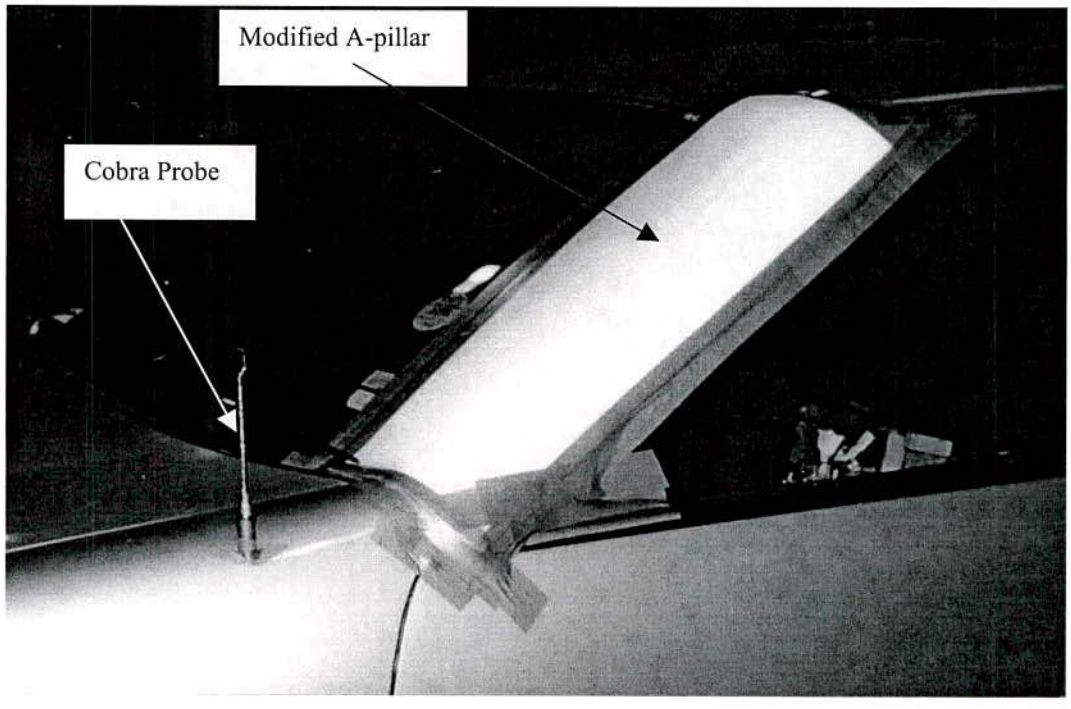

Figure 4.1: VR Commodore Station Wagon with Modified A-pillar and Cobra Probe

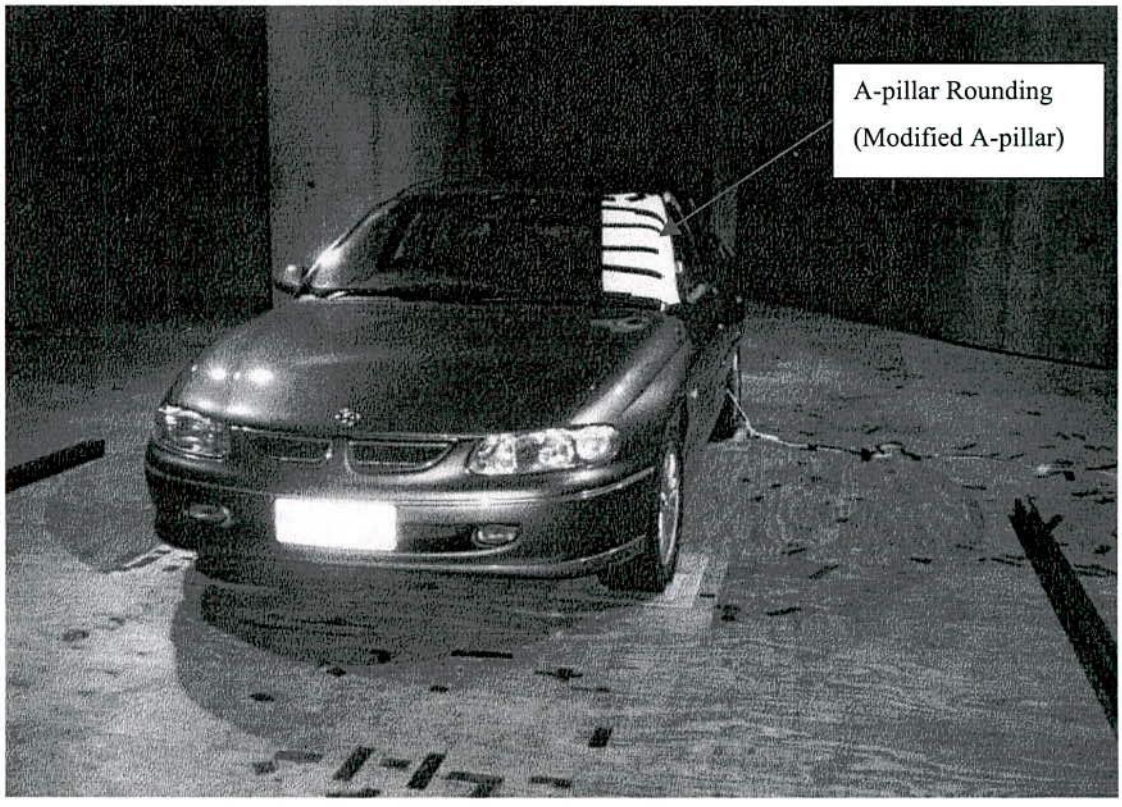

Figure 4.2: VT Calais with Modified A-pillar in the Monash/RMIT Universities' Wind-Tunnel

4.1 Effects of Increased A-pillar Radius on 'In-Cabin Noise' (VR Commodore)

The VR Commodore station wagon was tested in the wind-tunnel and on-road to evaluate the effects of increased rounding of the A-pillar of a production vehicle (Figure 4.1).

4.1.1 Wind-Tunnel Tests

In the wind-tunnel, the VR Commodore was tested over a range of tunnel air speeds (40, 60, 80, 100, 120 and 140 km/h) and yaw angles (±15° in increments of 5°). Flow visualisation was also carried out. As leeward side airflow under yawed conditions

plays a dominant role in aerodynamic noise generation in a passenger car, the flow visualisation was conducted at 0°, -5°, -10° and -15° yaw angles. The vehicle was tested with standard A-pillar and with the A-pillar modification. In both cases the side rear view mirror was not fitted. Still and video cameras were used to document the flow visualisation.

The data obtained from the Artificial Head System and the Cobra Probe were recorded on the SONY DAT Recorder described previously. During recording the signal was continuously monitored on a storage oscilloscope connected in series. The stored data were later down loaded for processing.

4.1.1.1 Effects of Modified A-pillar and Yaw Angle on 'In-Cabin Noise'

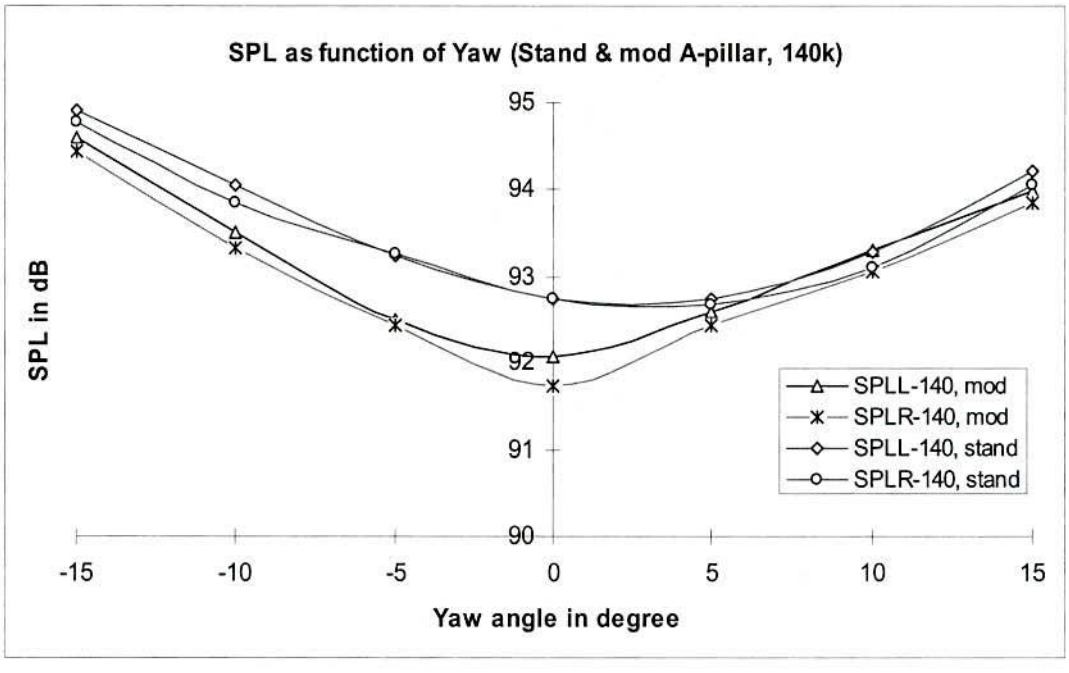

Figure 4.3: In-Cabin Noise Variation with Yaw Angles (Standard and Modified A-pillar), Speed = 140 km/h

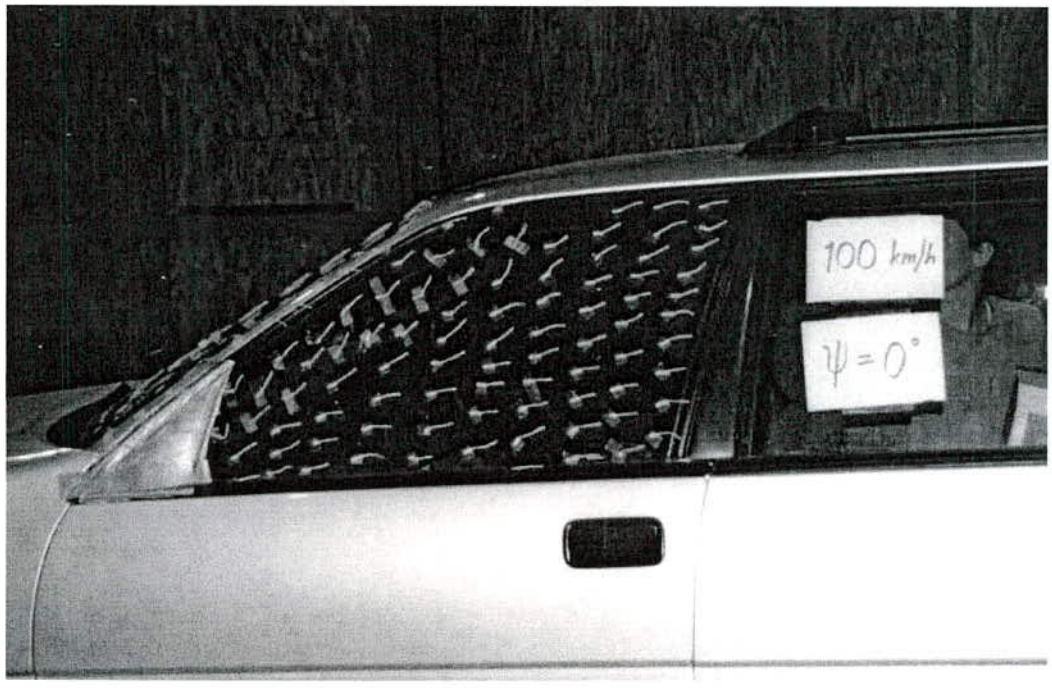

Figure 4.4: Side View of Flow Visualisation with Standard A-pillar, Yaw = 0°, Speed = 100 km/h

Figure 4.5: Side View of Flow Visualisation with Modified A-pillar, Yaw = 0°, Speed = 100 km/h

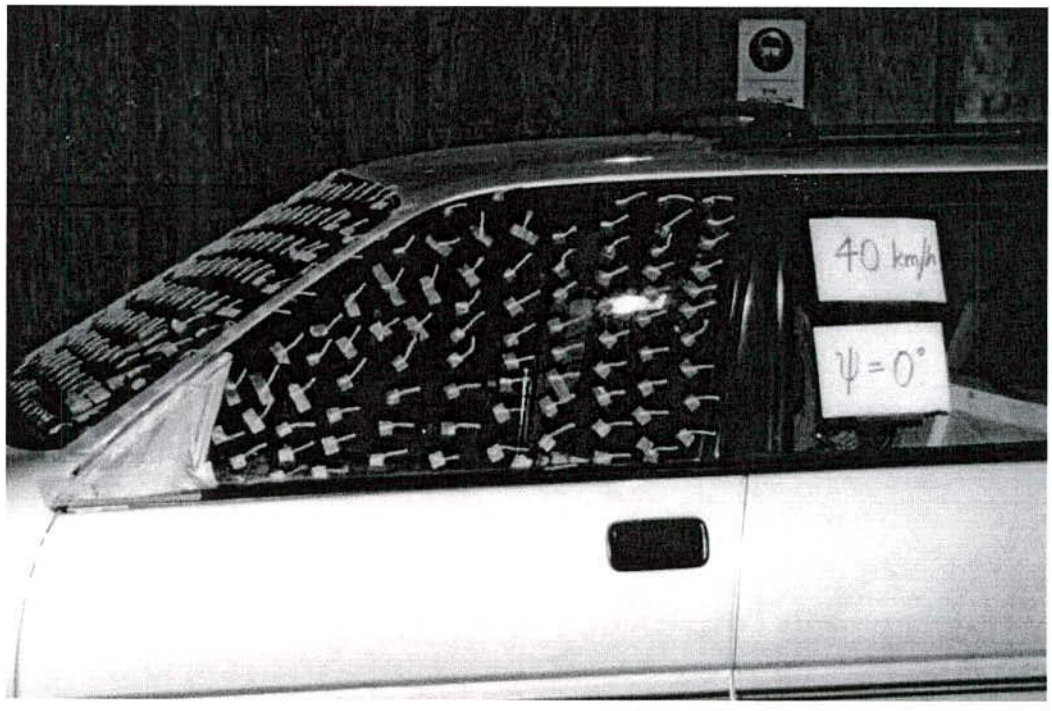

Figure 4.6: Side View of Flow Visualisation with Standard A-pillar, Yaw = 0°, Speed = 40 km/h

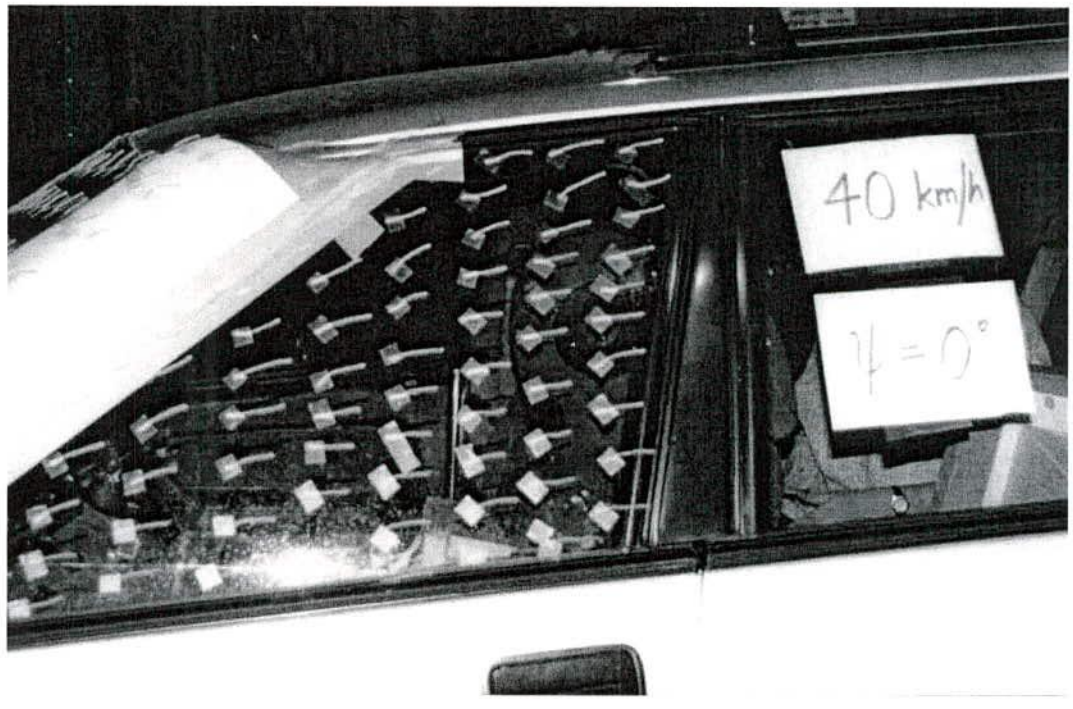

Figure 4.7: Side View of Flow Visualisation with Modified A-pillar, Yaw = 0°, Speed = 40 km/h

Figure 4.3 shows the interior noise level variation with yaw angles for the standard and modified A-pillar. It also shows the interior noise levels perceived by the left and right ears of the Artificial Head System. The plot also indicates that the noise levels vary with the yaw angles. The highest reduction of interior noise due to the increased rounding of the A-pillar was achieved at zero and low negative yaw angles (Figure 4.3). However, the A-pillar modification had little effect on the interior noise level at yaw angles greater than +5° (Figure 4.3). At positive yaw angles the flow separation is minimal and as the more positive yaw angles are encountered, the A-pillar vortex contracts. The SPLs for the other speeds (100 and 120 km/h) had similar trends.

The flow visualisation photographs (Figure 4.4, Figure 4.5, Figure 4.6 and Figure 4.7) showed that the modified A-pillar had a significant influence on the flow structures in the A-pillar region. Figure 4.4 and Figure 4.6 demonstrate that a strong conical vortex existed along the A-pillar edge on the side window and the flow was unsteady. However, the flow visualisation photographs of the modified A-pillar (Figure 4.5 and Figure 4.7) indicate that the flow was mostly attached and the A-pillar vortex almost disappears. The side views of flow visualisation at negative yaw angles demonstrated that the modified A-pillar had significant effects on the A-pillar flow structures (Figures not shown here).

4.1.2 On-Road Tests

On-road tests were carried out on smooth sections of highway in the absence of other traffic near Melbourne, Australia. Details and maps of on-road test sites have been given in Appendix L. Tests were carried out at 100, 120 and 140 km/h under a range of atmospheric wind speeds of 3 to 6 m/s, measured via the Cobra Probe.

4.1.2.1 Effects of Modified A-pillar on 'In-Cabin Noise'

The noise perceived by the left ear of the Aachen Head is plotted as a function of speed for zero yaw angle in Figure 4.8. For comparison with the on-road data, the 'in-cabin noise' data from the wind-tunnel tests are also shown in Figure 4.8. A significant effect on the noise reduction due to the increased rounding of the A-pillar is evident at higher speeds (120km/h and above). At lower speeds, the modified A-pillar has less effect. The similar trend is also noted for the wind-tunnel test. Therefore, it was shown in principle that the larger curvature of the A-pillar can reduce interior noise. During the wind-tunnel and on-road tests, the noise measured by the left ear of the Aachen Head was consistently higher than the right ear.

Figure 4.8 indicates that the average values of SPL for on-road testing were typically 6-10 dB higher than those measured in the wind-tunnel testing. The higher noise levels in on-road testing could be attributed to the extra mechanical noises produced by a fully operational vehicle which were not reproduced in the tunnel (that is, engine, exhaust, transmission and road tyre interaction noise) and atmospheric turbulence. The tunnel used had a longitudinal turbulence level of approximately 2.5% with relatively small-scale turbulence whereas the turbulence levels on-road typically were 5-6% (calculated from the Cobra Probe data).

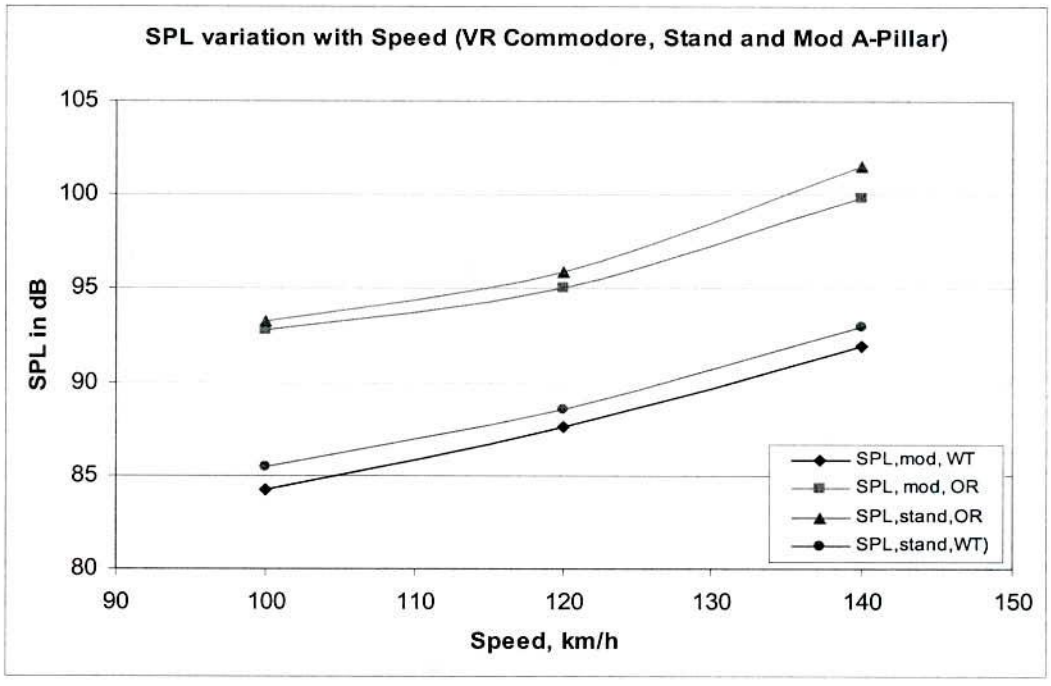

Figure 4.8: SPL variation with Speeds, Standard and Modified A-pillar, On-Road and Wind-Tunnel

4.1.2.2 Effects of Yaw Angles (Atmospheric Crosswinds)

Figure 4.9 and Figure 4.10 show the sound pressure variations for both ears of the Aachen Head at 100 and 140 km/h plotted against yaw angles averaged over 10 seconds. The flow yaw angles were measured by the Cobra Probe fitted on the car's bonnet close to the A-pillar. Prior calibration of the Cobra Probe to account for the proximity of the vehicle, the local yaw angles were determined using a relationship between the probe and turntable yaw angles (for more details, refer to Alam et al. 1999). No significant difference between the two ears of the Aachen Head is evident.

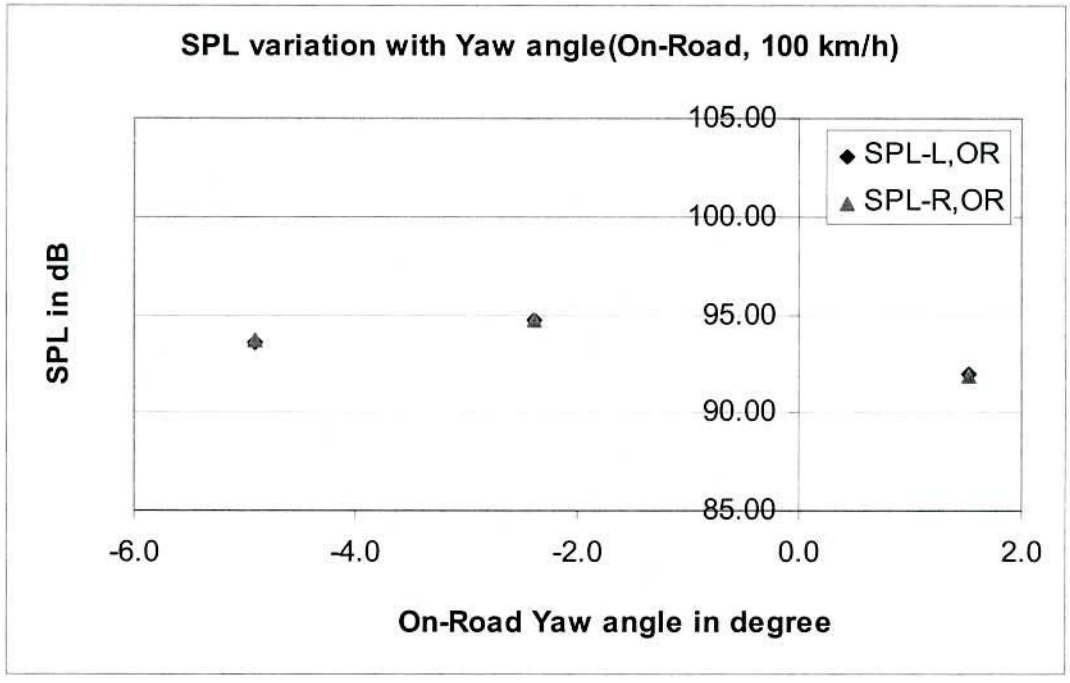

Figure 4.9: SPL Variation with Yaw Angles, 100 km/h, On-Road

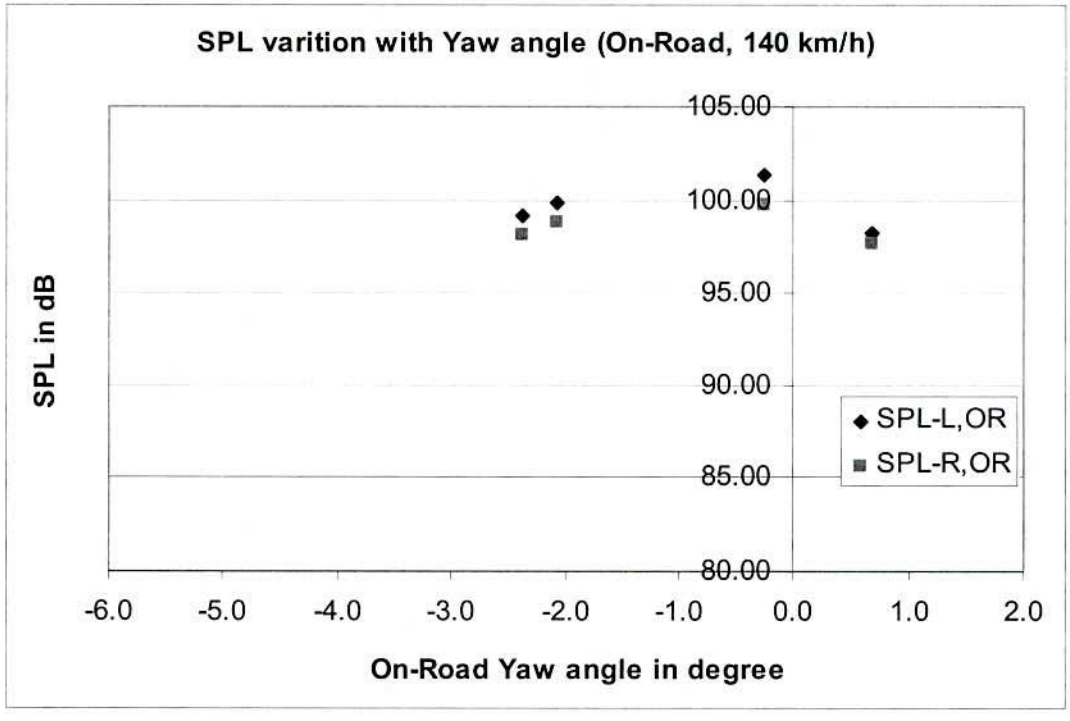

Figure 4.10: SPL Variation with Yaw Angles, 140 km/h, On-Road

NB: SPL-L and SPL-R in Figures 4.9 and 4.10 indicate the SPL measured by the left and right ear microphones of the Artificial Head System.

4.2 Effects of Increased A-pillar Radius on External Flow and 'In-Cabin Noise' (VT Calais)

The VT Calais sedan was used in wind-tunnel and on-road testing to measure the surface mean and fluctuating pressures and the interior noise (Figure 4.2). On-road tests were conducted in conjunction with another closely related Ph.D. research program by Zimmer (2001) and some data for the standard configuration were used here with permission.

4.2.1 Wind-Tunnel Tests

The vehicle was tested with the standard A-pillar first and later with a modified A-pillar under similar test conditions as the VR Commodore. In both cases the side rear view mirror was not fitted.

The data obtained from the Aachen Head, the flush mounted microphones on the side window and the Cobra Probe were stored on a digital audio tape using the SONY DAT Recorder. The surface mean pressures were recorded using a multi-channel Scanivalve system (the same system that was used for the model-scale testing) which was connected to a PC for the real-time pressure display as well as for the storage of pressure data on the computer's hard drive for processing. The stored data from the DAT was later down loaded into a PC to compute the surface fluctuating pressure coefficient (Cp rms) and the interior noise (SPL). The pressure spectra were also computed. The data were also used to compute velocity components.

Unavoidably, the first two positions at each row (top and bottom) close to the A-pillar edge were covered by the modified A-pillar. Therefore, the data presented here were from the 12 positions (2 rows of 6) for the wind-tunnel and on-road tests.

The surface pressure coefficients are plotted against the distance from the line of symmetry (at the front) of the production vehicle (for details of how the graphical results relate to the model geometry, refer to Figure 4.11). For compactness, when non-zero yaw angle data are presented, data from the upstream and downstream side are plotted on the same figure.

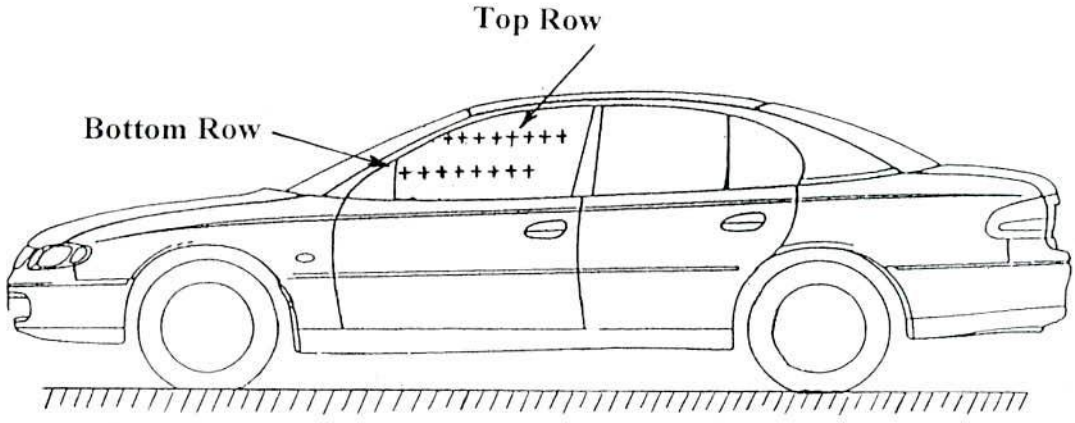

a). **Location of Pressure Measurements on the Production Vehicle, Side View**

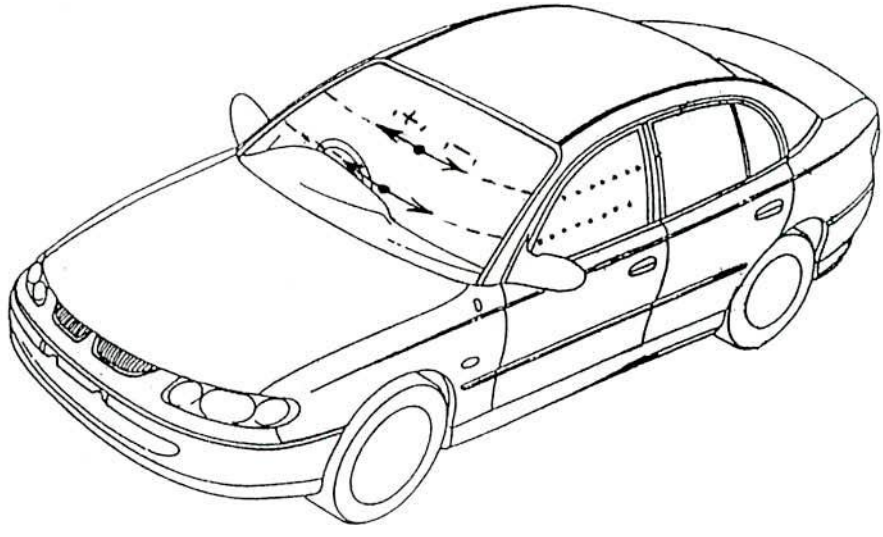

b). **Distance for the 1st hole from Vehicle's Centreline for Bottom Row-950 mm and Top Row-820 mm, Top View**

Figure 4.11: A Schematic of Data Presentation in Relation to Vehicle's Centre Line

4.2.1.1 Effects of Modified A-pillar and Yaw Angle on Surface Mean Pressure

The surface mean pressure coefficient variation with distance along the side window near the A-pillar from the centre-line of the vehicle is shown in Figures 4.12 to 4.15. The effects of Reynolds numbers on the surface mean pressure coefficients (for the standard and modified A-pillar) are evident at zero and negative yaw angles. However, no apparent Reynolds number sensitivity is evident at positive yaw angles.

Again, the area of the separated zone is much larger at negative yaw angles compared to zero yaw angles. At positive yaw angles, the separated area almost disappears and no A-pillar vortex is evident (Figure 4.13 and Figure 4.15).

The increased rounding (stream-ling) of the A-pillar has a significant effect on the surface mean pressure coefficient. It reduces the magnitude of surface mean pressure at all yaw angles (Figure 4.14 and Figure 4.15).

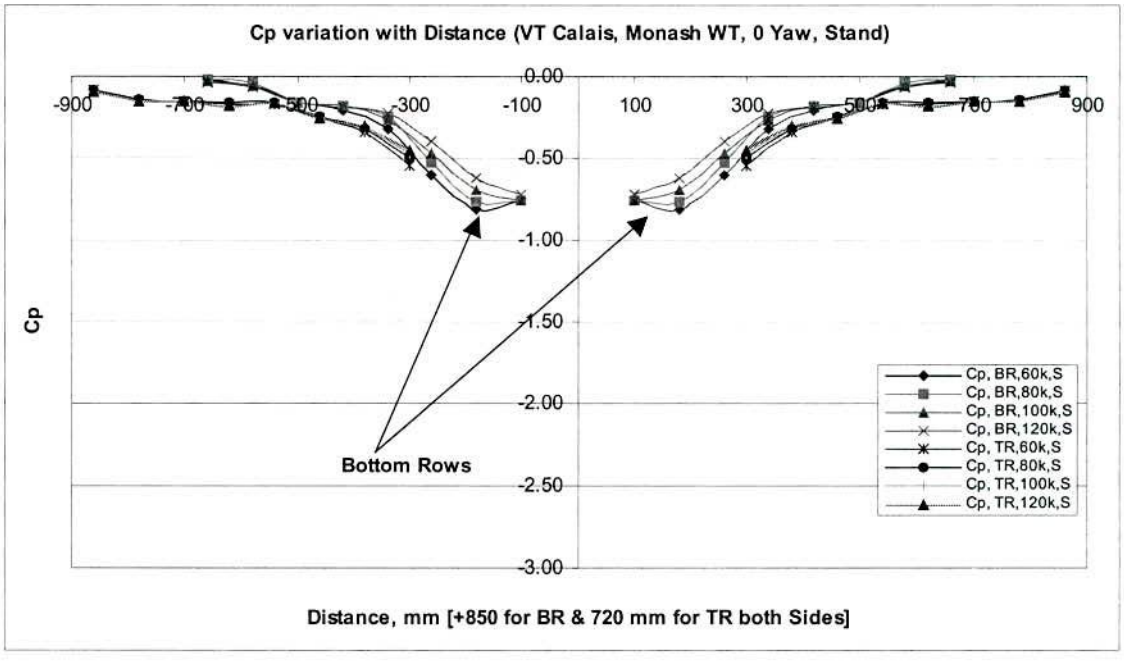

Figure 4.12: Surface Mean Cp Variation with Distance, Yaw = 0° (Standard A-pillar)

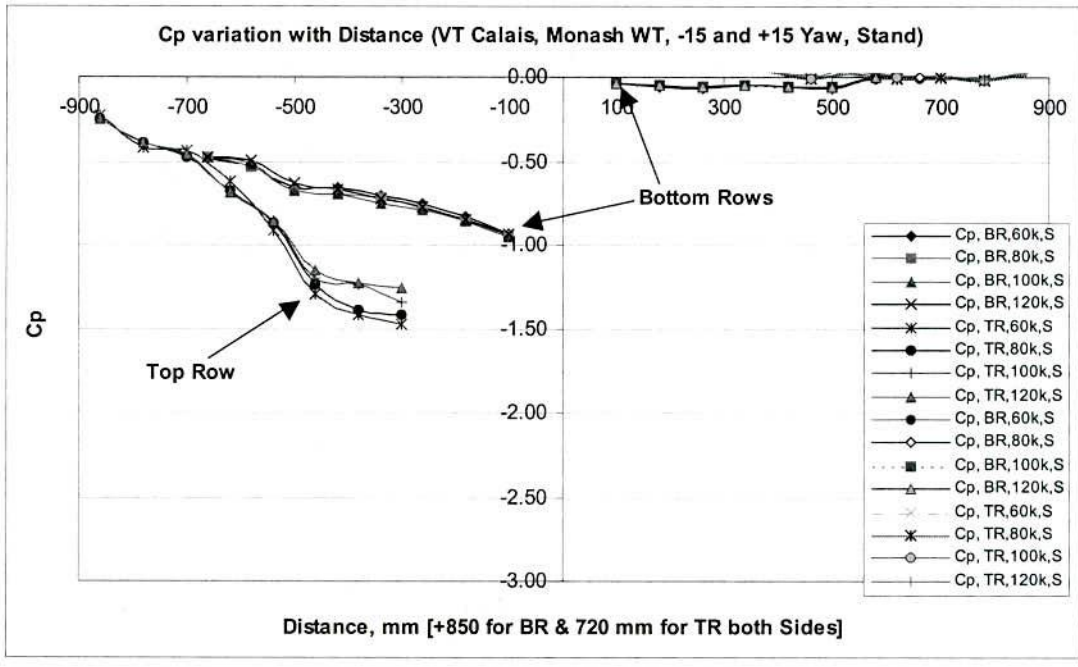

Figure 4.13: Surface Mean Cp Variation with Distance, Yaw = -15° and +15° (Standard A-pillar)

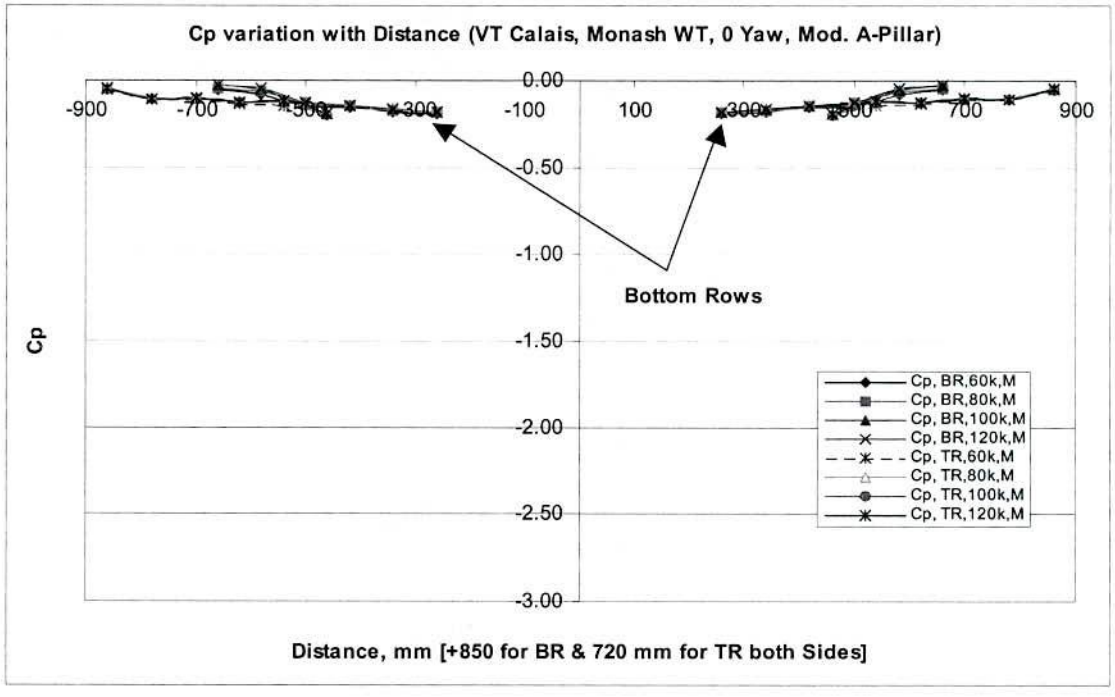

Figure 4.14: Surface Mean Cp Variation with Distance, Yaw = 0° (Modified A-pillar)

NB: S, M and k in Figures 4.12, 4.13, 4.14 and 4.15 indicate Standard and Modified A-pillar and km/h respectively.

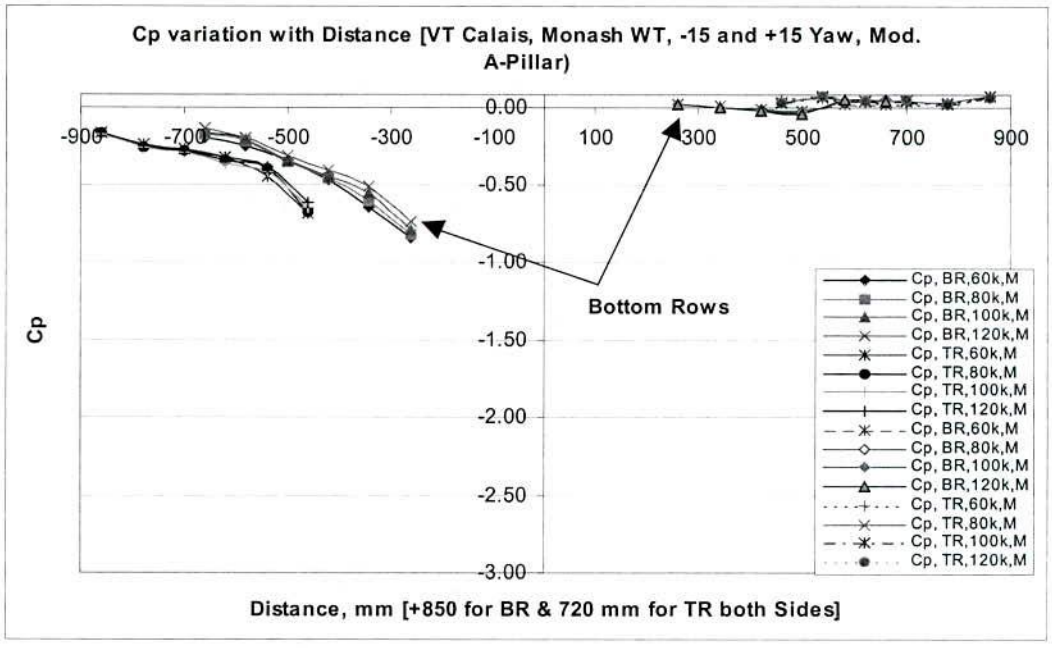

Figure 4.15: Surface Mean Cp Variation with Distance, Yaw = -15° and +15° (Modified A-pillar)

4.2.1.2 Effects of Modified A-pillar and Yaw Angle on Surface Fluctuating Pressure

The fluctuating pressure coefficient (Cp rms) variation with distance for the standard and modified A-pillar is shown in Figures 4.16 to 4.19. A variation of Reynolds numbers on the surface fluctuating pressure coefficient (standard and modified A-pillar) is evident at negative yaw angles (Figure 4.17 and Figure 4.19). These variations are more significant between the lower (60 km/h) and higher Reynolds numbers (80 km/h and higher speeds). However, the effect of Reynolds numbers is not evident at the positive yaw angles (Figure 4.17 and Figure 4.19).

Figures 4.16-4.19 demonstrate how the magnitude and shape of the separated flow change with yaw angles (standard and modified A-pillar). The increased radius of the A-pillar due to modification reduces the magnitude and size of the A-pillar vortex significantly. This reduction is evident at the negative and zero yaw angles (Figure 4.18 and Figure 4.19).

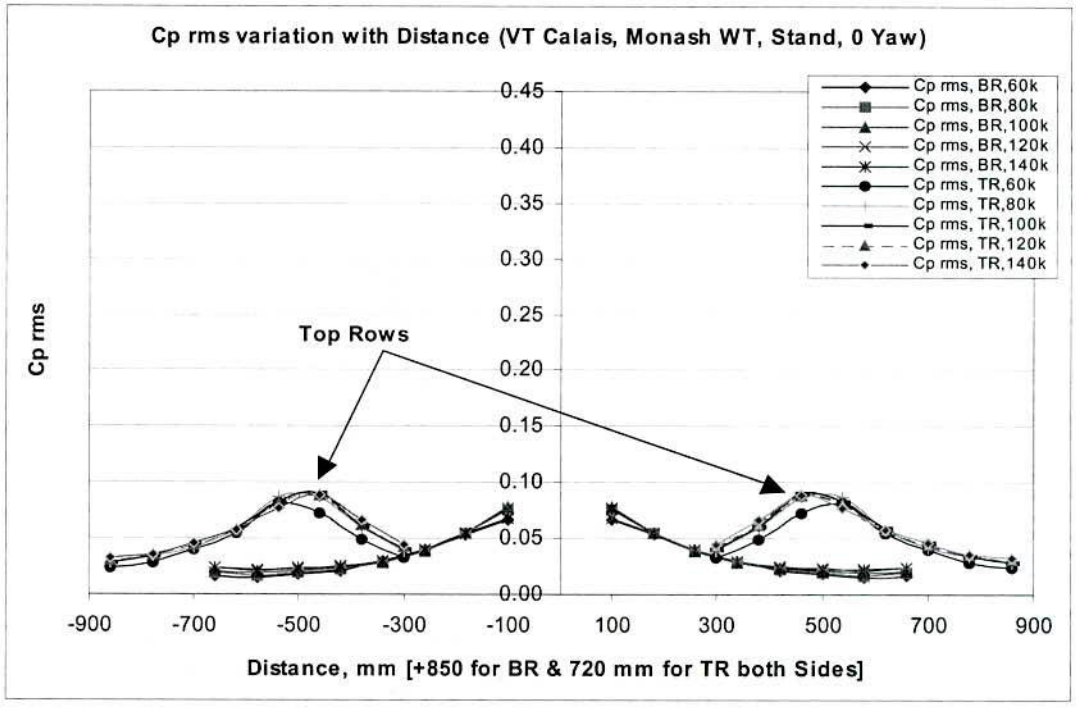

Figure 4.16: Surface Fluctuating Cp rms Variation with Distance, Yaw = 0° (Standard A-pillar)

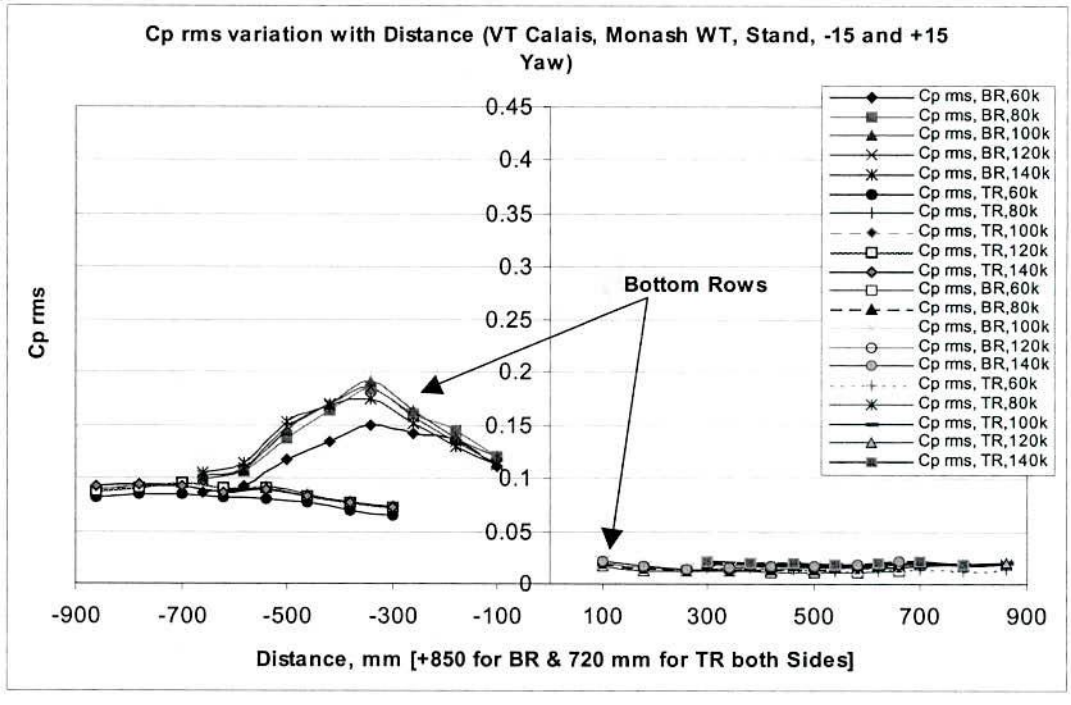

Figure 4.17: Surface Fluctuating Cp rms Variation with Distance, Yaw = -15° and +15° (Standard A-pillar)

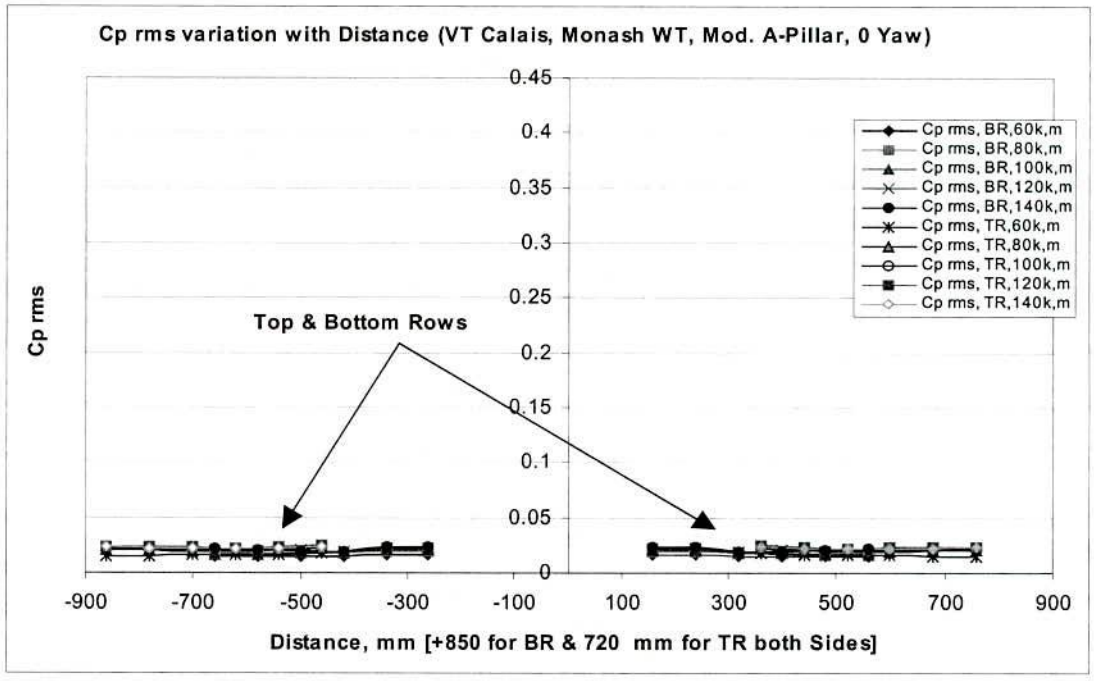

Figure 4.18: Surface Fluctuating Cp rms Variation with Distance, Yaw = 0° (Modified A-pillar)

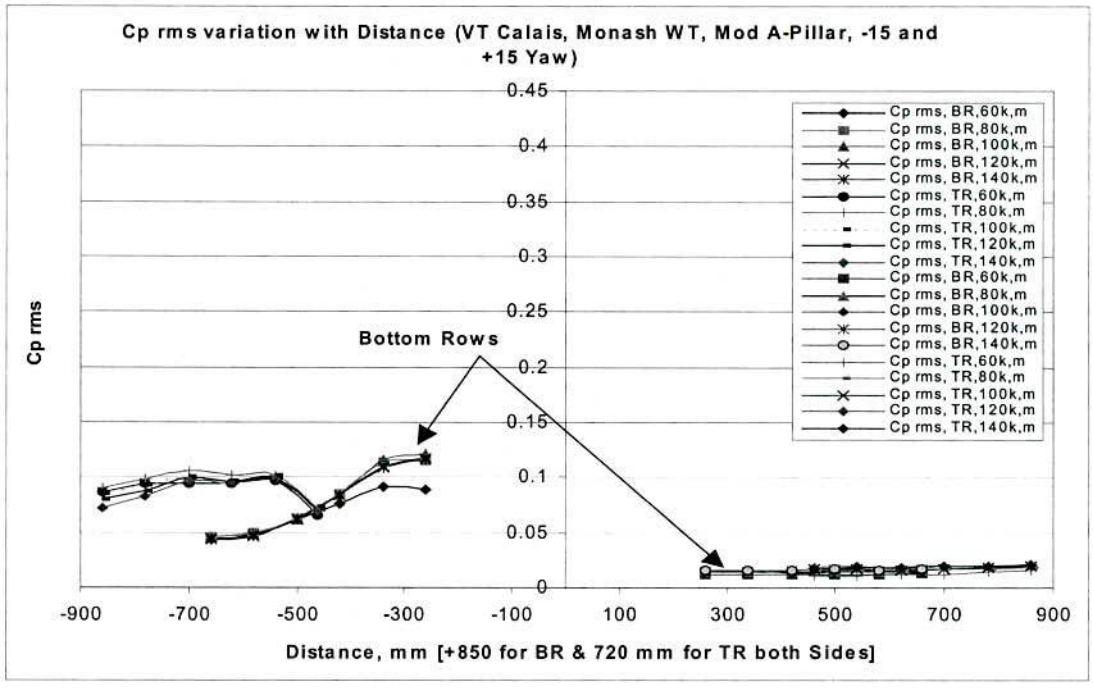

Figure 4.19: Surface Fluctuating Cp rms Variation with Distance, Yaw = -15° and +15° (Modified A-pillar)

4.2.1.3 Spectral Analysis (Fluctuating Pressures)

The Power Spectral Density (PSD) was used to document the energy characteristics of signals in the frequency domain. The procedure for PSD calculation is shown in Appendix E. In this study, the fluctuating pressure data, from the position where maximum fluctuating pressure was measured (at zero, positive and negative yaw angles) was used for the PSD analysis. Additionally, PSD is plotted against Strouhal numbers. The PSD for yaw angles of -15°, 0° and +15° are shown in Figure 4.20 and Figure 4.21 for the standard and modified A-pillar for the speed of 140 km/h (tunnel speed). The normalised PSD plots for zero yaw angle are also shown in Figure 4.22 for the standard A-pillar for the range of test speeds.

For the standard A-pillar (Figure 4.20), at negative yaw angles, the fluctuating pressure spectrum contains higher energy compared to the spectrum at zero yaw angles at frequencies below 300 Hz. However the pressure spectrum at positive yaw angles contains higher energy at frequencies above 300 Hz. The peak energy at negative yaw angles is close to 90 Hz. The spectrum at positive yaw angles contains the lowest energy compared to the spectra at negative and zero yaw angles.

For the modified A-pillar (Figure 4.21), the spectrum at negative yaw angles possesses highest energy compared to spectra at zero and positive yaw angles. Most energy was noted at low frequencies.

The normalised power spectra plot (Figure 4.22) for the standard A-pillar shows that all the three spectra (60, 80, 100, 120 and 140 km/h speeds) approximately collapse into a single line at Strouhal numbers below 50. However, a small variation is noted at Strouhal numbers above 50.

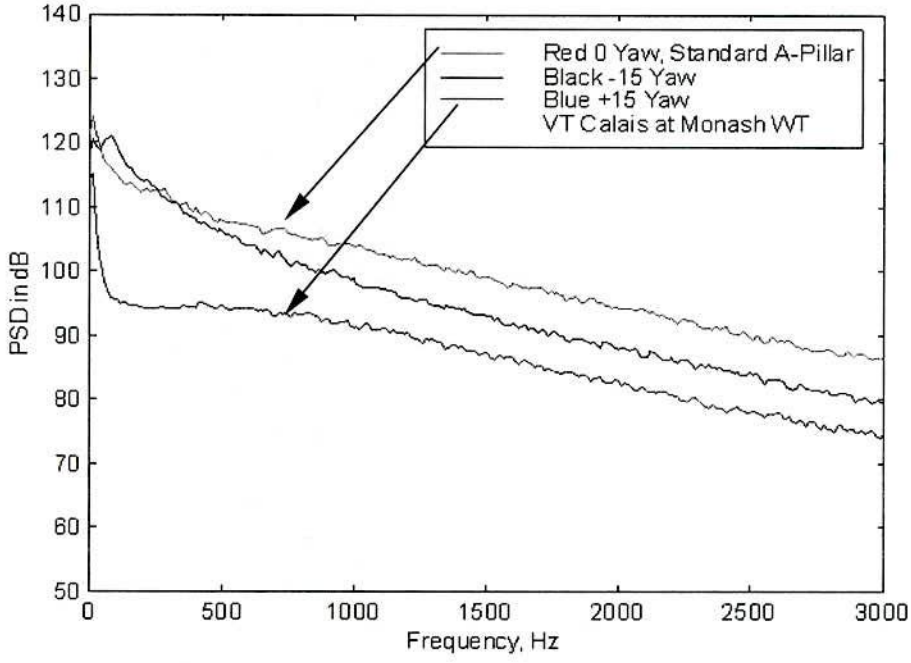

Figure 4.20: Power Spectra Plot of Peak Cp rms, Yaw = 0°, -15° and +15° (Standard A-pillar)

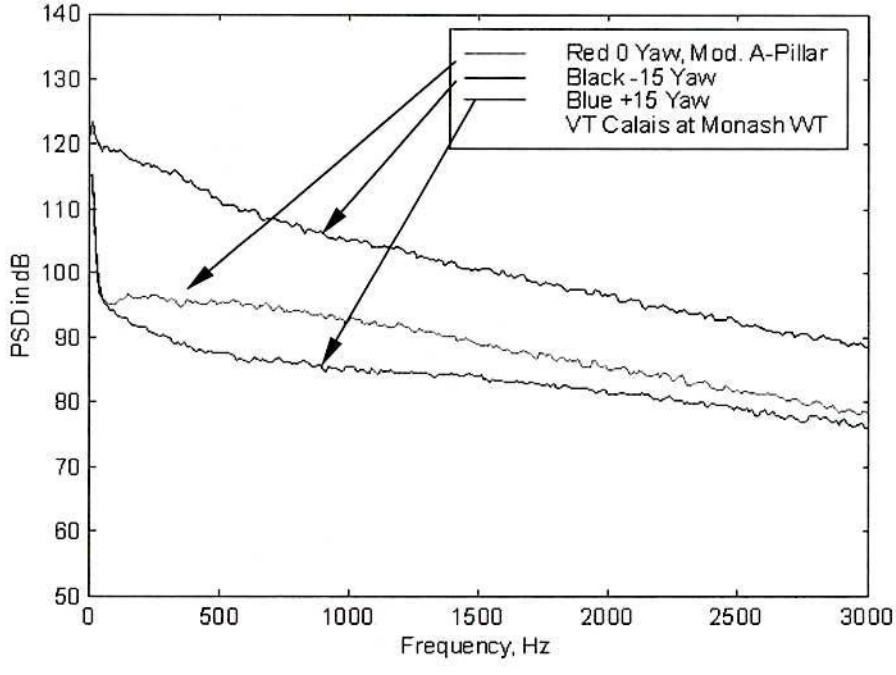

Figure 4.21: Power Spectra Plot of Peak Cp rms, Yaw = 0°, -15° and +15° (Modified A-pillar)

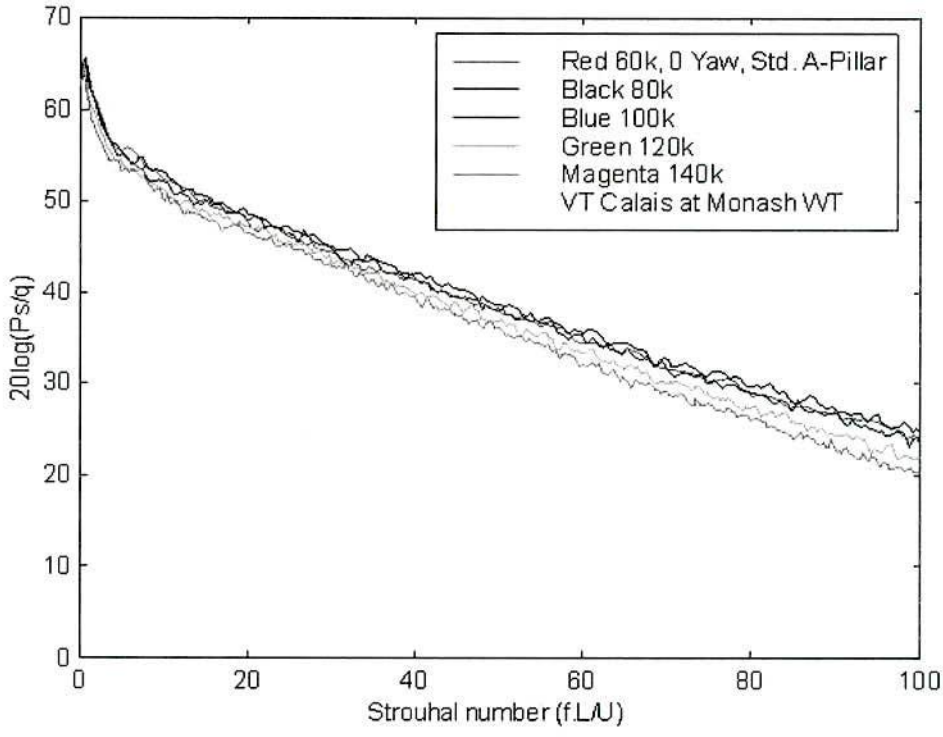

Figure 4.22: Normalised Power Spectra of Fluctuating Pressures, Yaw = 0° (Standard A-pillar)

4.2.1.4 Effects of Modified A-pillar and Yaw Angle on 'In-Cabin Noise'

The interior noise level varies with yaw angles and A-pillar curvature (Figure 4.23). Figure 4.23 indicates that increased rounding of A-pillar reduces the in-cabin noise at zero and negative yaw angles. For large positive yaw angles, there is evidence that the SPL increases with the modification. It is not known whether this is due to the higher speed of local flows or experimental errors. It may be noted that similar results were also found in a separate study conducted by Alam et al. (1999). The modified A-pillar has a relatively minor effect on the interior noise reduction as the vehicle encounters large positive yaw angles. The left ear (the side of the A-pillar modification) of Aachen Head perceived more noise compared to right ear (not shown here).

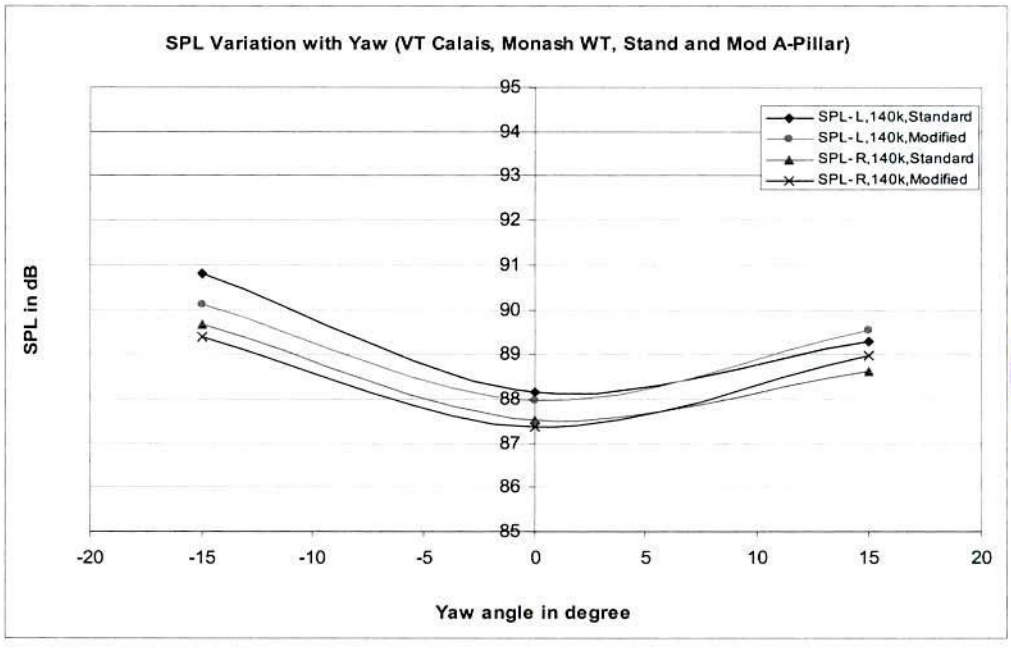

Figure 4.23: In-Cabin Noise Variation with Yaw angles, Standard and Modified A-pillar, Speed = 140 km/h

4.2.2 On-Road Tests (VT Calais)

The surface mean and fluctuating pressure, interior noise and local flow characteristics were measured and processed using similar techniques that were used for the wind-tunnel data processing.

4.2.2.1 Effects of Modified A-pillar on Surface Mean Pressure

The surface mean pressure coefficient (Cp) for the standard and modified A-pillar is shown in Figures 4.24 and 4.25. The effect of Reynolds numbers on the surface mean pressure in both cases is evident (Figure 4.24 and Figure 4.25). However, the Reynolds number sensitivity is more dominant for the standard A-pillar compared to the modified A-pillar. It was not possible to assess the wind yaw angles as only very light winds were encountered during testing (< 1 m/s). The increased rounding of the A-pillar has an effect on the surface mean pressure coefficients. It is clear that the modified A-pillar reduces the area of flow separation in the A-pillar region.

For the standard A-pillar configuration, a deviation of mean Cp and fluctuating Cp rms is noted for the top row (Figure 4.24 and Figure 4.26). The reason for this behaviour was not clear, however it can be due to a complex flow pattern around a fully operational vehicle and structural vibration during on-road testing.

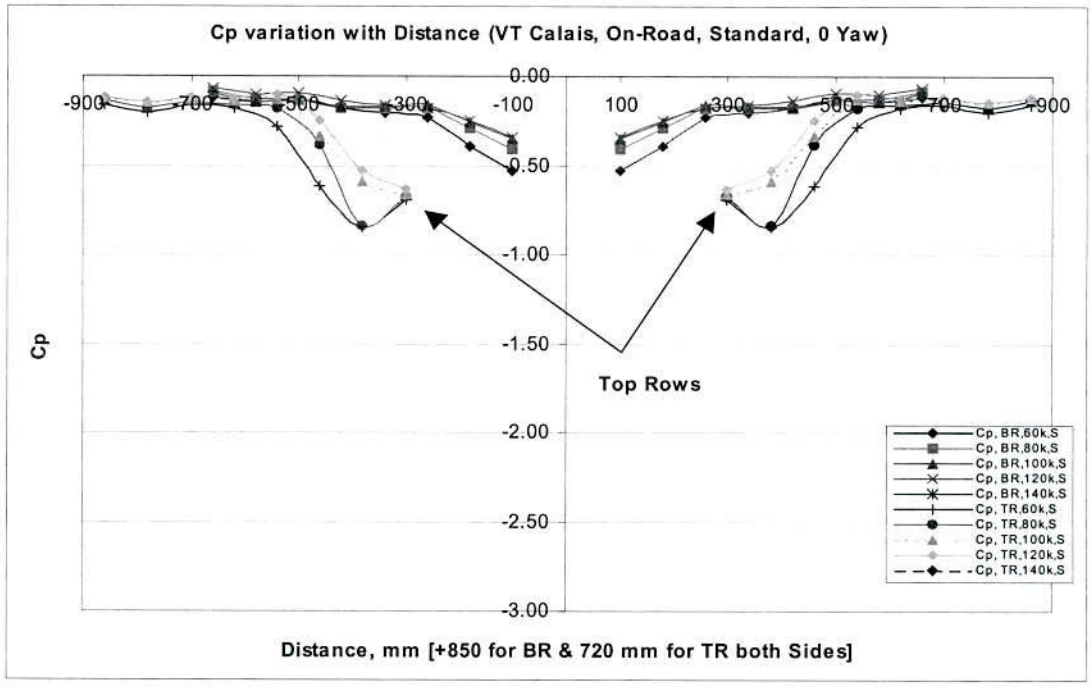

Figure 4.24: Surface Mean Cp Variation with Distance, Yaw = 0° (Standard A-pillar), On-Road

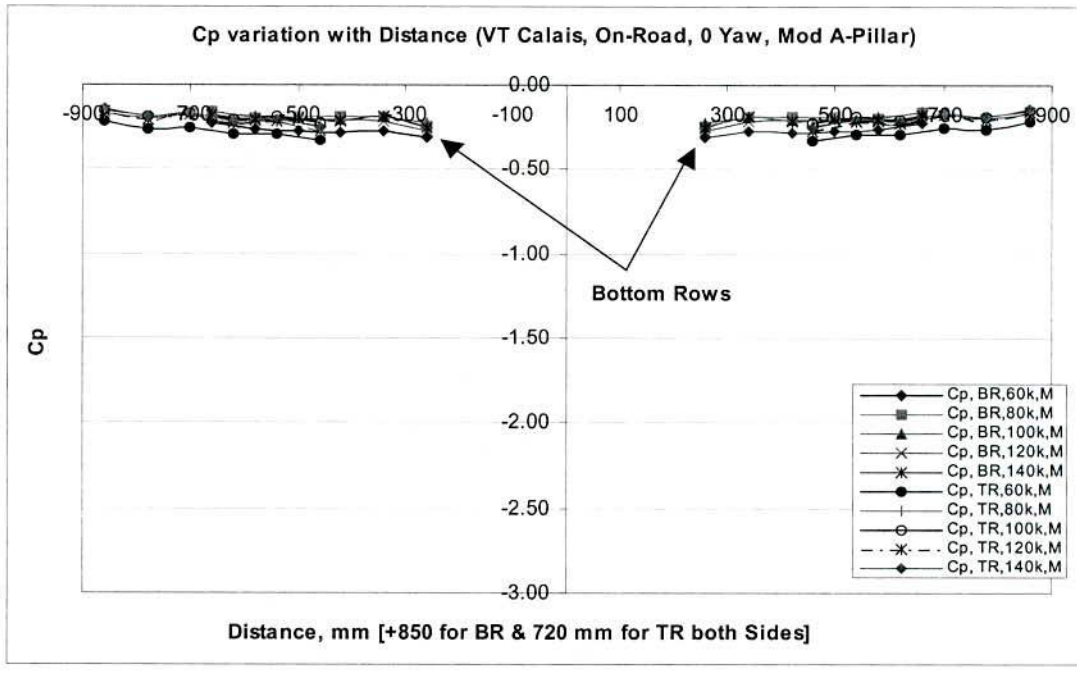

Figure 4.25: Surface Mean Cp Variation with Distance, Yaw = 0° (Modified A-pillar), On-Road

4.2.2.2 Effects of Modified A-pillar on Surface Fluctuating Pressure

Figures 4.26 to 4.27 show how the fluctuating pressure coefficient (Cp rms) for the standard and modified A-pillar varies with distance. A slight variation of Reynolds numbers on the surface fluctuating pressure coefficient (standard and modified A-pillar) is evident at zero yaw angles. However, the Reynolds number sensitivity is less prominent for the modified A-pillar. The Reynolds number variations are especially notable between higher (120 and 140 km/h) and lower (60, 80 and 100 km/h) Reynolds numbers for the top row. As mentioned earlier, on-road testing depends on many factors, the reason for this type of behaviour could not be determined. The effect of mean atmospheric wind (yaw angle) on the flow characteristics in the A-pillar regions was not evaluated due to very little or no wind condition during on-road testing. The increased rounding of the A-pillar reduces the magnitude of the A-pillar vortex. This reduction is evident in Figure 4.27.

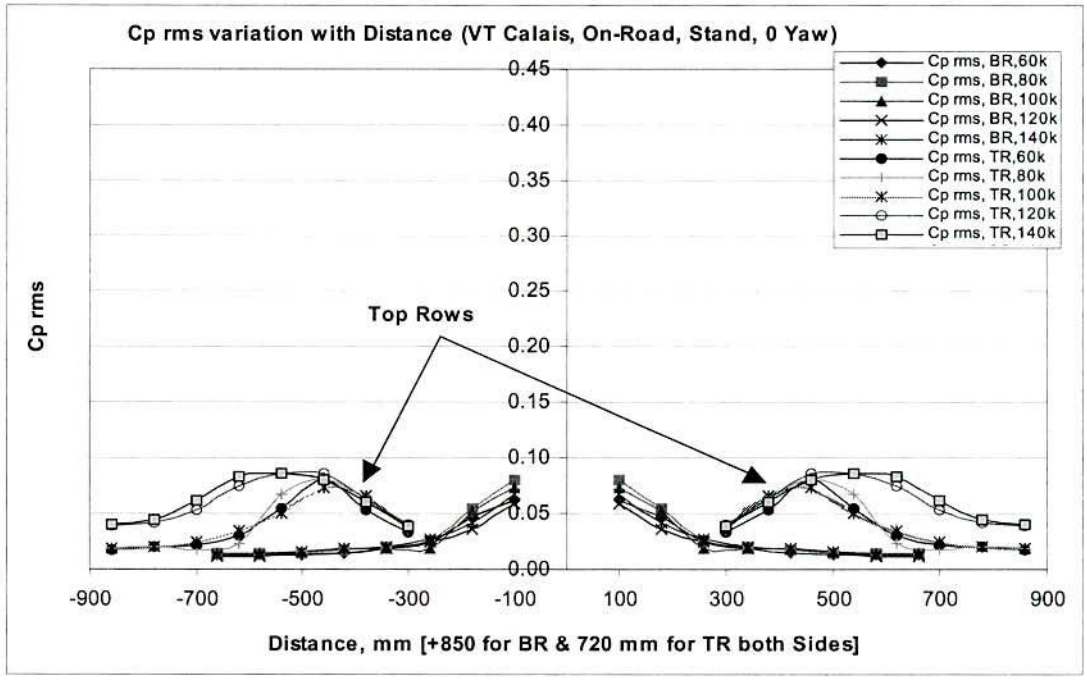

Figure 4.26: Surface Fluctuating Cp rms Variation with Distance, Yaw = 0° (Standard A-pillar), On-Road

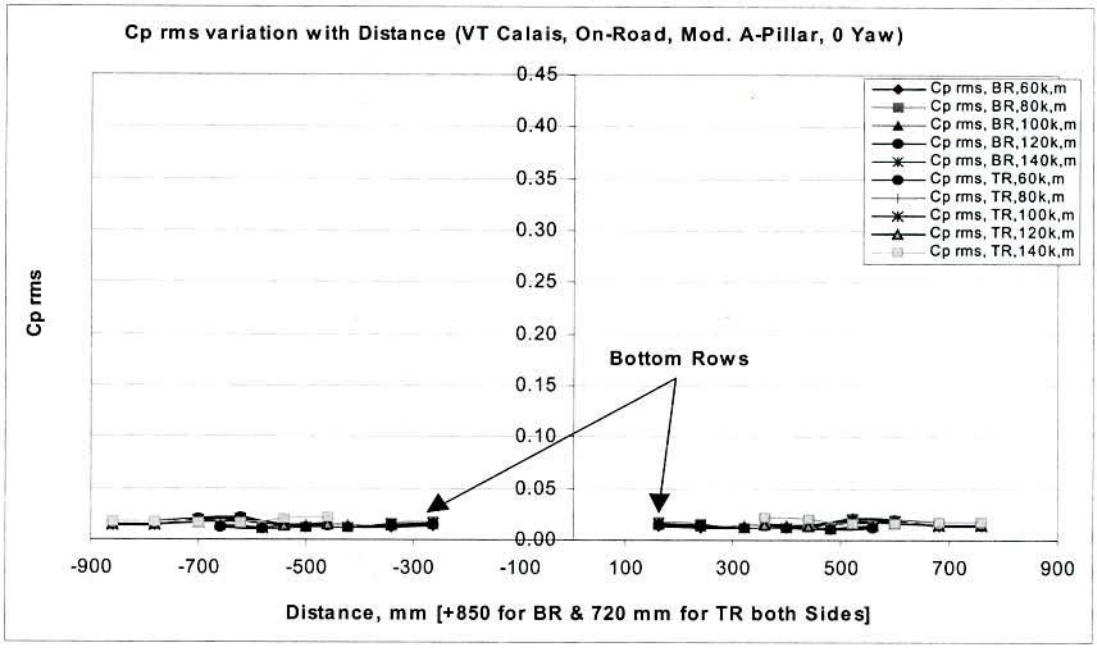

Figure 4.27: Surface Fluctuating Cp rms Variation with Distance, Yaw = 0° (Modified A-pillar), On-Road

4.2.2.3 Effects of Modified A-pillar on 'In-Cabin Noise' (On-Road)

Figure 4.28 shows the interior noise variation of the left and right ears of the Aachen Head with vehicle speeds for the standard and modified A-pillar. The interior noise levels from the wind-tunnel tests are also shown in Figure 4.29 (left ear). As no wind was encountered during the on-road tests, the SPL variation was only at zero yaw angle. Figure 4.28 indicates that the increased rounding of the A-pillar reduces the interior noise at higher speeds (above 120 km/h). At lower speeds, it is not effective. It may be noted that the noise generated by pressure fluctuations is not dominant at lower speeds as engine, mechanical, road/tyre interaction noises are dominant at lower speeds.

Figure 4.29 shows that the values of SPL for on-road testing are typically 6-10 dB higher than those measured in the wind-tunnel. The higher noise levels in on-road testing could be attributed to the extra mechanical noises produced by a fully operational vehicle, which were not reproduced in the tunnel.

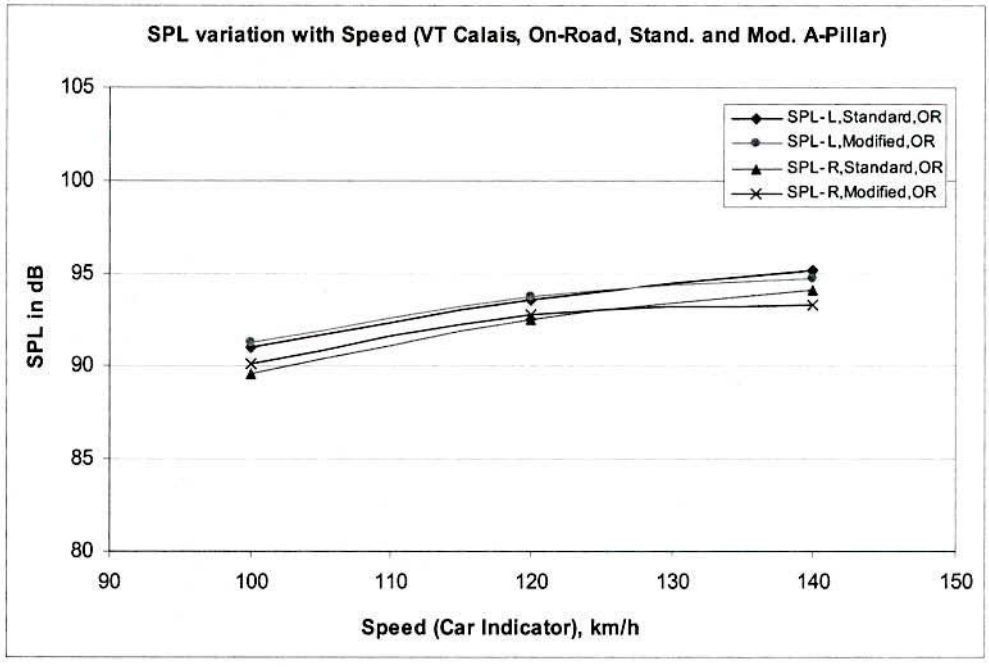

Figure 4.28: SPL variation with Speeds, On-Road, Standard and Modified A-pillar

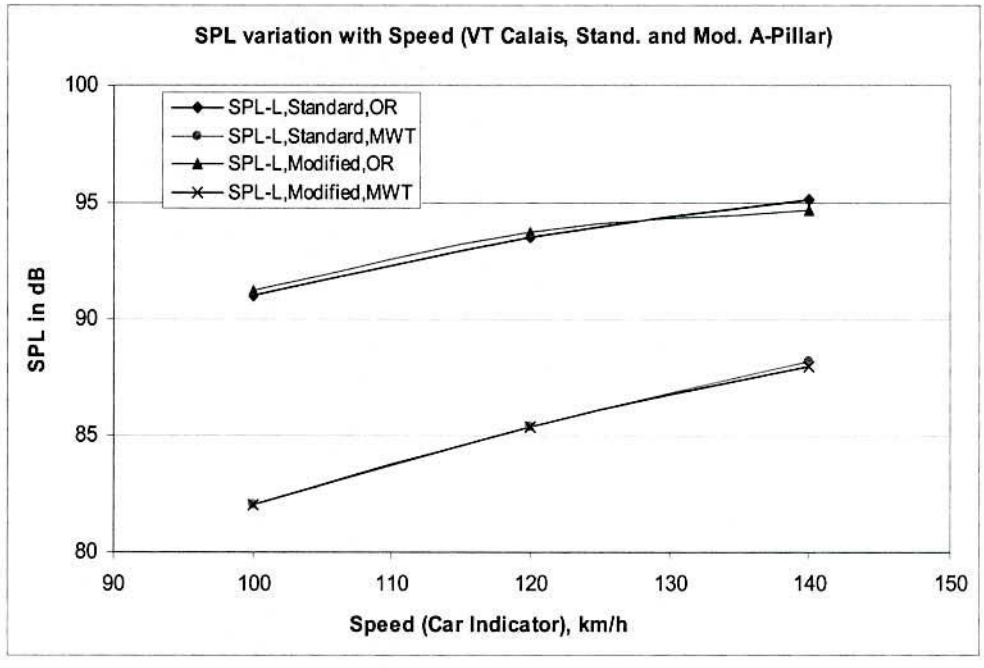

Figure 4.29: SPL variation with Speeds, On-Road and Wind-Tunnel, Standard and Modified A-pillar, Left Ear Only

Chapter Five

GENERAL DISCUSSION

In production vehicles, simple scaling of in-cabin noise with velocity is difficult as several noise generation mechanisms exist. These include vortex, cavity, aspiration and broad band noises, which were reviewed in Chapter 1. The frequency and amplitude of noise generation mechanisms will vary significantly with speed, and some strong noise sources occur because of feedback mechanisms such as Helmholz resonation or trailing edge feedback from cavities or gaps. Additionally, in-cabin noise arises from a mixture of structural and airborne sources; this is complicated by the non-linear transmission loss from the outside to the inside of the vehicle. However, the scope of this work is restricted to furthering the understanding of external surface pressure fluctuations, which are relatively broad band with no feedback mechanisms. Hence in this chapter the discussion will concentrate on broad band noise arising from the A-pillar region. Comparisons of the idealised vehicles with the production vehicles will also be drawn and industrial implications will be discussed.

5.1 Reynolds Number Effects on Fluid Mechanic Quantities and Comparison with Published Data

As discussed in Chapter 3, the surface mean and fluctuating pressure coefficients are relatively independent of Reynolds numbers (this was varied by changing the test velocity rather than dimensional scale) for all generic scale models except some minor variations in separated regions at zero and negative yaw angles.

For the production vehicle (described in Chapter 4), variations of mean and fluctuating pressure coefficients with Reynolds numbers at zero and negative yaw angles were noted. Reynolds number sensitivity was not found at positive yaw angles.

The normalised spectra at different speeds under constant yaw angles for the scale models and production vehicle (Figure 4.22 in Chapter four) showed that all spectra collapsed onto a single curve except for some minor variations. The measurements of the normalised velocity and turbulence intensities close to the A-pillar region of a production vehicle in the wind-tunnel showed no Reynolds number sensitivity at higher speeds and a minor sensitivity at the lower speeds (for more details, refer to Alam et al. 1998).

Since the interior cabin noise is influenced by the external fluctuating pressures (and these are much greater in separated flow than attached flow) and as car manufacturers are considering using scale models to identify broad band noise sources at an early stage in vehicle design, the effects of Reynolds numbers in attached (including reattached) and separated flows are described in the next three subsections.

5.1.1 Fluctuating Pressures in Attached Flows

Minimal in-cabin noise can be attained if the airflow remains attached over the cabin area with particular emphasis on the A-pillar regions since it is close to the driver's ears. Even for the attached flow, noise can be generated due to turbulent boundary layers, but the magnitude of noise will be much less compared to the noise generated by separated flows and in particular, in regions where vortex separation occurs. The scale models used in this study had a mixture of separated and attached flow in the A-pillar regions.

From the magnitude of the Cp rms indicated along the side of the unyawed models (not including the sharp-edged models), it appears that the attached flow exhibits a turbulent boundary layer. This is concluded since the Cp rms measured on the models are of the order of 0.02, whilst the Cp rms on the wind-tunnel floor (for which it is known that a turbulent boundary layer of 20 mm typical displacement thickness exists at the test location) is 0.007. This latter value also compared closely to the values found by other researchers for turbulent boundary layers (eg. see data from Blake in Table 5.1).

Comparison of the power spectral density plots for separated flow (for the slanted sharp-edged model) and attached flow (for the large ellipsoidal model) showed that the overall pressure fluctuations were much larger for the separated flow. However under the turbulent boundary layer they were more intense than in separated flow at very high frequencies. For vehicles experiencing attached flow, it is useful to consider the effects of Reynolds numbers on the potential for noise generation, both on unseparated (but turbulent boundary layer) flow and reattached flow. Understanding the scaling of amplitudes and frequencies with velocity and length scale is considered essential if model scale data are to be used for full-scale prediction.

The fluctuating pressures beneath a turbulent boundary layer have been well studied. A review by Willmarth (1975) summarised the published results on the fluctuating pressures beneath a turbulent boundary layer up to 1975. Blake (1970, 1986), Bradshaw (1967) and more recently Callister (1996) studied the fluctuating pressures in the turbulent boundary layer beneath the attached flow. The fluctuating pressure coefficients measured in this study on the floor of the RMIT University Wind-Tunnel beneath a turbulent boundary layer (at various speeds) compared to the values measured by Blake (1970) on a smooth wall are shown in Table 5.1. As mentioned earlier, the comparison shows a relatively close agreement. However, the value for the root mean squared fluctuating pressure coefficients beneath the attached flow on the model surface is approximately two and half times that of Blake's data. Also, the values of Cp rms under the turbulent boundary layer found by Callister (1996) were similar to the work presented here. Scaling of the frequency and amplitude with velocity in the attached flow under the turbulent boundary layer in this study shows a good agreement with Blake's study (1970).

Typical Values from Current Study			Blake's Study
Speed, km/h	Cp rms on Floor	Cp rms on Small Ellipsoidal Model	Cp rms on Smooth Surface
80	0.0070	0.0230	0.00876
100	0.0071	0.0240	0.00876
120	0.0071	0.0230	-
140	0.0072	0.0240	0.00876

Table 5.1: Cp rms Beneath the Turbulent Boundary Layer in the Attached Flow

The flows behind a fence (including flows after reattachment) were studied by Fricke and Stevenson (1968), Fricke (1971), Mohsen (1967) and more recently by Callister (1992). A comparison of Cp rms values under the turbulent boundary layer in the re-attached flows for the rectangular and slanted sharp-edged models was made with the values found by Fricke (1971) and Fricke and Stevenson (1968). These values of Cp rms in the re-attached flow found in this study and also by Fricke and Stevenson are shown in Table 5.2. Although it is realised that the pressure gradient along the flat plate (as used by Fricke and Stevenson) is different from the current study, relatively close agreement was found. The frequency and amplitude scaled well with the velocity in the reattached flow and was found to be in good agreement with Fricke and Stevenson's finding (1968) in the reattached flow behind a fence.

It may be noted that the Cp rms values shown in Table 5.2 have been taken from the reattached areas of the rectangular and slanted sharp-edged models at zero and positive yaw angles (where the flow re-attached after separation).

Fricke and Stevenson's Study		Typical Values from Current Study		
Distance Behind Fence	Cp rms	Model Type	Yaw	Cp rms
15 (Fence Height)	0.036	Slanted Sharp-Edged Model	0	0.030
20 (Fence Height)	0.032	Slanted Sharp-Edged Model	15	0.023
30 (Fence Height)	0.026	Rectangular Model	15	0.039

Table 5.2: Cp rms Behind a Fence in the Re-attached Area on a Flat Plate and in the A-pillar Region

5.1.2 Fluctuating Pressures in 'Naturally' Separated Flows

Achieving the optimal body shape for modern passenger cars, thereby allowing the flow to remain closely attached, does not necessarily mean that "natural separation" (defined as due to the overall body shape, rather than the influence of small flow trippers, such as rain gutters) can be avoided especially at negative yaw angles. Whether the flow will remain attached largely depends on the pressure gradient (favourable or unfavourable), as a favourable pressure gradient delays separation. The

pressure gradient becomes increasingly unfavourable as either the radius reduces or (for the leeward side) the yaw angle decreases. However, the proper selection of "effective corner radius" (i.e., the local radius at the A-pillar) will minimise this natural separation even at negative yaw angles. The surface mean and fluctuating pressure measurements showed that even the small ellipsoidal model had little separation at negative yaw angles.

Reynolds number sensitivity was evaluated using a Reynolds number based on the local radius at the A-pillar as a characteristic length instead of the vehicle width, vehicle length, vehicle wheelbase, or the square root of projected frontal area, as have been used by others. Cooper (1984, 1992) and Watkins (1990) reported that it is useful to evaluate the Reynolds number based on the local length or radius as the radius can play a vital role in determining if there is local flow separation. However it is realised that the right parameter selection is very difficult as it depends upon a variety of factors. The peak fluctuating pressure coefficient variation with the computed Reynolds number is shown in Figure 5.1 and Figure 5.2 for zero and negative yaw angles respectively. The local radii used in the calculation are the asymptotic corner radii of the ellipses. The plot for positive yaw angles is shown in Appendix H and is similar to the plot for zero yaw angles.

With the exception of the slanted sharp-edged model, the fluctuating pressure coefficients do not vary significantly with Reynolds number (based on effective corner radii) for all scale models at zero and positive yaw angles. However, a small increase of the fluctuating pressure coefficient with increasing speed is evident at negative yaw angles for the small ellipsoidal and circular models (Figure 5.2). Nevertheless, no variation in fluctuating pressure coefficient with speed is found for the large ellipsoidal model at negative yaw angles. Whilst there is no clear data collapse with Reynolds numbers based on effective corner radii, more data are needed in the range 0 to 3E+05 to cover the normal operating speeds of passenger cars (up to at least 120 km/h).

For relatively sharp-edged vehicles (such as some commercial vehicles) separation can occur even at positive yaw angles. The values of mean Cp and fluctuating Cp rms for the rectangular and slanted sharp-edged models found in this study and also by

Popat (1991) exhibited a close agreement. A comparison of these values was described earlier in Chapter 3.

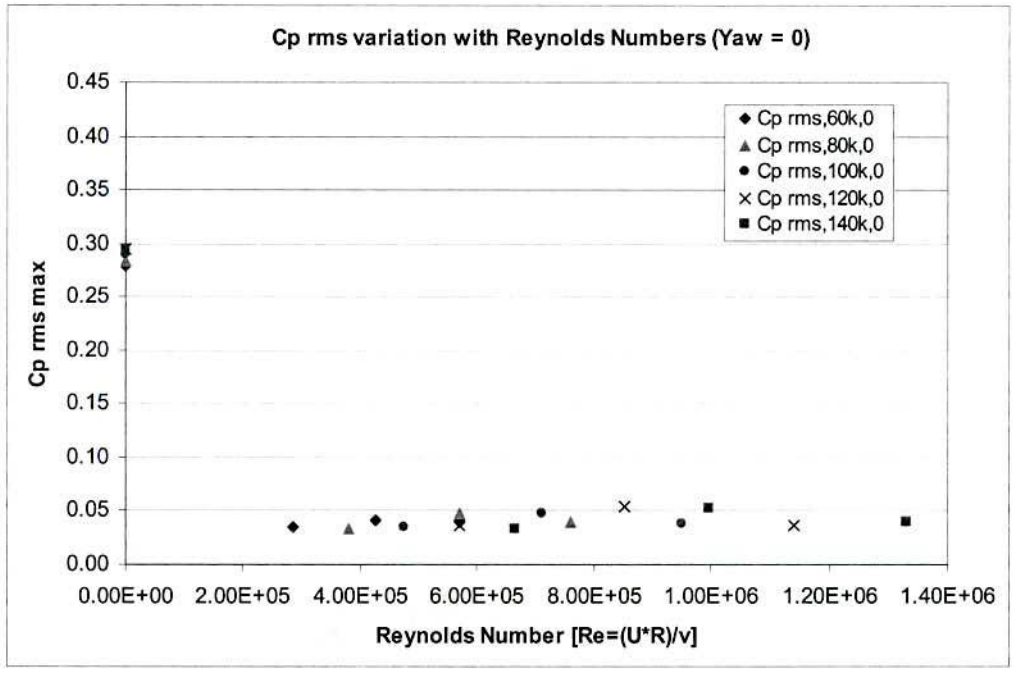

Figure 5.1: Fluctuating Cp rms Variation with Reynolds Number based on Local Radius, Yaw = 0°

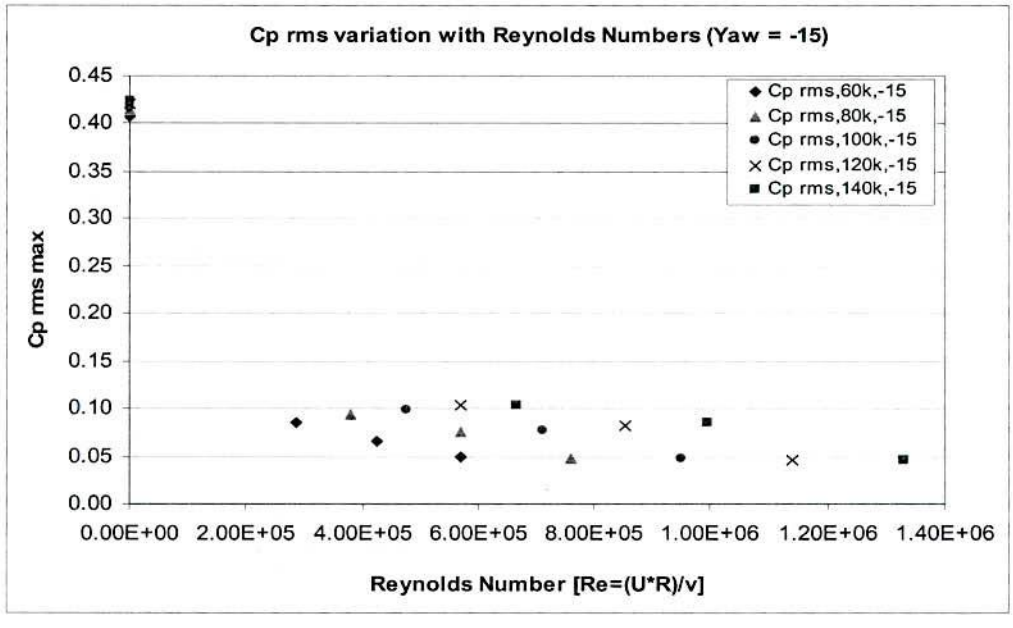

Figure 5.2: Fluctuating Cp rms Variation with Reynolds Number based on Local Radius, Yaw = -15°

5.1.3 Fluctuating Pressures in the 'Tripped' Separations

A production vehicle always has some devices such as rain gutters, body cavities and seals, which are potential sources of flow separation. Flow around the A-pillar has a relatively high velocity, so any exposed sharp edge or cavity has the potential to generate both high levels of (acoustic) noise and hydrodynamic fluctuating pressures.

An exposed rain gutter in the A-pillar region generates pressure fluctuations by forcing the flow to separate. As discussed in Chapter 3, a 15 mm high step was used on the smooth surface in the A-pillar region of the large and small ellipsoidal models to simulate the flow behind a rain gutter. The magnitude of the fluctuating pressure coefficients could be as high as 6 times the corresponding value with no trip. The power spectral density plot showed that the fluctuating pressure spectrum behind a step contained higher energy in all frequencies up to 8000 Hz compared to the attached flow. The highest energy was found at frequencies close to 200 Hz. An average of 16 dB variation (between trip and no trip) was measured at 80 km/h compared to 13 dB in a separated flow behind a 10 mm fence on a flat plate at approximately 79 km/h reported by Fricke (1971). The amplitude and frequency of the fluctuating pressure studied here scaled well with the velocity and was found to be in good agreement with findings by Fricke and Stevenson (1968) in separated flows behind a fence.

5.2 Comparison of Model-Scale Results with Production Vehicles

The normalised results from the scale models can be compared to the results of the production vehicle although it is realised that the geometries are different. The surface mean and fluctuating pressure coefficients were independent of the Reynolds number at positive yaw angles for the idealised models as well as for the production vehicle. Some Reynolds number sensitivities were evident in separated flows at negative and zero yaw angles for both models and production vehicle. The pattern of surface mean and fluctuating pressures on the side windows for the production vehicle and the slanted sharp-edged model were similar, however a significant difference between the magnitude of pressures (surface mean and fluctuating) was noted. The frequency-based analysis showed that most of the fluctuating pressures were generated in the low frequencies (100-400 Hz) for the slanted sharp-edged model and the production vehicle, and the normalised power spectra exhibited similarities.

The values of the fluctuating pressure coefficients found behind a trip in the smooth flow close to the A-pillar of the scale models and in a similar region (downstream of the rain gutters but without any extra flow trip) of a production vehicle were compared. The comparison shows good agreement, although the scale model and production vehicle's geometries are different.

5.3 Implication of Model-Scale Results: An Aeroacoustic Testing Tool for Car Manufacturers

The fluctuating pressures generated in the A-pillar region impinge upon the side window and cause it to vibrate. The vibrating window panel radiates noise into the passenger compartment of a vehicle. Knowing the fluctuating pressures on the side window and material properties of the side window panel, it is possible to predict the radiated noise level inside the cabin of a production vehicle. A semi-empirical method developed by George and Callister (1996) can be used to predict the interior aerodynamic noise level if the pressure fluctuation on the side window is known. Previously, it was difficult to predict the interior aerodynamic noise level as little knowledge on the flow separation on the side window in the A-pillar region was available.

The selection of optimal curvature of the A-pillar and windshield is very important during the initial design stage of vehicle manufacturing. Therefore, the graphical relationship of the A-pillar curvature and the fluctuating pressure coefficients established (Figure 3.65 in Chapter 3) in this study will be useful in selection of the optimal geometry of the A-pillar and windshield.

The effects of Reynolds numbers on the A-pillar flow were relatively unknown. For the restricted range of Reynolds number and geometries investigated, the current study has revealed that the effects of Reynolds number are relatively small. However it must be noted that (as is common in many model-scale tests) the full-scale Reynolds number was not achieved. Although the amplitude and frequency of the fluctuating pressure scale well with velocity head and Strouhal number, the effects of the source length scale are not well understood. Prior work indicates (Fricke and Stevenson-1968 and Blake-1970) that generally if the frequency and amplitude scale with velocity head then they also scale with source length. Therefore, a scale model, which is a replica of a full-size vehicle, can be used for the assessment of the surface hydrodynamic pressure in the A-pillar region of a production vehicle (in absence of

atmospheric turbulence and wind gusts) as frequency and amplitude of the fluctuating pressure scale well with velocity head and Strouhal number.

Current technology for forming laminated glass sets a relatively low limit for three-dimensionality in windscreens. However, the availability of more advanced materials such as Polycarbonate offers the possibility of larger radii, as has been investigated in this work of a vehicle's A-pillar and windscreen for the future. Its use as A-pillar and windshield components has the potential to minimise the blind spots created by the A-pillars and improve the driver's visibility.

The practical implementation of knowledge from this work (restricted range of geometries and in absence of rear view mirrors) may lead to reducing the flow separation, thus reducing the interior noise and lowering the cost of a new production vehicle, as less expenditure will be required for composite sealing acoustic materials.

Additionally this work will also be of benefit to the manufacturers of commercial vehicles (buses and trucks). The windshield of a bus or a truck is similar to the windshield of the rectangular model studied in this work. The study of fluctuating pressure on the side window in the A-pillar region shows that the vertical windshield is capable of producing significant noise even at positive yaw angles. Therefore, optimisation of heavy vehicle windshields (leading edge radii, curvature, etc.) can eliminate the potential noise sources.

Chapter Six

CONCLUSIONS

The main objectives of this work were to understand the effects of curvature, yaw angle and Reynolds number in the A-pillar location on the surface mean and fluctuating pressures. The following conclusions apply within the assumptions made in the analysis and experiments, the sensitivity of the measurements and the limits of scientific and engineering inference. In particular, it is emphasised that these conclusions apply to the range of model shapes and motor cars tested and to within the range of test conditions investigated. It is possible that some of the conclusions have much wider applications. The following conclusions are therefore drawn:

- The surface mean and fluctuating pressure coefficients were found to be independent of Reynolds number for scale models except for some minor variations at negative (on the leeward side) and zero yaw angles. This minor dependency was evident in separated regions but not evident in re-attached areas. The non-dimensional power spectral density also showed no significant effects of the Reynolds number.

- A graphical relationship between the maximum fluctuating pressure coefficient and local A-pillar radii and Reynolds number (based on local radii) was established. This relationship can be used to assist in the selection of the local radius in the initial stage of vehicle design.

- The frequency-based analysis indicated that most energy from the fluctuating pressures in the A-pillar region was between Strouhal number 5 to 12 and the peak energy was close to Strouhal number 8. However, the position of peak energy shifted with yaw angle.

- The surface mean and fluctuating pressure coefficient plots, in conjunction with the flow visualisation, showed that the maximum hydrodynamic pressure fluctuation occurs between the separated and re-attached areas rather than at the re-attachment points as has been proposed by other researchers.

- As has been shown by others, local flow "trips" (such as rain gutters) were found to be capable of generating a significant amount of fluctuating pressure compared to the fluctuating pressure level generated in the A-pillar region by the typical vehicle body shape with no surface protrusion.

- These results suggest that a scale model of a full-size vehicle can be used for the assessment of the surface hydrodynamic mean and fluctuating pressures in the A-pillar region, as the effects of Reynolds number were found to be minimal, and the frequency and amplitude of the fluctuating pressure scaled well with the velocity head and Strouhal number.

- The magnitude of fluctuating pressure and the area of flow separations close to the A-pillar region depended largely on the local radii. The magnitude of the maximum surface fluctuating pressure coefficient, which arose from fluctuating pressures in the turbulent boundary layer for the scale model with larger local radii (no flow separation evident), was significantly lower than the corresponding value for the scale model with a sharp edge on the A-pillar (flow separation occurred at this sharp edge).

- Yaw angle had a significant influence on the magnitude of the surface pressures and the area of flow separation in the A-pillar region. Yaw could increase the area and magnitude of flow separation on the leeward side by an order of magnitude compared to the windward side for the slanted sharp-edged generic models. However, the generic model with no slant angle (i.e., a vertical windshield) is capable of producing an intense but relatively small flow separation on the windward side when yawed. Yaw angles had negligible effect on the fluctuating pressures for generic models that had corner radii (i.e., those found to have negligible separation).

- The surface mean and fluctuating pressure coefficients for production vehicles were also found to be independent of Reynolds number except for some minor variations at lower speeds.

- Increased rounding of the A-pillar for production vehicles significantly reduced the magnitude of the external fluctuating pressure and, to a lesser extent the 'in-cabin noise'.

Chapter Seven

Suggestions for Further Work

After conducting the work presented here and reviewing the literature available in the public domain, the following suggestions are made for further study:

1) In this study the available instrumentation, a two-channel microphone system, was used to measure the time-varying fluctuating pressure. However, for better understanding of pressure field spatial correlation, multiple phase-matched microphones are required.

2) The surface mean and fluctuating pressures were not studied at local radii between 0 and 250 mm in the current work. Since the equivalent local radii of some current passenger cars fall into this range, this is thought worthy of study.

3) The time-varying components of velocity and yaw angle that are present on-road (due to atmospheric turbulence) were not considered. This unsteadiness needs to be studied in order to quantify its effect, including low frequency modulation of the pressure fluctuations and resulting 'in-cabin noise'.

4) For further understanding of noise transmission, correlation between the external fluctuating pressure and the in-cabin noise is useful. However, it is realised that such study must be limited to specific vehicles.

5) The effects of length scale of the noise sources were not investigated in this work. It is believed that the frequency of the fluctuating pressure decreases with an increasing length scale of the noise sources. Therefore, for better understanding, the effects of length scales are worthy of investigation.

6) In the current work, the boundary layer thickness was not measured and for better understanding of the potential for separation, it is worthwhile studying the boundary layer characteristics in the A-pillar region.

7) The generic models used in this work were not intended to faithfully represent real vehicles. Some parameters of passenger vehicles, such as the side window inclination (typically 15° relative to vertical), rotating wheels, underbody flow and wheel arches were not duplicated on the models. It is believed that these parameters might have some minor effects on the A-pillar flow characteristics. It would be useful to vary these parameters in A-pillar flow studies.

8) The effects of the rear view mirror on the A-pillar flow characteristics were not considered in this work. For the future generation of vehicles, mirror location may be shifted from the A-pillar region. The airflow in the A-pillar region is extremely complex and the presence of mirror in this area can make the flow more complex. However, the influence of mirror on the A-pillar vortex is worthy of further study.

REFERENCES

Alam, F., Watkins, S. and Zimmer, G., "Wind-Tunnel and On-Road Comparison of Aerodynamic Noise due to Car Modifications", The 6th International Congress on Sound and Vibration, Copenhagen, Denmark, Vol. 7, PP 3457-3464, 5-8 July, 1999.

Alam, F., Watkins, S., Song, B., Steiner, T. and Humphris, C., "The Flow Around a Car A-pillar", The 13th Australasian Fluid Mechanics Conference, Melbourne, Australia, PP 461-464, 13-18 December, 1998.

Anderson, J. S. and Bratos-Anderson, M., "Noise- its Measurement, Analysis, Rating and Control", Ashgate Publishing Company, ISBN 0 291 397948, Vermont, USA, 1993.

Barlow, J. B., Rae Jr., W. H. and Pope, A., "Low-Speed Wind Tunnel Testing", Third Edition, John Wiley & Sons, Inc., ISBN 0 471 55774 9, New York, USA, 1999.

Bearman, P. W., De Beer, D. and Harvey, J. K., "Experimental Studies of Road Vehicle Flow Fields", AIAA Paper 89-1887, PP 1-9, 1989.

Bendat, J. S. and Pierson, A. G., "Engineering Applications of Correlation and Spectral Analysis", John Wiley, New York, 1980.

Blake, W. K., "Mechanics of Flow-Induced Sound and Vibration" Volume II, Academic Press Inc, Orlando, Florida, 1986.

Blake, W. K., "Turbulent Boundary-Layer Wall-Pressure Fluctuations on Smooth and Rough Walls", Journal of Fluid Mechanics, Vol. 44, Part 4, PP 637-660, 1970.

Bradshaw, P., "'Inactive' Motion and Pressure Fluctuations in Turbulent Boundary Layers", Journal of Fluid Mechanics, Vol. 30, Part 2, PP241-258, 1967.

Buchheim, R., Dobrzynski, W., Mankau, H. and Schwabe, D., "Vehicle Interior Noise Related to External Aerodynamics", International Journal of Vehicle Design, Vol. 3, No. 4, PP 398-410, U.K., 1982.

Callister, J. R., "The Transmission of Aerodynamically-Generated Noise Through Panels in Automobiles", M.Sc. Thesis, Department of Mechanical and Aerospace Engineering, Cornell University, Ithaca, New York, USA, 1992.

Callister, J. R. and A. R. George, "Measurement and Analysis of Automobile Wind Noise," SAE Paper No. 930299, USA, 1993.

Callister, J. R. and George, A. R., Dobrasevic, Z. D., Puskarz, M. M., Petz, W. M. and Freeman, G. E., "Aeroacoustic and Acoustic Testing of Automobile Side Windows", SAE Paper No. 960902, USA, 1996.

Callister, J. R., "Measurement, Prediction and Production of the Transmission of Separated Flow Noise through Panels", Ph.D. Thesis, Cornell University, Ithaca, New York, USA, 1996.

Cooper, K. R., "Bluff-Body Aerodynamics as Applied to Vehicles," Second International Colloquium on Bluff Body Aerodynamics and Applications (BBAA II), Vol. 1, Melbourne, Australia, 7- 10 December, 1992.

Cooper, K. R., "Atmospheric Turbulence with Respect to Moving Ground Vehicles", Journal of Wind Engineering and Industrial Aerodynamics, 17 (2), PP 215-218, 1984.

Cooper, K. R., "The Effects of Front-Edge Rounding and Rear-Edge Shaping on the Aerodynamic Drag of Bluff Vehicles in Ground Proximity", SAE Paper No. 850288, SAE, USA, 1985.

Curle, N., "The Influence of Solid Boundaries on Aerodynamic Sound", Proceedings of Royal Society, London, Series A, Vol 231, No. 1187, PP 505-514, 1955.

Dobrzynski, W. and Soja, H., "Effect on Passenger Car Wind Noise Sources of Different A-Post Configurations", Inter-Noise-94, PP 387-390, Yokohama, Japan, August 29-31, 1994.

Dobrzynski, W., Buchheim, R., Mankau, H. and Schwabe, D., "Vehicle Interior Noise Related to External Aerodynamics," International Journal of Vehicle Design, Special Publication, SP3, PP 197-209, U.K., 1983.

Dowling A. P. and Ffowcs-Williams, J. E., "Sound and Sources of Sound" Ellis Horwood Ltd., West Sussex, England, 1983.

Farabee, T. M., "An Experimental Investigation of Wall Pressure Fluctuations Beneath Non-Equilibrium Turbulent Flows", Ph.D. dissertation, The Catholic University of America, 1986, and/or David W. Taylor Naval Ship Research and Development Centre, Betheada, Maryland, USA, 1986.

Ffowcs-William, J. E. and Hall, L. H., "Aerodynamic Sound Generation by Turbulent Flow in the Vicinity of a Scattering Half Planes", Journal of Fluid Mechanics, Vol 40, Part 4, PP 657-670, 1970.

Fricke, F. R. and Stevenson, D. C., "Pressure Fluctuations in a Separated Flow Region", Journal of the Acoustic Society of America, Vol 44 No. 5, PP 1189-1200, 1968.

Fricke, F. R., "Pressure Fluctuations in Separated Flows", Journal of Sound and Vibration, Vol 17, No. 1, PP 113-123, 1971.

George, A. R. (Ed.), "Automotive Wind Noise and its Measurement" An Information Report of the SAE Wind Noise Measurement Committee, SAE, USA, August, 1996.

George, A. R. and Callister, J. R., "Aeroacoustics of Passenger Cars- State- of- the-Art", Seminar on Aerodynamics and Powertrain Automobile Noise, Industrie Pininfarina, Aerodynamic & Aeroacoustic Research Centre, Grugliasco, Italy, 9th October, 1996.

George, A. R. and Callister, J. R., "Recent Advances in Understanding Automobile Aerodynamic Noise," AIAA Journal, No. 4, PP 1-16, 1995.

George, A. R., "Automobile Aerodynamic Noise", SAE Transactions, USA, 1990.

George, A. R., "Automobile Aeroacoustics", AIAA Paper 89-1067, USA, 1989.

Goldstein, M. E., "Aeroacoustics", McGraw-Hill Book Company, 1976.

Gutin, L., "On the Sound Field of a Rotating Propeller", NACA TM 1195, 1948.

Hamel, T. A. and Ahuja, K. K., "Wind Noise Measurements on an Automobile Side Glass with A-pillars of Different Height", AIAA Journal, USA, 1996.

Hansen, C. H. and Bies, D. A., "Engineering Noise Control", Second Edition, London, 1996.

Haruna, S., Nouzawa, T., Kamimoto, I. and Hiroshi, S., "An Experimental Analysis and Estimation of Aerodynamic Noise Using a Production Vehicle," SAE Paper No. 900316, USA, 1990.

Hooper, J. D. and Musgrove, A. R., "Multi-hole Pressure Probes for the Determination of the Total Velocity Vector in Turbulence Single-Phase Flow," 4th International Symposium Transport Phenomena in Heat and Mass Transfer, Sydney, Australia, July 14-19, 1991.

Hooper, J. D. and Musgrove, A. R., "Reynolds Stress, Mean Velocity, and Dynamic Static Pressure Measurements by a Four-Hole Pressure Probe", Journal of Experimental Thermal and Fluid Science, Vol. 15, PP 375-383, 1997.

Howe, M. S., "The Generation of Sound by Turbulent and Separated Flows", Boston University College of Engineering, Journal of Wind Engineering and Industrial Aerodynamics, Vol. 49, 1993.

Howe, M. S., "The Influence of Mean Shear Layer on Unsteady Aperture Flow, with Application to Acoustical Diffraction and Self-sustaining Cavity Oscillations", Journal of Fluid Mechanics, Vol. 109, PP 125-146, 1981.

Howe, M. S., "Surface Pressures and Sound Produced by Turbulent Flow over Smooth and Rough Walls", The Journal of the Acoustical Society of America, Vol. 90 No. 2, PP 1040-1047.

Howe M. S., "The Displacement-Thickness Theory of Trailing Edge Noise", The Journal of Sound and Vibration, Vol. 75(2), PP 239-250, 1981.

Hucho, W-H. (Ed.), "Aerodynamics of Road Vehicles" 4th Edition, SAE International, Warrendale, PA, USA, 1998.

Hucho, W-H. (Ed.), "Aerodynamics of Road Vehicles", Butterworths, London, UK, 1987.

Janvey, P. L., "The Sound Power from Turbulence: A Theory of the Exchange of Energy between the Acoustic and Non-acoustic Fields", Journal of Sound and Vibration, Vol 131, No. 1, PP 37-66, 1989.

Kartz, J., "New Direction in Race Car Aerodynamics- Designing for Speed", Robert Bently Publishers, Cambridge, USA, ISBN 0-8376-0142-8, 1995.

Kumarasamy, S. and Karbon, K., "Aeroacoustics of an Automobile A-pillar Rain Gutter: Computational and Experimental Study", SAE Special Publication 1457, Detriot, USA, March, 1999.

Kunstner, R., Potthoff, J. and Essers, U., "The Aeroacoustic Wind Tunnel of Stuttgart University", SAE Paper No. 950625, Detroit, USA, Feb 27- March 2, 1995.

Lighthill, M. J., "On Sound Generated Aerodynamically: Part 1", Proceedings of the Royal Society of London, 211A, 1107, PP 564-587, 1951.

Lighthill, M. J., "On Sound Generated Aerodynamically: Part II - Turbulence as a Source of Sound", Proceedings of the Royal Society of London, 222A, 1148, PP 1-32, 1954.

Lindener, N. and Geib, W., "Aeroakustische Effekte an Fahrzeugen analysiert im BMW-Akustikwindkanal", Proceedings of the Symposium 'Akustik und Aerdynamik des Kraftfahrzeugs', Haus der Technik, Essen, Germany, 1994.

Maskell, E. C., "Flow Separation in Three Dimensions", R.A.E. Aero.2565, November, 1955.

Mercker, E., Donavan, P. R., Clark, P. J. F., Every, D. H. and Wiedemann, J., "Acoustic Wind Tunnels", Chapter VI in George, A. R. (Ed.), Automobile Wind Noise and its Measurement, SAE SP-1184, SAE, USA, 1996.

Mohsen, A. M., "Experimental Investigation of the Wall Pressure Fluctuations in Separated Flows", Boeing Company Report D6-17094, USA, 1967.

Musgrove, A. R. de L. and Hooper, J. D., "Pressure Probe Measurement of the Turbulent Stress Distribution in a Swirling Jet", Proceedings of the Third World Conference on Experimental Heat Transfer, Fluid Mechanics and Thermodynamics, 31 October-5 November, PP 172-179, Honolulu, Hawaii, USA, 1993.

Nguyen, T. M., "The Sideways Dynamic Force on Passenger Cars in Turbulent Winds", SAE Paper No. 970405, SAE, USA, 1997.

Nienaltowska, E., "Separated Flow on the Car Body: Spectral and Spatial Characteristics Analysed from the Aeroacoustic Viewpoint," International Journal of Vehicle Design, Vol. 14, No. 5-6, U.K., 1993.

Norton, M. P., "Fundamentals of Noise and Vibration Analysis for Engineers", Cambridge University Press, Cambridge, U.K., 1989.

Ogawa, S. and Kamioka, T., "Review of Aerodynamic Noise Prediction Using CFD", SAE SP-1441, SAE, Warrendale, Pennsylvania, USA, 1999.

Peric, C. A., Watkins, S., Lindqvist, E. and Saunders J., "Effects of On-Road Turbulence on Automotive Wind Noise: Comparing Wind-Tunnel and On-Road Tests", SAE Paper No. 970406, SAE, Detroit, Michigan, USA, 1997.

Popat, B. C., "Study of Flow and Noise Generation from Car A-pillars", Ph.D. Thesis, Department of Aeronautics, Imperial College of Science, Technology and Medicine, The University of London, U.K, 1991.

Powell, A., "Aerodynamic Noise and the Plane Boundary", Journal of the Acoustical Society of America, Vol. 32(8) PP 982-990, 1960.

Sadakata, O., "A Consideration of Wind Noise Reduction by Air Flow Control", 22nd FISITA No. 885115, PP 182-189, 1988.

Saunders, J. W. and Mansour, R. B., "On-Road and Wind Tunnel Turbulence and Its Measurement using a Four-Hole Dynamic Probe ahead of Several Cars", SAE Paper No. 2000-01-0350, PP 5-24, SAE, Detroit, USA, 2000.

Strumolo, G. S., "The Wind Noise Modeller", SAE Paper No. 971921, PP 417-424, SAE, Detroit, USA, 1997.

Tam, C. K. W., "Computational Aeroacoustics: Issues and Methods", AIAA Journal, Vol. 33, No. 10, October, 1995.

Watanabe, M. and Harita, M., "The Effects of Body Shapes on Wind Noise", SAE Paper No. 780266, SAE, USA, 1978.

Watkins, S., Riegel, M. and Wiedemann, J., "The Effects of Turbulence on Wind Noise: A Road and Wind-Tunnel Study", 4th Stuttgart International Symposium on Automotive and Engine Technology, Stuttgart, Germay, ISBN 3-8169-1981-2, PP 326-340, 20-22 February, 2001.

Watkins, S. and Oswald, G., "The Flow Field of Automobile Adds-ons–with Particular Reference to the Vibration of External Mirrors", Journal of Wind Engineering and Industrial Aerodynamics, Vol 83, PP 541-554, 1999.

Watkins, S., Oswald, G., Czydel, R. and Saunders, J., "Aerodynamically-Induced Noise and Vibration of Automobile Adds-Ons- External Mirrors, Aerials and Roof-racks", The 9th International Pacific Conference on Automotive Engineering (IPC-9), Bali, Indonesia, 16-21 November, 1997.

Watkins, S. and J. W. Saunders, "Turbulence Experienced by Road Vehicles under Normal Driving Conditions," SAE Paper No. 950997, SAE, USA, 1995.

Watkins, S., "Wind Tunnel Modelling of Vehicle Aerodynamics: With Emphasis on Turbulent Wind Effects on Commercial Vehicle Drag", Ph.D. Thesis, RMIT University, Melbourne, Australia, 1990.

Wiedemann, J., Wickern, G., Ewald, B. and Mattern, C., "Audi Aeroacoustic Wind Tunnel", SAE Paper No. 930300, SAE, Detroit, Michigan, USA, 1993.

Willmarth, W. W., "Pressure Fluctuations Beneath Turbulent Boundary Layers", Annual Review of Fluid Mechanics, Vol. 7, PP 13-38, 1975.

Zhu, M., Hanaoka, Y., Aoki, K., Miyata, H. and Terada, I., "A Numerical Study of Wind Noise Around Front Pillar", SAE Paper No. 930296, SAE, USA, 1993.

Zhu, M., Hanaoka, Y. and Miyata, H., "Numerical Study on the Mechanism of Wind Noise Generation About a Car-Like Body", Transactions of the ASME, Vol. 116, PP 424-432, September, 1994.

Zimmer, G., "Wind-Tunnel and On-Road Comparison of Interior Noise of a Production Vehicle with Particular Emphasis on Atmospheric Turbulence", Ph.D. Thesis (expected to submit in 2001), Department of Mechanical and Manufacturing Engineering, RMIT University, Melbourne, Australia, 2001.

BIBLIOGRAPHY

Alam, F., Watkins, S., Zimmer, G. and Humphris, C., "Effects of Vehicle A-pillar Shape on Local Mean and Time-Varying Flow Properties", SAE Paper No.2001-01-1086 and also SAE Special Publication SP-1600, Detroit, Michigan, USA, 5-8 March, 2001.

Alam, F., "Flow and Flow Induced Noise Measurements on a Series of Idealised Road Vehicle Models", Young Engineers Conference, SAE-Australasia, Melbourne, Australia, 5-6 October, 2000.

Baker, C. J., "Ground Vehicles in High Crosswinds, Part 1, 2 and 3", Journal of Fluids and Structures, Vol. 5, PP 69-90, 91-111, 221-241, 1991.

Bearman, P. W. and Morel, T., "Effects of Free Stream Turbulence on the Flow Around Bluff Bodies", Progress in Aerospace Sciences, Vol. 20, PP 97-123, 1983.

Bearman, P. W., De Beer, D., Hamidy, E. and Harvey, J. K., "The Effects of a Moving Floor on Wind-Tunnel Simulation of Road Vehicles", SAE Paper No. 880245, SAE, USA, 1988.

Blake, W. K., "Mechanics of Flow-Induced Sound and Vibration", Volume I, Academic Press Inc., New York, USA, 1986.

Blevins, R. D., "Flow-Induced Vibration", Van Nostrand Reinhold Co, New York, USA, 1977.

Bradshaw, P., "An Introduction to Turbulence and Its Measurement", Pergamon Press Ltd, Oxford, U.K., 1975.

Bruel & Kjaer, "Measuring Sound", Information Bulletin, DK-2850 Naerum, Denmark, 1984.

Cogotti, A., "Aeroacoustics Development at Pininfarina," SAE Paper No. 970402, SAE, USA, 1997.

Ford, R. D., "Introduction to Acoustics", Elsevier Publishing Company Limited, London, U.K., 1970.

Foss, J. F., "Report of the Working Group: Automotive Aerodynamics," Report No. MSU-006-96, Michigan State University, USA, 1996.

Genuit, K. and Burkhard, M., "Artificial Head Measurement Systems for Subjective Evaluation of Sound Quality", Journal of Sound and Vibration, PP 18-23, March, 1992.

Gotz, H., "Bus Design Features and Their Aerodynamic Effects", International Journal of Vehicle Design, Special Publication SP 3, PP 229-255, U.K., 1983.

Heller, H. H., "Flow Induced pressure Oscillations in Shallow Cavities", Journal of Sound and Vibration, Vol. 18 (4), PP 545-553, 1971.

Her, J. Y., Lian, M., Lee, J. J. and Moore, J., "Experimental Assessment of Wind Noise Contributor to Interior Noise," SAE Paper No. 971922, SAE, USA, 1997.

Hinze, J. O., "Turbulence", 2nd edition, McGraw-Hill inc., New York, USA, 1975.

Holmes, J. D., "A Review of Tubing Techniques for Measurement of Fluctuating Surface Pressures", Second World Conference of Experimental Heat Transfer, Dubrovnik, Croatia, 1991.

Humphris, C., "The Aerodynamic Development of the AU Falcon", SAE-Australasia Journal, PP 38-41, Melbourne, Australia, September/October, 1998.

Krane, M. H. and Pauley, W. R., "Estimation of the direct acoustic radiation form a transitional boundary layer using velocity measurements", Journal of Sound and Vibration, Vol. 181(5), PP 737-763, 1995.

Leslie D. C., "Developments in the Theory of Turbulence", Clarendon Press, Oxford, U.K., 1973.

Morse, P. and Ingard, K., "Theoretical Acoustics", Princetown University Press, New Jersey, USA, 1986.

Newland, D. E., "An Introduction to Random Vibrations, Spectral and Wavelet Analysis", Third Edition, Wiley and Sons Inc., ISBN 0582 21584 6, New York, 1993.

Oswald, G., "Aerodynamically Induced Noise and Vibration of Automotive External Rear View Mirrors," Ph.D. Thesis, Department of Mechanical and Manufacturing Engineering, RMIT University, Melbourne, Australia, 1999.

Peters, J. L., "Aerodynamics of Very High Speed Trains and Maglev Vehicles: 'State-of-the-art' and Future Potential", International Journal of Vehicle Design, Special Publication SP3, U.K., 1983.

Randall, R. B., "Frequency Analysis", Bruel & Kjaer, ISBN 87 87355 07 8, Denmark, 1987.

Rockwell, D. and Knisely, C., "Observations of the Three-dimensional Nature of Unstable Flow Past a Cavity", Physics of Fluids, Vol. 23(3), March, 1980.

Rockwell, D. and Naudascher, E., "Self-sustained Oscillations of Impinging Free Shear Layers", Ann. Rev. Fluid Mechanics, (11), PP 67-94, 1979.

Rockwell, D. and Knisley, C., "The Organised Nature of Flow Impingement Upon a Corner", Journal of Fluid Mechanics, Vol. 93, Part 3, PP 413-432, 1979.

Saunders, J. F., Watkins, S. and Melbourne, W. H., "Monash/RMIT Vehicle Aeroacoustic Wind Tunnel: Turbulence for Car Aerodynamics Testing", Proceeding of the Ninth International Pacific Conference on Automotive Engineering, Bali, Indonesia, November, 1997.

Schlichting, H. and Gersten, K., "Boundary Layer Theory", 8th Revised and Enlarged Edition, Springer, Berlin, ISBN 3540662707, 2000.

Sumitani, K. and Shinohara, T., "Research on Aerodynamic Noise around Automobiles," Japanese SAE: Review, Vol. 16, PP 157-164, 1995.

Takagi, M., Hayashi, K., Shimpo, Y. and Uemura, S., "Flow Visualization Techniques in Automotive Engineering", International Journal of Vehicle Design, Special Publication SP 3, PP 500- 511, U.K., 1983.

Watkins, S., Alam, F., O'Shea, P. and Zimmer, G., "Analysis of Airflow Impinging on the A-pillar of a Car and Comparison with Interior Noise", The 6th International Congress on Sound and Vibration, Copenhagen, Denmark, Vol. 7, PP 3449-3456, 5-8 July, 1999.

Wilson, T. A., "Experiments on the Fluid Mechanics of Whistling", Journal of the Acoustical Society of America, Vol. 50, No. 1, Part 2, PP. 366-372

Zimmer, G., Alam, F., Watkins, S. and Peric, C., "Comparison of High Blockage Wind-Tunnel, Open Jet Wind-Tunnel and On-Road Testing With Respect to External Surface Pressures", SAE Paper No. 2001-01-1087 and also SAE Special Publication, SP-1600, Detroit, Michigan, USA, 2001.

APPENDICES

Appendix A

RMIT University and Monash/RMIT Universities' Aeroacoustic Wind-Tunnels Calibrations

The RMIT University Aeroacoustic Wind-Tunnel and Monash/RMIT Universities' Aeroacoustic Wind-Tunnel were calibrated for this work. Local pressures in the RMIT Wind-Tunnel were measured at the location where the model was mounted via a NPL modified ellipsoidal head pitot static tube, which was connected to a MKS Baratron reference pressure transducer. Dynamic pressure was measured vertically from 150 to 600 mm in increments of 150 mm from the tunnel floor thus covering the heights of the models used. The nominal tunnel air speed was 30, 40, 50, 60, 80, 100, 120 and 140 km/h. The local velocity was normalised by dividing by the wall reference velocity and plotted against the height for 60, 100 and 140 km/h and is shown in Figure A.1. Figure A.1 shows that the local velocity does not vary significantly in reference to the tunnel wall-mounted reference velocity for the given speed. However, a small variation of normalised velocity can be seen near the tunnel floor (Figure A.1). No correction of velocity was deemed necessary as local flow velocity does not vary significantly with wall mounted reference velocity or height. The accuracy of the velocities measured with various speeds across the plane was estimated to be $\pm 1.0\%$. Hence the tunnel reference velocity was used in the calculation of pressure coefficients.

In Monash/RMIT Universities' Aeroacoustic Wind-Tunnel, a four-hole Cobra Probe was used to measure the flow properties across the plane at different locations vertically and horizontally in the test section. Details of the Cobra Probe were given in Chapter Two and also in Appendix B. The reference speed was measured by using Honeywell Pressure Transducers, which were connected to two wall mounted reference Pitot-static tubes located upstream of the jet. The local velocity in the test section was calculated from the pressure data measured by the Cobra Probe and plotted against the height across the plane in the test section, and is shown in Figure A.2. Figure A.2 shows that the variation of velocity profile across the test plane at

mid car position is approximately ±2.0%. Therefore, no correction was made to the test data.

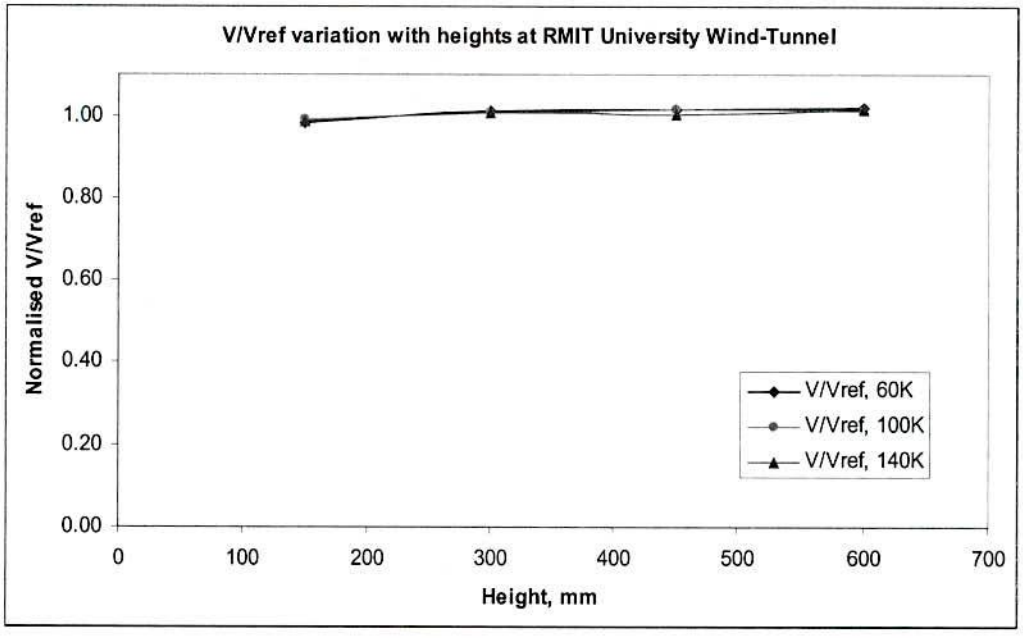

Figure A.1: Normalised Local Velocity Variation with Height in Relation to Reference Velocity

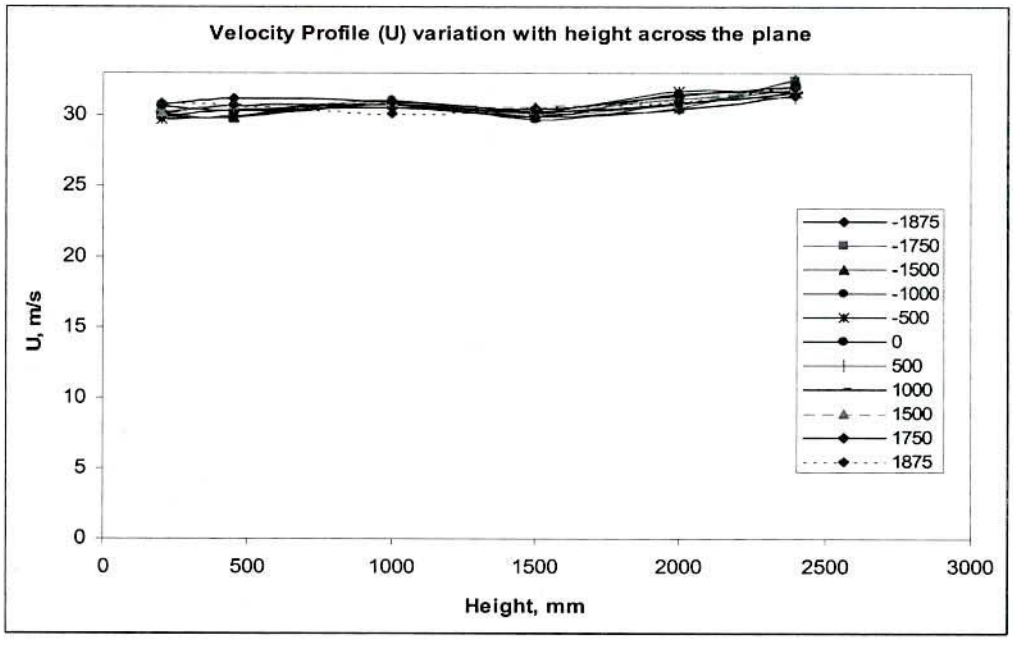

Figure A.2: Velocity Profile Variation with Height across the Test Plane (Monash/RMIT Universities' Aeroacoustic Wind-Tunnel)

Appendix B

Multi-Hole Cobra Probe: Use and Calibration

B.1 Theory and Principle

A four-hole Cobra Probe is a commercially available device which features a triangular shaped head with a maximum width of 2.5 mm. Three 45° facetted faces surround a central face. A 0.5 mm hole is located in each face, with each hole connected via 250mm of 0.5 mm internal diameter stainless steel tubing to pressure transducers located in the main body of the probe (see Figure 2.1 in Chapter Two). The overall length of the probe is approximately 400 mm.

As mentioned in Chapter Two, a four hole Cobra Probe was used to measure the transient flow properties (e.g. all three orthogonal velocity components u, v and w, and static pressure). As well as providing the time history of each variable, the turbulence intensities and Reynolds stresses can be calculated using the proper software. The principle of operations was described by Hooper et al. (1991). The magnitude of the instantaneous local velocity vector, the flow yaw and pitch angles (within a range of ±45°) and the local instantaneous static pressure, are detected by four pressure taps located on faceted head. The four pressure values are later converted to two non-dimensional ratios of X1 and X2 and are used as independent variables. The independent variables of X1 and X2 are related to the four independent variables of total pressure, dynamic pressure, flow yaw and pitch angles through pre-calculated calibration surfaces. The surfaces are determined through calibration at a constant mean velocity and the procedure is considered valid due to the relative insensitivity of the calibration surfaces to the probe Reynolds number. According to Hooper et al. (1991) this Reynolds number insensitivity is considered to be due to the fact the separation angles of the flow are largely set by the angle of the incident velocity vector to the faceted surface. Surface roughness elements have little effect on

the separation angle, and the effect of free stream turbulence intensity is also minimised.

Hooper et al. (1997 and 1991) reported that the spatial resolution of the probe head is 2.6 mm and the probe can resolve flow structures above a scale of approximately ten times that of the probe's head size. At an average velocity of 50 m/s, a frequency response of the probe approximately 1.5 kHz is needed to match the spatial resolution of the turbulent flow field around the probe head. The pressure from the 0.5 mm diameter pressure taps in the head is captured by low volume piezo-resistive pressure transducers through a tubing system in the frequency range 0 to 1.5 kHz with a maximum 0.4 amplitude reduction. During the data recording phase, the tubing resonance that creates amplitude and phase distortion is generally not corrected for. However, these amplitude and phase distortions of the signal are overcome by using a two steps fast Fourier transform into the frequency domain, and the resultant amplitude spectra is then linearised by dividing by the known complex transfer function of the pressure tubing system (for more details, refer to Musgrove and Hooper, 1993). However, a small distortion at the beginning and end of the signal is expected due to the window effect. Therefore, the regained undistorted pressure signals are used to form the estimate of four dependent quantities: total pressure, dynamic pressure, and yaw and pitch angles. The time dependent quantity such as u(t), v(t) and w(t) can be determined.

B.2 Calibration

The Probe's dynamic calibration was done by Hooper et al. (1997). The dynamic calibration does not change significantly with atmospheric variations over a period of time. However, static calibration is required to be checked after a certain interval. The Cobra Probe pressure to voltage calibration is important. Therefore, calibration was done several times during the test procedures and data acquisitions. Figure B.1 shows the schematic set up of pressure to voltage calibration. The pressure to voltage calibration plot for all four channels is shown in Figure B.2.

Out of 48 channels, only 33 channels were used in this study. The system was checked by simultaneously connecting the Scanivalve acquisition system to a precision inclined manometer and a Baratron pressure transducer through a wall-mounted reference Pitot-static tube. The Scanivalve system and the calibration apparatus is shown in Figure C.2. The pressure against the voltage output graph is shown in Figure C.3. The tunnel was run at a range of speeds whereby the acquisition system was found to give readings within ±0.5 Pascal of both the Baratron and the inclined manometer.

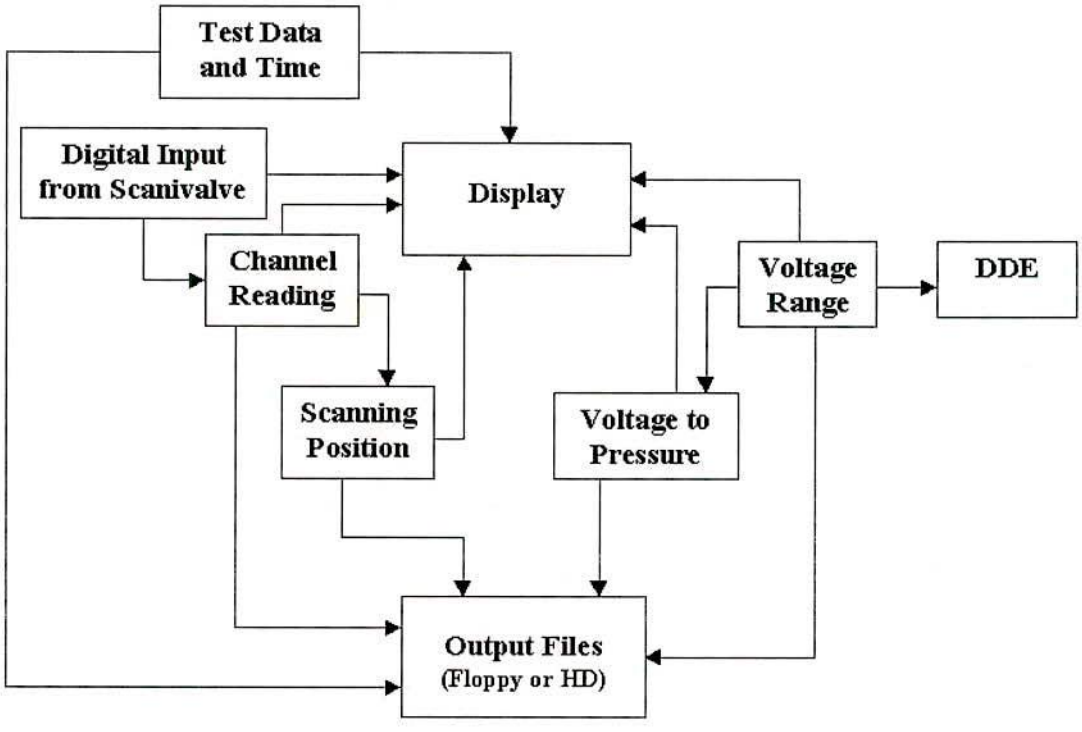

Figure C.1: Block Diagram of Scanivalve Pressure Data Acquisition System

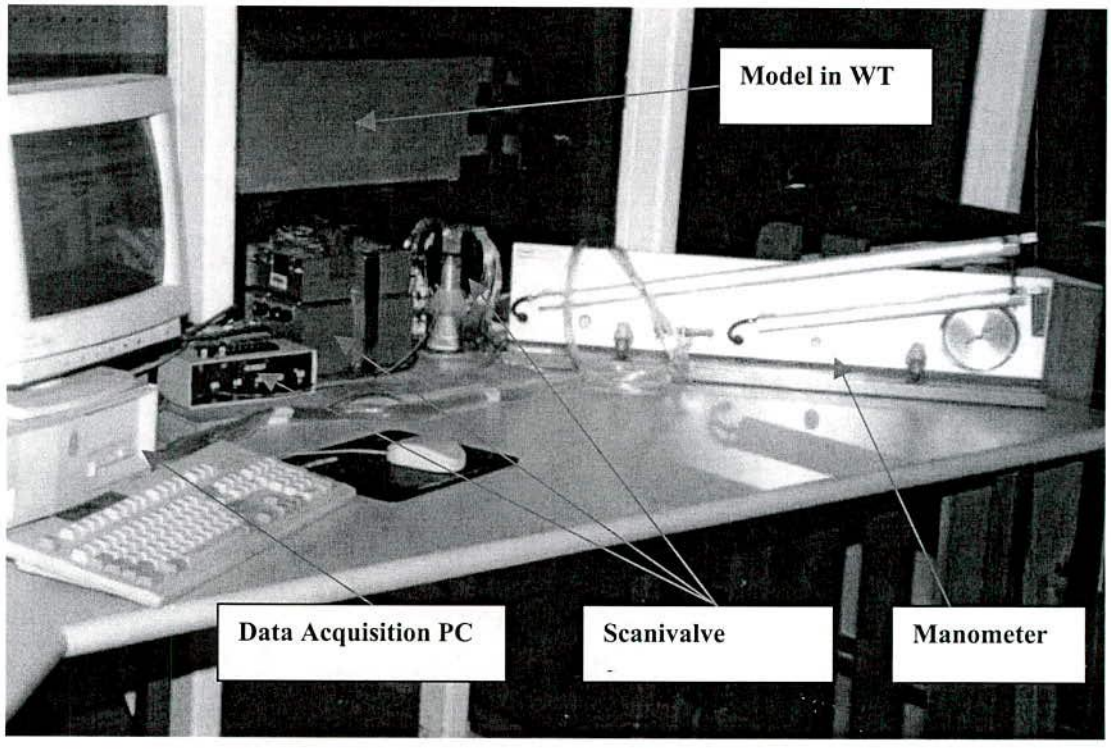

Figure C.2: Pressure to Voltage Calibration Apparatus Set Up

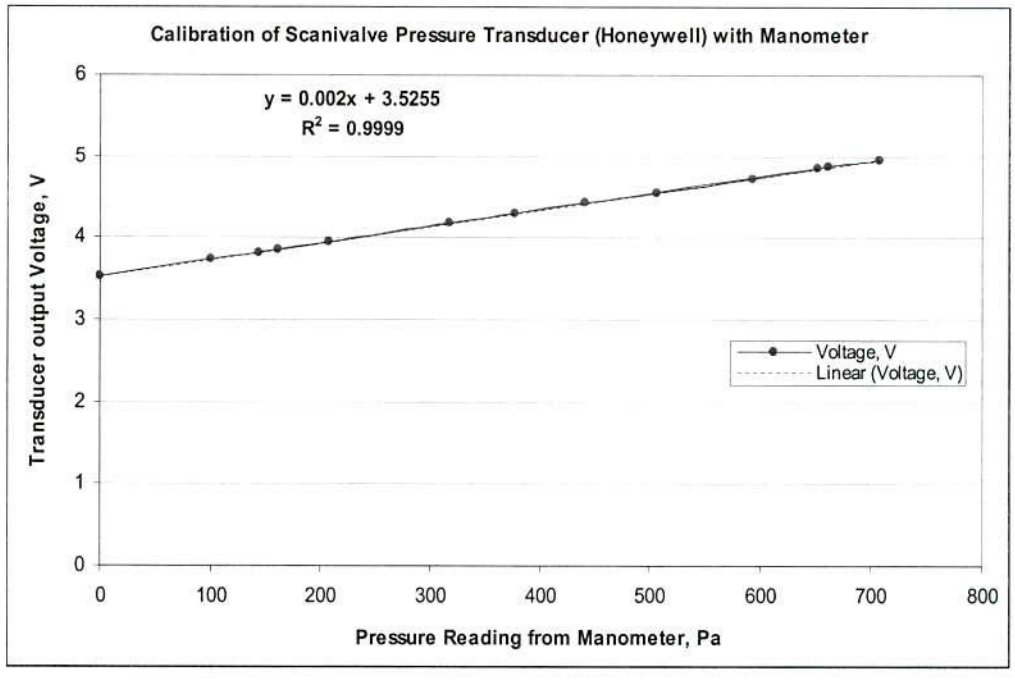

Figure C.3: Scanivalve Pressure Sensor Output: Pressure to Voltage Calibration

Appendix D

Microphone Characteristics and Calibration

D.1 G.R.A.S. Microphone Characteristics

The G.R.A.S. ¼ inch microphone, Type 40 BF, was manufactured by the G.R.A.S. Sound and Vibration Company. The G.R.A.S. ¼ inch microphone was made with stainless steel protection grid, diaphragm and housing for durability and longevity. The microphone can be used for large amplitude and high frequency measurements. The low sensitivity of the microphone allows one to measure the sound pressure level up to 168 dB. The small size reduces disturbances in the sound field, resulting in a frequency range up to 100 kHz. According to the user's manual, which was supplied by the G.R.A.S Sound and Vibration, the G.R.A.S. ¼ inch microphone complies with the requirements in IEC Standard 1094 Part 4 and also fully compatible with a B & K ¼ inch microphone.

A DC (direct current) polarisation voltage of 200 V is used for the G.R.A.S. ¼ inch microphone. A preamplifier, Type 26 AC, with 2 m cable terminated in a 7 pin LEMO 1B plug. The G.R.A.S. ¼ inch microphone was powered by a Power Module, Type 12AA. The Power Module has two microphone preamplifier input connectors for the G.R.A.S. 26 AC preamplifier. Each power module can be used for power supply to two microphones. Both channels have overload indicators and the gain can be selected individually in steps of –20 dB, 0 dB, +20 dB and +40 dB.

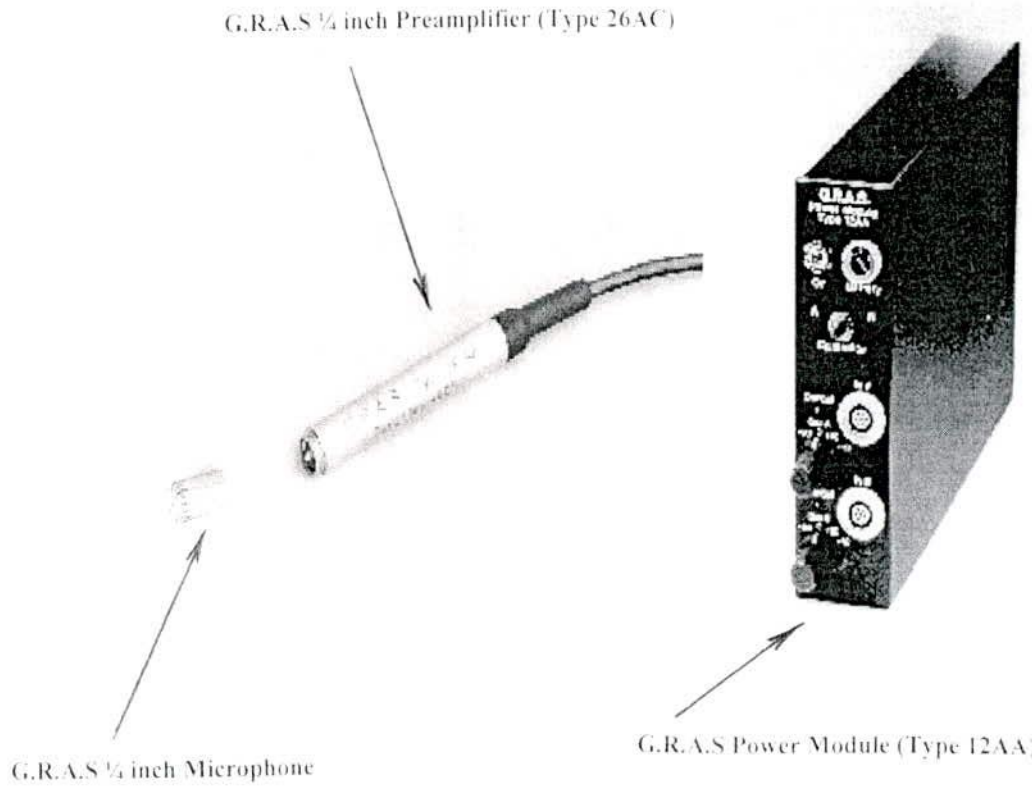

Figure D.1: G.R.A.S. ¼ inch Microphone with Preamplifier and Power Module

The Power Module also includes A-weighting and high-pass filters for pre-conditioning of the input signals. Figure D.1 shows the G.R.A.S. ¼ inch microphone (Type 40 BF), the preamplifier (Type 26 AC) and the power module (type 12 AA). Specifications of the G.R.A.S. ¼ inch microphone, preamplifier and power module are shown in Table D.1 and Table D.2. For this work the high-pass filter was set at 20 Hz and there was no A-weighting.

The dynamic calibration was performed by the manufacturer (G.R.A.S. Sound & Vibration, Copenhagen, Denmark) and compared to a Calibration Reference Microphone Cartridge Type 40 AG, traceable to the National Physical Laboratory, U.K. The stated sensitivity for the microphone cartridge was the open circuit sensitivity. The sensitivity was 0.2 dB lower when used with a preamplifier (Type 26 AC). Figure D.2 shows the dynamic calibration chart of G.R.A.S. ¼ inch microphone (type 40 BF). The lower curve is pressure response and the upper curve is the free field response for 0° incidence with protecting grid mounted on the microphone (see Figure D.2). For this work, a flat calibration curve was used since the maximum frequencies of interest were less than 3,000 Hz and generally in the range 100 to 400 Hz. A reference calibration signal was also recorded using a Pistonphone (Type RIO 7) before and after each set of tests. The calibration level was 94 dB re 20 μPa. The signal was recorded on the DAT tape and processed using MATLAB signal processing software to establish a calibration factor and its variation. This was performed using the same equipment and analysis methods and software was used for all tests in the wind tunnel and on the road.

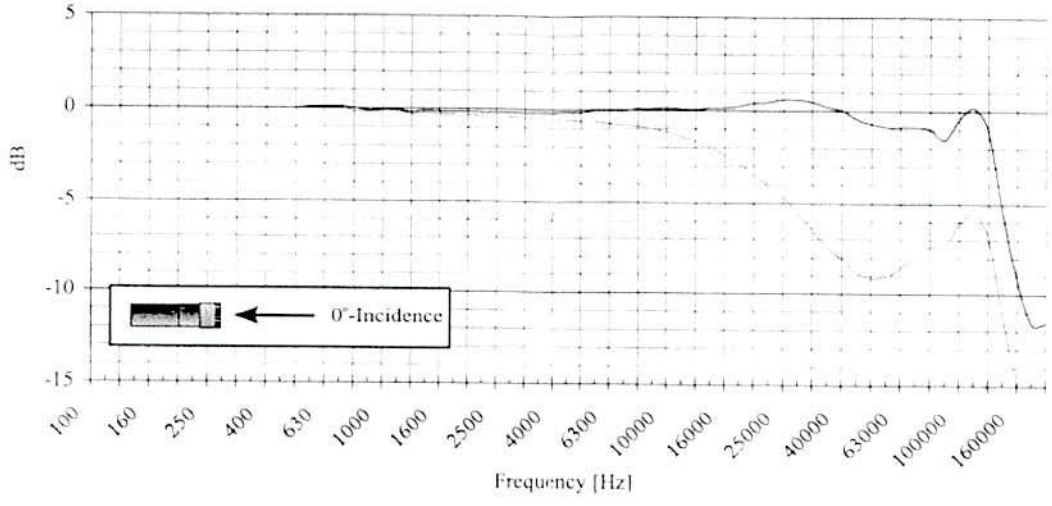

Figure D.2: Frequency Response of the G.R.A.S. ¼ inch Microphone (Type 40 BF)

The general specifications of G.R.A.S. ¼ inch microphone, preamplifier and power module in Table D.1 and Table D.2 are quoted from the papers supplied with the G.R.A.S. microphone unit by the G.R.A.S. Sound and Vibration.

Table D.1: Specifications G.R.A.S. ¼ inch Microphone & Preamplifier (after G.R.A.S. User Manual)

General Specifications of G.R.A.S. microphone	
Nominal Open Circuit Sensitivity at 250Hz	4 mV/Pa
Frequency Response: ±2dB ±1dB	 4Hz – 100kHz 10Hz- 40kHz
Polarisation Voltage	200V
Upper Limit of Dynamic Range (3% distortion)	166dB re. 20μPa
Lower Limit of Dynamic Range (Thermal Noise)	30dB re. 20μPa
Sensitivity to Vibrations: Equivalent SPL for 1m/s^2 perpendicular to diaphragm	 59dB re. 20μPa
Temperature Range	-40 to +150°C
Length with protection grid	10.5 mm
Diameter with protection grid/ without protection grid	6.9 mm/ 6.35 mm(1/4")
General Specifications of G.R.A.S. Preamplifier (Type 26 AC)	
Frequency Range (±0.2 dB)	2 – 200,000 Hz
Input Impedance	20 GΩ, 0.2 pF
Output Impedance (Cs = 20 pF, f = 1000 Hz)	55Ω typical
Output Voltage Swing (Peak)	Min. ±50 to ±10V
Noise (measured with 20 pF ½ inch dummy microphone) Linear (20 - 20,000 Hz) Linear (20 – 200,000 Hz) A-weighted	 < 6 μV < 8 μV < 2.5 μV
Gain (Typical)	-0.25 dB
Power Supply	120 V 2.3 mA to 28 V 0.7 mA
Temperature: (Operation)	-20° to +60°C
Dimensions : Diameter x Length x Weight (without cable)	6.35 x 43 mm x 6 g

Table D.2: Specifications of G.R.A.S. Power Module (after G.R.A.S. User Manual)

G.R.A.S. Power Module (Type 12 AA)	
Channels	2 Lemo 1B7 pin microphone sockets 2 BNC output sockets
Gain	-20 dB, 0 dB, +20 dB, + 40dB
Preamplifier Supply	28 V or 120 V (Preamplifier supply) 200 V or 0 V (Polarisation voltage)
Frequency Response	3.5 –200,000 Hz (±1.0 dB) 2 – 250,000 Hz ((±3.0 dB)
Battery Life	Approximately 8 hours
Output impedance	30Ω
Power supply	10xAA alkaline batteries or 12-28 V DC Line adaptor for 220 V or 115 V AC
Dimensions (Height x Width x Depth)	132.6 x 34.6 x 196.0 mm
Weight (without battery)	770 g
Operating Temperature Range	-10°C to +50°C

Appendix E

Methods and Algorithms Used in Signal Processing

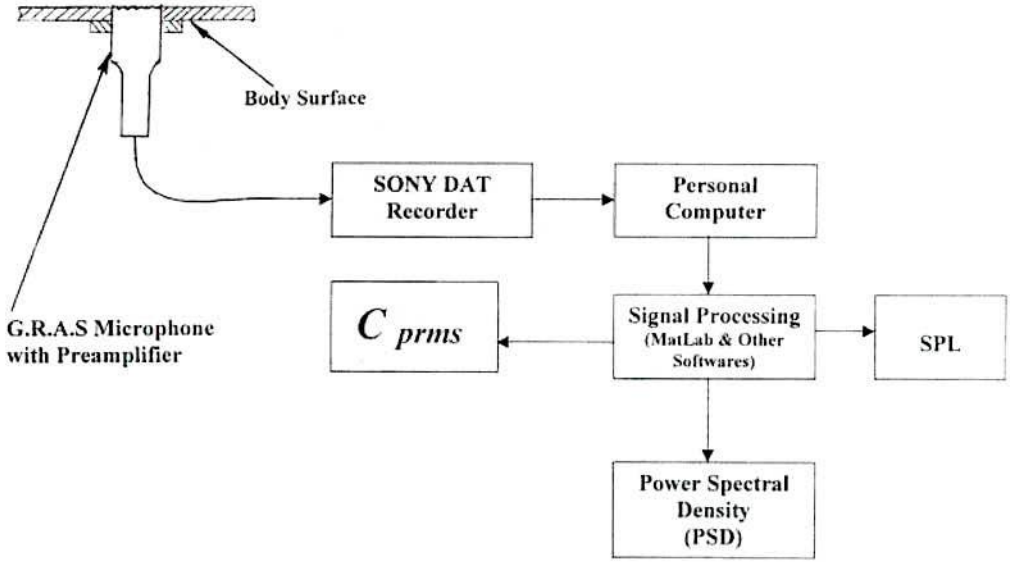

Figure E.1: Fluctuating Pressure Measurement and Analysis Stages

The fluctuating pressure coefficients (Cp rms) were calculated using Matlab software. 10 seconds of data were converted to fluctuating pressures and a standard deviation was calculated. The fluctuating pressure coefficient ($C_{prms}=\frac{p_{std}}{\frac{1}{2}\rho V^2}$) was obtained dividing the value of standard deviation by the mean velocity head (q). The mean velocity head was obtained from the tunnel data acquisition system.

For spectral analysis, aliasing problems were avoided by anti-aliasing filters, which were in-built into the SONY PC 116A DAT Recorder. The Power Spectral Density and normalised Pressure Spectra were calculated using Signal Processing TOOLBOX available in Matlab Software. Subroutines and codes were developed as required.

As most of the aerodynamic noise is not periodic, a leakage problem is present. This leakage problem was minimised by using a Hanning time-window function. The Picket-fence effect which was created as a result of using the Hanning window was minimised by multiplying the power spectrum by a correction factor of 8/3. For more details on aliasing, leakage and picket-fence effect, refer to Anderson et al. (1993) and Bendat et al. (1980). The signal processing parameters for signal processing in this study is given in Table E.1

Table E.1: Signal Processing Parameters

• Number of Over Laps	50%
• Sample length	30 sec
• Processing Sample length	10 sec
• Sampling Frequency	48000 Hz
• Number of FFT	4096
• Frequency Resolution	11.72 Hz
• Averaging	Linear
• Window	Hanning

Appendix F

Artificial Head System: Use and Calibration

The left and right ear microphones of the Aachen Head were calibrated using a Pistonphone calibrator (Type RIO-7). This is a miniature, portable, battery operated calibrator designed for both laboratory and field calibration. It operates at a frequency of 1000 Hz, and is therefore independent of any frequency-weighting network, which may be selected on the indicating instrument. The calibration level is 94 dB re 20 μPa. The signal was recorded on the DAT tape and later processed the recorded signal using a signal processing software to establish a calibration factor. This was performed using the same equipment and analysis methods and software as was used for all tests in the wind tunnel and on the road. The recording of the calibration signal via the left ear microphone of the Aachen Head is shown in Figure F.1.

The main error in the calibration of the system might arise from the fact that the reference signal that is applied at a single frequency is a pure tone. As the area of a power spectrum remains constant and independent of frequency resolution, a change in the frequency resolution of a discrete power spectrum produces a different value of the magnitude of a pure tone. This would then alter the calibrated factor that is then applied across the full frequency spectrum. To minimise this effect the same frequency resolution was used for the calculation of the calibration factor and analysis of the test data.

As the acquired data and the calibration were all processed in exactly the same manner, the accuracy of the calibration was estimated to be ±0.3 dB at 22°C. The Aachen Head was used in wind-tunnel and on-road testing. Extra care was taken to set up the Artificial Head in the correct position to avoid the unwanted acoustic influences.

The technical specifications of the Aachen Head is given in Table F.1.

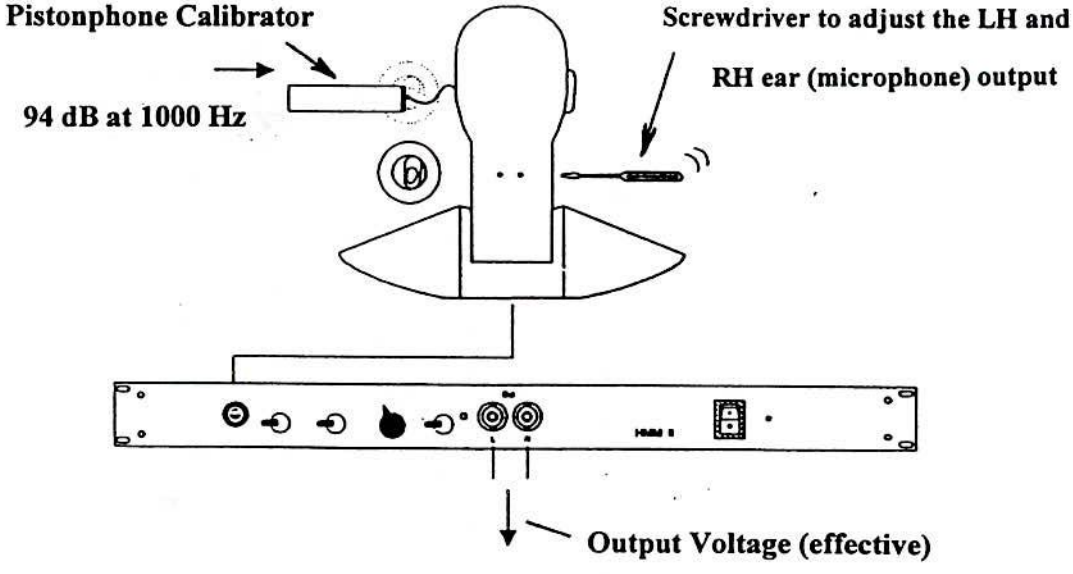

Figure F.1: Schematic of the Aachen Head Microphone Calibration

Table F.1: Technical Specifications of Artificial Head System (HMM II) (Extracted from the User Manual)

Measurement Unit	
Frequency response	3 Hz- 20 kHz, ±0.2 dB
S/N ratio at full modulation	> 110 dB, typical 112 dB
Cross-talk attenuation at nominal level	> 83 dB (1 kHz)
Distortion factor at nominal level	< 0.01% (1 kHz)
Sound Pressure Level (SPL) pre-settings (selectable)	94 dB, 104 dB, 114 dB and 124 dB
Peak overflow margin	6 dB
High pass filter, switchable	22.4 Hz
Equalisation	Independent-of-direction (ID), Free field (FF) and Linear
Directional pattern	Corresponds to the mean structural directional pattern of the human outer ear
Analog Output	
Line	BNC, unbalanced
Nominal output voltage	1 V (effective)
Maximum output voltage	2 V (effective)
Output resistance	500 Ω
Power Supply	
Mains operation	90-120 V/ 50 Hz/60 Hz 200-250 V/ 50 Hz/60 Hz
Max. power consumption	12 W
Battery operation (Battery version HMM II)	10-18 VDC, typical 12 VDC
Operating time with battery	> 2 hours

Appendix G

Flow Visualisation Supplementary Results

The flow visualisation photographs were taken from a stationary position while varying yaw angles and air speeds. The shutter speed was manually controlled and was set at 1/8th of a second. The flow visualisation photographs are shown here first at zero yaw angles varying speeds (60, 80, 100 and 120 km/h) and then at 120 km/h varying yaw angles (-15, -10, -5, 0, +5, +10 and +15). The first set of flow visualisation photographs shows the change of the flow pattern with Reynolds numbers (if any). The second set of flow visualisation photographs demonstrates how the flow pattern on the side window in the A-pillar region varies with yaw angles. The flow pattern on the side window of the rectangular model is shown in Figures G.1 to G.11. Figures G.12-G.22 demonstrate the side views of flow visualisation for the slanted sharp-edged model and Figures G.23-G.33 shows the flow pattern on the side window of the small ellipsoidal model. The general structure of the flow field on the side window of the circular and large ellipsoidal models are shown in Figures G.34-G.44 and Figures G.45- G.55 respectively.

The flow pattern does not vary with the Reynolds number at zero yaw angles for the rectangular model (Figure G.1-Figure G.4), slanted sharp-edged model (Figure G.12-Figure G.15), small ellipsoidal model (Figure G.23-Figure G.26) and circular model (Figure G.34-Figure G.37). A very small variation of the flow pattern with the Reynolds number at zero yaw angles for the large ellipsoidal model is noted (Figure G.45-Figure G.48). No apparent variation with Reynolds numbers is evident at positive and negative yaw angles (the flow visualisation photographs are not shown here).

A strong A-pillar flow separation is noted at negative, zero and positive yaw angles (Figure G.5-Figure G.11) for the rectangular model. However, the separated zone is smaller at positive yaw angles compared to negative yaw angles. The A-pillar flow separation is also noted at all yaw angles for the slanted sharp-edged model (Figure

G.16-Figure G.22). However, the separated area is much smaller at positive yaw angles compared to negative yaw angles.

No A-pillar flow separation is evident at zero and positive yaw angles for the small ellipsoidal model, circular model and large ellipsoidal model (Figure G.30-Figure G.33, Figure G.41-Figure G.44 and Figure G.52-Figure G.55 respectively). However, a small A-pillar conical vortex formation is noted at negative yaw angles for the small ellipsoidal and circular models (Figure G.27-Figure G.29 and Figure G.38-Figure G.40 respectively).

G.1 Rectangular Model

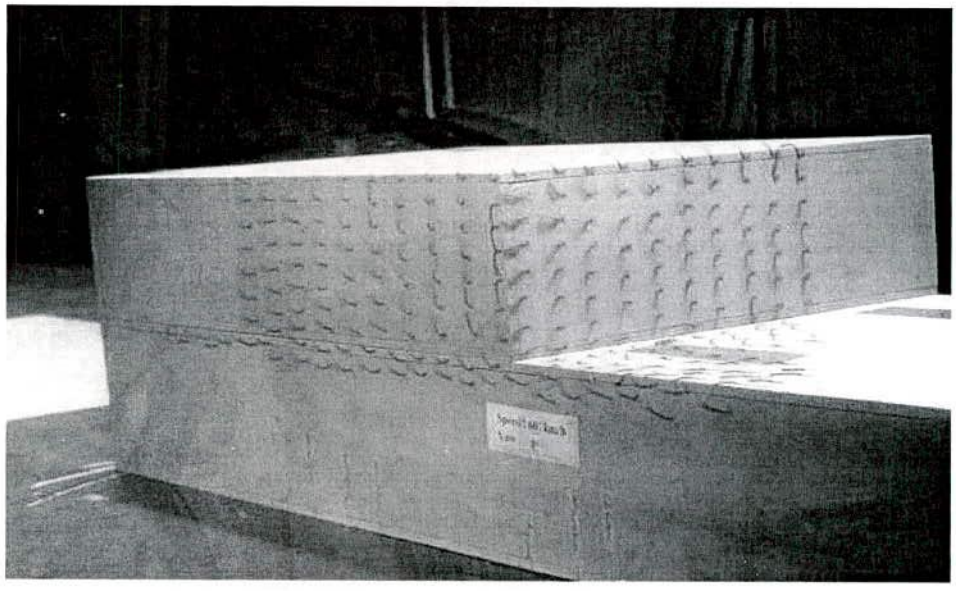

Figure G.1: Side View, Rectangular Model, 60 km/h, Yaw = 0°

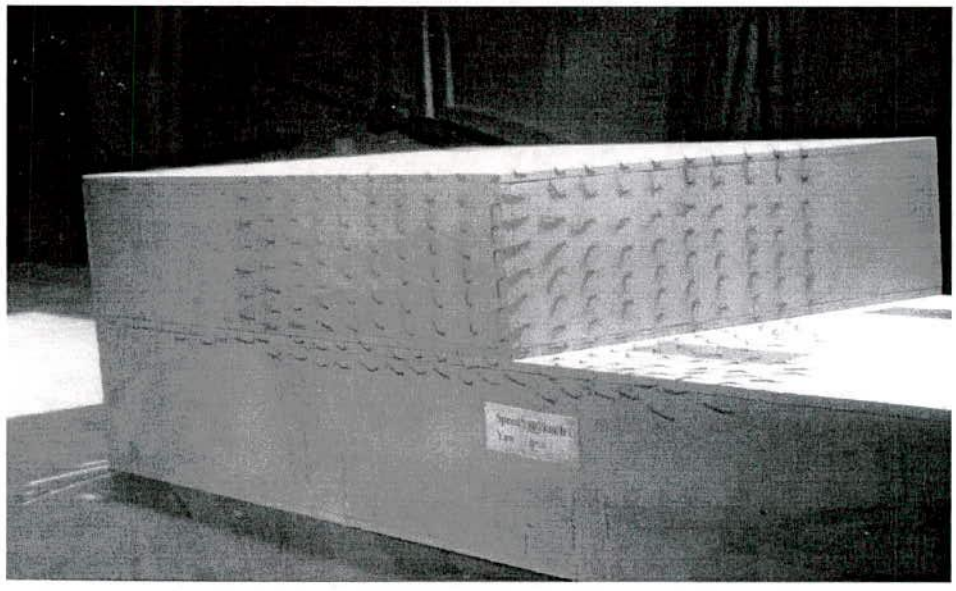

Figure G.2: Side View, Rectangular Model, 80 km/h, Yaw = 0°

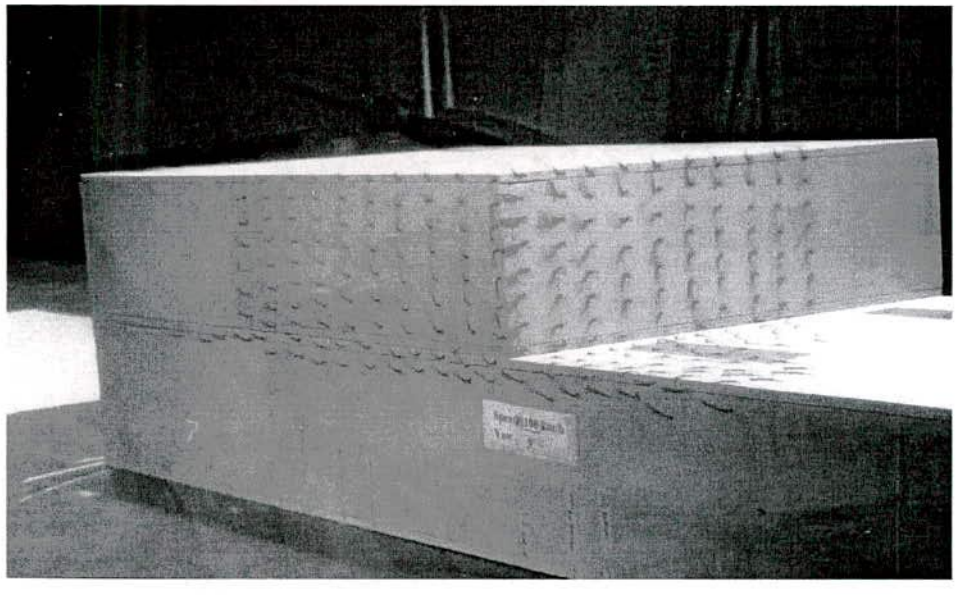

Figure G.3: Side View, Rectangular Model, 100 km/h, Yaw = 0°

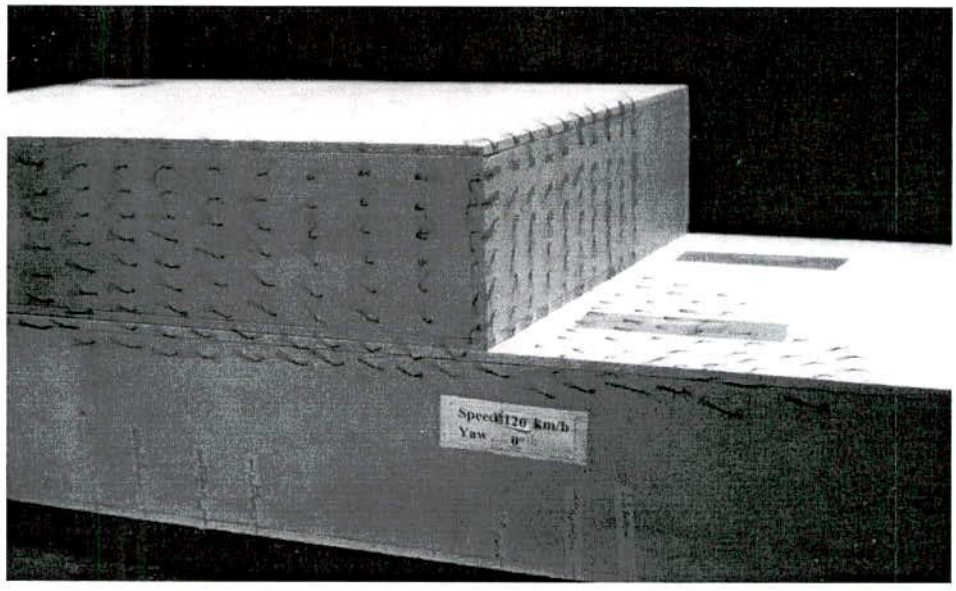

Figure G.4: Side View, Rectangular Model, 120 km/h, Yaw = 0°

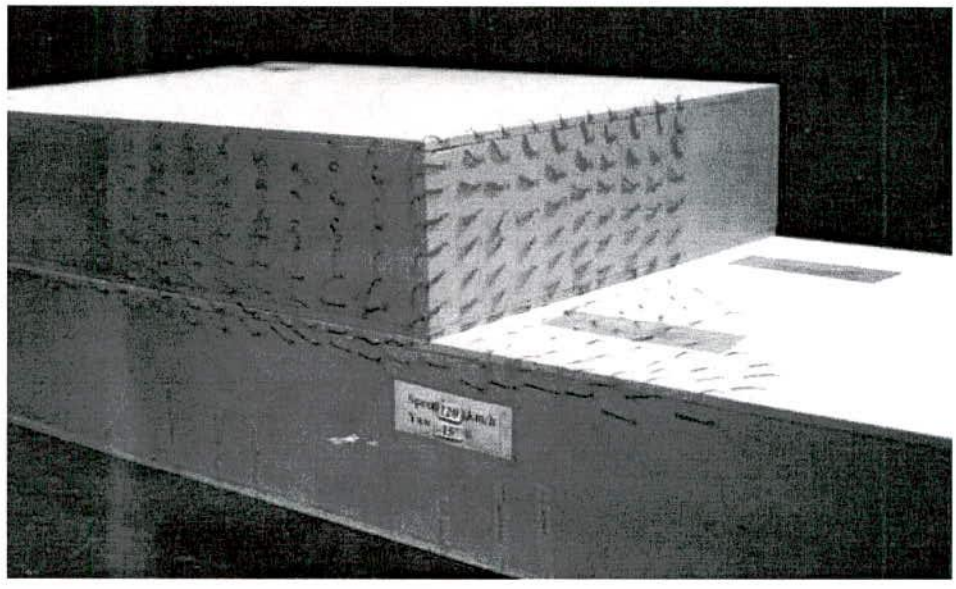

Figure G.5: Side View, Rectangular Model, 120 km/h, Yaw = -15°

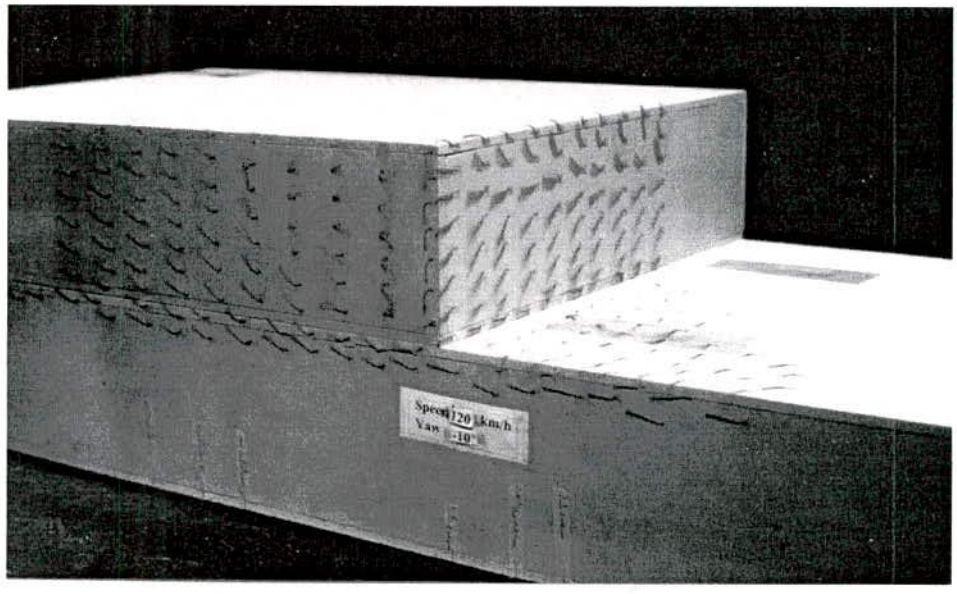

Figure G.6: Side View, Rectangular Model, 120 km/h, Yaw = -10°

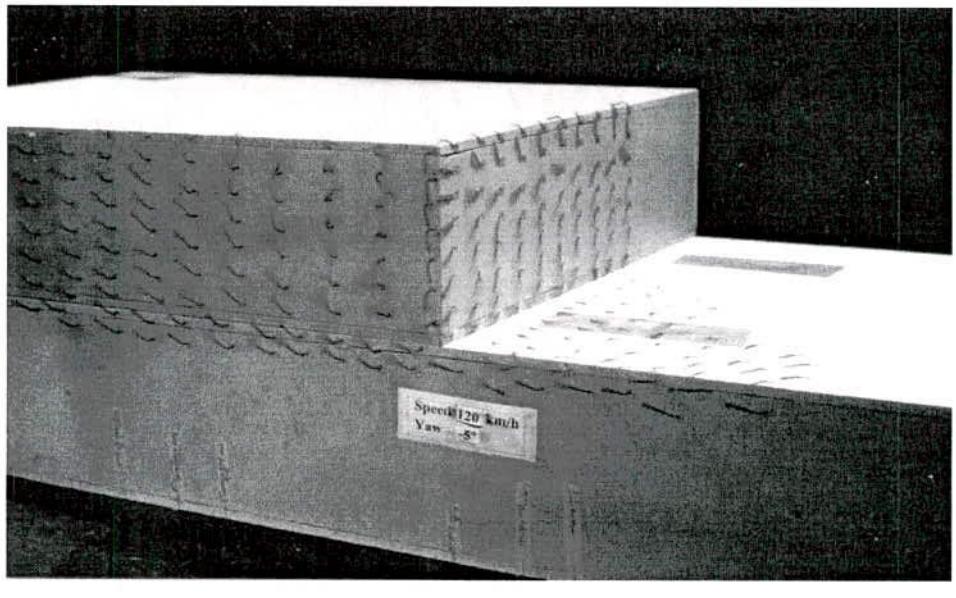

Figure G.7: Side View, Rectangular Model, 120 km/h, Yaw = -5°

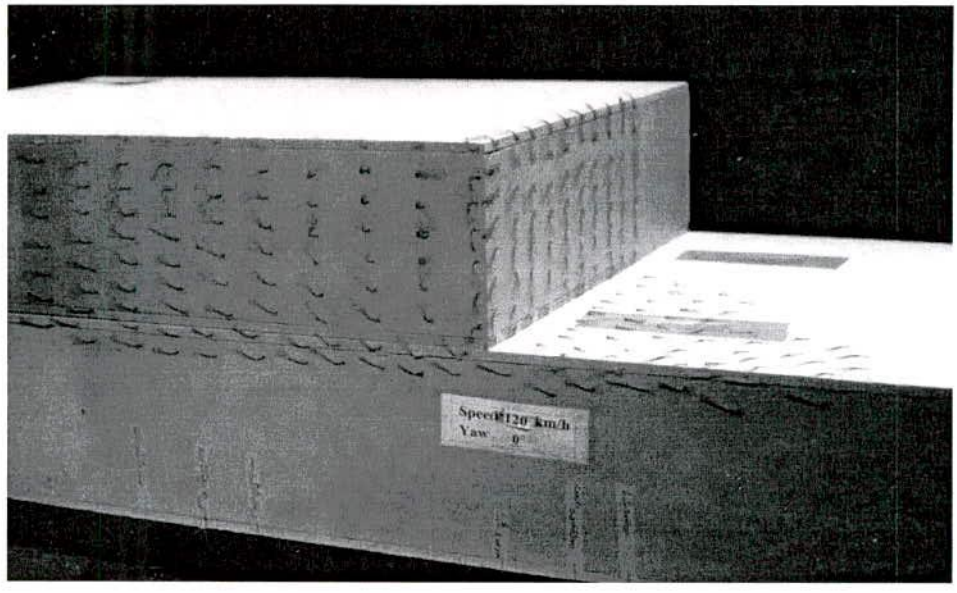

Figure G.8: Side View, Rectangular Model, 120 km/h, Yaw = 0°

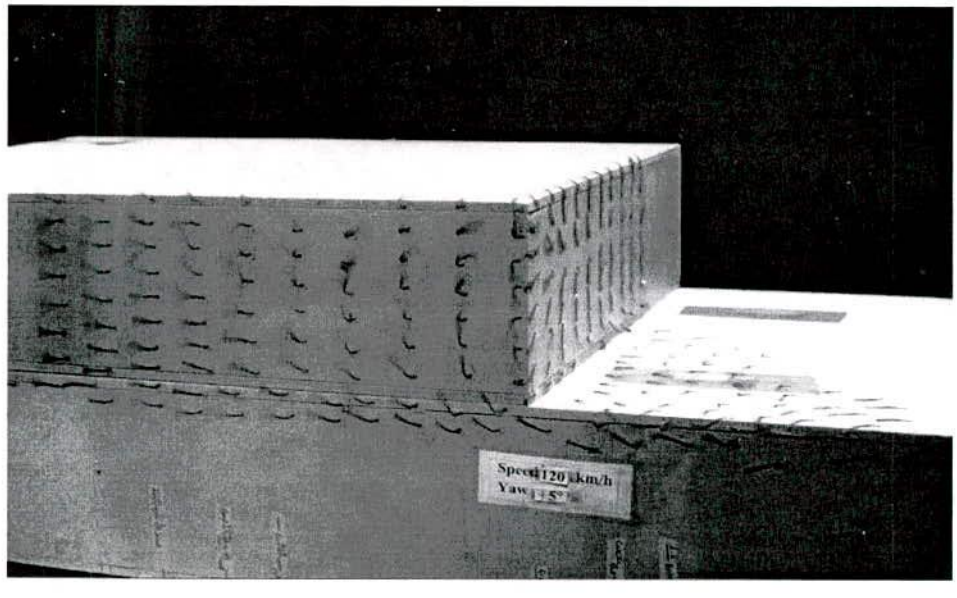

Figure G.9: Side View, Rectangular Model, 120 km/h, Yaw = +5°

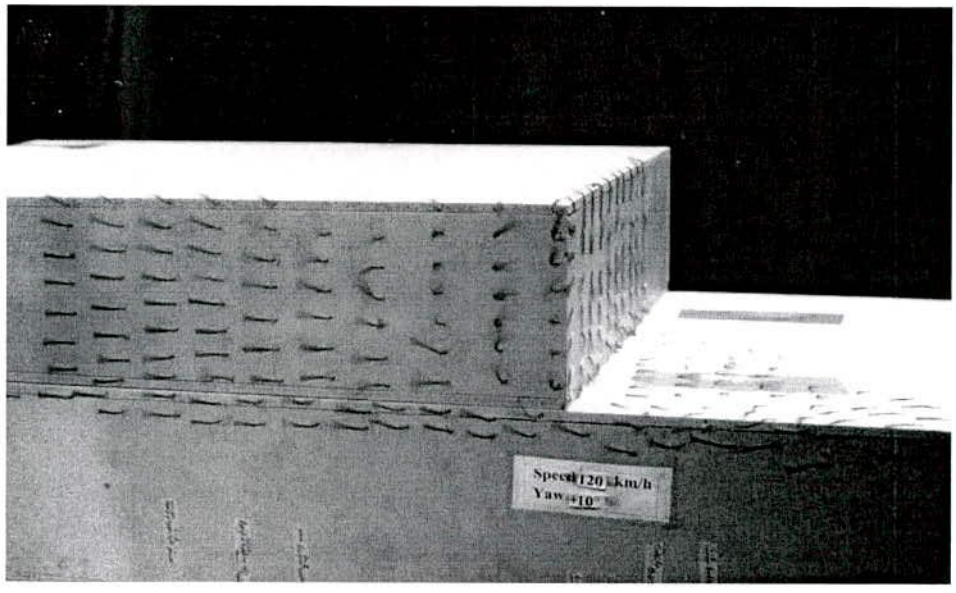

Figure G.10: Side View, Rectangular Model, 120 km/h, Yaw = +10°

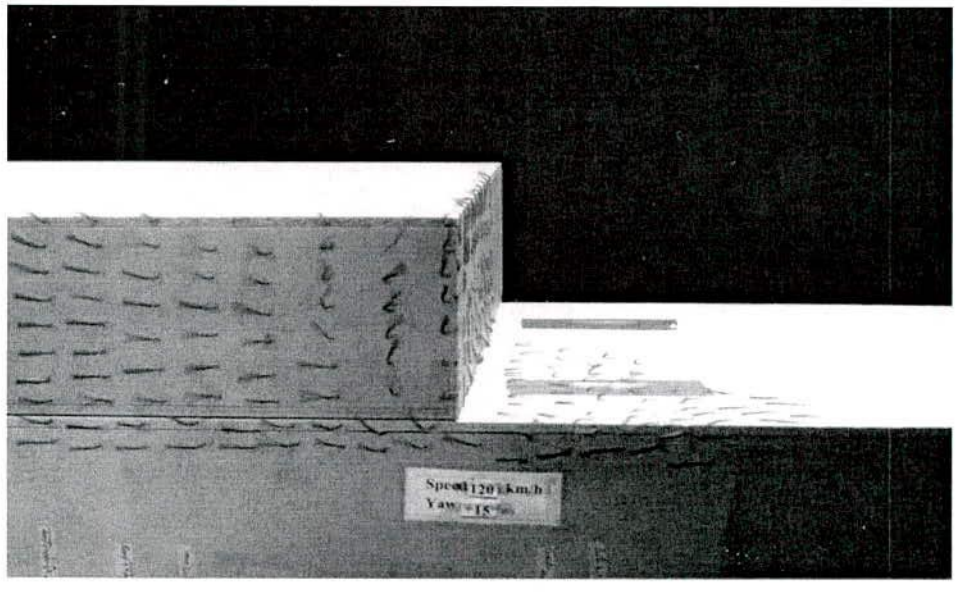

Figure G.11: Side View, Rectangular Model, 120 km/h, Yaw = +15°

G.2 Slanted Sharp-edged Model

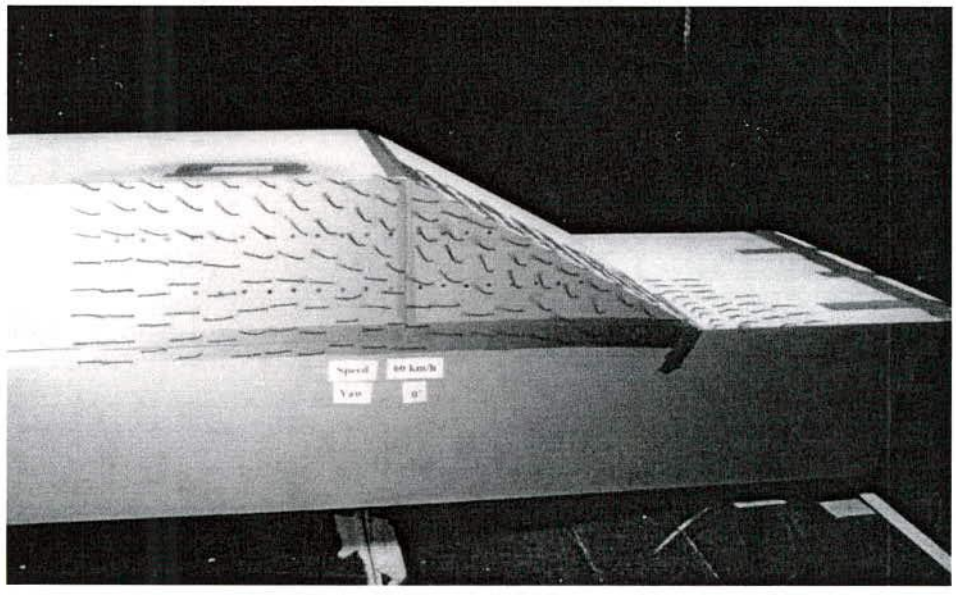

Figure G.12: Side View, Slanted Sharp-edged Model, 60 km/h, Yaw = 0°

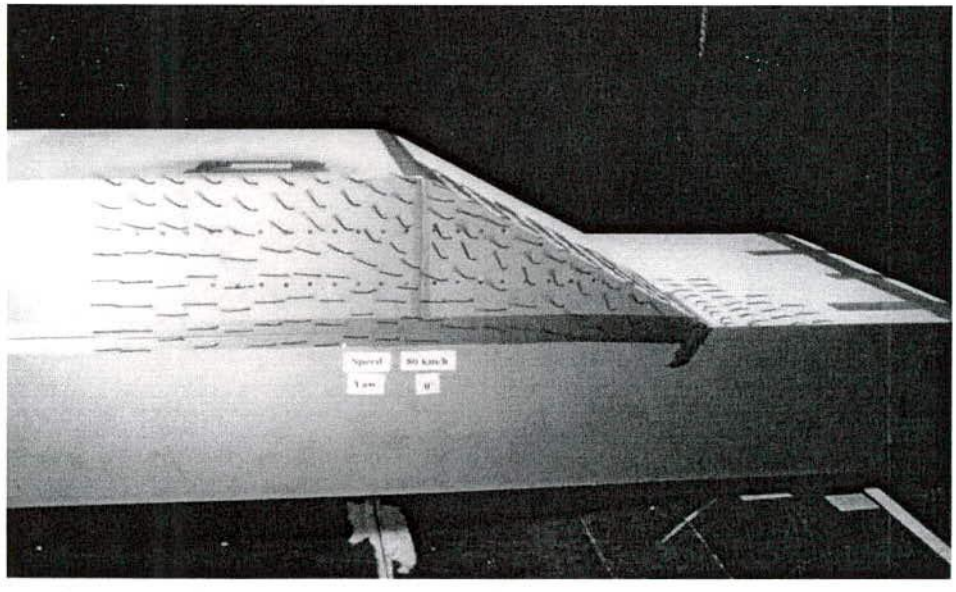

Figure G.13: Side View, Slanted Sharp-edged Model, 80 km/h, Yaw = 0°

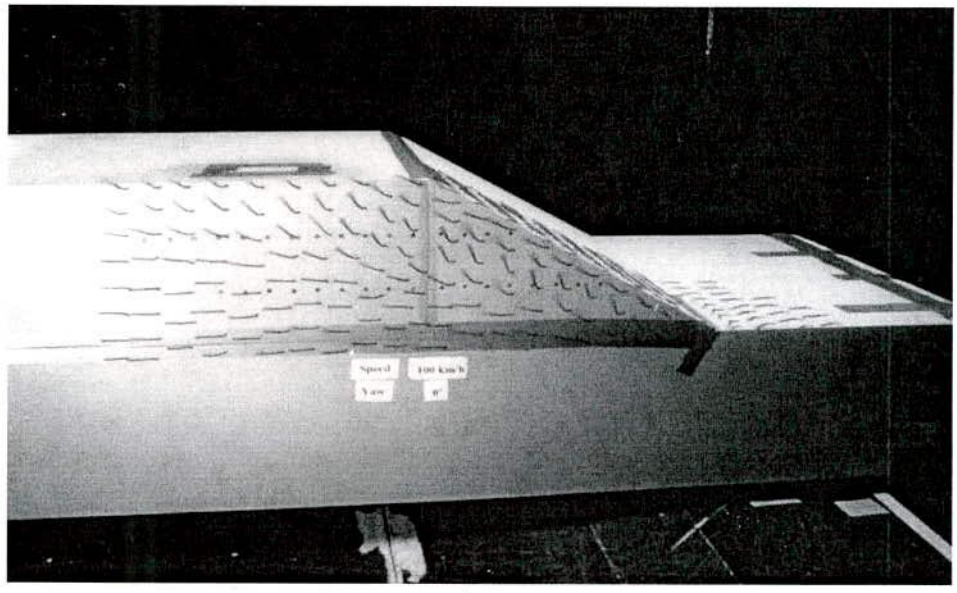

Figure G.14: Side View, Slanted Sharp-edged Model, 100 km/h, Yaw = 0°

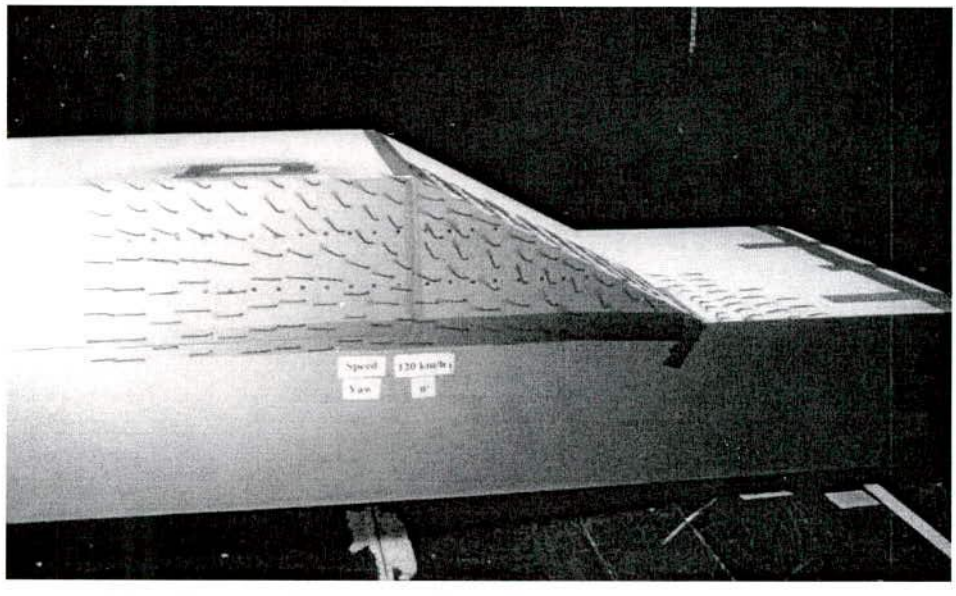

Figure G.15: Side View, Slanted Sharp-edged Model, 120 km/h, Yaw = 0°

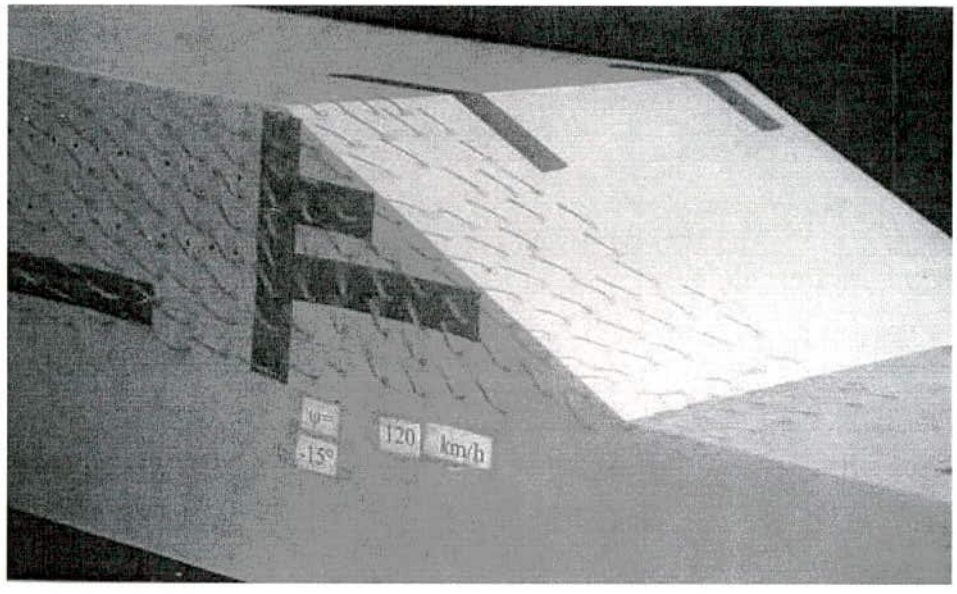

Figure G.16: Side View, Slanted Sharp-edged Model, 120 km/h, Yaw = -15°

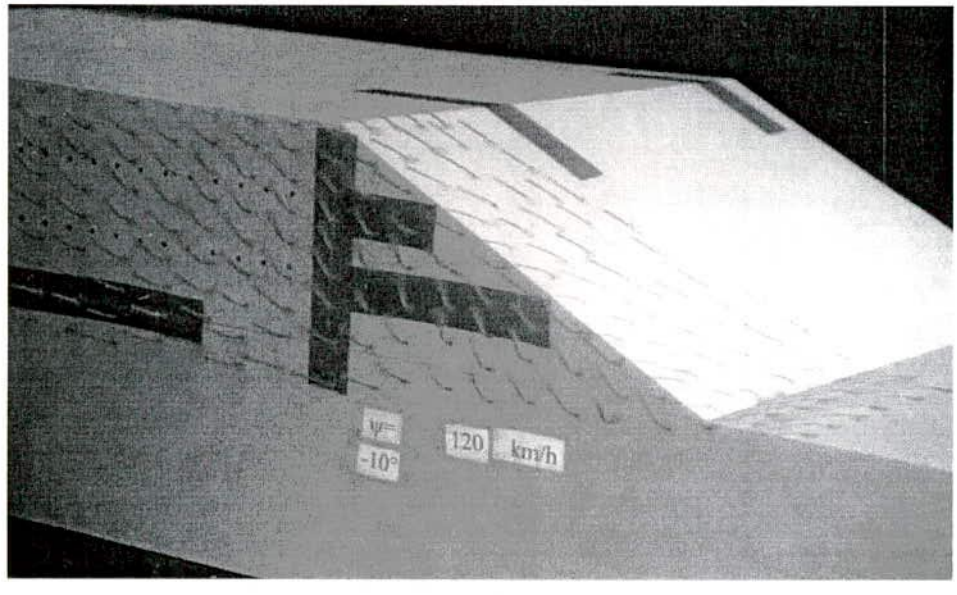

Figure G.17: Side View, Slanted Sharp-edged Model, 120 km/h, Yaw = -10°

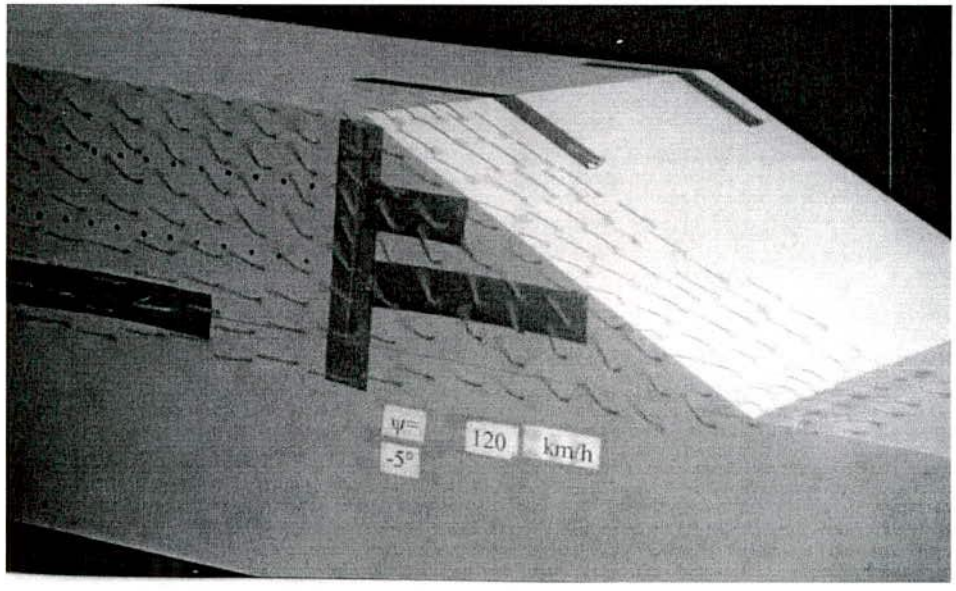

Figure G.18: Side View, Slanted Sharp-edged Model, 120 km/h, Yaw = -5°

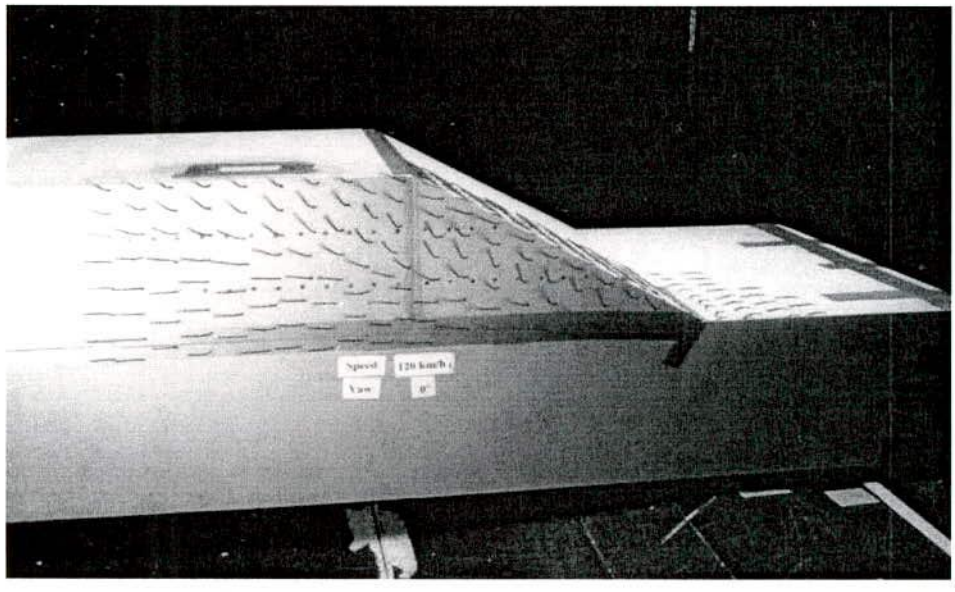

Figure G.19: Side View, Slanted Sharp-edged Model, 120 km/h, Yaw = 0°

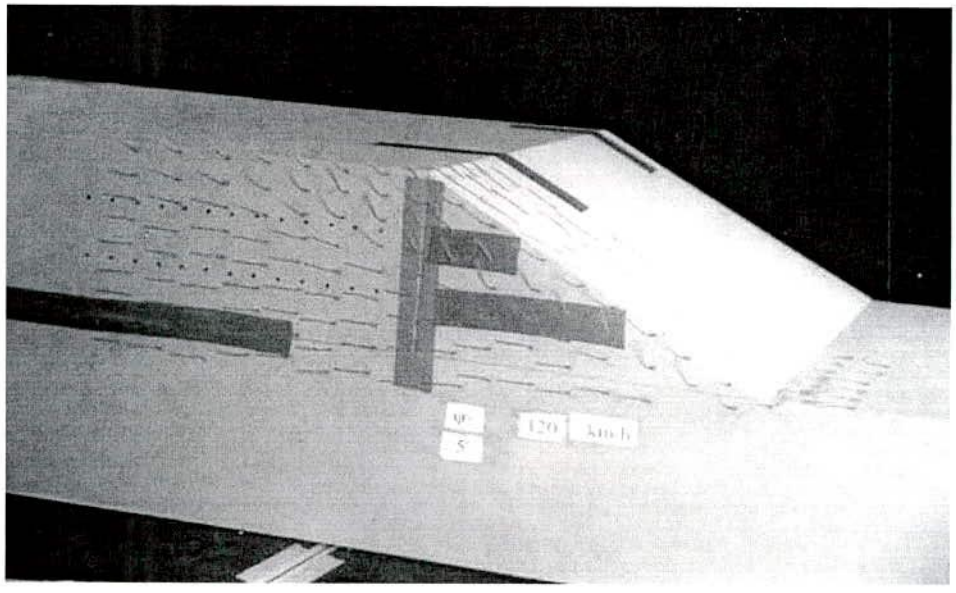

Figure G.20: Side View, Slanted Sharp-edged Model, 120 km/h, Yaw = +5°

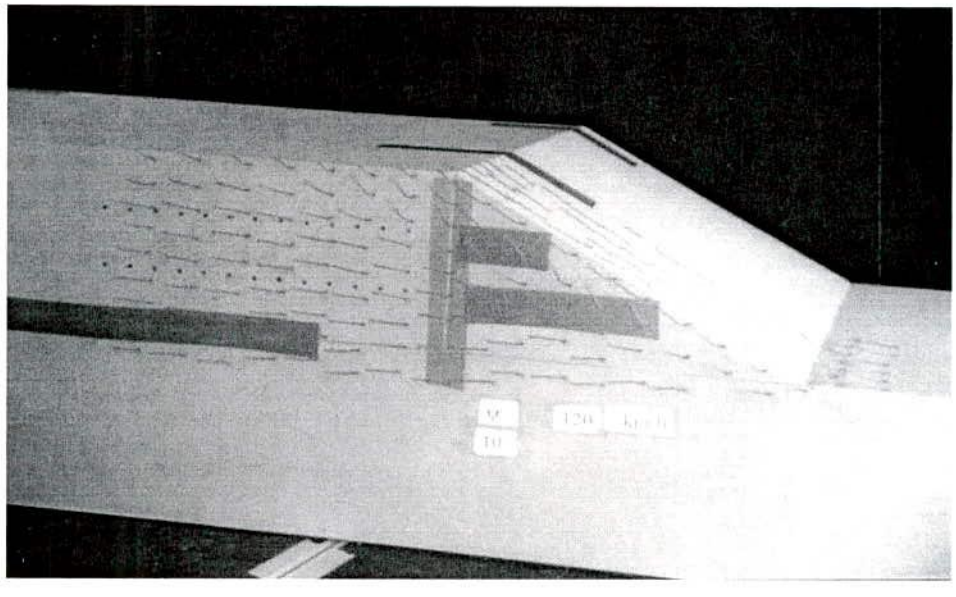

Figure G.21: Side View, Slanted Sharp-edged Model, 120 km/h, Yaw = +10°

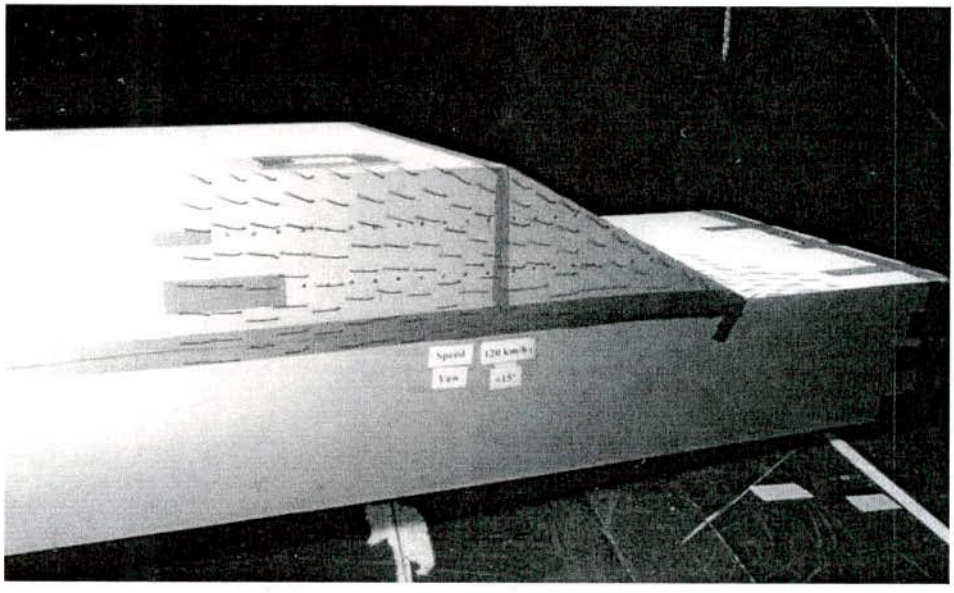

Figure G.22: Side View, Slanted Sharp-edged Model, 120 km/h, Yaw = +15°

G.3 Small Ellipsoidal Model

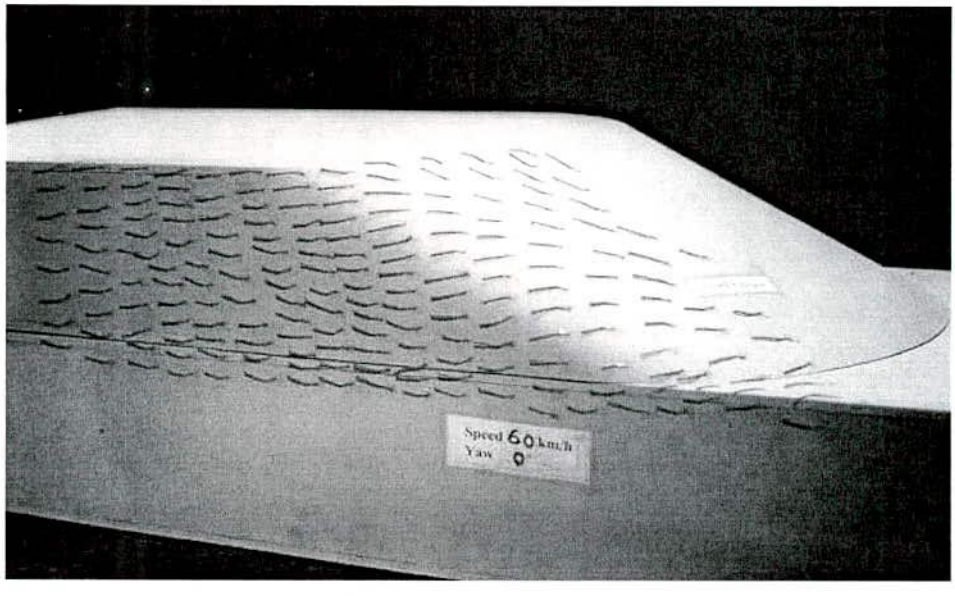

Figure G.23: Side View, Small Ellipsoidal Model, 60 km/h, Yaw = 0°

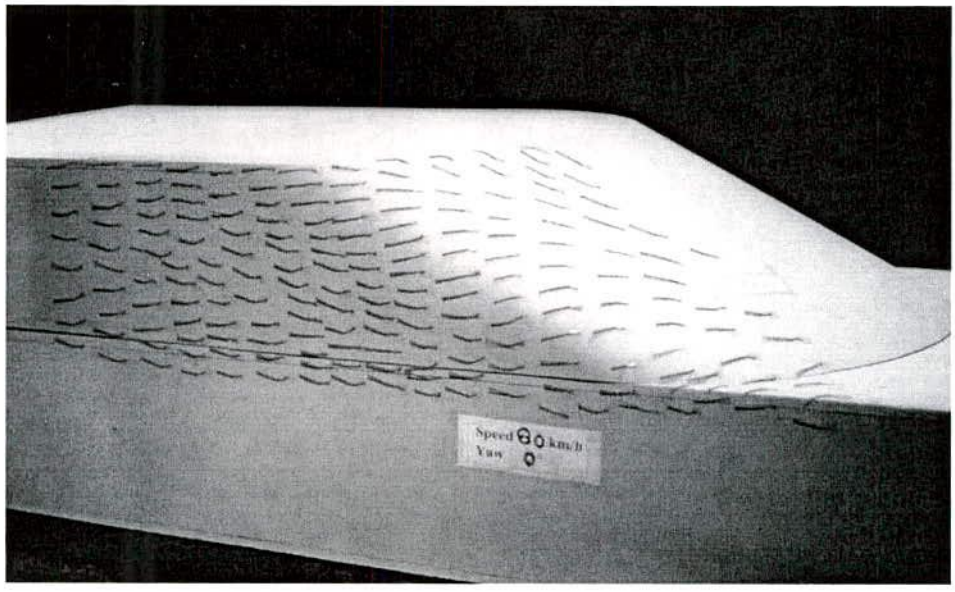

Figure G.24: Side View, Small Ellipsoidal Model, 80 km/h, Yaw = 0°

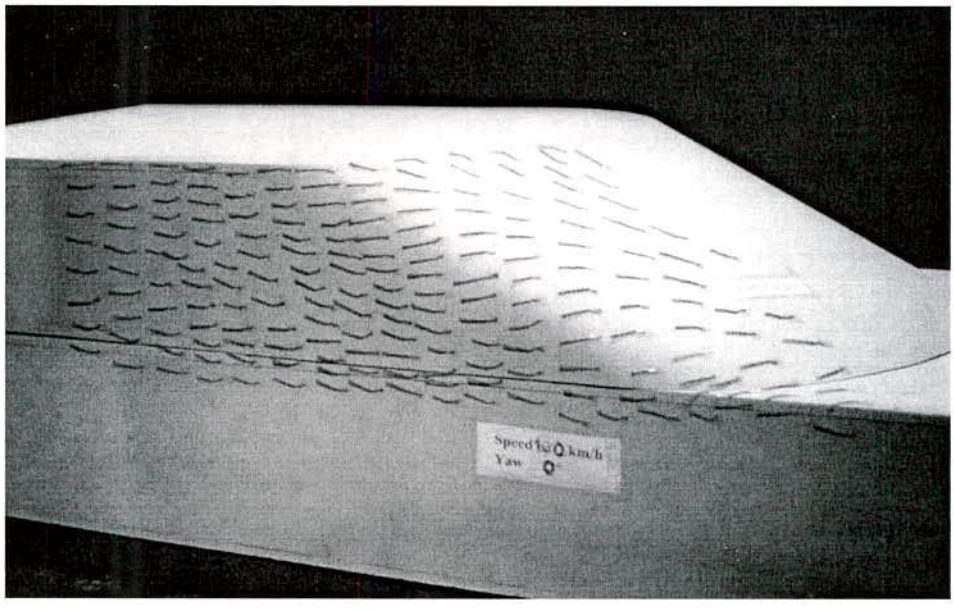

Figure G.25: Side View, Small Ellipsoidal Model, 100 km/h, Yaw = 0°

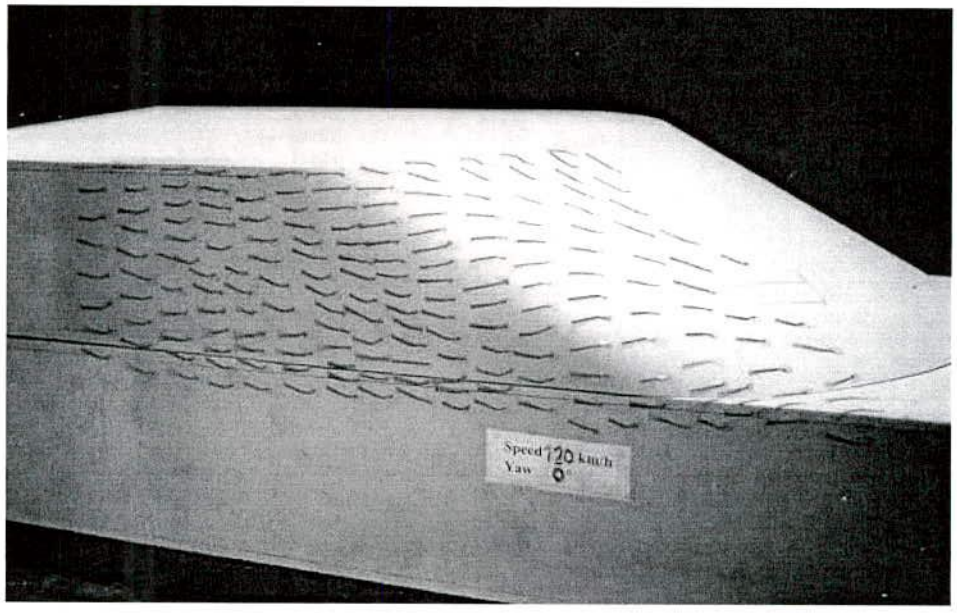

Figure G.26: Side View, Small Ellipsoidal Model, 120 km/h, Yaw = 0°

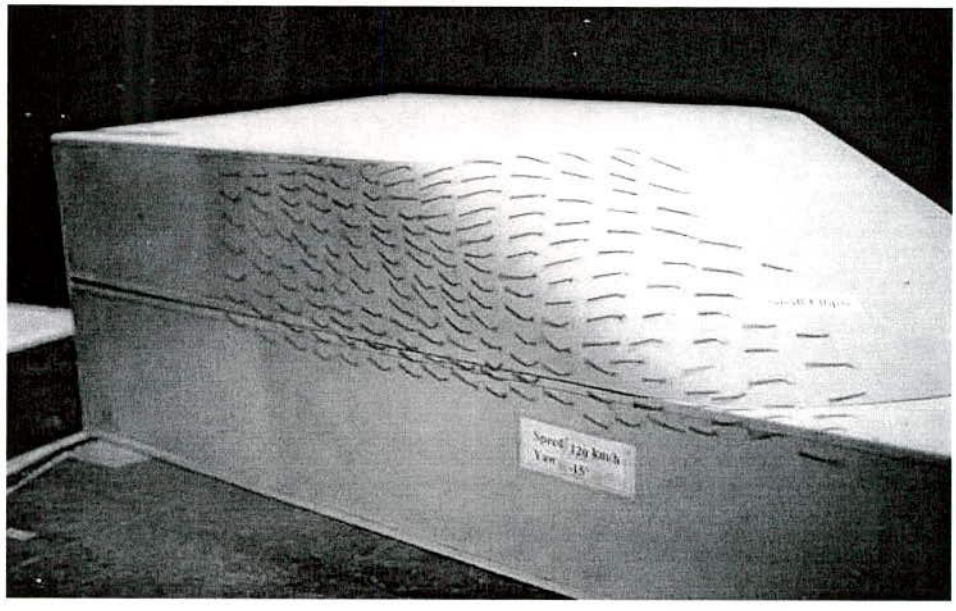

Figure G.27: Side View, Small Ellipsoidal Model, 120 km/h, Yaw = -15°

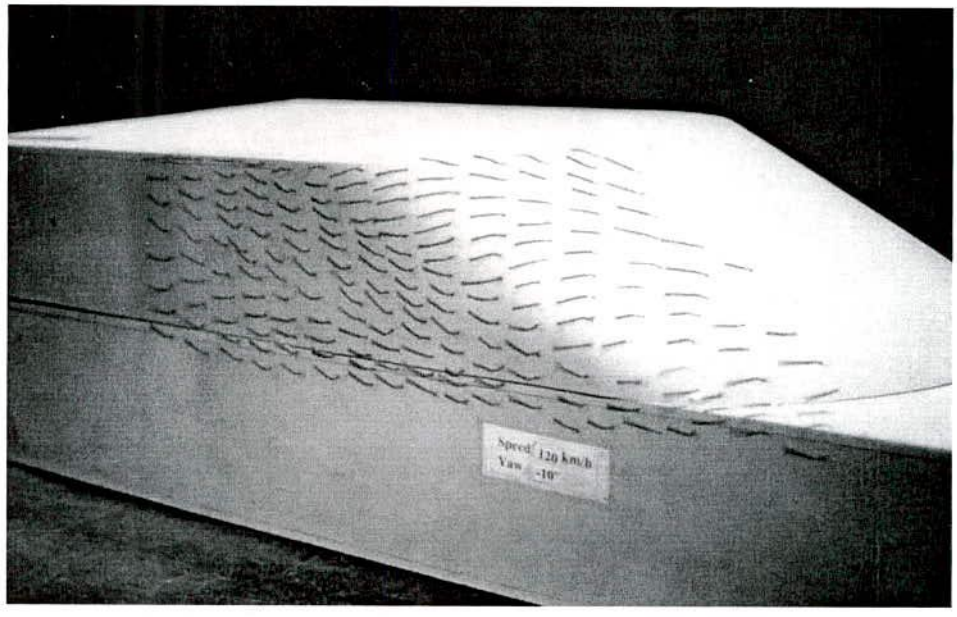

Figure G.28: Side View, Small Ellipsoidal Model, 120 km/h, Yaw = -10°

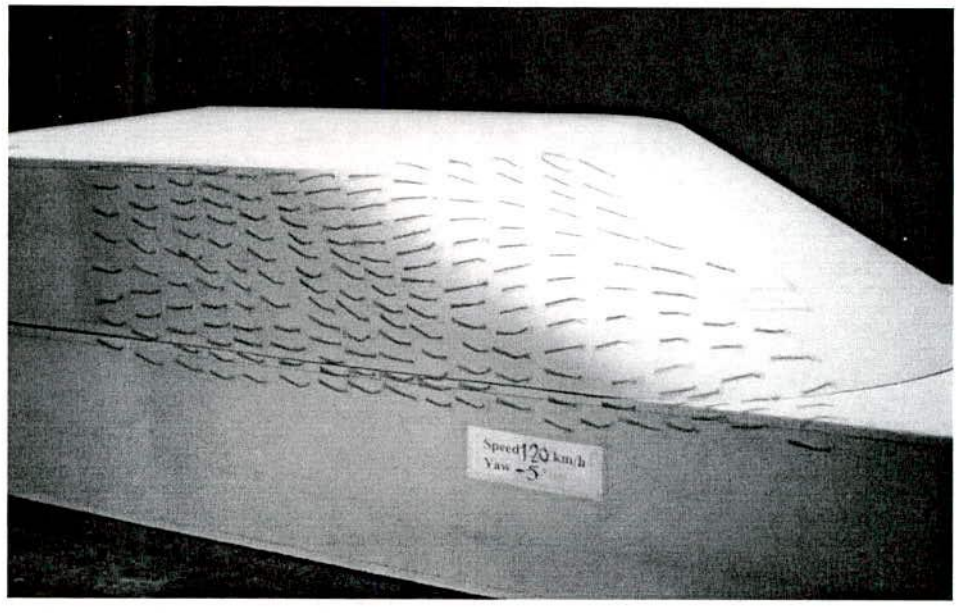

Figure G.29: Side View, Small Ellipsoidal Model, 120 km/h, Yaw = -5°

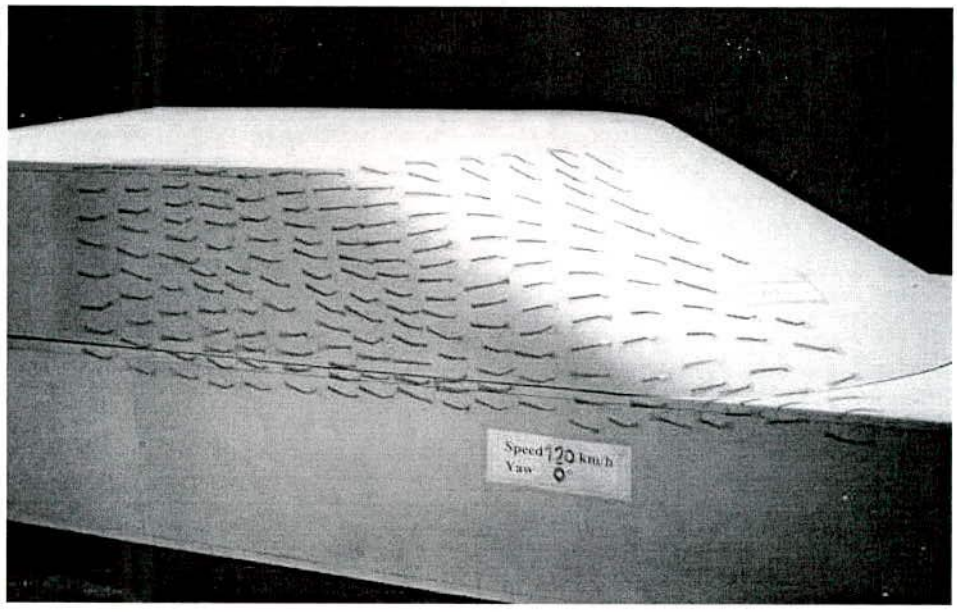

Figure G.30: Side View, Small Ellipsoidal Model, 120 km/h, Yaw = 0°

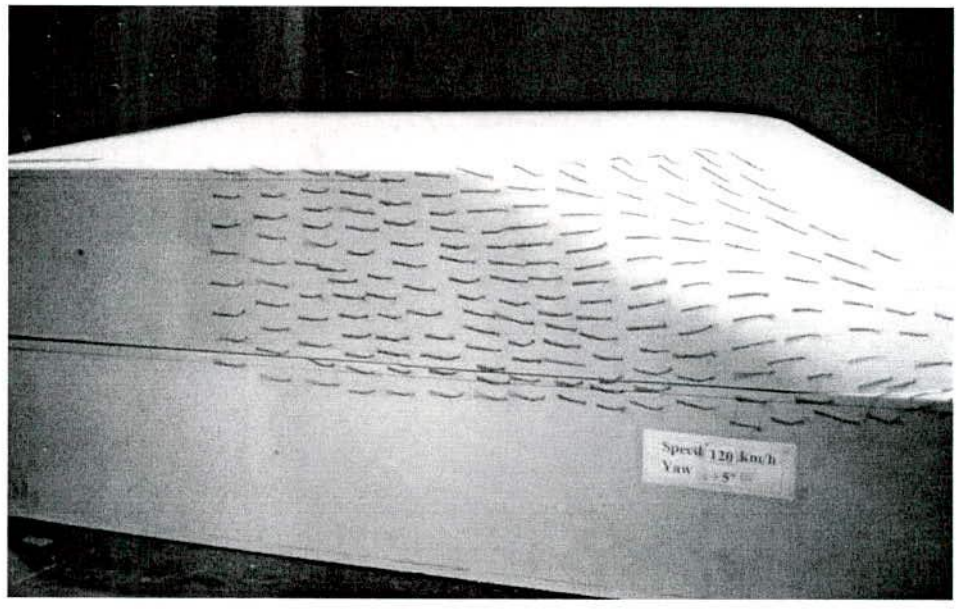

Figure G.31: Side View, Small Ellipsoidal Model, 120 km/h, Yaw = +5°

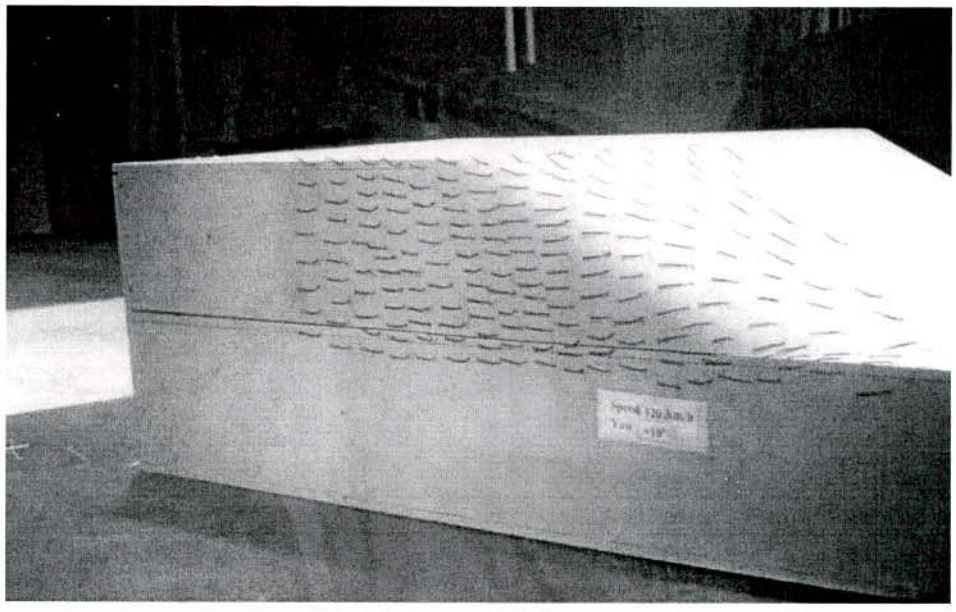

Figure G.32: Side View, Small Ellipsoidal Model, 120 km/h, Yaw = +10°

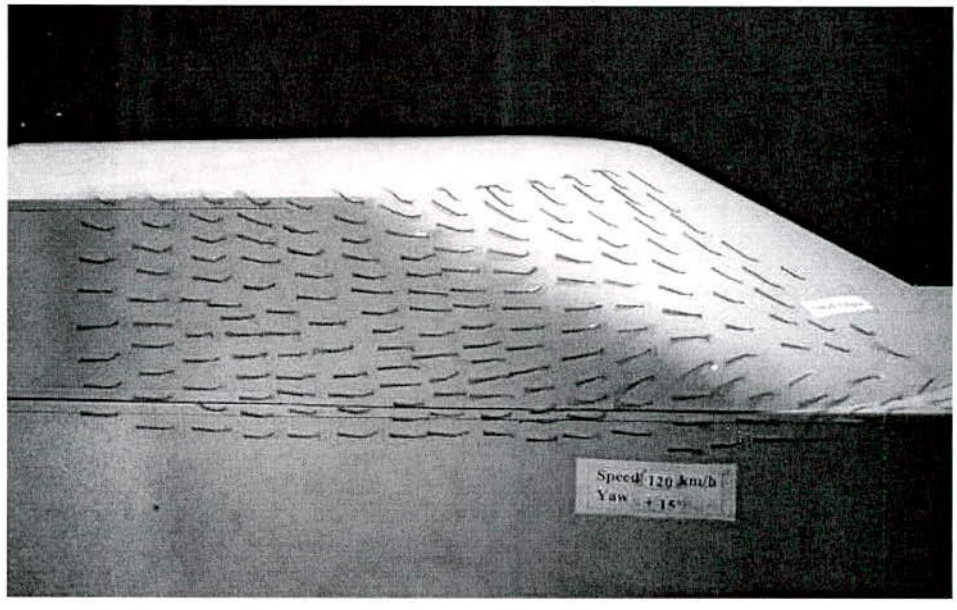

Figure G.33: Side View, Small Ellipsoidal Model, 120 km/h, Yaw = +15°

G.4 Circular Model

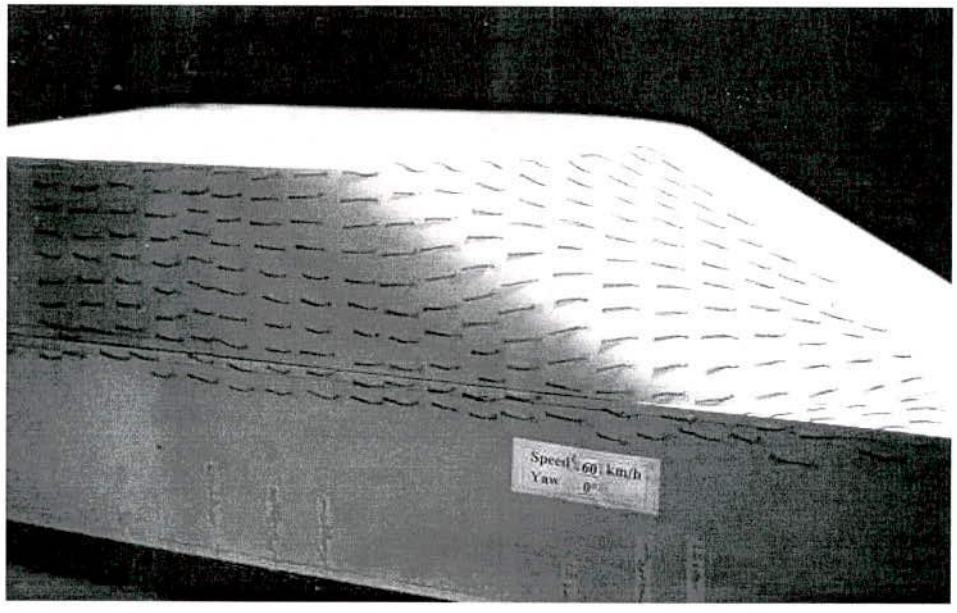

Figure G.34: Side View, Circular Model, 60 km/h, Yaw = 0°

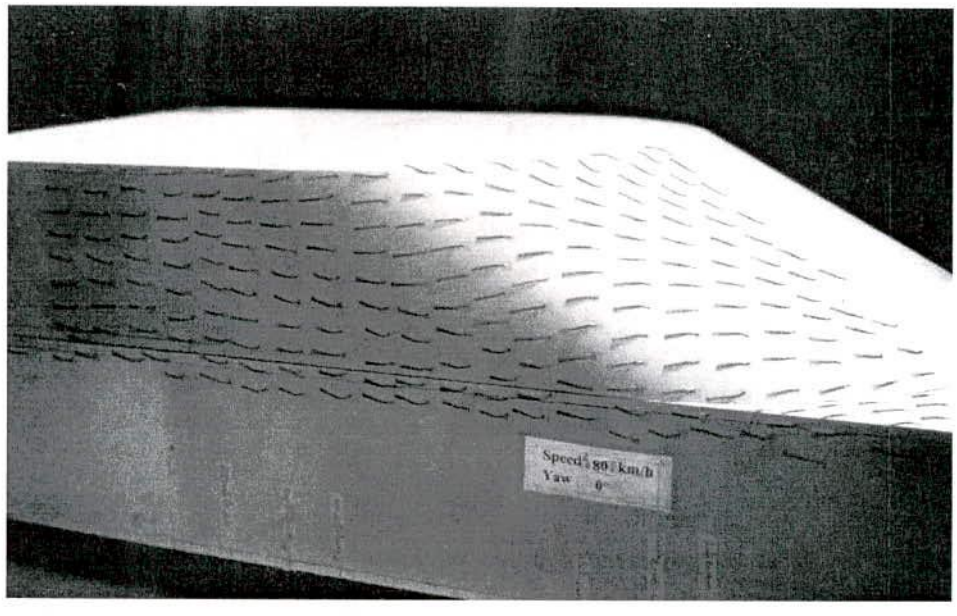

Figure G.35: Side View, Circular Model, 80 km/h, Yaw = 0°

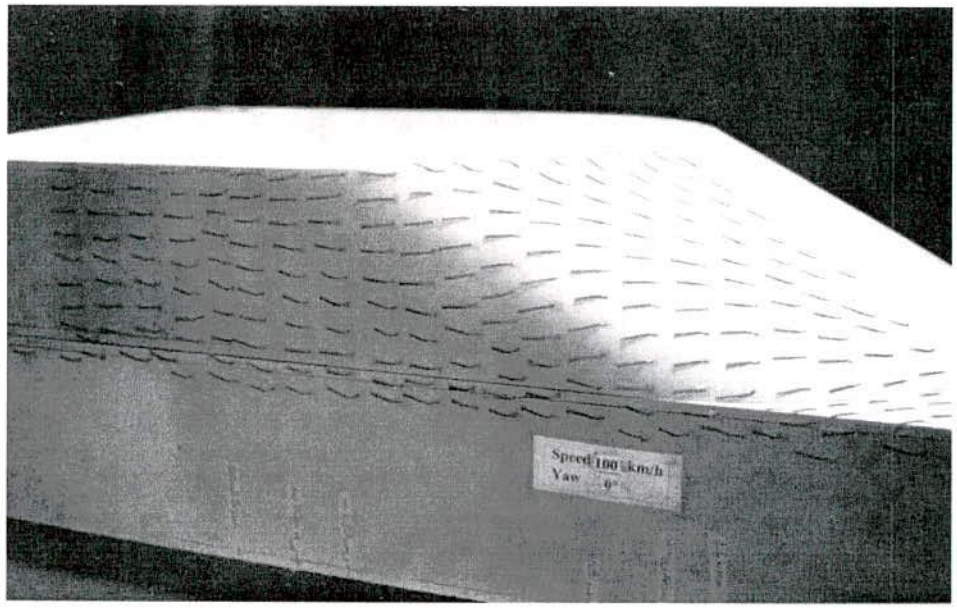

Figure G.36: Side View, Circular Model, 100 km/h, Yaw = 0°

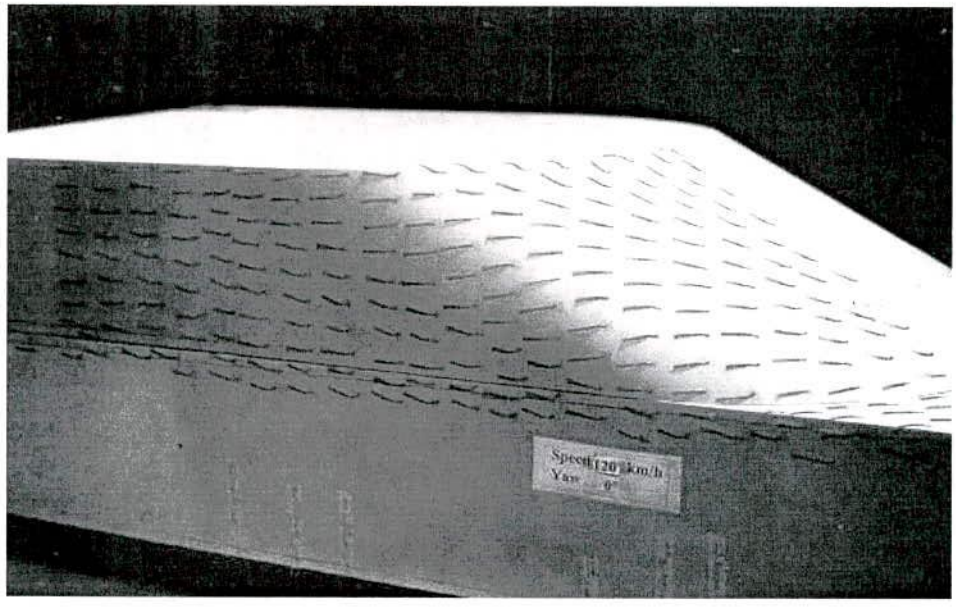

Figure G.37: Side View, Circular Model, 120 km/h, Yaw = 0°

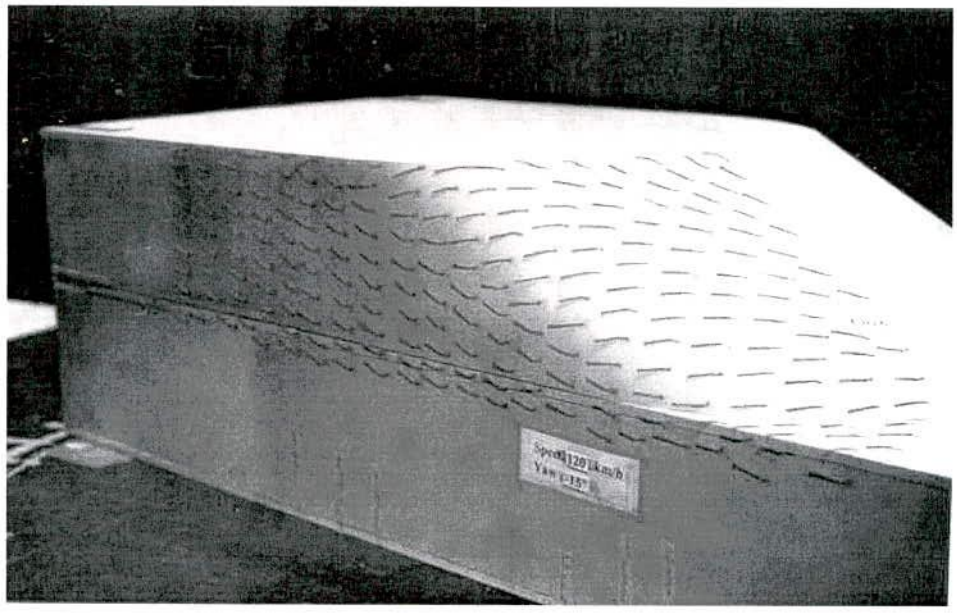

Figure G.38: Side View, Circular Model, 120 km/h, Yaw = -15°

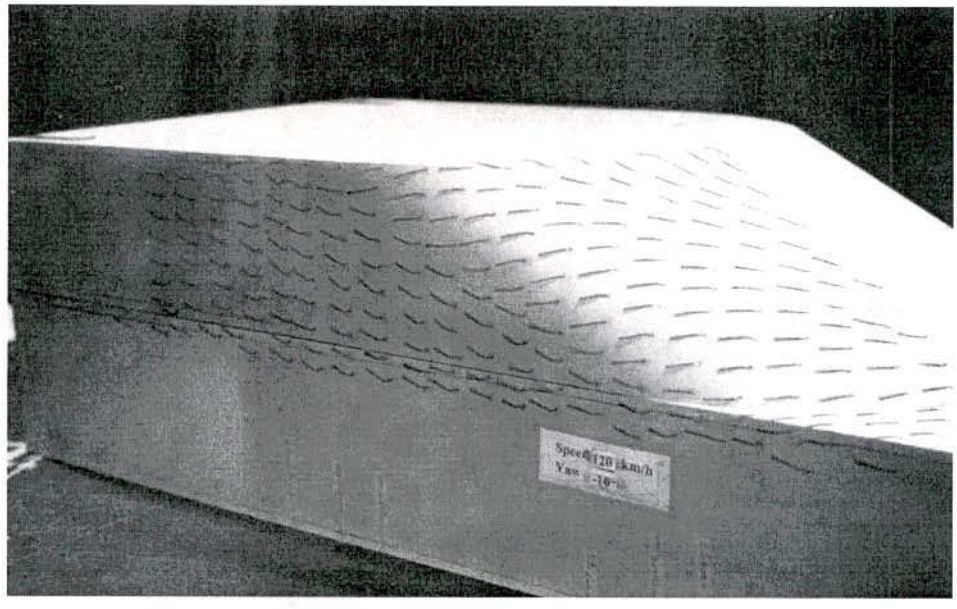

Figure G.39: Side View, Circular Model, 120 km/h, Yaw = -10°

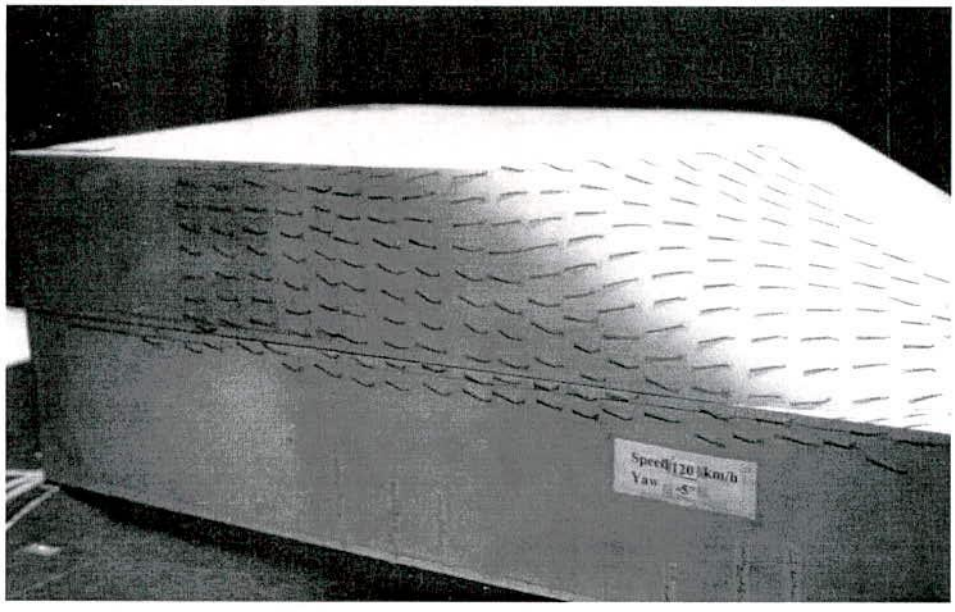

Figure G.40: Side View, Circular Model, 120 km/h, Yaw = -5°

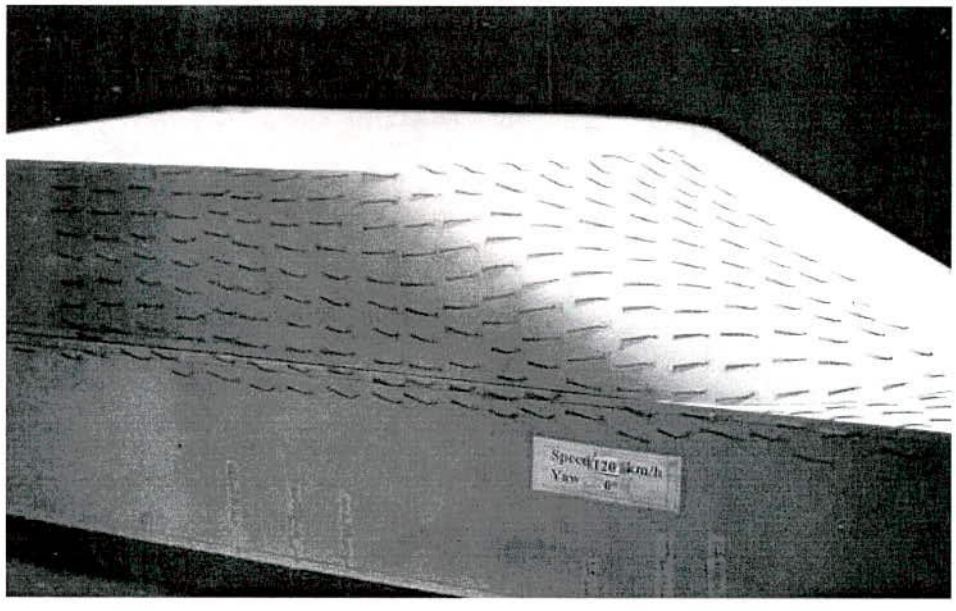

Figure G.41: Side View, Circular Model, 120 km/h, Yaw = 0°

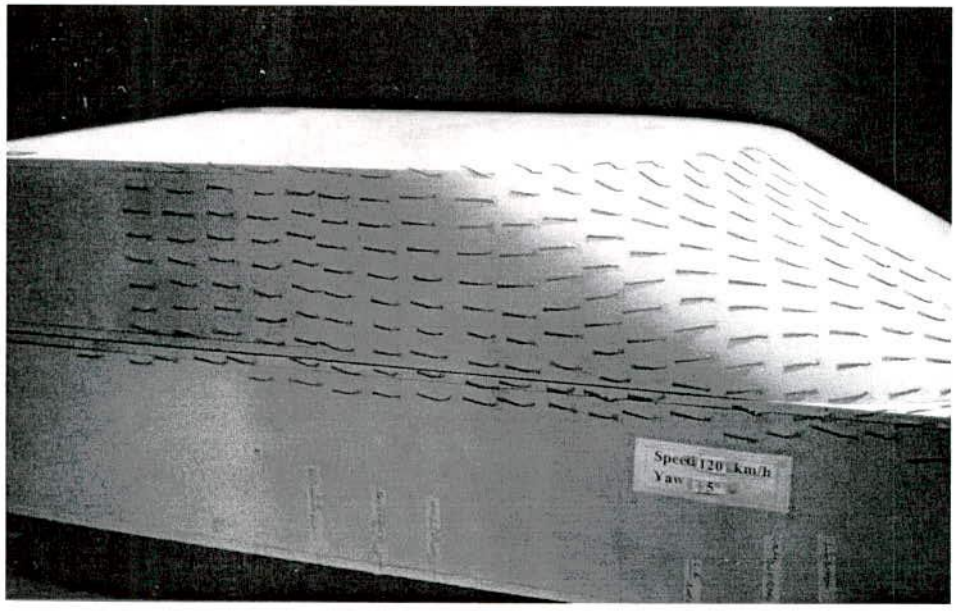

Figure G.42: Side View, Circular Model, 120 km/h, Yaw = +5°

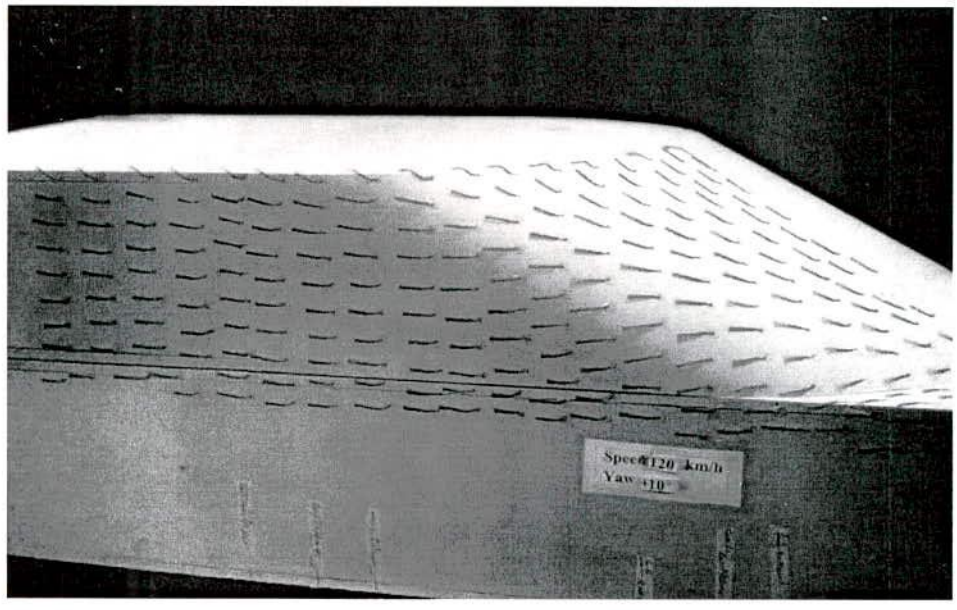

Figure G.43: Side View, Circular Model, 120 km/h, Yaw = +10°

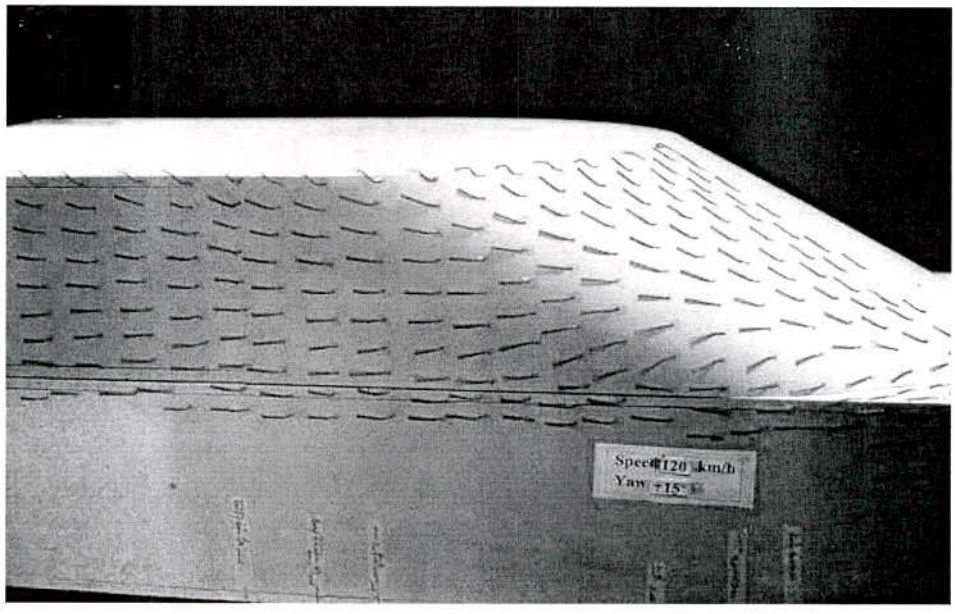

Figure G.44: Side View, Circular Model, 120 km/h, Yaw = +15°

G.5 Large Ellipsoidal Model

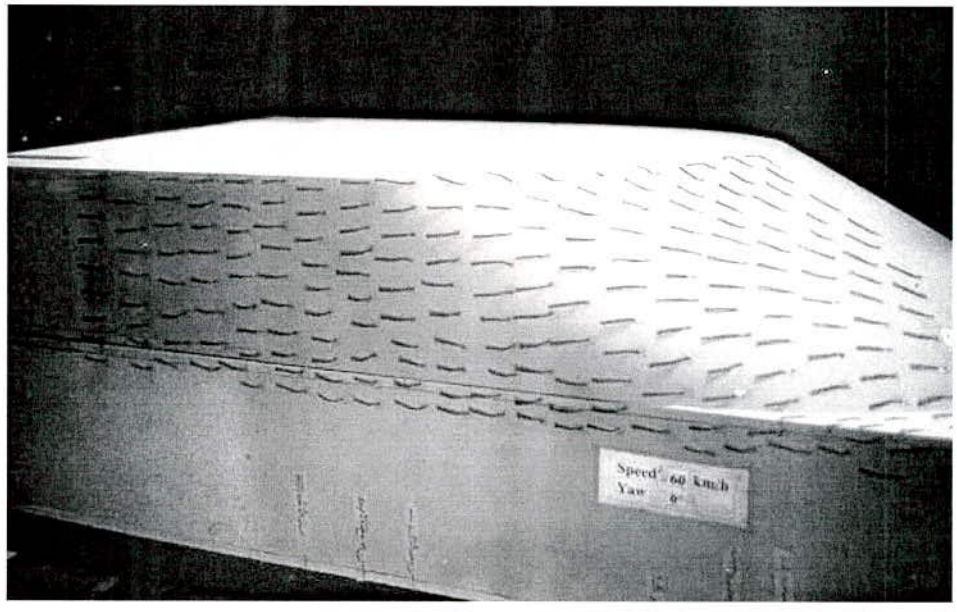

Figure G.45: Side View, Large Ellipsoidal Model, 60 km/h, Yaw = 0°

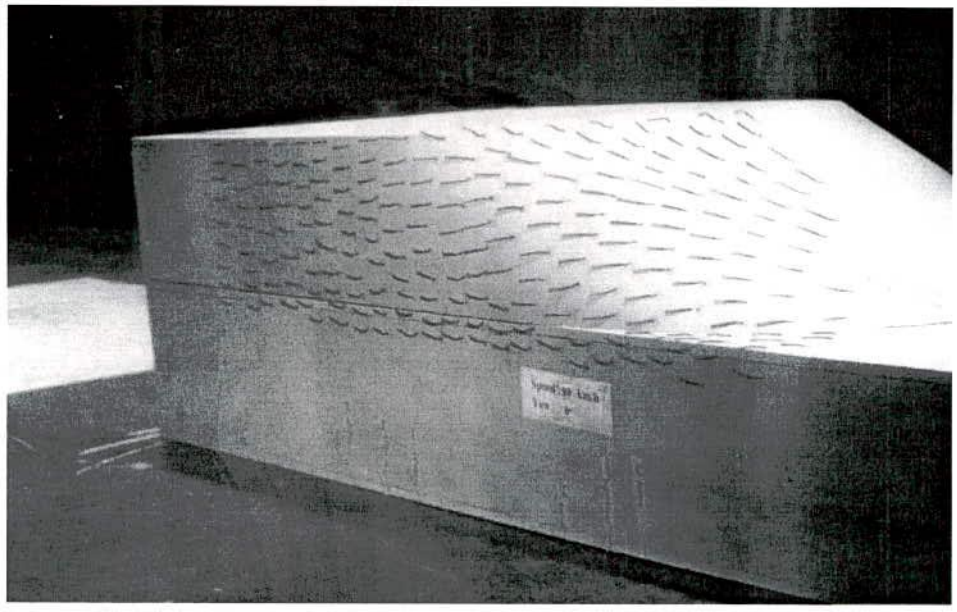

Figure G.46: Side View, Large Ellipsoidal Model, 80 km/h, Yaw = 0°

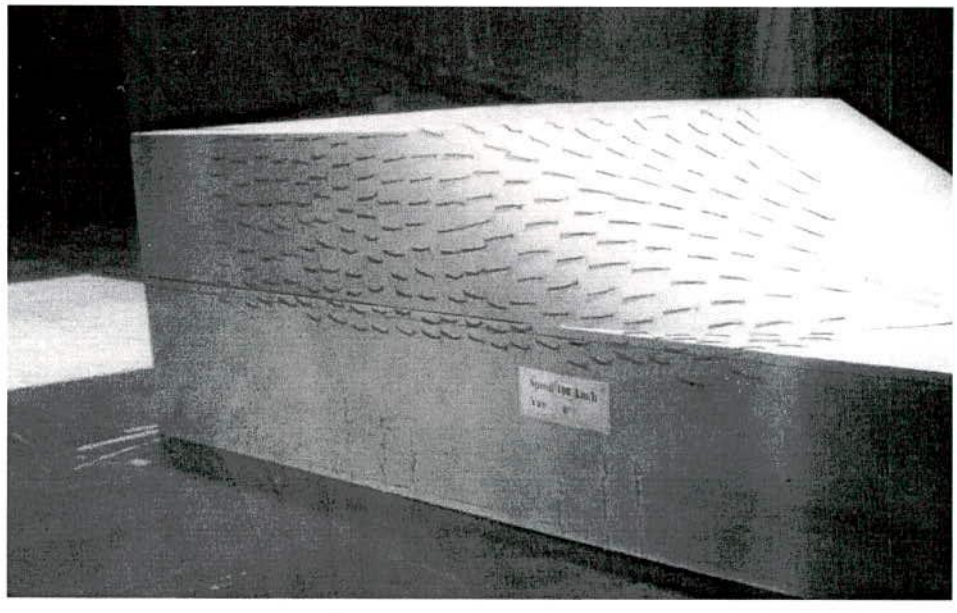

Figure G.47: Side View, Large Ellipsoidal Model, 100 km/h, Yaw = 0°

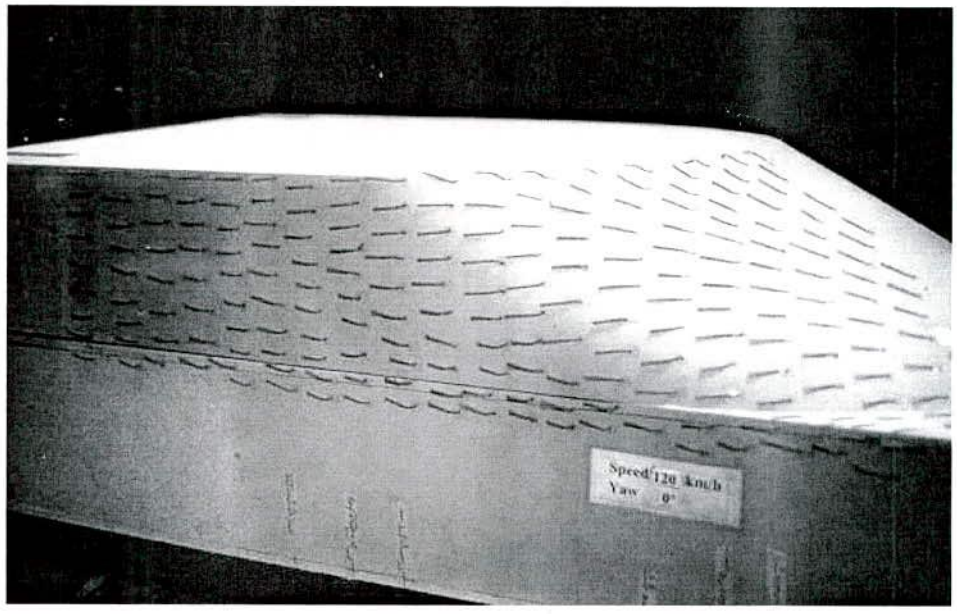

Figure G.48: Side View, Large Ellipsoidal Model, 120 km/h, Yaw = 0°

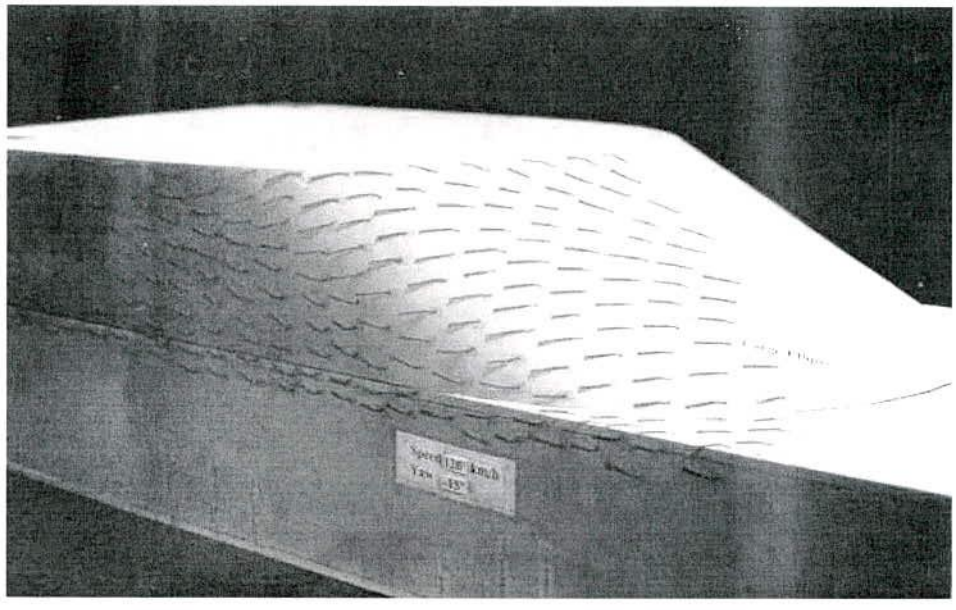

Figure G.49: Side View, Large Ellipsoidal Model, 120 km/h, Yaw = -15°

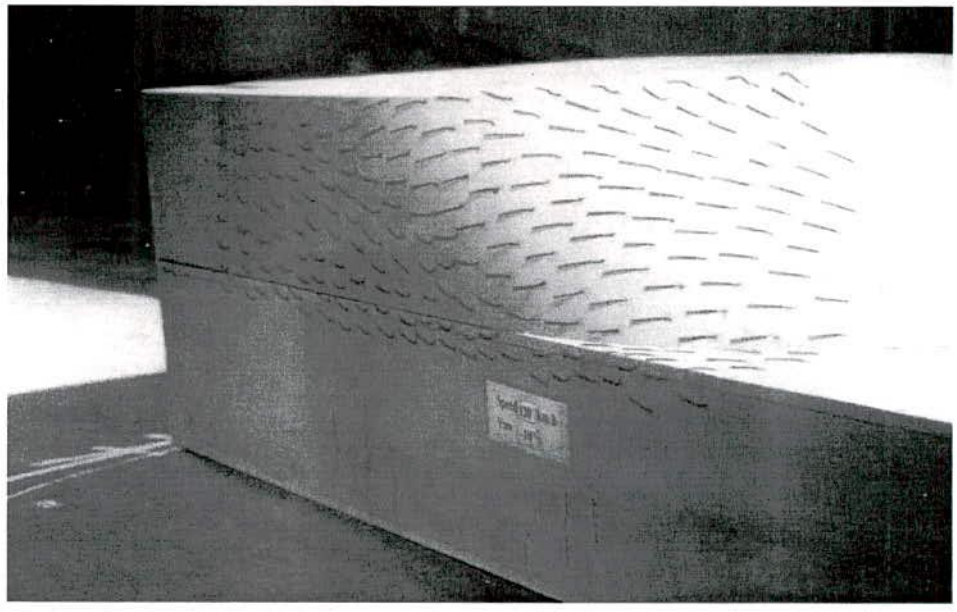

Figure G.50: Side View, Large Ellipsoidal Model, 120 km/h, Yaw = -10°

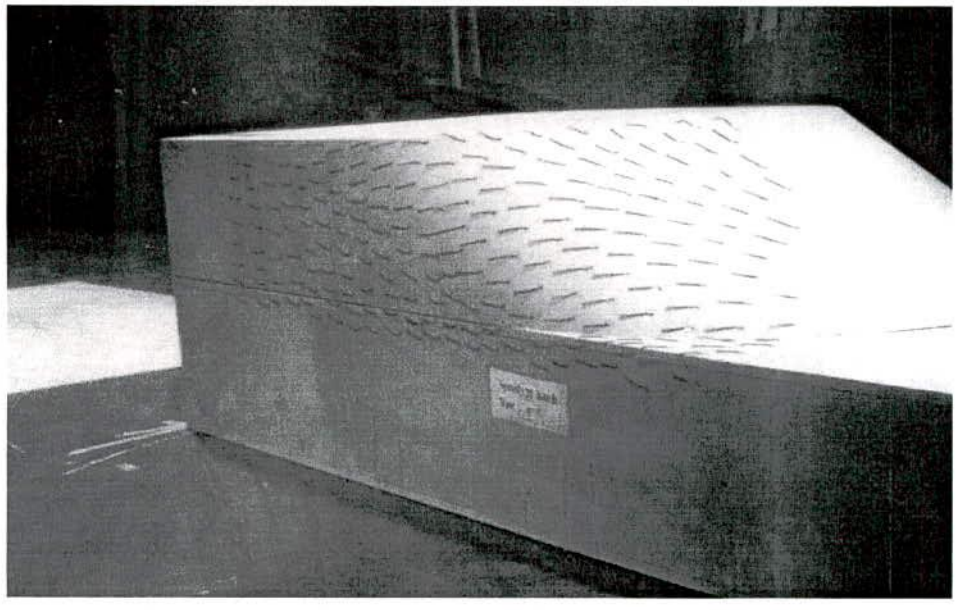

Figure G.51: Side View, Large Ellipsoidal Model, 120 km/h, Yaw = -5°

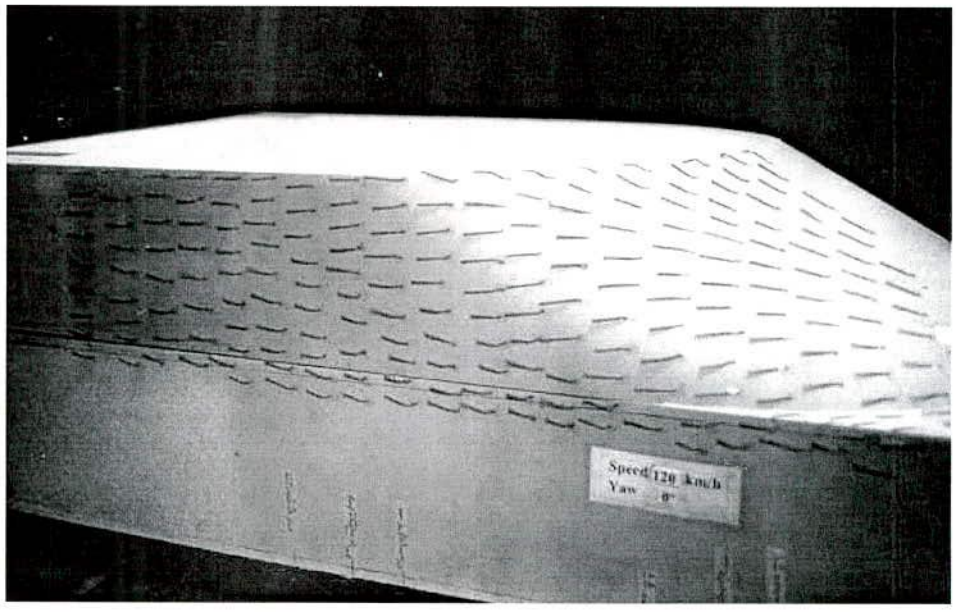

Figure G.52: Side View, Large Ellipsoidal Model, 120 km/h, Yaw = 0°

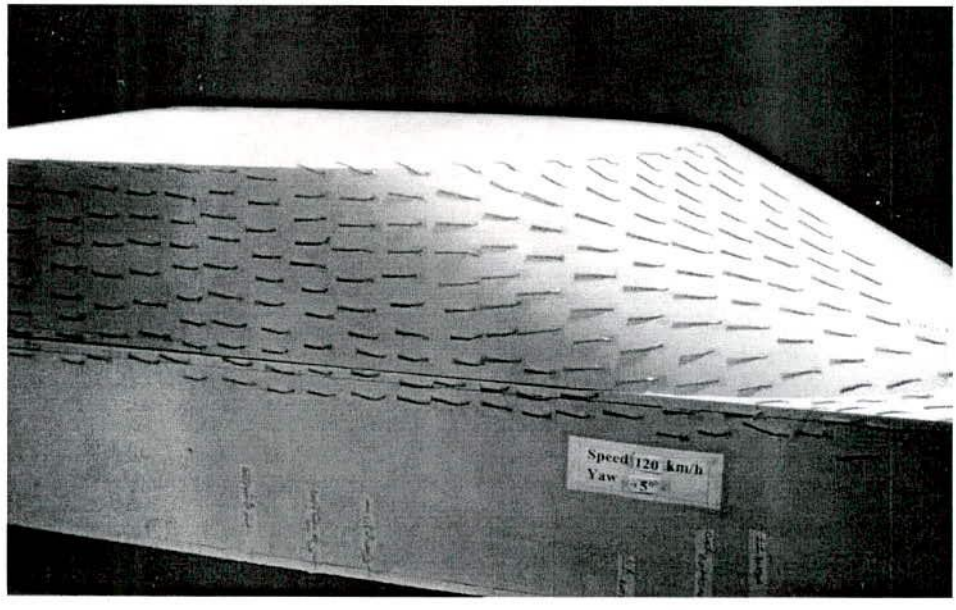

Figure G.53: Side View, Large Ellipsoidal Model, 120 km/h, Yaw = +5°

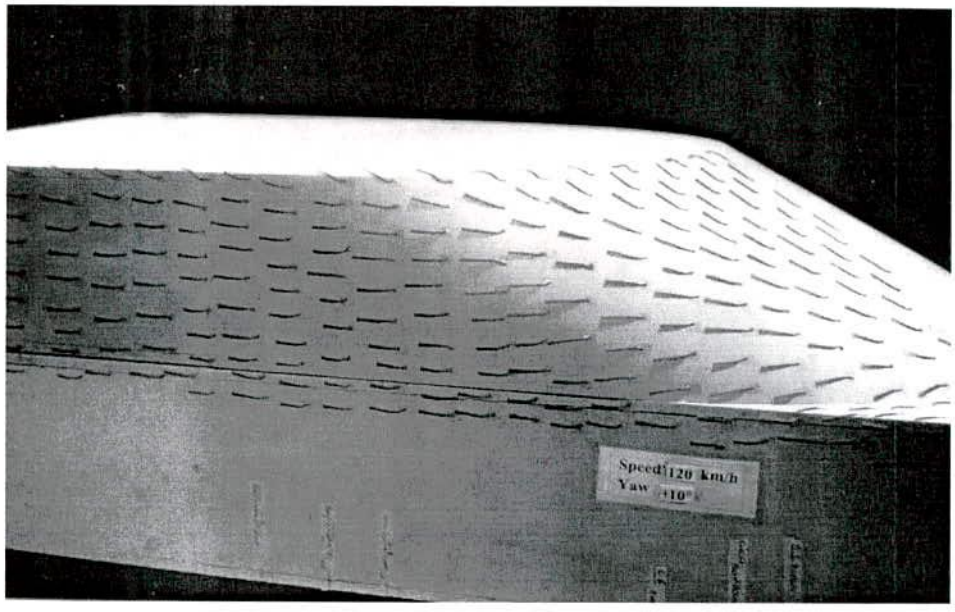

Figure G.54: Side View, Large Ellipsoidal Model, 120 km/h, Yaw = +10°

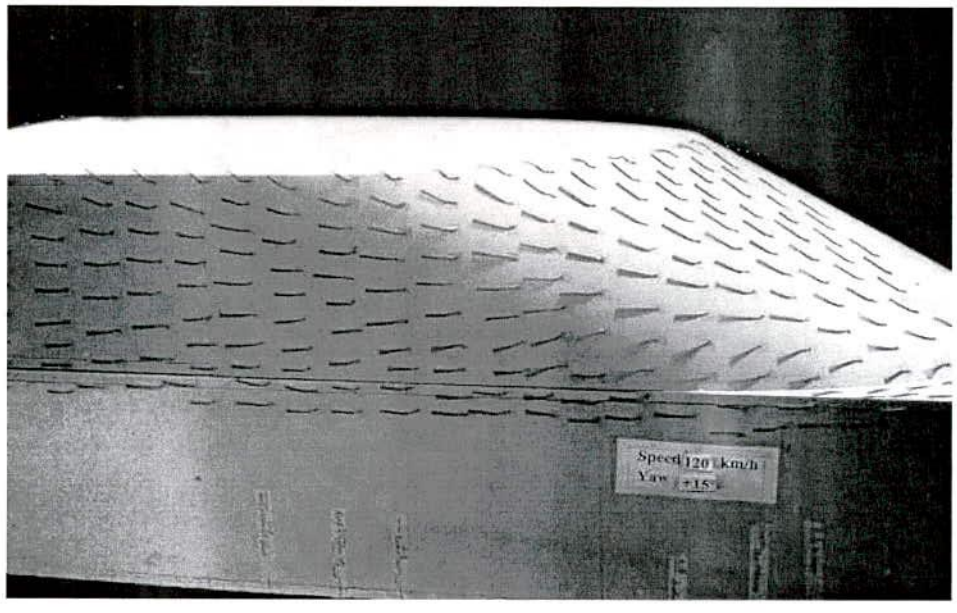

Figure G.55: Side View, Large Ellipsoidal Model, 120 km/h, Yaw = +15°

Appendix H

Surface Mean Cp and Normalised Power Spectra for Idealised Models

H.1 Rectangular Model

H.1.1 Surface Mean Pressure Coefficients at Intermediate Reynolds Number and Yaw Angles

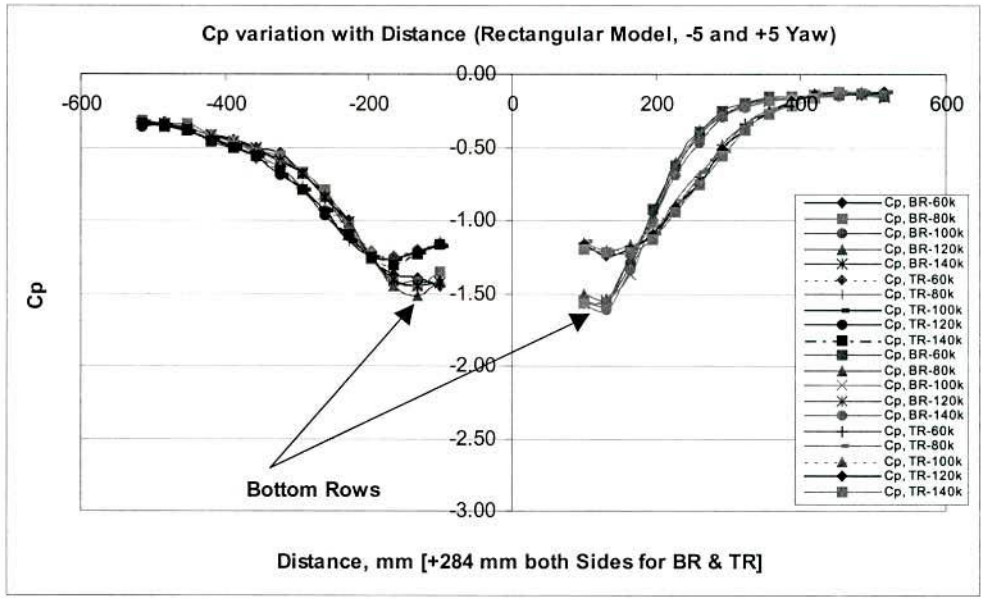

Figure H.1: Surface Mean Cp Variation with Distance, Yaw = -5° and +5° (R)

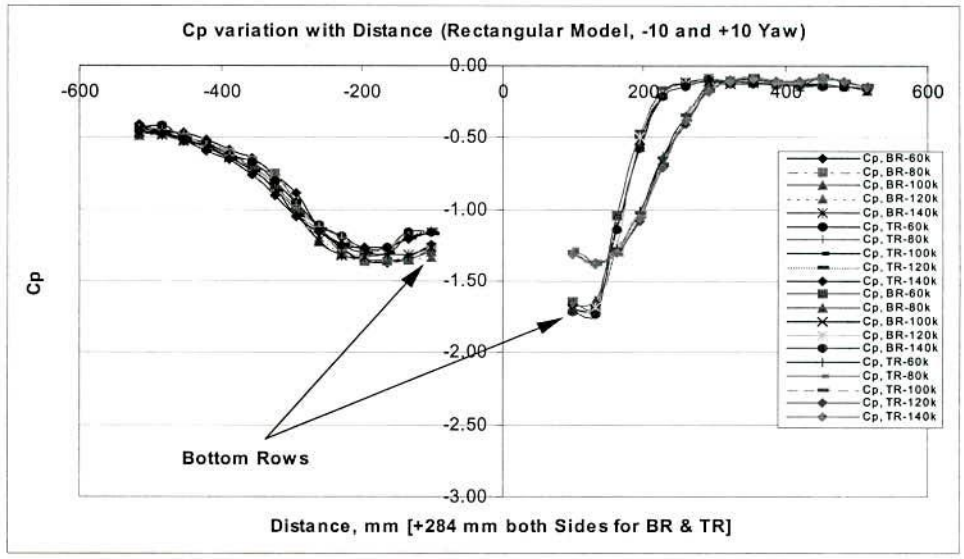

Figure H.2: Surface Mean Cp Variation with Distance, Yaw = -10° and +10° (R)

H.1.2 Normalised Power Spectra at Intermediate Reynolds Number and Yaw Angles

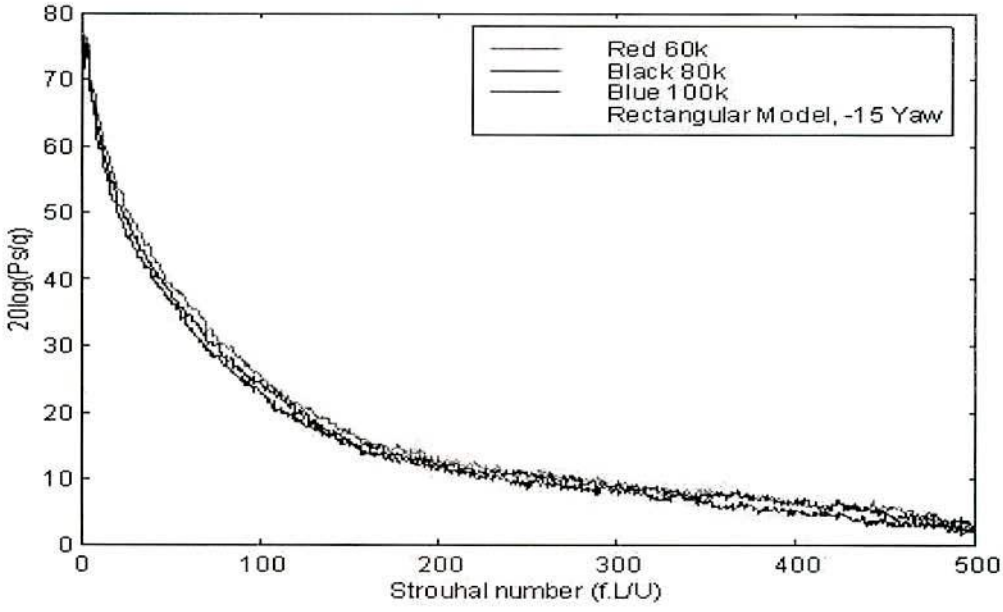

Figure H.3: Normalised Power Spectra of Peak Cp rms, Yaw = -15° (R)

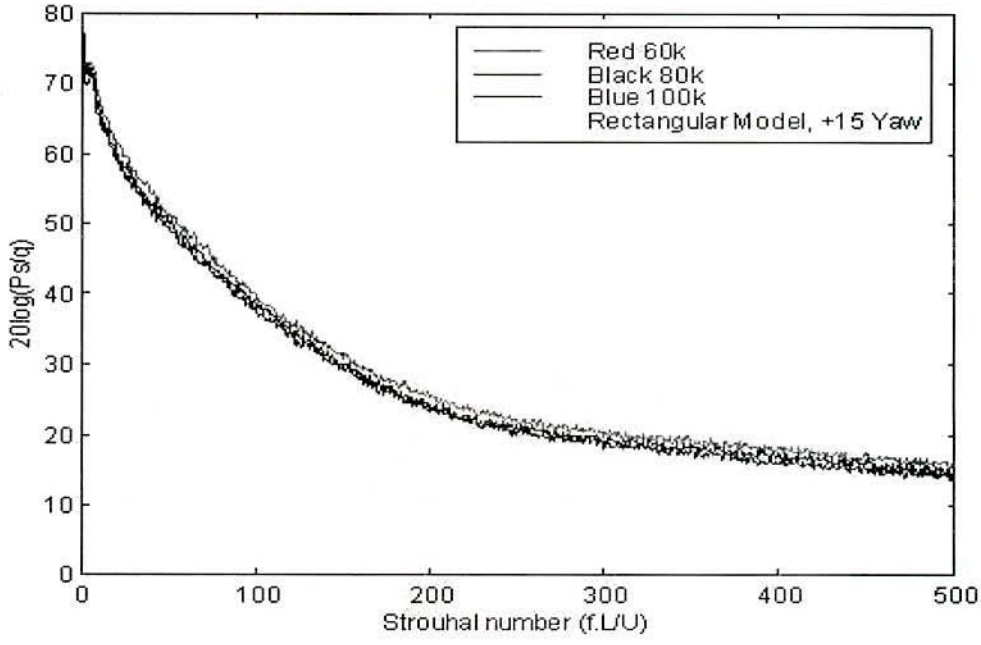

Figure H.4: Normalised Power Spectra of Peak Cp rms, Yaw = +15° (R)

H.2 Slanted Sharp-edged Model

H.2.1 Surface Mean Pressure Coefficients at Intermediate Reynolds Number and Yaw Angles

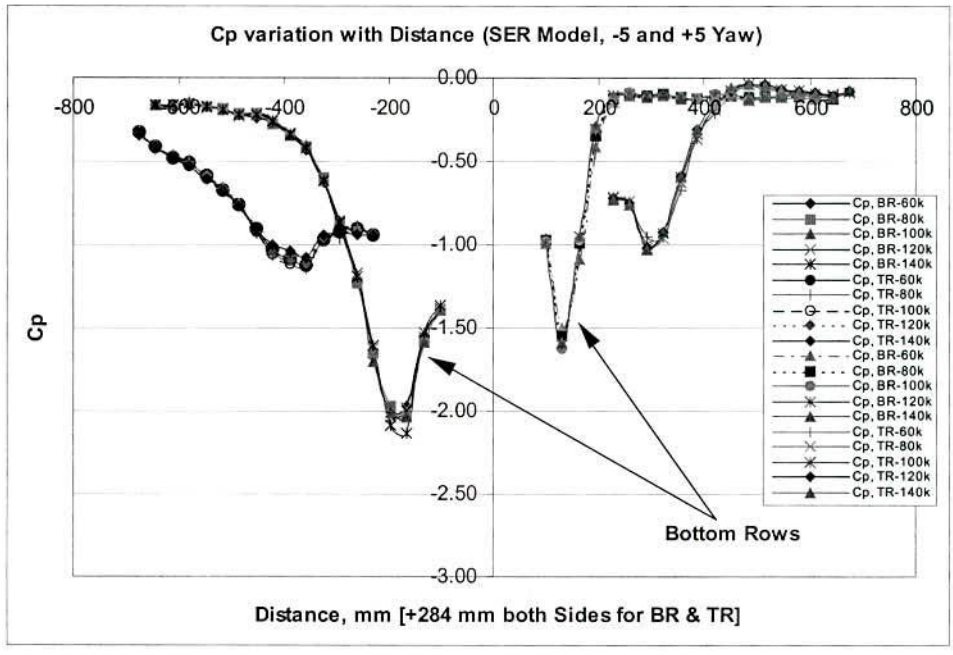

Figure H.5: Surface Mean Cp Variation with Distance, Yaw = -5° and +5° (SER)

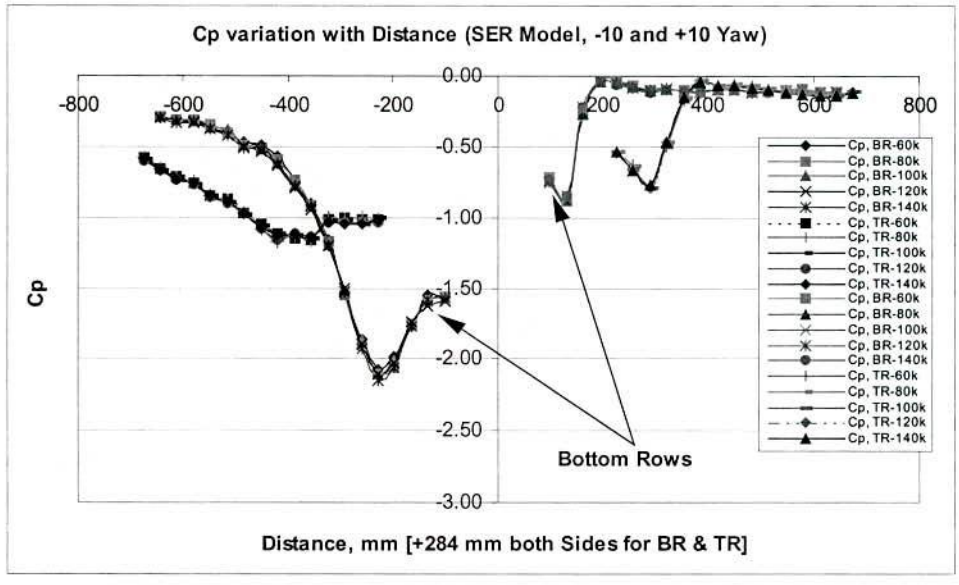

Figure H.6: Surface Mean Cp Variation with Distance, Yaw = -10° and +10° (SER)

H.2.2 Normalised Power Spectra at Intermediate Reynolds Number and Yaw angles

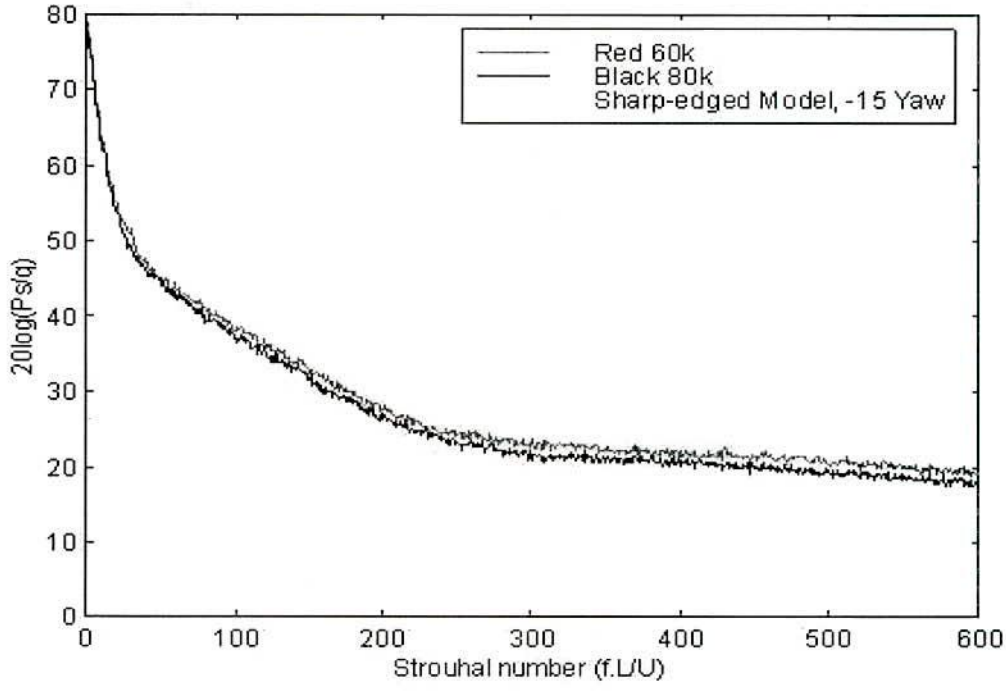

Figure H.7: Normalised Power Spectra of Peak Cp rms, Yaw = -15° (SER)

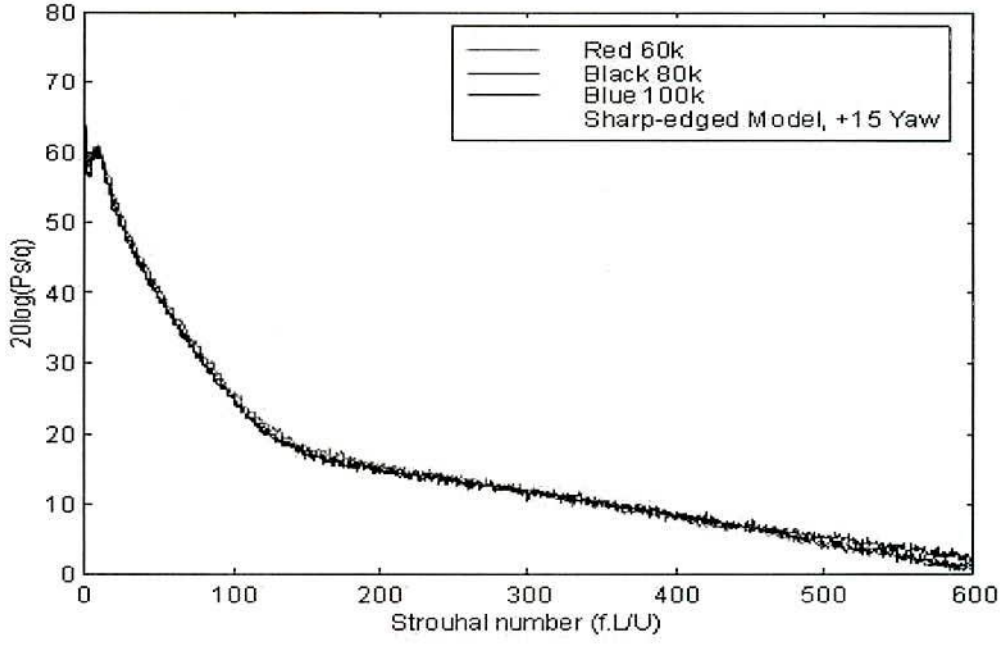

Figure H.8: Normalised Power Spectra of Peak Cp rms, Yaw = +15° (SER)

H.3 Small Ellipsoidal Model

H.3.1 Surface Mean Pressure Coefficients at Intermediate Reynolds Number and Yaw Angles

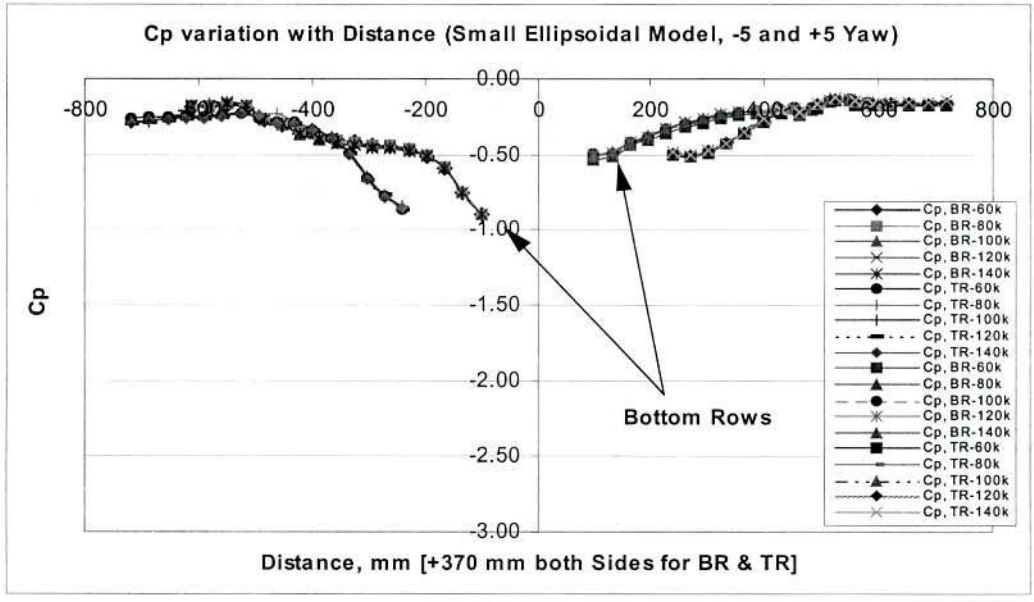

Figure H.9: Surface Mean Cp Variation with Distance, Yaw = -5° and +5° (SE)

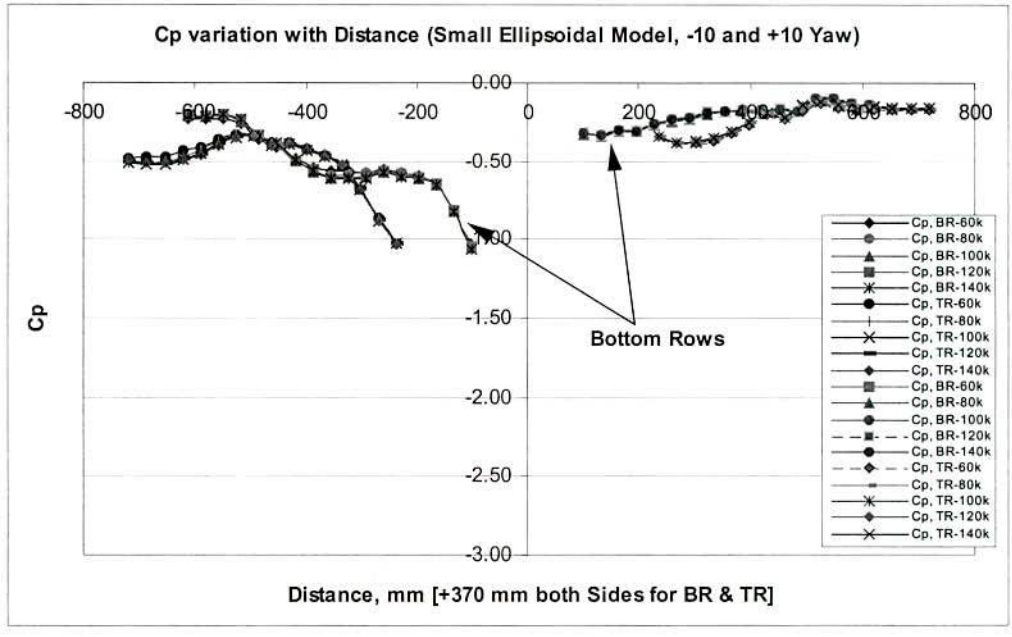

Figure H.10: Surface Mean Cp Variation with Distance, Yaw = -10° and +10° (SE)

H.3.2 Normalised Power Spectra at Intermediate Reynolds Number and Yaw angles

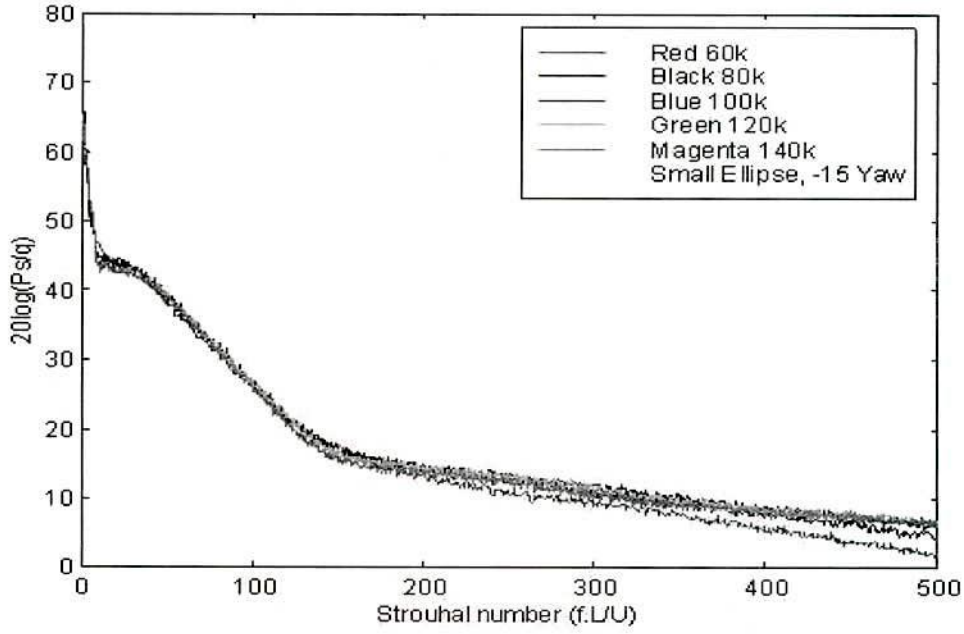

Figure H.11: Normalised Power Spectra of Peak Cp rms, Yaw = -15° (SE)

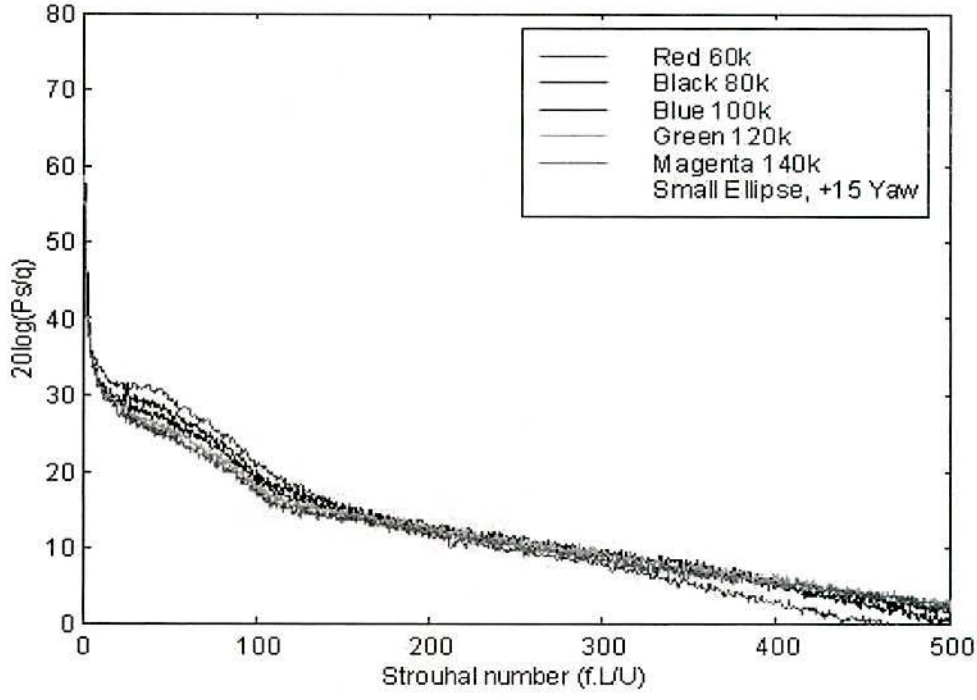

Figure H.12: Normalised Power Spectra of Peak Cp rms, Yaw = +15° (SE)

H.4 Circular Model

H.4.1 Surface Mean Pressure Coefficients at Intermediate Reynolds Number and Yaw Angles

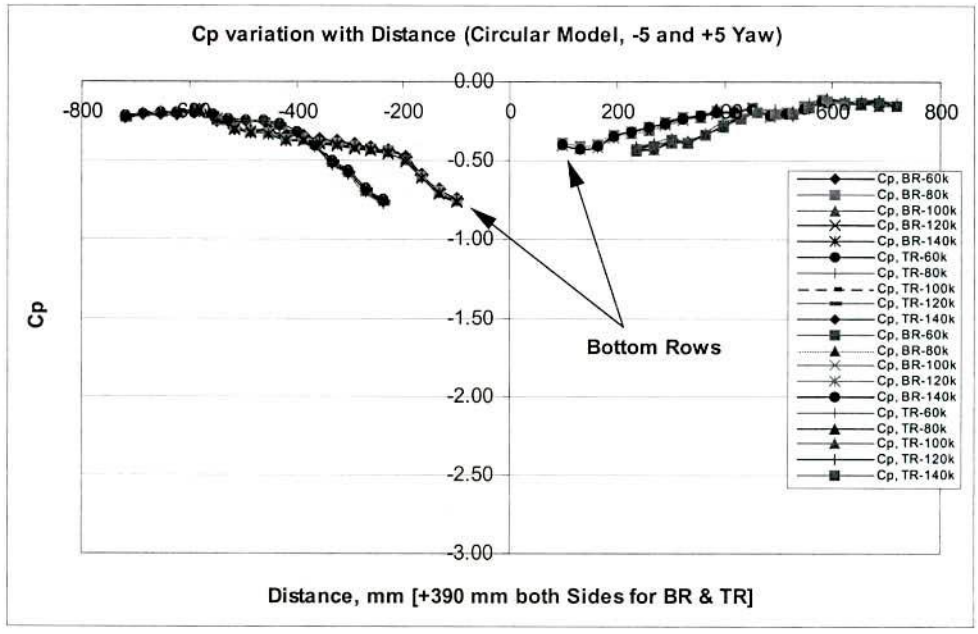

Figure H.13: Surface Mean Cp Variation with Distance, Yaw = -5° and +5° (C)

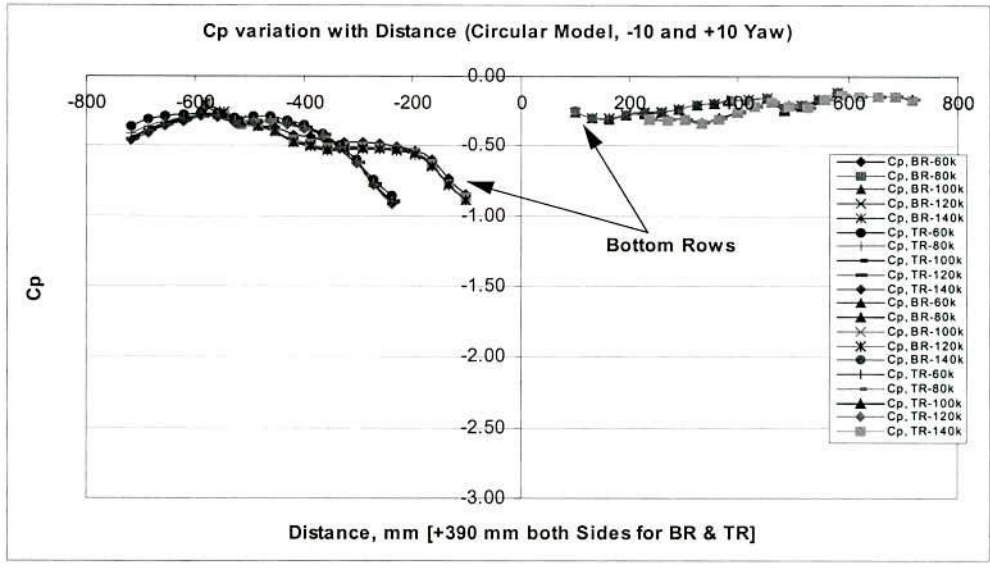

Figure H.14: Surface Mean Cp Variation with Distance, Yaw = -10° and +10° (C)

H.4.2 Normalised Power Spectra at Intermediate Reynolds Number and Yaw angles (C)

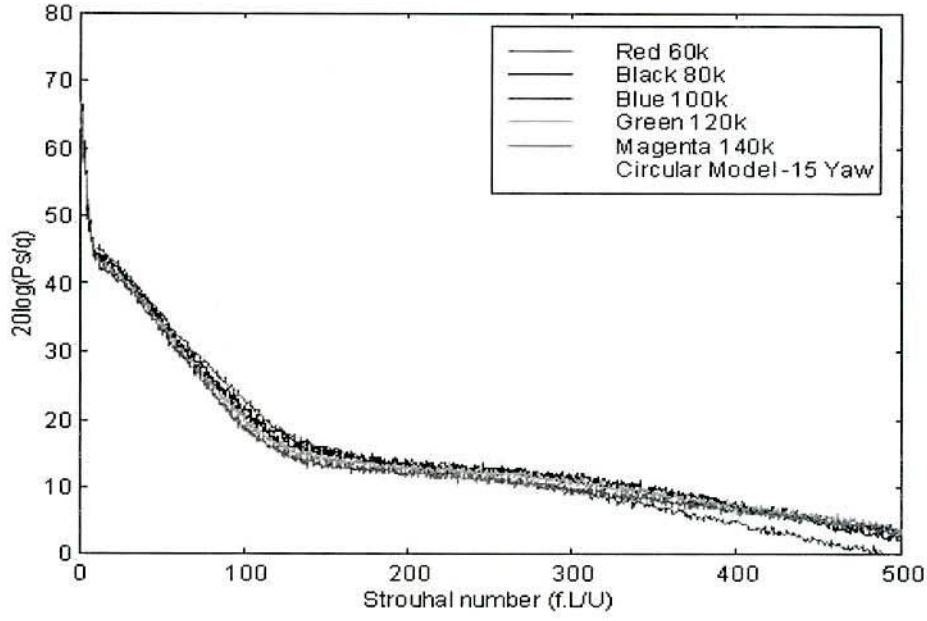

Figure H.15: Normalised Power Spectra of Peak Cp rms, Yaw = -15° (C)

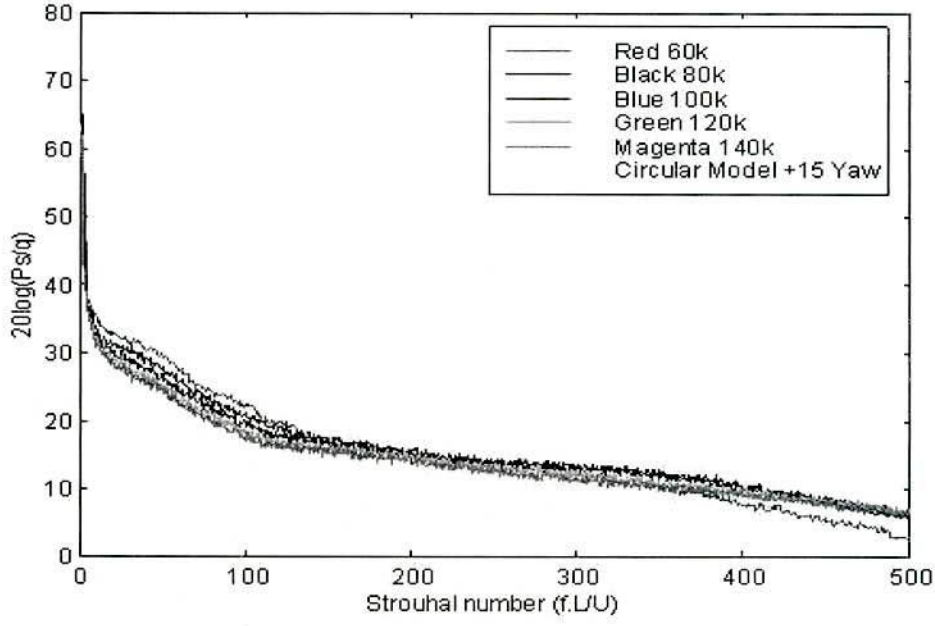

Figure H.16: Normalised Power Spectra of Peak Cp rms, Yaw = +15° (C)

H.5 Large Ellipsoidal Model

H.5.1 Surface Mean Pressure Coefficients at Intermediate Reynolds Numbers and Yaw Angles

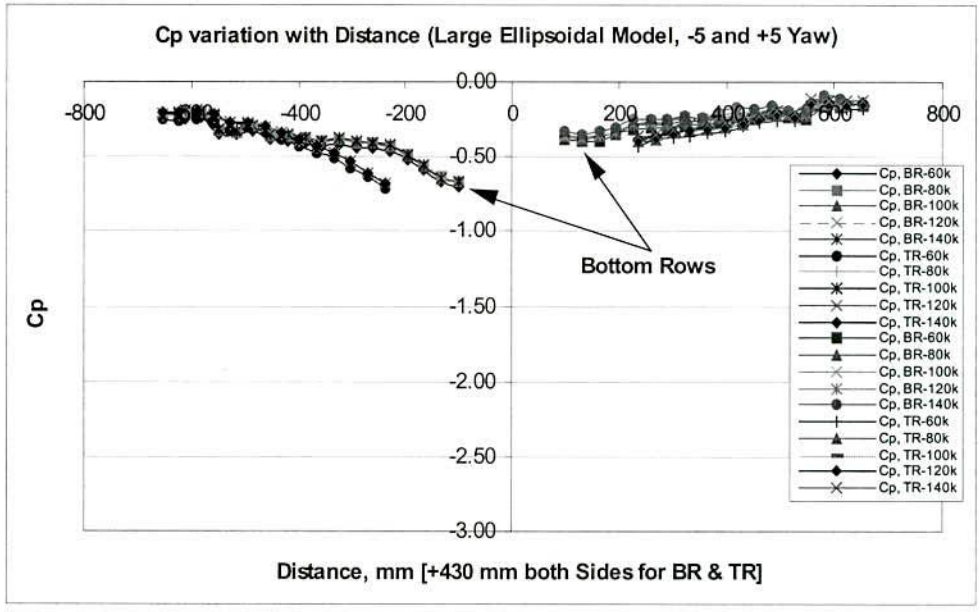

Figure H.17: Surface Mean Cp Variation with Distance, Yaw = -5° and +5° (LE)

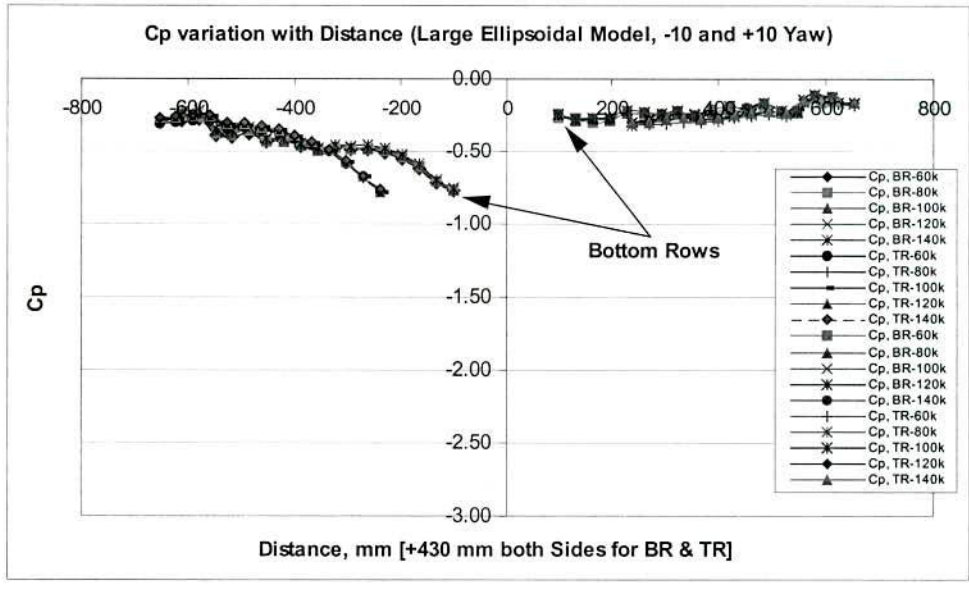

Figure H.18: Surface Mean Cp Variation with Distance, Yaw = -10° and +10° (LE)

H.5.2 Normalised Power Spectra at Intermediate Reynolds Number and Yaw angles

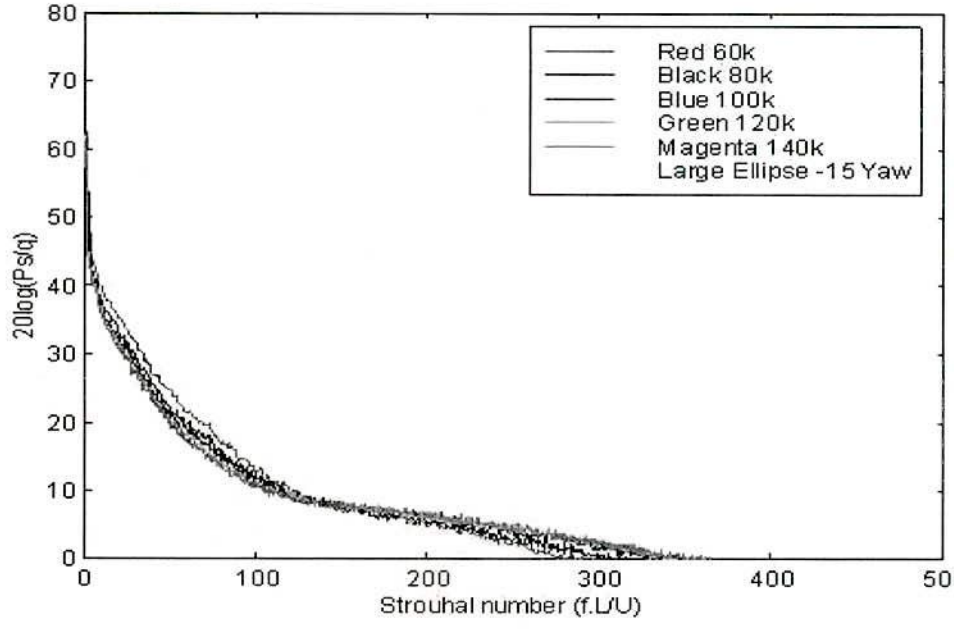

Figure H.19: Normalised Power Spectra of Peak Cp rms, Yaw = -15° (LE)

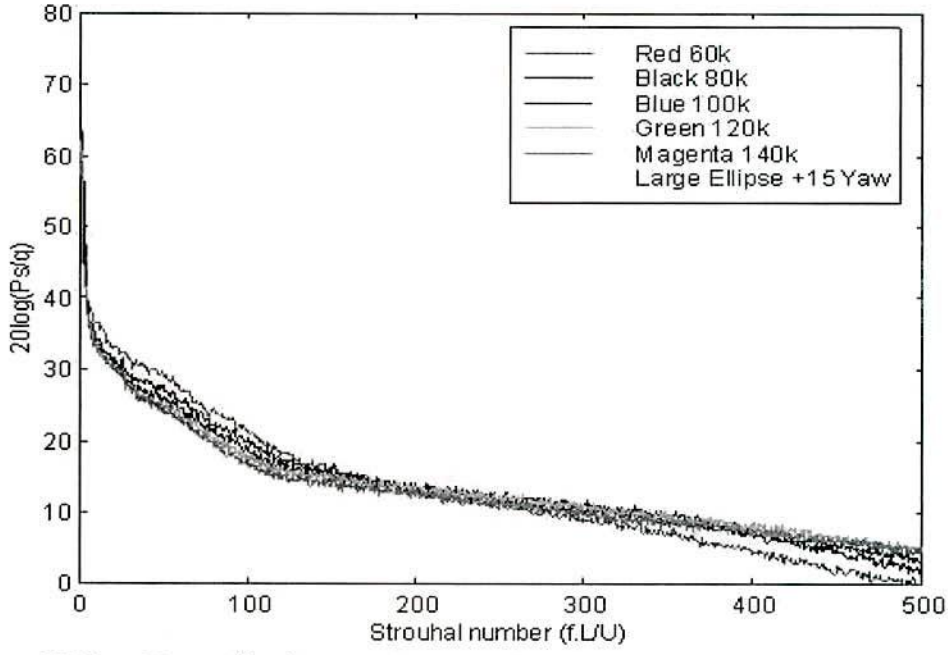

Figure H.20: Normalised Power Spectra of Peak Cp rms, Yaw = +15° (LE)

H.6 Fluctuating Cp rms Variation with Reynolds Number based on Local Radius

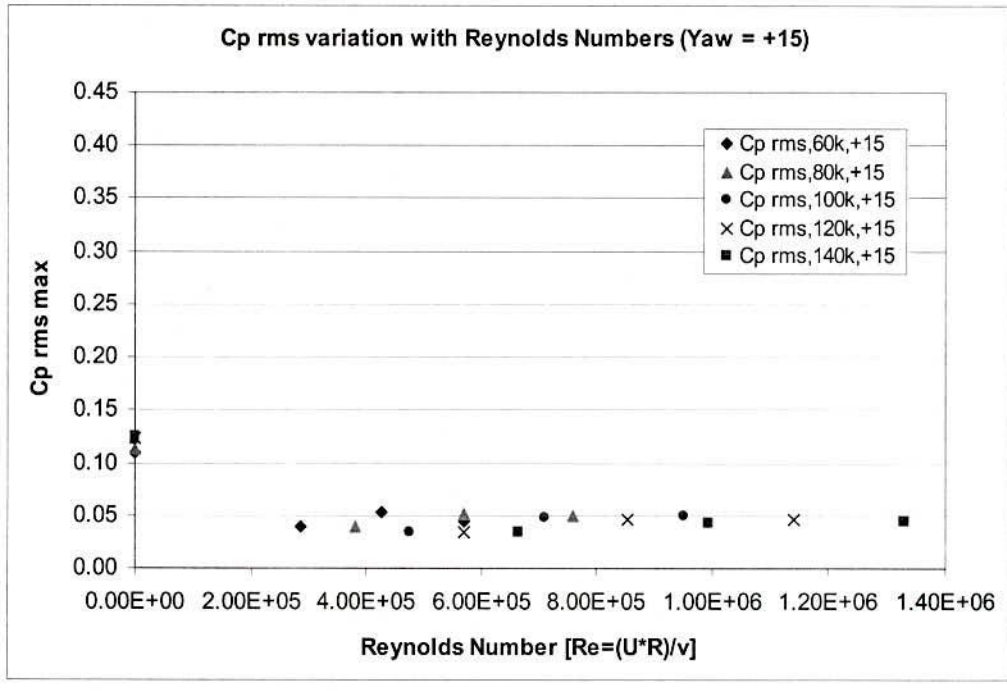

Figure H.21: Fluctuating Cp rms Variation with Reynolds Number based on Local Radius, Yaw = +15° (All Models)

Appendix I

Surface Mean Cp and Normalised Power Spectra for Production Vehicle

I.1 Full-Size Vehicle Tests in Monash/RMIT Wind-Tunnel

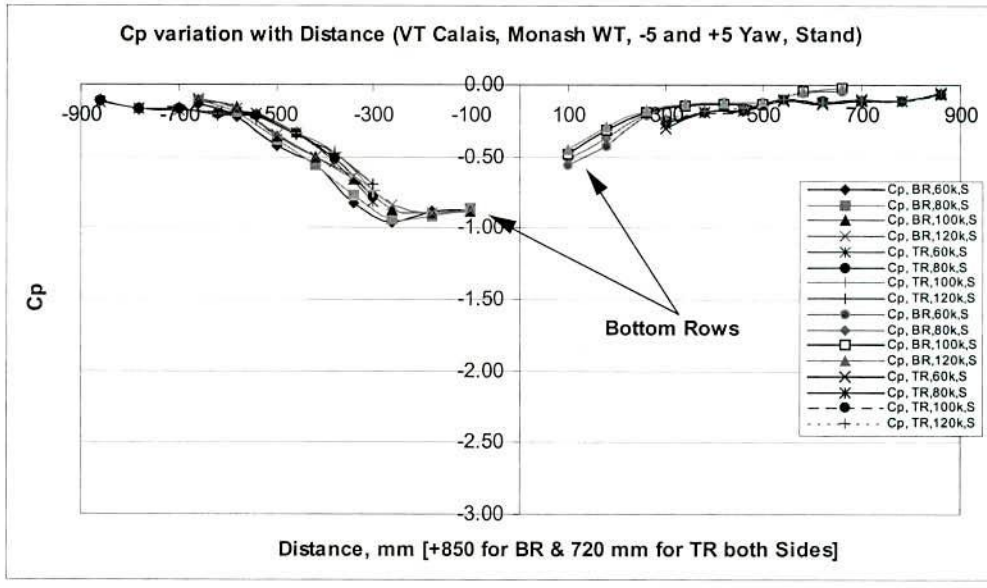

Figure I.1: Surface Mean Cp Variation with Distance, Yaw = -10 and +10, MWT, Standard A-pillar

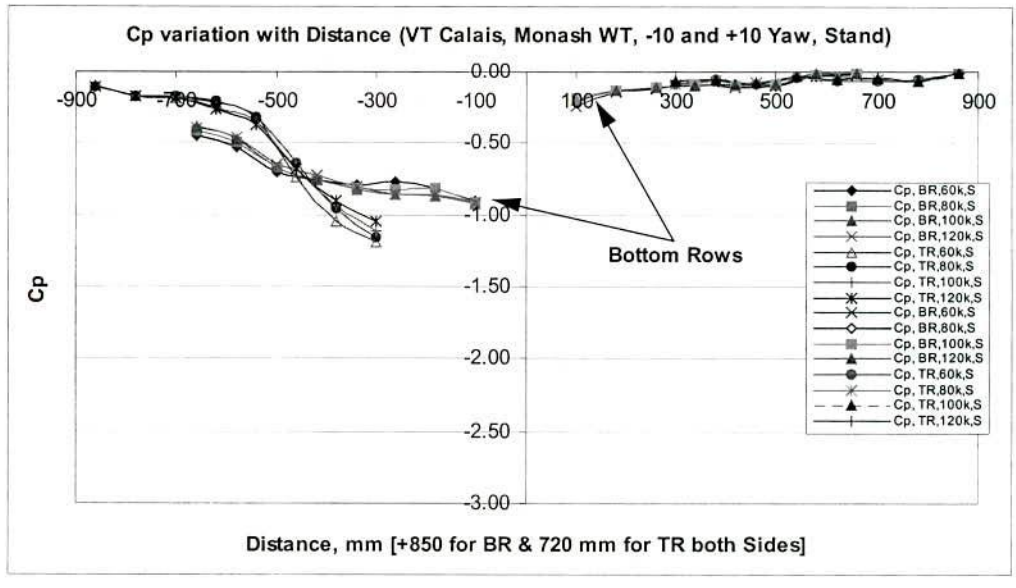

Figure I.2: Surface Mean Cp Variation with Distance, Yaw = -10 and +10, MWT, Modified A-pillar

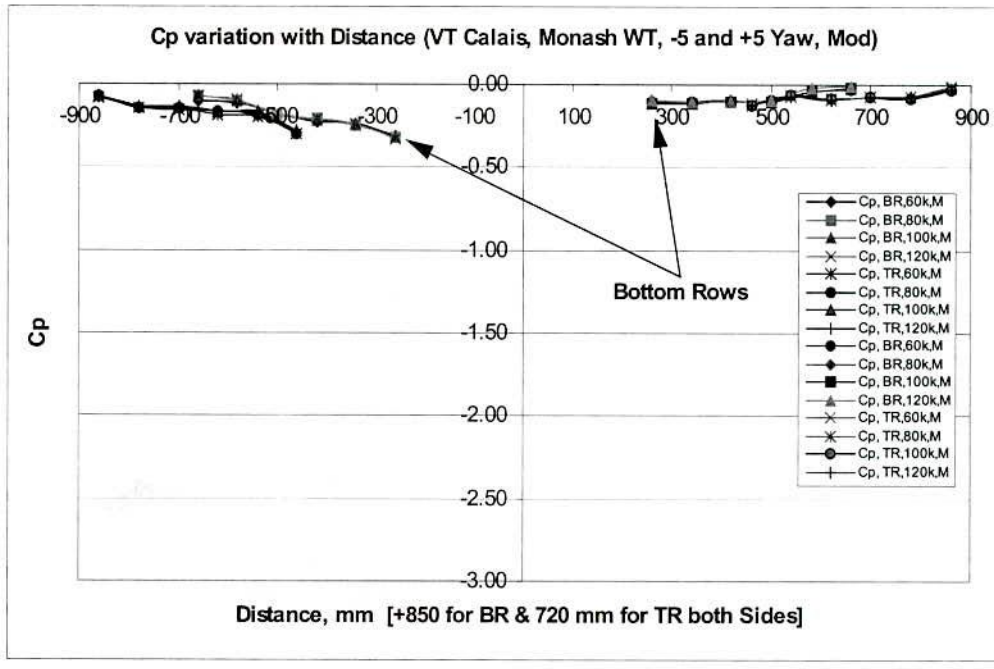

Figure I.3: Surface Mean Cp Variation with Distance, Yaw = -5 and +5, MWT, Standard A-pillar

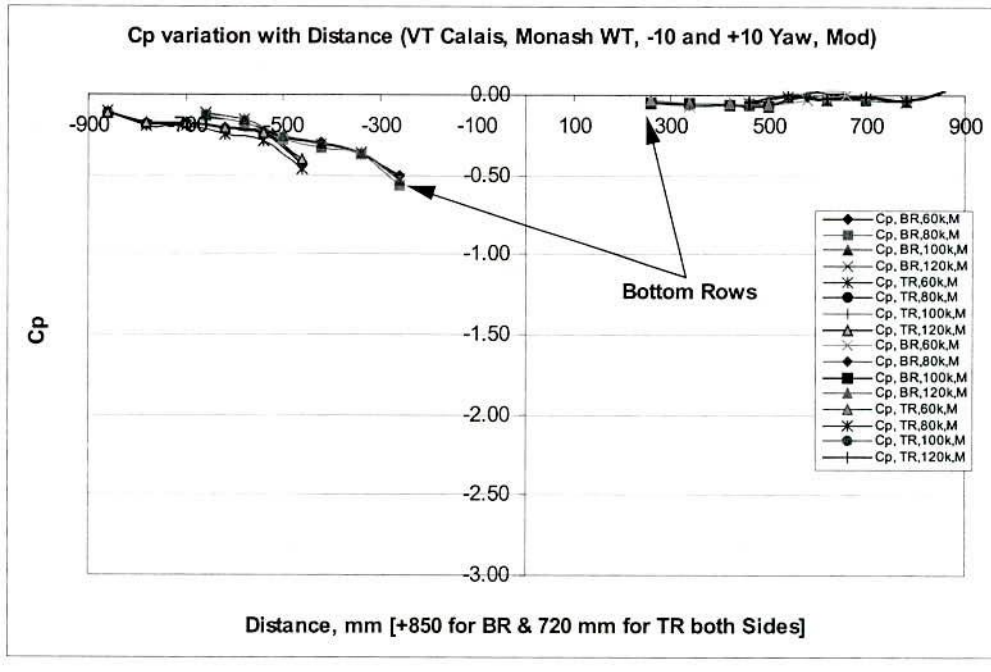

Figure I.4: Surface Mean Cp Variation with Distance, Yaw = -5 and +5, MWT, Modified A-pillar

I.2 Spectral Analysis (Monash/RMIT Wind-Tunnel)

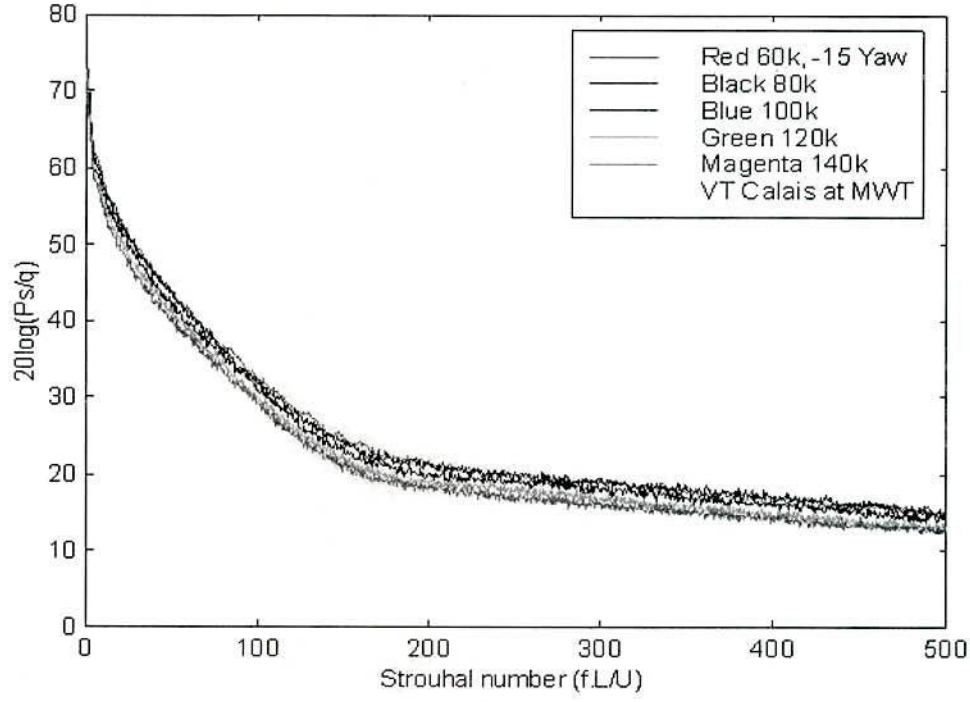

Figure I.5: Normalised Power Spectra Plot, Yaw = -15, MWT, Standard A-pillar

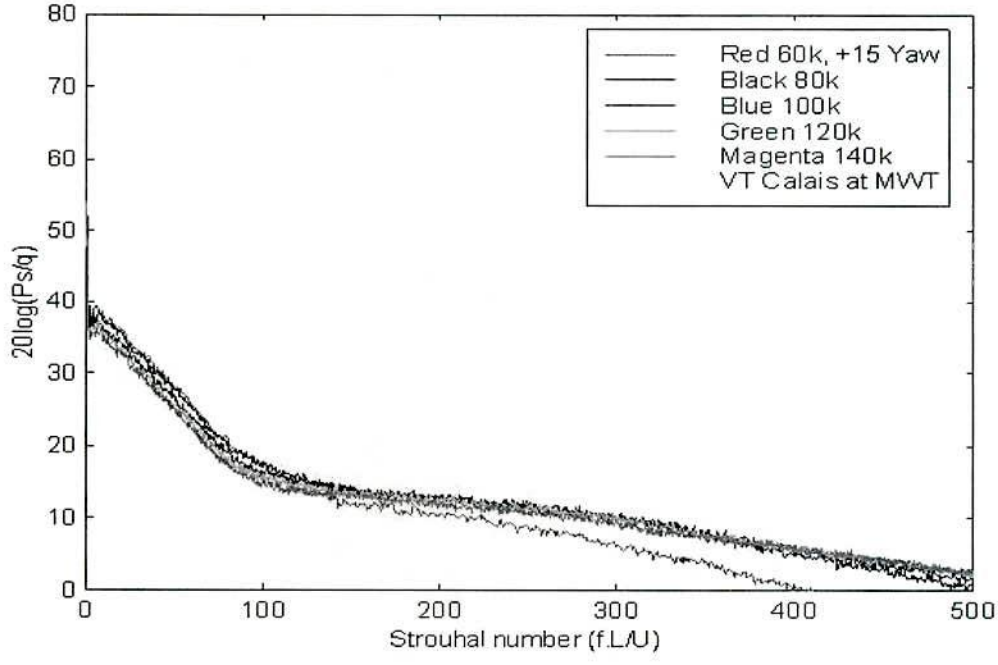

Figure I.6: Normalised Power Spectra Plot, Yaw = +15, MWT, Standard A-pillar

Appendix J

External Dimensions and Isometric Projections of Idealised Models

Simplified Models' external dimensions are shown in Figure J.1. The parameter 'a' is the ½ major axis and parameter b is the ½ minor axis of the ellipsoidal shapes. The general mathematical equation of an ellipse is $\frac{x^2}{a^2}+\frac{y^2}{b^2}=1$, where a is the ½ major axis and b is the ½ minor axis. The equation for the small ellipsoidal model is $\frac{x^2}{374^2}+\frac{y^2}{229^2}=1$. For the large ellipsoidal model, b = 449 mm (20% more than the ½ width of the model) and the equation is $\frac{x^2}{374^2}+\frac{y^2}{449^2}=1$. For the circular model, $b = a$ = 374 mm (½ width of the model) and the equation is $\frac{x^2}{374^2}+\frac{y^2}{374^2}=1$ or $x^2+y^2=374^2$.

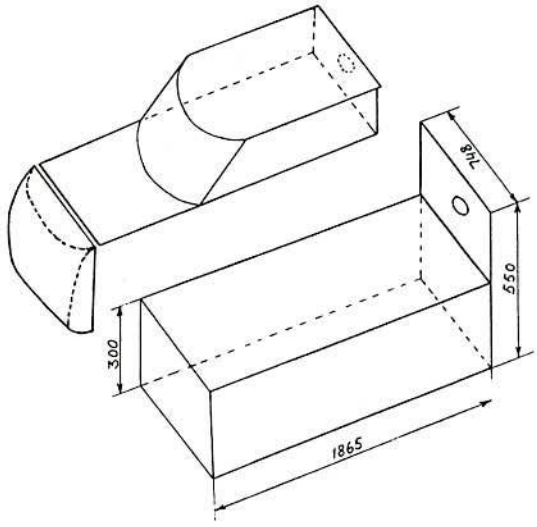

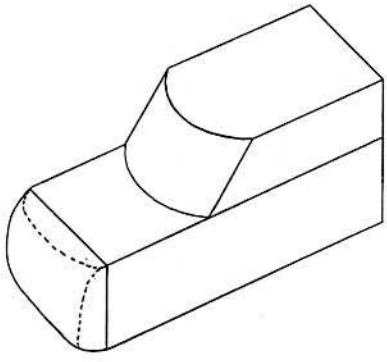

a). Pictorial View (Small Ellipsoidal Model)

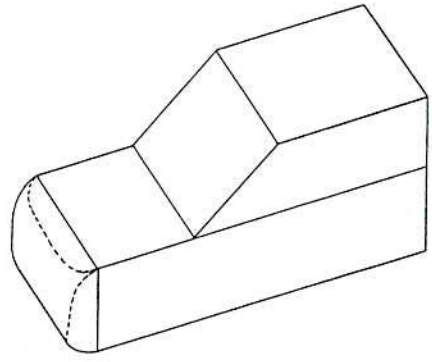

d). Pictorial View (Slanted Sharp-edged Model)

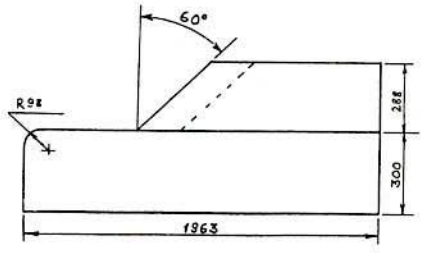

b). Front View (Small Ellipsoidal Model)

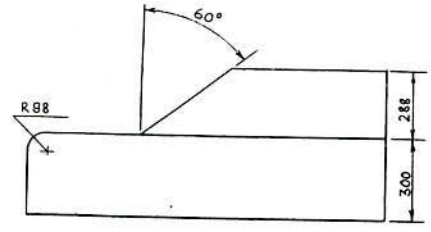

e). Front View (Slanted Sharp-edged Model)

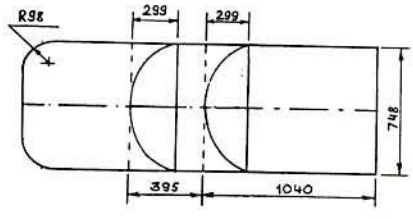

c). Top View (Small Ellipsoidal Model)

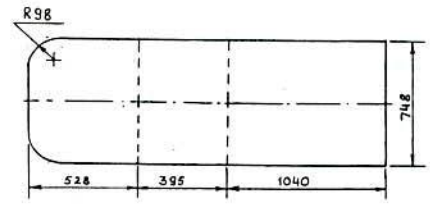

f). Top View (Slanted Sharp-edged Model)

Figure J.1: Schematic of Simplified Models with External Geometry (All Dimensions in mm)

Appendix K

Comments on Calibration and Accuracy

As all experimental work in this research was conducted on model-scale and full-scale vehicles in wind-tunnels and on the road, experimental errors will be discussed separately in the next two subsections.

K.1 Wind-Tunnel Tests

K.1.1 Random Errors

During the surface mean and fluctuating pressure and in-cabin noise measurements using the RMIT and Monash/RMIT Universities' Aeroacoustic Wind-Tunnels, random errors might have occurred for a variety of reasons, such as alignment errors and slow changes in tunnel speed. However, these errors can be assessed by the degree of data repeatability.

K.1.1.1 Repeatability of Results

For every scale model and production vehicle test in the wind tunnels, data were first acquired at zero speed before and after test. This was to measure the noise in the systems arising from electrical and electro-magnetic influence due to wind-tunnel controllers and power supplies with no "physical" inputs from the airflow to the transducers. Additionally, at each test speed, data were acquired several times to check the repeatability. The typical repeatability of surface mean pressure (Cp) and fluctuating pressure (Cp rms) coefficients was estimated to be ±0.5% and ±0.4% respectively.

K.1.1.2 Wind-Tunnel Speed Errors

During the test, the air speed in the RMIT University Wind-Tunnel was measured with a NPL modified ellipsoidal head Pitot-static tube connected to a MKS Baratron-reference pressure transducer. The air speed was also measured via an Honeywell (160 PC) pressure transducer to compare the data with MKS Baratron pressure transducer. In the Monash/RMIT University Wind-Tunnel, the air speed was measured by a pair of ellipsoidal head Pitot-static tubes that were connected to Honeywell (160 PC) pressure transducers. The air speed was also measured via a Betz manometer. The deviation of tunnel air speed measurements from nominal in both tunnels was less than 1%.

K.1.1.3 Temperature and Pressure Errors

Slow fluctuations of tunnel temperature and ambient pressure were accounted for in the acquisition systems and proper corrections were made (where needed) during the data processing.

K.1.1.4 Alignment Errors

Changing yaw angles in the RMIT University Aeroacoustic Wind-Tunnel and Monash/RMIT Universities' Aeroacoustic Wind-Tunnel may vary. Yaw angles were determined by aligning the scale on the turntable with existing markers on the floor. Alignment errors were minimised by taking extra care during data reading, equipment handling and set up. The error was less than $\pm 0.2°$ for the Monash/RMIT Wind-Tunnel and $\pm 0.1°$ for the RMIT Wind-Tunnel.

K.1.1.5 Data Acquisition

Surface mean pressure was measured with a Scanivalve System, which was calibrated against the MKS Baratron pressure transducer and also a precision inclined-manometer. Data acquisition was fully computerised and without human intervention. Surface fluctuating pressure was measured using G.R.A.S. microphones, which were calibrated against a Pistonphone Calibrator (Type Rio-7) and also compared to a calibrated ¼ inch B & K microphone. Negligible variation was found. The Artificial

Head System was sent back to the manufacturer for calibration just before the tests were commenced and checked using a 94 dB in-built reference signal.

Various tests were carried out to assess the background noise (both acoustic and electrical) in the test sections of RMIT and Monash/RMIT Universities' Wind-Tunnels at different speeds. At the RMIT Wind-Tunnel, the microphone was flush mounted on the floor, whereas at Monash/RMIT Universities' Wind-Tunnel, the microphone was inside the test vehicle and the background noise was measured by keeping the test vehicle out of the flow. The fluctuating pressure coefficients at both wind-tunnels are shown in Table K.1. For interests, also shown is the measured Cp rms with the wind on and the microphone inside the vehicle (which would also pick up the tunnel background and externally generated vehicle acoustic noise, albeit inside rather than outside the car body). Values for Cp rms show a significant difference in magnitudes compared to the values of Cp rms measured on the side window close to the A-pillar (typical values are 0.05 and the minimum value is 0.03 for the small ellipsoidal model). As the difference between the Cp rms measured on the side window close to the A-pillar and the background Cp rms is at least an order of magnitude, the results presented in Chapter 3, 4 and 5 are negligibly affected.

Table K.1: Cp rms for Background Noise at RMIT and Monash/RMIT Universities' Aeroacoustic Wind-Tunnels

Cp rms (background) in Monash/RMIT University Wind-Tunnel					Cp rms (background) at RMIT Wind-Tunnel
	Vehicle in the Flow			Vehicle out of the Flow	Microphone flush on the Tunnel Floor
	Standard A-Pillar	Modified A-Pillar		Standard A-Pillar	
	Microphone inside the Vehicle			Microphone inside the Vehicle	Empty Tunnel (No model in the Tunnel)
Speed (km/h)	Cp rms	Cp rms		Cp rms	Cp rms
60	0.0011	0.0012		0.0006	0.0071
80	0.0013	0.0013		0.0009	0.0070
100	0.0014	0.0014		0.0012	0.0071
120	0.0015	0.0014		0.0014	0.0071
140	0.0015	0.0016		0.0016	0.0072

K.2 On-Road Tests

As most of the on-road tests were conducted on highways, events beyond the control of the experimenters such as passing vehicles, changes of local wind conditions and car speed variations had some influence on the data. However, data were generally obtained under very low traffic conditions and the driving speed was held constant to within ±2 km/h. In addition, microphone and surface mean pressure tap settings, the Artificial Head and Cobra Probe positioning have some effects on precision errors.

Nevertheless, these errors were minimised carefully measuring and repeating locations.

K.2.1 Bias (Systematic) Errors

The test car speedometer was not calibrated. Wind speed and yaw angle measurements might have some influence on accuracy. However, the error of the speedometer reading was measured by the time travelled between the two measured points and was found to be 1-5 km/h more from the actual speed.

K.3 Solid Blockage Correction

In a closed circuit wind tunnel's test section, the presence of the tunnel walls restraining the flow around a vehicle reduces the area through which the air flows as compared to free air condition on the road. By using the Continuity and Bernoulli's equation it can be shown that the air velocity increases as it flows in the vicinity of the vehicle. This effect is called Solid Blockage, expressed as the ratio of the projected unyawed frontal area of a test vehicle and the tunnel's test section area. Solid Blockage affects the mean static pressure distribution, which can be corrected using Maskell's formula (1955). The corrected surface mean pressure coefficient by using Maskell's formula is as follows:

$C_{p_c} = 1 - \left(1 - \frac{A_m}{A_T}\right)^2 (1 - C_{p_m})$ where C_{p_c} is the correct surface mean pressure coefficient, A_m and A_T are the cross sectional areas of scale model and wind tunnel, and C_{p_m} is the measured surface mean pressure coefficient. The solid blockage ratio for the models used in this work is approximately 6%, which might overestimate the measured value of surface mean pressure coefficients up to 10%.

K.4 Conclusion on Errors

After reviewing relevant error estimations, it can be concluded that none of the conclusions made in this work will be affected by any instrumental or procedural errors.

Appendix L

On-Road Test Sites

L.1 Details of On-Road Test Sites

The on-road tests were conducted at several locations in the vicinity of the Melbourne metropolitan area in Australia. During the site selection for on-road tests, the amount of traffic, surrounding terrain and road surface condition- all were taken into consideration. An overview of such test sites is shown in Figures L.1 to L.3. The location of the test section can be found in Greater Melbourne Street Directory "Melway Map No. 182" (25th edition, 1998).

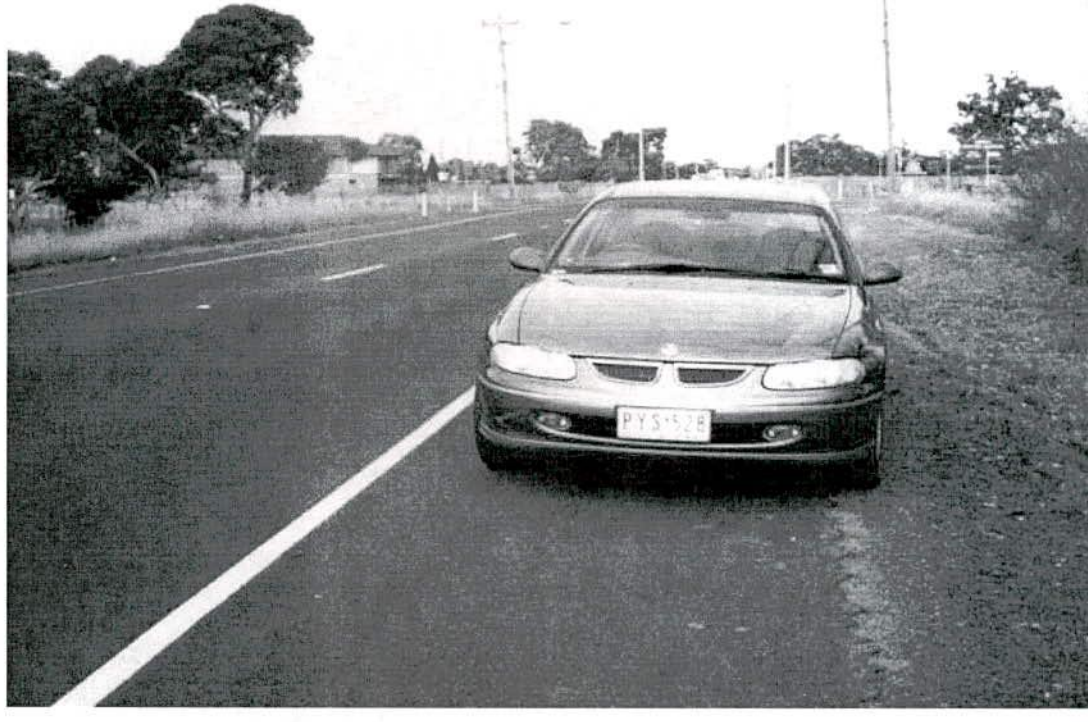

Figure L.1 VT Calais at the Test Site During On-Road Tests

Figure L.2: A Section of On-Road Test Route Near Melbourne, Australia

Figure L.3: The Test Vehicle (VT Calais) on a Test Section During On-Road Tests Near Melbourne, Australia

Appendix M

The Effects of the Underbody Flow on the A-pillar Flow Structures

The primary objective of this investigation was to determine the effect of underbody flow on the A-pillar vortices, in order to evaluate whether an underbody flow would be needed for the simplified models. An experimental investigation of the flow characteristics in the A-pillar regions of a 30% scale model car was conducted in the RMIT University Aeroacoustic Wind-Tunnel. The model was a Commodore sedan, which was a large Australian family passenger car, manufactured and sold by General Motors-Holden from 1997 and is shown in Figure M.1. This model featured comprehensive detailing and was an extremely accurate replica. It was tested with and without the side rear-view mirror. Although it was desirable to measure surface pressures, permission was not given to install any pressure taps on this model, hence exterior transient flow properties were measured in the A-pillar region using a four-hole Cobra Probe. The flow properties were measured at different positions from the side window. The model was not yawed. The model was tested with standard configuration first and then with a wrapped skirt permitting no underbody airflow (Figure M.1).

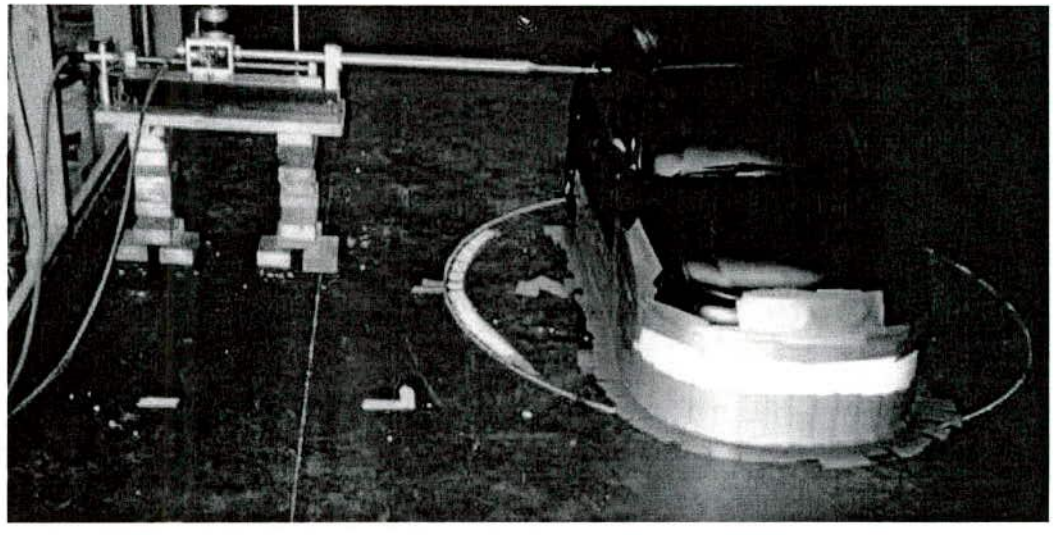

Figure M.1: A Model Car in the Test Section of RMIT Aeroacoustic Wind-Tunnel

Flow Measurements

The flow properties were measured on the right side of the model at 7 different heights, which covered the side window area in vertical increments of 25 mm from the belt line. The belt line starts from 255-mm from floor level and the gutter level ends at 395 mm from the floor level. At each height, the flow was measured at four positions from the side window at distances of 10, 20, 40 and 60 mm. The probe was secured to the floor of the Tunnel. A fully automatic traversing gear (2 linear and 1 rotational) connected and controlled by computer was used to position the probe tip at various locations from the side window. The tunnel test speeds were 80, 100, and 120 km/h. The local velocity was normalised by dividing by the free stream velocity and turbulence intensity was calculated from the time history flow properties (orthogonal velocity components of u, v and w).

Flow visualisation was also carried out in the A-pillar region of the model to supplement the flow measurement data. Flow visualisation with wool tufts was conducted with and without the external rear view mirror at 40, 80, 100 and 120 km/h. As discussed before, the model was not yawed. Flow structures were documented with video and still cameras.

Results and Discussions

The normalised velocity and turbulence intensity were plotted against the distance from the side window. Only the longitudinal velocity and turbulence intensity (Iu) variations with the distance from the side window will be discussed here. For simplicity and for the comparison with simplified models, local normalised velocity and turbulence intensity against the distance was plotted in two vertical increments. These two vertical increments were approximately ½ (305 mm) and ¾ (380 mm from the floor) distance from the window belt line towards the roof. The normalised velocity and turbulence intensity against the distance from the side window for two speeds (80 and 100 km/h) are shown in Figure M.2, Figure M.3, Figure M.4 and Figure M.5.

In all figures, the letter 's' indicates that the model was wrapped with a skirt and the letter 'f' indicated the model was free of wrapping, i.e., the standard model permitting underbody airflow.

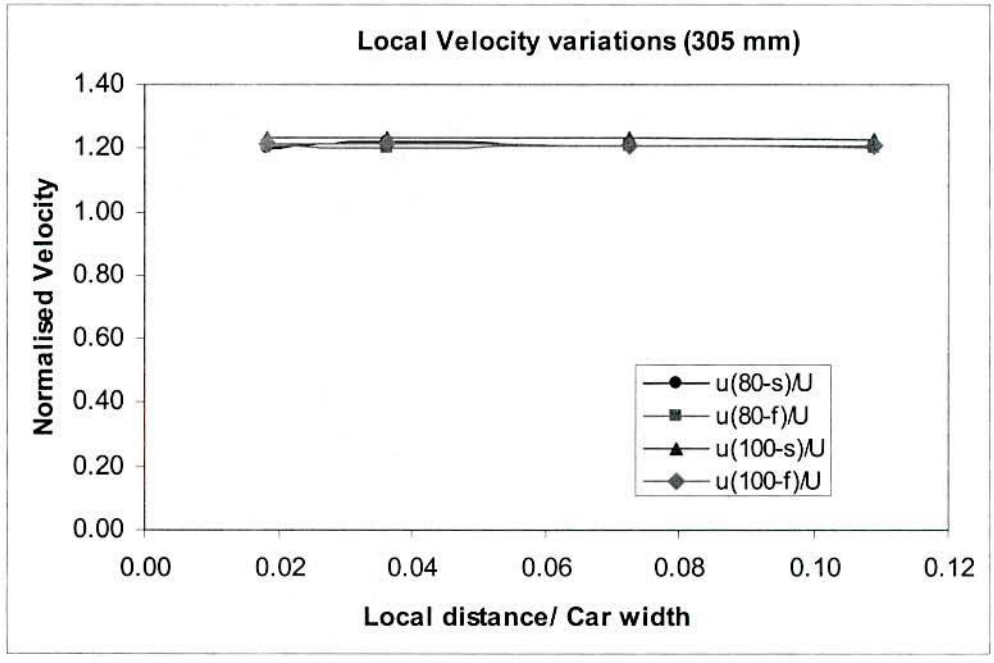

Figure M.2: Normalised Local Velocity Variations, Height = 305 mm

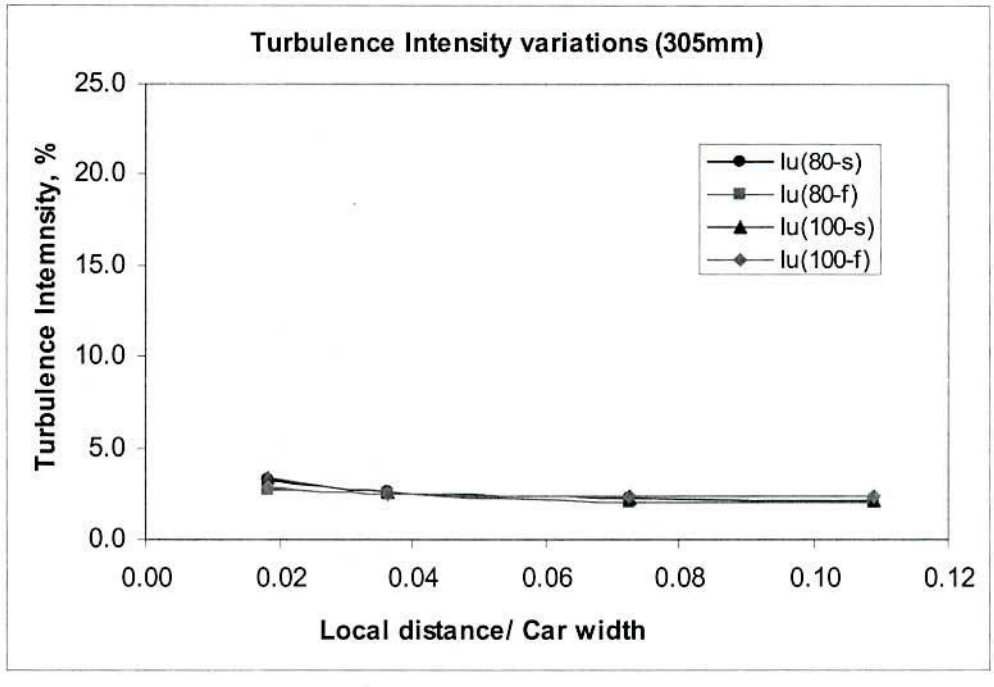

Figure M.3: Longitudinal Turbulence Intensity Variations, Height = 305 mm

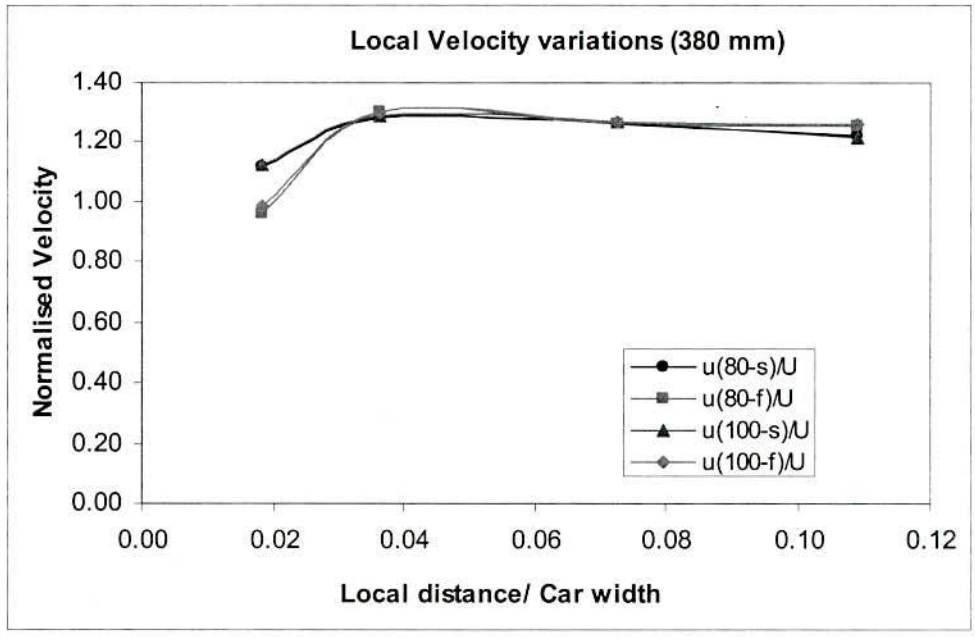

Figure M.4: Normalised Local Velocity Variations, Height = 380 mm

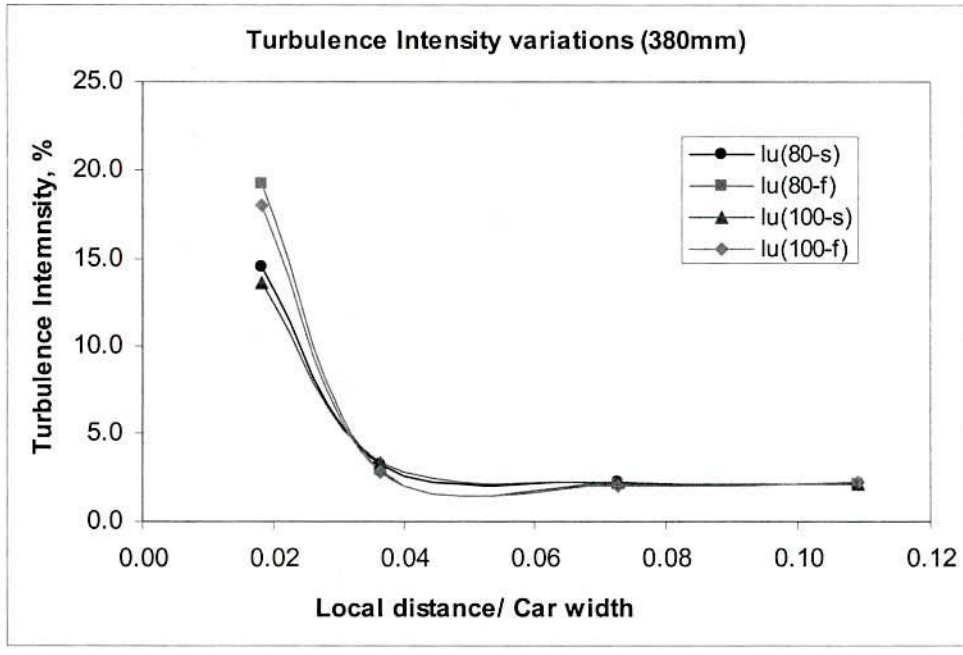

Figure M.5: Longitudinal Turbulence Intensity Variations, Height = 380 mm

The normalised velocity does not vary significantly with the distance from the side window at a vertical distance of 305 mm (which is the middle of the side window), see Figure M.2. The figure also shows that the skirt has no significant effect on the velocity. However, some velocity variations due to underbody flow are evident in Figure M.4. The magnitude of normalised velocity with underbody flow is less than

the magnitude of the no underbody flow case close to the side window surface. But the difference disappears with distance from the side window as the local flow approaches the free stream velocity.

The underbody flow has no effect on the turbulence intensity variations with distance from the side window for the vertical distance of 305 mm (Figure M.3). However, for the position of 380 mm (close the rooftop) the trend for the turbulence intensity is not similar (Figure M.5). The magnitude of turbulence intensity of the underbody flow case is higher than that of no underbody flow case close to the side window surface. But the effect of underbody flow on the normalised velocity and turbulence intensity is not significant for other cases.

Conclusions

Based on the above discussion, the following conclusions can be drawn:

- The underbody flow has no significant effect on the flow (local velocity and turbulence intensity) along the vertical plane of the side window in the A-pillar regions. However a small variation has been noted close to the rooftop.
- A simplified model without underbody flow can be tested for the study of flow in the A-pillar regions as it is well beyond the influence of the tunnel floor's boundary layer.